CENTRIFUGE AND NUMERICAL MODELLING OF SOFT CLAY-PILE-RAFT FOUNDATIONS SUBJECTED TO SEISMIC SHAKING

SUBHADEEP BANERJEE

NATIONAL UNIVERSITY OF SINGAPORE
2009

CENTRIFUGE AND NUMERICAL MODELLING OF SOFT CLAY-PILE-RAFT FOUNDATIONS SUBJECTED TO SEISMIC SHAKING

SUBHADEEP BANERJEE
(M.Tech., IIT Roorke)

A THESIS SUBMITTED

FOR THE DEGREE OF DOCTOR OF PHILOSOPHY

DEPARTMENT OF CIVIL ENGINEERING

NATIONAL UNIVERSITY OF SINGAPORE

2009

“If we knew what it was we were doing, it would not be called research, would it?”

……. Albert Einstein

ACKNOWLEDGEMENTS

This thesis represents the hard work of many individuals to whom I could never express the extent of my gratitude. First and foremost, I express my sincere and profound gratitude to my supervisors, Prof. Lee Fook Hou and Asst. Prof. Goh Siang Huat for their erudite and invaluable guidance throughout the study. Their gratitude, analytical and methodical way of working has inspired me and under their guidance I have learned a lot. Whether the troubleshooting for the centrifuge experiments or the debugging of the constitutive relationship, they have always a number of solutions at their disposal. Prof. Lee and Dr. Goh's assistances during the preparation of this thesis are also appreciated.

I am extremely grateful to Dr. Zhao Pengjun for sparing his valuable time to give me necessary training and suggestion on shaking table and centrifuge operation before the test.

Grateful thanks are extended to the staff of the Geotechnical Centrifuge Laboratory, National University of Singapore for their assistance rendered throughout the study. Mr. L. H. Tan and Mr. C. Y. Wong had been extremely helpful during the centrifuge tests. Madam Jamilah, Mr. H. A. Foo and Mr. L. H. Loo provided all the necessary expertise and support during the advanced triaxial and resonant column tests. Mr. Shaja Khan, Mrs. Leela and Miss Sandra generously provided all the transducers and computer facilities.

I wish to thank all the final year students and the exchange students, of which Ma Kang from China and Celine Barni from France need special mention, for their constant help in those grueling days of experiments.

The friendship and collaboration with a number of my fellow graduate students has also been invaluable. Special thanks are given to Mr. Xiao Huawen, Mr. Sanjay Kumar Bharati, Mr. Yi Jiangtao, Mr. Yeo Chong Hun, Mr. Zhao Ben, Mr. Sindhu Tjahyono, Miss Gan Cheng Ti, Mr. Chen Jian, Mr. Karma, Mr. Krishna Bahadur Chaudhary, Mr. Tan Czhia Yheaw, Dr. Ong Chee Wee, Dr. Xie Yi, Dr. Teh Kar Lu, Dr. Cheng Yonggang, Dr. Ma Rui, Dr. Zhang Xiying, Dr. Okky Ahmad Purwana and Dr. Gu Quian. Mate, if I miss your name, call me; I will buy you lunch!

I would also like to acknowledge NUS for providing all necessary financial and academic support without which my Ph.D. would have been a distinct dream.

Words are not enough to thank my family for the support they have given me during this long and often difficult journey. I can only grab this opportunity to remember their endless support to my pursuit of higher education.

A final word for all of you, who have been asking for the last one year, "When are you submitting ?" Well. Its my turn now!!

TABLE OF CONTENTS

SUMMARY

The behavior of pile foundations under earthquake loading is an important factor affecting the performance of structures. Observations from past earthquakes have shown that piles in firm soils generally perform well, while those installed in soft or liquefiable soils are more susceptible to problems arising from ground amplification or excessive soil movements.

The current thesis presents the details and results of a study on the seismic response of pile-raft systems in normally consolidated kaolin clay due to far-field earthquake motions. The research comprises four major components: (1) element testing using the cyclic triaxial and resonant column apparatus to characterize the dynamic properties of kaolin clay, the results of which were subsequently incorporated into a hyperbolic-hysteretic constitutive relationship; (2) dynamic centrifuge tests on pure kaolin clay beds (without structure) followed by 3-D finite element back-analyses; (3) dynamic centrifuge tests on clay-pile-raft systems and the corresponding 3-D finite element back-analyses and (4) parametric studies leading to the derivation of a semi-analytical closed-form solution for the maximum bending moment in a pile under seismic excitation.

The element test results showed that strain-dependent modulus reduction and cyclic stiffness degradation feature strongly in the dynamic behaviour of the clay specimens. In the centrifuge tests involving uniform clay beds without piles, the effects of modulus reduction and stiffness degradation were manifested as an increase in the resonance periods of the clay layers with the level of shaking and with successive earthquakes. For the pile systems tested, the effect of the surrounding soft clay was primarily to impose an inertial loading onto the piles,

thereby increasing the natural frequency of the pile over and above that of the pile foundation alone. There was also some evidence that the relative motion between piles and soil leads to aggravated softening of the soil around the pile, thereby lengthening its resonance period further.

In terms of the bending moment response, the maximum bending moment was recorded near the fixed head connection between the pile and the raft. The bending moment was found to increase almost linearly with the scaled earthquake ground motion. It was also observed that the bending moment increases with the flexural rigidity of the pile material and with increasing added masses on the pile raft.

The centrifuge model tests were back-analysed using the finite element code ABAQUS. The analyses, which were carried out using a user-defined total-stress hyperbolic-hysteretic constitutive relationship (HyperMas), gave reasonably good agreement with the experimental observations. The ability of the numerical model to reasonably replicate the centrifuge tests suggests that the former may be used to analyze conditions not considered in the centrifuge experiments, as well as to carry out sensitivity studies. To facilitate the parametric studies, the method of non-dimensional analysis, using Buckingham-π's theorem, was carried out to derive the dimensionless terms associated with the maximum bending moment in a seismically loaded pile. The resulting semi-analytical solution for the maximum bending moment was calibrated through parametric studies involving the pile length, moment inertia, pile and soil modulus, mass of the raft and peak ground motion.

Key words: earthquake, pile, soft clay, stiffness degradation, strain softening, resonance period, amplification, bending moment, dimensionless groups

LIST OF TABLES

LIST OF FIGURES

LIST OF SYMBOLS

a_0	Frequency ratio
a_b	Bedrock acceleration
c_u	Undrained shear strength
d	Diameter of the pile
D	Damping ratio
d_e	Equivalent diameter
e	Void ratio
e_0	Initial void ratio
EI	Flexural rigidity
f_i	Gravity vector
F_t	Dimensionless frequency factor for torsional motion
f_t	System resonant frequency for torsional motion
G	Shear modulus
G_{max}	Shear modulus at very small strain
G_s	Specific gravity of the soil
G_{sec}	Secant shear modulus
l_c	Critical length
l*	Slenderness ratio
l_p	Length of the pile
M	Friction coefficient
m	Mass of raft
M_{max}	Maximum bending moment

M^*	Dimensionless bending moment
OCR	Over consolidation ratio
p'	Mean effective stress
p	pore pressure
P_a	Atmospheric pressure
PI	Plasticity index
q	Deviator stress
Q	Shear
q_f	Deviator stress at failure
S	Tangent modulus of stress-strain curve
S_{max}	Tangent modulus at very small strain
t	Damage parameter
u_i	Displacement vector
V_s	Shear wave velocity
α	Dimensionless acceleration
β	Mass ratio
δ	Degradation index
γ	Shear strain
ε_m	Maximum strain
ε_s	Generalized shear strain
ε_{ur}	Unloading-reloading shear strain
λ	Slope of normal compression line.
κ	Recompression index
ρ	Bulk density of soil

ϕ	Angle of friction
θ	Reversal angle
σ'_{ij}	Effective stress tensor
τ	Shear stress

CHAPTER 1 INTRODUCTION

1.1 Introduction

Many cities are built overlying soft soils. These cities include Shanghai, Bangkok, Mumbai, Kuala Lumpur, Jakarta and Singapore. In such cities, pile foundations are very extensively used to achieve the bearing capacity required to support heavy super-structure loading, such as that imposed by tall buildings. Many cities, including Bangkok, Kuala Lumpur, Shanghai and Jakarta, are underlain by thick deposits of soft clays and piles are widely used as foundation elements for infrastructure. In such situations, the behavior of pile foundations under earthquake loading is an important factor affecting the integrity of infrastructures.

In Singapore, about one quarter of the land is underlain by soft marine clay with thickness ranging from 5m to 45m. The areas overlying soft clay include much of the central business district as well as many coastal areas all round the island (Pitts, 1984). Moreover, Singapore has carried out many land reclamation projects since 1960's and the reclaimed land often overlies on soft clay deposit (Figure 1.1).

Singapore is sometimes affected by earth tremors induced by far-field earthquakes occurring in Sumatra, Indonesia, more than 300 km away from the Singapore Island, most of which originate from the subduction zone in and around the Sunda Arc (Figure 1.2). Anecdotal evidences in Singapore suggest that far-field earth tremors are often most distinctly felt over areas overlying

soft marine clay (Yu and Lee, 2002, Banerjee et al., 2007). These evidences also reveal that earthquake waves propagating through the soft marine clay layer are amplified.

1.2 Performance of Pile Foundations in Soft Clay: Past Experience

The behavior of pile foundations under earthquake loading is an important factor affecting the serviceability of many essential inland or offshore structures such as bridge, harbors, tall chimney, and wharf. Wilson (1998) noted that piles in firm soils generally perform well during earthquakes, while the performance of piles in soft or liquefied ground can raise some questions.

There is a significant history of observed soil-pile interaction effects, having often resulted in pile and/or structural damage or failure. For instance, the potential significance of damage to piles was clearly demonstrated during the 1995 Kobe earthquake and more recent 2005 Sumatran earthquake. Many of these case histories have been recorded in liquefiable cohesionless soils, but the potential for adverse performance of pile-supported structures founded on soft, strain sensitive cohesive soils is also of great concern.

In the 1906 San Francisco earthquake, the most severe damage on pile-supported structures was reported along reclaimed city shorelines overlying soft bay mud (Figure 1.3). Margasson (1977) provided evidence on failure of a waterfront dock supported on pile foundation on Alaskan clay during the 1964 Alaska earthquake. The City Dock suffered a huge collapse although it was

supported on very strong 16 to 42 in diameter steel pipe piles driven to the stiff bottom clay.

The magnitude 7.8 Off-Takachi earthquake (May, 1968) and its subsequent magnitude 7.2 aftershock caused substantial damage to northern Japan. A post-earthquake inspection to a damaged bridge resting on piles driven through very soft peaty clay revealed serious cracks on the top part of the piles along with a lateral displacement of over 2ft (Tamura et al., 1973). In the 1985 Mexico City earthquake, cyclic strength degradation and subsequent loss of pile soil adhesion led to catastrophic damage of many tall buildings (Girault, 1986) (Figure 1.4). Comprehensive studies on failure of highway systems in 1989 Loma Prieta earthquake, also revealed gap and slippage formation of soft organic soil due to cyclic shearing (Figure 1.5). Figure 1.6 shows a schematic diagram of tilting of a tower block during 2001 Bhuj Earthquake (Dash et al., 2009). The soil at the site consisted of 10 m of clay overlaid by a 12 m deep sandy soil layer. Besides liquefaction, the paper suggested that that most of the clay stratum except the top 2m undergoes cyclic failure resulting in ground deformation and cracking.

Thus performance of various pile-supported structural systems in clay under seismic excitations has been the subject of considerable attention in recent years. However, as will be shown in the next chapter, studies on the response of pile foundations in soft clay to earthquake excitation remain relatively scarce.

1.3 Current Approaches for Designing Pile Foundations Against Earthquake Loading

This section will examine the current codes of practice and approaches for designing pile foundations against earthquake loadings. Although many of these codes incorporate simplified soil-structure interaction analysis methods, they acknowledge the need for site-specific studies for piles founded on soft soils subject to strong levels of shaking.

1.3.1 Different Code provisions

1.3.1.1 Uniform Building Code

The 1997 Uniform Building Code (ICBO, 1997) and the companion Blue Book Recommended Lateral Force Requirements and Commentary (SEAOC, 1996) do not provide any particular requirements for consideration of soil-structure interaction. However, Chapter 18 of the UBC, "*Foundations and Retaining Walls*", provides minimal design guidelines for foundation construction in high seismic zones, but emphasizes consideration of the potential for soil liquefaction or strength loss. Emphasis is also placed on the capacity of the foundation to sustain the base shear and overturning forces transmitted from the superstructure, and for the adequacy of the connections between superstructure and foundation. The SEAOC recommendations call general attention to cyclic degradation, pile group effects, pile cap resistance, pile flexure and ductility, and kinematic loadings, but offer no specific requirements for design. Chapter 16 of the UBC, "*Structural Design Requirements*", considers both response spectrum and time history analyses

for earthquake design; however there are no provisions to account for soil-structure interaction in either method. In short, the UBC partially addresses pile integrity under kinematic and inertial loadings, but does not explicitly account for the influence of the pile foundation on the ground motions imparted to the superstructure.

1.3.1.2 Eurocode recommendations

Eurocode 8 (EN 1998-5) provides some requirements, criteria and rules for foundation elements against earthquake forces. According to Clause 5.4.2(1), under seismic conditions, the pile should be designed to resist the inertial forces transmitted from the superstructure onto the head of the pile. The pile needs to be checked for the effect of kinematic soil movement only for some relatively infrequent cases (eg. high seismic zone with soft liquefiable soil).

The code recommends that, in almost all cases, the pile-soil interaction can be treated as an elastic problem. However, it also suggests that, if the elastic theory can not be applied, then a full non-linear approach, such as one involving p-y curves, should be adopted. Clause 5.4.2(1) reads *"… the calculation of the transverse resistance of a long slender (i.e. flexible) pile may be carried out using the theory of a beam loaded at the top and supported by a deformable medium characterized by a horizontal modulus of subgrade reaction…"*.

For problems where kinematic interaction can not be ignored, the idealized equivalent static soil deformation should be imposed statically at the

supports of the springs of the beam-on-elastic foundation model, in addition to the usual inertial loads acting on the pile head.

Hence, Eurocode 8 acknowledges the importance of accounting for soil-pile interaction in a more fundamental manner, although the recommendations are still largely predicated on simple, equivalent pseudo-static approaches.

1.3.1.3 Caltrans Bridge Design Specifications

The current Caltrans Bridge Design Specifications (ATC-32) includes specific recommendations for the seismic design of pile foundations. According to the specification, inelastic static analysis (push-over method) is only required for important bridges. Inelastic dynamic analysis may be performed in place of inelastic static analysis; but the type of soil-pile model for these inelastic analyses is not specified by ATC-32.

It also acknowledges that the methods recommended only account for inertial loading from the superstructure into the piles, and do not consider the effects of kinematic loading on the overall response of the structure.

In summary, the ATC-32 guidelines do not represent the state-of-the-art for soil-pile interaction, as a detailed nonlinear foundation model can be uneconomical for complex bridge structures.

1.3.1.4 Indian Seismic Code Recommendations

The Indian earthquake code of practice (IS-1893; 2002) does not explicitly incorporate soil-structure interaction into the design practice. Even

though it provides some rough guidelines for shallow footings, it does not mention any special requirement for pile foundations.

In liquefiable soils, the code states that piles should be designed for lateral loads, ignoring the lateral resistance of the soil layer that is likely to liquefy. The effect of soft soils, however, is not explicitly considered in the code.

1.3.1.5 People's Republic of China Aseismic Building Design Code

The People's Republic of China Aseismic Building Design Code (PRC, 1989) recognizes the beneficial effects of soil-structure interaction in period lengthening and increased damping for longer period structures, thereby decreasing design forces. However, it does not consider the potentially unconservative force increase for very short period structures; nor does it recognize potentially greater displacements due to rocking. With respect to piles, the code requires piles in liquefiable layers to have minimum embedment in more stable layers, but this requirement ignores the damage potential arising at the interface between two zones of hjghly contrasting soil stiffnesses.

1.3.1.6 Japanese Seismic Design Specifications

Japanese seismic design of pile foundations is usually adopted to counter liquefaction which has historically been the major seismic hazard for pile foundations in Japan. The 1990 specifications included revisions that addressed the classification of ground conditions, the inertia forces applied to substructures, the provision of column ductility, and improvements in evaluating the resistance of sandy soils to liquefaction.

Unjoh and Terayama (1998) published a translation of the complete Seismic Design Specifications of Highway Bridges, issued by the Japanese Public Works Research Institute in 1996 to reflect the lessons learnt from the 1995 Kobe earthquake. The 1996 code provides detailed guidelines for the design of foundations at sites vulnerable to soil instability. Apart from the assessment of liquefaction potential, these guidelines consider the decrease in bearing capacity of weak cohesive soils.

1.3.2 Current State-of-Art Practice for Seismic Soil-Pile-Interaction Design

Due to the complexity of the problem and the unavailability of standardized and validated analysis techniques, designers routinely ignore or greatly simplify the presence of pile foundations in their analyses (Hadjian et al., 1992). Instead of a unified system, soil-structure interaction problems are often broken into two disciplines, geotechnical and structural engineering. As such, a geotechnical engineer may idealize a complex multimode superstructure as a single degree of freedom oscillator and the structural engineer will often represent the potentially nonlinear soil-pile interaction with a simple linear spring.

Hadjian et al. (1992) conducted a global survey of eminent design professionals to ascertain the then state-of-practice with respect to the seismic response of pile foundations. The report revealed that engineers often ignored seismic soil-pile interaction effects or at most considered them in a simplified fashion. For example, a geotechnical designer would provide load-deflection and -moment diagrams to the structural engineer, who would in turn select a

foundation spring value to be used in the structural analysis. Although the load-deflection and moment diagrams are usually developed with nonlinear soil-properties in a "p-y" type analysis, this nonlinearity is lost when the structural engineer ignores the strain and frequency dependence of the loading. In short, Hadjian et al. (1992) identified the uncoupling of the analysis between the geotechnical and structural engineer as a prime limitation on advancing the state-of-practice in this field.

At a 1994 ASCE Technical Workshop on the Lateral Response of Pile Foundations in San Francisco, representatives from major geotechnical engineering firms discussed a variety of methods for analysis of lateral loading of single piles, ranging from simplified chart solutions to the advanced computer codes (Meymand, 1998). Group effects were treated with Poulos' elastic/static interaction factors and empirical results from Reese (1990). Finally, the lateral response of piles in liquefaction-susceptible soils was addressed with a method for degrading the p-y curves based on soil index properties.

To analyze earthquake and liquefaction-induced pile curvatures, two methods were outlined. The first method involves using a site response analysis (i.e. SHAKE91) to determine the soil displacements with depth, and then imposing these as far-field displacements on the pile to compute the moment and shear distributions along the pile. The second method involves using a nonlinear dynamic 2-D or 3-D finite element analysis (i.e. SASSI) that models both piles and soil.

Meymand (1998) commented that the first approach was conservative in that it did not account for soil-pile interaction. On the other hand, the

second approach is complex, costly to implement, and does not capture important soil-pile interface nonlinearities.

In order to standardize the design practice of bridge piles in soft California Bay Mud, Abghari and Chai (1995) attempted to couple the substructure and superstructure components of the soil-pile-interaction problem by modeling a single pile extracted from a pile group that incorporated the superstructure contribution to that pile. A SHAKE91 (Idriss et al., 1990) site response analysis was carried out, and the resultant free-field displacement time history was applied to nodal points of the dynamic soil-pile interaction code PAR.

Lam and Kapuskar (MCEER-98-0018) proposed another design methodology which was also based on the idea of breaking down the soil-pile-structure system into two uncoupled problems, the superstructure and the foundation, and then finding solutions to each that were compatible with the expected response of both parts. In the first step of the analysis, the linear dynamic response of the superstructure is calculated by replacing the foundation with a set of springs that represent the effective foundation stiffness. The structure and foundation system is then analyzed using a nonlinear push-over analysis, where the superstructure was statically pushed to the displacement level established in the linear dynamic analysis step. The pseudo-static response of the foundation was modeled using Beam-on-Nonlinear-Winkler-Foundation method. The design procedure, however, completely ignored the inertial loads imposed by the surrounding soil mass.

Recently, Puri and Prakash (2008) reviewed the current design procedures of pile foundations in soft or liquefied soils, stating that the common methods currently in use for design of piles in liquefying soil are ;

1. The force or limit equilibrium analysis and
2. The displacement or p-y analysis.

The foregoing discussion suggests that the nonlinear dynamic analysis of piles incorporating superstructural effects, has not been adequately addressed in engineering practice. Instead, approximate methods for extending psudo-static single pile analyses to the complex problem are commonly adopted. These methods ignore two important features of seismic response: kinematic interaction between pile and soil, and the effects of ground motion on the stiffness of the foundation soils. Kinematic bending moments are important whenever there is a sharp difference in stiffness between adjacent layers. It is particularly important at soft clay sites (Finn, 2005). The potential importance of kinematic moments is also recognized by Eurocode 8: Part 5, which specifies the conditions under which kinematic interaction should be taken into account.

1.4 Overview of Soil-Pile Interaction

The principal characteristics of seismic soil-pile- interaction (SSPI) for an individual pile are illustrated schematically in Figure 1.7. The system components include the superstructure, the pile cap, the pile(s), the soil (here idealized into near field and far field domains), and the seismic energy source.

The modes of system interaction include kinematic, inertial, and physical interaction, and radiation damping, and are described below.

Kinematic interaction is the seismic response of the soil profile transmitted to the pile foundation, which attempts to deform with the soil, and results in the superstructure experiencing a different ground motion than the "free-field" soil. Inertial interaction consists of structural inertial forces being transferred to the pile foundation. These forces impose lateral loads which are concentrated near the pile head, and axial loads on the pile, if the structure has significant rocking modes. Important physical interactions between the pile and soil occur before and during seismic loading. During initial pile installation and loading, soil displacement, load transfer, and downdrag forces set up a unique stress state in the pile and surrounding soil, upon which any seismically-induced stresses will be superimposed. During seismic loading, gaps may open between the soil and the pile near the ground surface; in cohesionless soils, the gap may fill in and be compacted; however in cohesive soils, the gap may stand open, resulting in a reduction of soil-pile lateral stiffness. If submerged, water alternately drawn in and ejected from the gap during each load cycle may scour the soil adjacent to the pile, resulting in a further reduction of stiffness. Radiation damping occurs due to the stiffness contrast between the soil and pile. Piles vibrate at much higher frequencies than the surrounding soil, but soil-pile contact forces the soil to also vibrate at these high frequencies, resulting in the transmission of high frequency energy away from the pile into the surrounding soil. Radiation damping is most pronounced at high frequencies and low levels of soil damping, and cannot propagate through "gaps" opened between the pile and soil. The pile cap and

the super-structural load can also be an important source of radiation damping. However, above interaction has not considered the fact that clay usually behaves in a non-linear, strain-softening manner and it may suffer from stiffness degradation with successive cycles. It is thus evident that SSPI in a non-linear, strain-softening, degrading material such as clay is a complex issue that merits serious study.

1.5 Objectives

In this project, the problem of soil-pile-raft interaction in soft clay during seismic events will be examined using an experimental approach involving dynamic centrifuge model tests and numerical back-analyses using non-linear soil models to model the soft clay.

The main objective of the study is to understand the effects arising from stiffness degradation of the clay structure due to repetitive shaking over several earthquakes, which affect the predominant period and amplification of free-field ground motion and, more importantly, its effects on pile foundation installed into soft ground during earthquake events.

In addition to centrifuge model tests, triaxial and resonant column tests are also conducted to investigate the behaviour of soft kaolin clay subjected to cyclic loading. Based on these tests, a hyperbolic-hysteretic total stress model is developed to replicate the highly non-linear stiffness degrading behavior of kaolin clay under dynamic condition.

The third and final objective of this research is to develop a rational framework for designing pile for earthquake excitations.

1.6 Organization of Thesis

This PhD thesis consists of seven chapters. Chapter 2 discusses previous work done in the area of dynamic soil-pile interaction. Through an examination of current literature, it will be demonstrated that there is a need for more research on soil-pile interaction with emphasis on soft soil degradation

In this context, Chapter 3 discusses results of the triaxial and resonant column tests. This is followed by formulation of the proposed non-linear total stress soil model.

A detailed description of centrifuge modeling techniques, scaling relations and experimental set-up along with the tests observation on kaolin clay in absence of any structure is given in Chapter 4. Numerical back-analyses are also conducted to simulate the centrifuge tests. This chapter provides some critical insight on behavior of kaolin clay under earthquake loading.

Then Chapter 5 describes the results of the centrifuge tests on different clay-pile-raft systems. The centrifuge results will then be compared with the ABAQUS back-analyses.

In Chapter 6, the numerical analyses will then be extended to a series of parametric studies. The objective of these parametric studies is to develop some framework for estimating the maximum bending moments developed in piles under earthquake loading.

Finally, some important conclusions and findings along with a few recommendations for the further studies are given in Chapter 7.

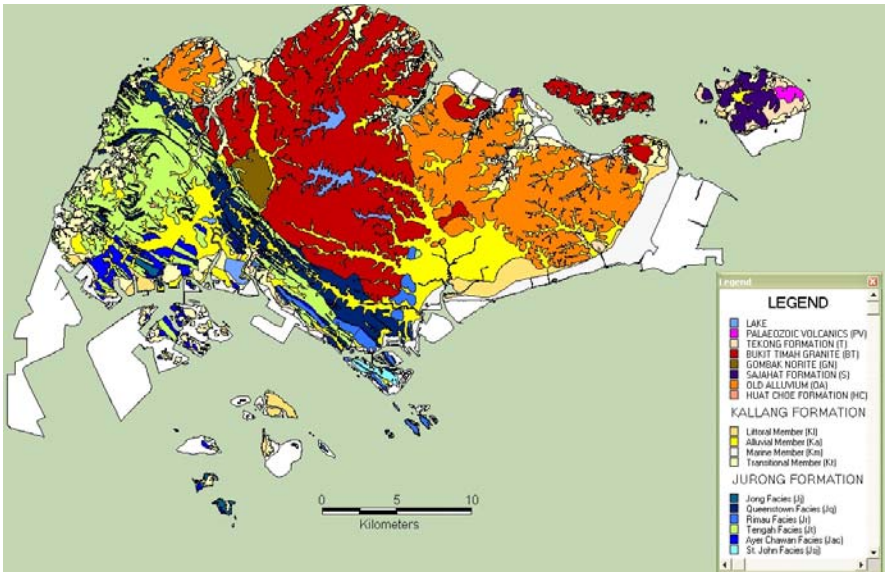

Figure 1.1 Geological map of Singapore (Pan et al., 2007)

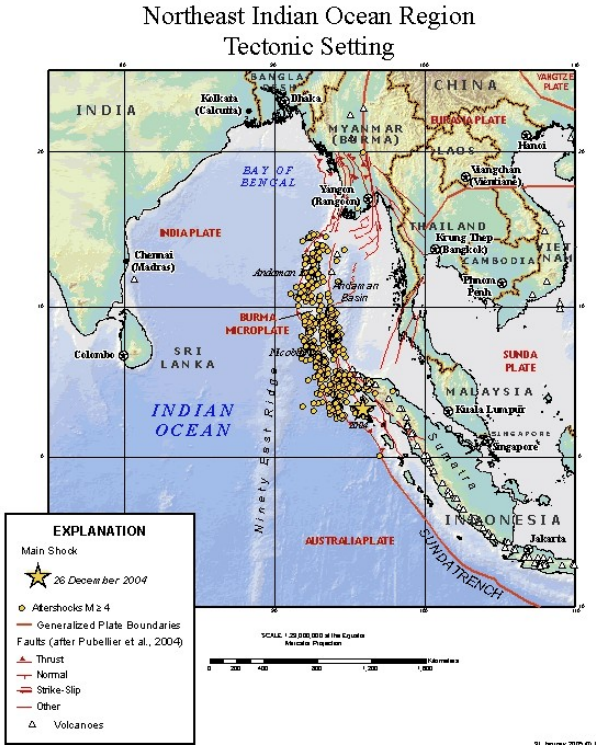

Figure 1.2 Plate tectonics of Indian ocean region (Source: USGS)

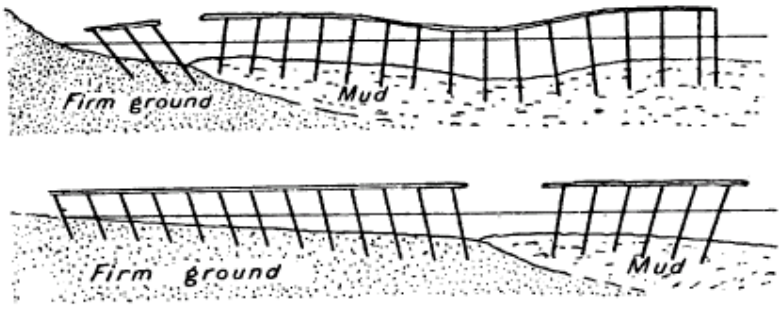

Figure 1.3 Pile failures in 1906 San Francisco earthquake (Wood, 1908)

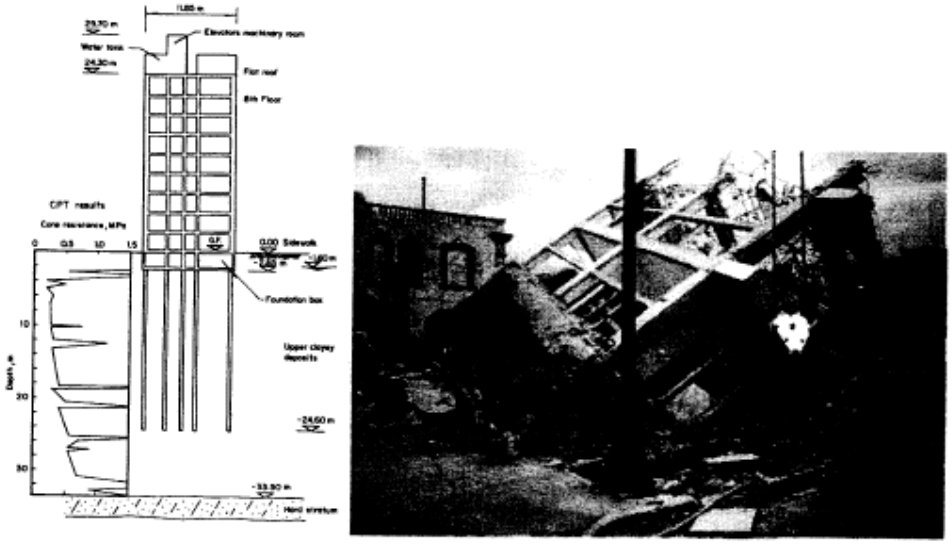

Figure 1.4 Failure of pile supported ten-storey building during 1985 Mexico earthquake (Mendoza and Auvinet, 1988)

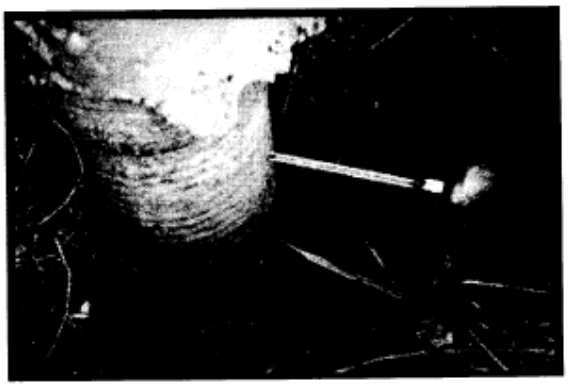

Figure 1.5 Formation of gap during 1989 Loma Prieta earthquake (Seed et al., 1990)

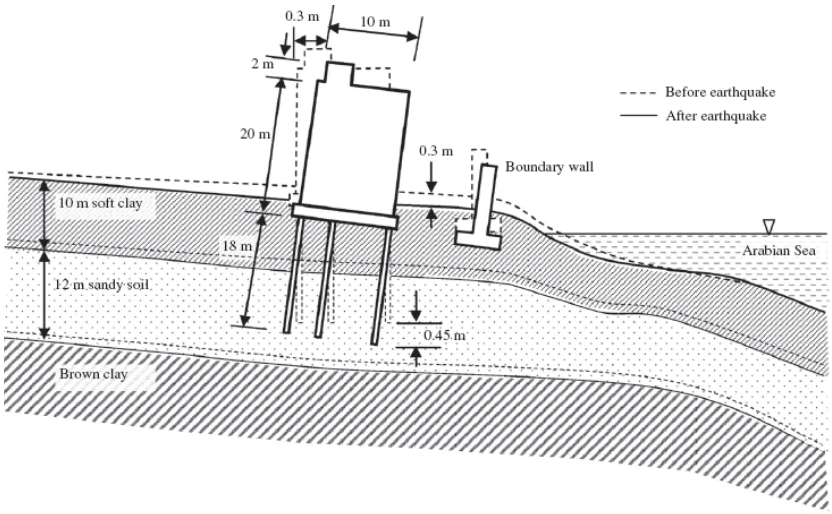

Figure 1.6 Tilting of a tower block during 2001 Bhuj Earthquake

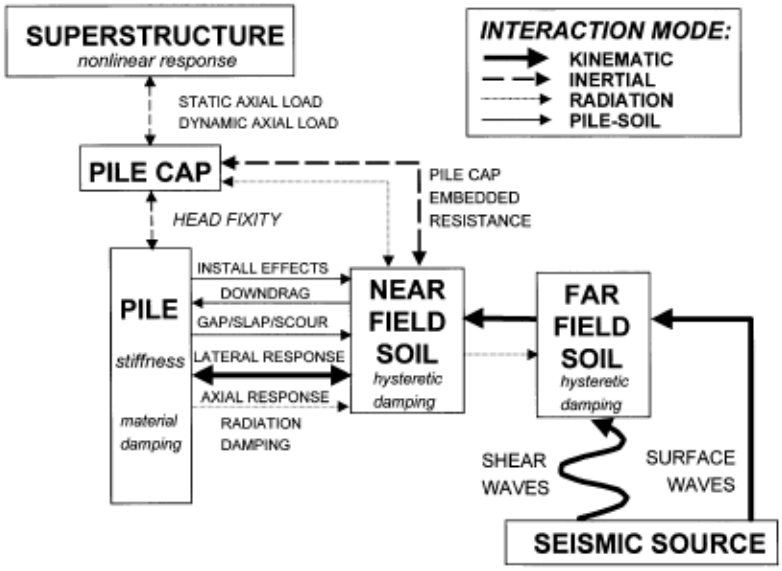

Figure 1.7 Soil-pile interaction (Meymand, 1998)

CHAPTER 2 LITERATURE REVIEW

2.1 Dynamic Soil-Pile Response

2.1.1 Empirical Charts and Design Procedures

Since early 70's pile-soil response has been extensively studied to fulfill the demands of two sectors, offshore oil production activities, and to a lesser extent, the nuclear power industry (Meymand, 1998). Since then various design procedures, empirical charts and methodologies have been developed for clay-pile interaction. Barkan (1962) proposed one of the first such empirical design methodologies for machine foundation problems from laboratory cyclic load tests. Fukuoka (1966) later used Barkan's method for designing of foundation of bridge piers in Niigata. Richart et al. (1962) proposed some design charts to calculate resonant frequency of soil-pile systems which consider the effects of axial load, pile length and pile material (Figure 2.1). For pipe piles, stiffness and damping ratio can be calculated. An approximate graphical technique was also introduced by Novak (1974) to derive stiffness and damping ratio of piles and pile group embedded in a linear elastic soil. Later Prakash and Chandrasekaran (1977) modified Novak's analysis for non-homogeneous soil the stiffness of which increases with depth. This method seemed to work well with sand and small harmonic excitations. Novak and El-Sharnouby (1983) included solutions for shear modulus decreasing upward in a quadratic manner for piles. Sheta and Novak (1982) presented an approximate design method for pile groups that accounted

dynamic group interaction, weakening of soil around pile because of high strain, soil layering and arbitrary tip condition but method seemed to fail for loose sand and soft clay. Hence it can be concluded that none of the above procedures and charts is universally accepted as they tend to be quite site-specific.

2.1.2 Analytical Methods

For relatively flexible piles in stiff soils, soil-pile-structure interaction may be reasonably modelled by applying the free field ground surface motion to a set of springs at the pilehead representing the stiffness of the foundation. In the case of stiff piles that penetrate through soft soil deposits it is important to have a procedure to account for the dynamic interaction between the various layers of soil, the pile, and the superstructure (Wilson, 1998). Three approaches in numerical modeling have been used to study seismic pile-soil interaction problems

1. Elastic continuum approach,
2. The lumped mass model and
3. Finite element methods.

2.1.2.1 Elastic Continuum Approaches

In this approach, the pile is considered as a beam on an elastic foundation subjected to time-dependent loading and analyzed by finite differences. Moment, stresses and displacements along the length of the pile may be analyzed, and impact loads as well as harmonic loads can be incorporated (Matlock and Resse, 1960). Most of the methods are based on the

solution of a beam on an elastic foundation with the governing differential equation,

$$\frac{d^4x}{dz^4} = (\alpha k_h + k_0)^n x \tag{2.1}$$

(Howe, 1955; Matlock and Reese, 1960; Bowles, 1974), where z is the depth and x is the lateral displacement.

Equation 2.1 exactly defines the problem if the boundary conditions can be evaluated and if $(\alpha k_h + k_0)^n$ correctly defines the lateral modulus of subgrade reaction at all points along pile.

Penzien et al. (1964) were some of the first researchers to present a method for seismic pile response analysis, and focused their efforts on the problem of bridge structures supported on long piles driven through soft clays. They constructed a multi-degree of freedom discrete parameter system for modeling the soil medium response initiated by seismic base excitation. Their dynamic computation, however, were found to be quite insensitive to effective clay masses.

Agarwal (1973) used discrete-element method to develop an analytical approach for pile under harmonic lateral load assuming soil as infinitely closely spaced springs. The governing differential equation of the pile vibration included the viscous damping as well as pile and soil mass.

Using similar approach, Novak (1974) proposed an approximate analytical method, assuming linear elasticity, to obtain closed-form solution for pile stiffness and damping. The method was particularly useful for high frequency machine vibrations.

Subsequently, Singh et al. (1977) working with Novak's method, proposed a single degree of freedom mass spring dashpot model termed as "Equivalent Cantilever Concept".

Dobry (1982) also proposed simple expressions developed for the horizontal spring and damping coefficients as a function of soil-pile relative stiffness at the top of an end bearing pile embedded in a uniform linear soil.

Nonlinear soil pile (p-y) spring used by Matlock et al. (1978) is another simplified approach that can account for nonlinear soil-pile-structure interaction (Figure 2.2). The p-y curves, however, were mostly calculated from static and cyclic lateral load tests on single pile .

Kagawa and Kraft (1980) developed a nonlinear dynamic Winkler model using the equivalent linear method. The pile was modeled by a continuous beam with near field soil elements comprised of parallel springs and dashpots, and with superstructure elements that generated the inertial component of response. The input excitation applied as lateral ground displacements at the end of the near-field soil elements. As an extension, Wang et al. (1998) included a linear "far-field" spring in parallel with the radiation damping dashpot, and that combination in series with a non-linear "near-field" spring.

Trochanis et al. (1991) showed that the response of laterally loaded piles predicted using a non-linear soil spring formulation agreed well with static load test data and nonlinear 3-D finite element analyses. Trochanis et al. (1991) used a degrading constitutive model developed by Wen (1976) to represent the p-y springs.

Shen and Teh (2004) also proposed a variational solution for laterally loaded piles. The soil was modeled using a simple spring-dashpot model the stiffness of which could be increased with depth.

A number of advanced analytical models have also been introduced to study the dynamic stiffness and damping ratio of pile-soil system (e.g. Gazetas et al., 1983; Budhu and Davies, 1987 and 1988; Saha and Ghosh, 1986; Liu and Novak, 1994). Most of these studies considered both inertial and kinematic effects in their dynamic analysis. However, their application are mostly limited to harmonic or cyclic type of loadings.

Almost all the researchers mentioned above, had acknowledged that it is very difficult to get a closed-form solution of pile-soil interaction problem under earthquake loading without making certain assumptions. Consequently, the usage of such solutions is often restricted to highly simplified geometries, uniform soil conditions or idealized loadings.

2.1.2.2 The Lumped Mass Model

In practice, pile cross sections, soil conditions and loading conditions may vary with depth. For complicated geometries, it may be impracticable to obtain closed form solutions on the dynamic response of piles. For such situations, numerical solutions have been obtained by discretizing the pile and and lumping its mass at various nodal points (Chandrasekaran and Prakash, 1980; Chandrasekaran et al., 1987) (Figure 2.3). The effects of the surrounding soil may also be discretized using the series of linear Winkler springs. This renders the number of degrees of freedom of the system finite

and the system's dynamic characteristics could be evaluated using suitable numerical techniques. Using this approach, Chandrasekaran et al. (1987) concluded that the dynamic response of the pile subjected to earthquake was mainly governed by the variations of soil modulus with depth. They also concluded that piles embedded in sandy soils were also subjected to greater dynamic deflection and stress than those in clayey soils (Chandrasekaran et al., 1987). Finally, the stiffness of soils in the top regions controls the dynamic response of piles subjected to earthquakes. The first mode frequency and mode shapes were the principal contributing factors towards the total dynamic effect. It should be noted that all these findings were contingent upon the validity of the model used.

2.1.2.3 Finite Element Analysis

Lumped-mass models are useful in problems wherein the main complexity lies in the variation in soil properties with depth, that is, in highly layered soil profiles. Lumped mass model may not be applicable in cases involving irregular boundary condition e.g. non-horizontal or varying ground surface and abrupt or rapid changes in material properties. The finite element method has been widely used to deal with such problems.

Kuhlemeyer (1979) studied laterally loaded piles using finite element method. Solutions were obtained for both static and sinusoidal load cases, applied at the pile head. The main limitation of his analysis is that he had assumed linear elastic soil behaviour.

Kagawa and Kraft (1981a,b) also presented a finite element model to show that besides the soil reaction, factors which significantly affected the

dynamic load deflection relationships were the modulus and material damping of the soil layer.

Angelides et al. (1981) extended the study further to explore the effect of nonlinear soil behavior on the dynamic stiffness of piles using the hyperbolic constitutive model (Hardin and Drnevich, 1972) and equivalent linearization technique. The method, however, ignored the cyclic stiffness degradation of soil.

Maragakis et al. (1994) proposed a finite element model of the foundation with an equivalent linear iterative procedure to account the strain-dependent stiffness and damping of soil. This is the similar approach used earlier by Schnabel et al. (1972) and Idriss et al. (1973) in software such as SHAKE and QUAD4.

Bhowmik and Long (1991) and El Naggar and Novak (1995) showed that pile-soil relative stiffness can be greatly influenced by nonlinear behavior of the soil adjacent to the pile as well as various factors like slippage and gapping at the soil-pile interface. Their studies, however, only considered the laterally loaded piles.

Badoni and Makris (1996) reported their study on one-dimensional finite element formulation as an aid to predict dynamic response of pile under lateral loads accounting nonlinearity of soil. A single pile embedded in a layered soil and subjected to lateral motion was considered as a linear elastic beam with circular cross-section and subsequently the surrounding soil was assumed to be as inhomogeneous deposits whose geotechnical properties such as density, shear wave velocity, angle of internal friction etc. varies with depth. The soil-pile interface was modeled as a Winkler foundation interacting

with the pile through continuously distributed nonlinear springs and dashpots. Thus, finite element formulation actually reduced the problem to the analysis of a beam on a nonlinear Winkler foundation. They commented that, under low frequency excitation, pile response is dominated by non-linear soil behaviour. However, as the frequency increases the component of soil reaction due to radiation damping increases and the non-linear characteristics of the responses become less dominant.

Zhang et al. (2000) simulated quasi-static field tests on a pile foundation with a three-dimensional elasto-plastic finite element analysis (DGPILE-3D). In the numerical analysis, particular attention was paid to the stress-strain relation of the soil. Different constitutive models, including the Drucker-Prager model and Cam-clay model were used in the analysis to investigate the differences in the results arising from different constitutive models. Based on the analysis, the authors proposed a numerical method for evaluating the mechanical behavior of a pile foundation subjected to cyclic lateral loading. However, cyclic degradation was not accounted in the model.

Khodair and Hassiotis (2003) incorporated nonlinear soil-pile interactions into a 3D finite element model using the finite element software, ABAQUS. Their results showed that the bending stresses along the depth of the pile calculated by the finite element model agreed well with those measured from a fully instrumented bridge.

Based on Biot's dynamic coupled consolidation theory, Huang et al. (2004) proposed a three-dimensional effective stress finite element method to predict earthquake response of pile foundations. In this paper, a cyclic non-degrading elasto-viscoplastic constitutive model was used for soft clay. They

concluded that the numerical simulation could capture the fundamental aspects of the pile-soil seismic interaction.

Hence, from the above discussions, it is found that the advent of finite element methods for the soil-pile problems started with the effort to measure the lateral response of piles under cyclic or quasi-static loadings. But their application on real earthquakes are relatively scarce. Importance of considering soil non-linearity and hystertic strain-dependent soil behaviour had been acknowledged by most of the researchers, but its systematic incorporation to FEM code still remains scarce. For simplicity, most of the FEM code ignored cyclic degradation of the soil during dynamic loading. Finally, there are extremely limited cases available where finite element results were compared with the measured response from the actual dynamic tests on pile done in field or centrifuge.

2.1.3 Field Pile Dynamic Tests

Most of the full-scale pile and pile group tests were conducted to ascertain pile stiffness under dynamic loads, rather than to assess pile response during earthquakes. The energy needed to simulate earthquake effects on prototype piles are too large to be realistically applied artificially (Meymand, 1998). In these tests, a mass is commonly fixed to the pile head to elicit a resonance and damping characteristics of the pile.

Ringdown tests consist of quickly releasing the pile from some imposed, initial lateral displacement, and measuring the ensuing free vibrations of the pile as it attempts to rebound to its original position (Alpan,

1973; Gyoten et al., 1980). Pile stiffness and damping values can be derived from measurements of the free vibration response of the pile by the logarithmic decrement method.

Impact tests are an even smaller strain version of a ringdown test, where a blow to the pile generates free vibrations in the pile to be measured (Puri and Prakash, 1992). Forced vibration tests involve mounting an eccentric mass shaker to the pile head, whose motors spin eccentrically fixed masses, thereby inducing vibrations into the pile head (Hayashi et al., 1965; Ishi and Fujita, 1965; Blaney et al., 1987; Han and Vaziri, 1992). By adjusting the orientation, motor speed, and fixed mass, this test offers the flexibility of generating horizontal, vertical, or rocking vibrations over a range of frequencies and amplitudes. Electrodynamic oscillators are also employed in forced vibration tests, and can deliver much higher frequencies to the pile head than the mechanical type, which is limited to about 100 Hz (Sy and Siu, 1992). Soil-pile stiffness and damping can be interpreted directly from the test data resonance curves with the half-power bandwidth method. Comparisons of observed and predicted behavior are good when the response remains linear and soil elastic properties are well-characterized. Conversely, when higher load levels generate nonlinear soil-pile response, models of predicted response are less accurate (Meymand, 1998).

Lam and Cheang (1995) reported cyclic load test data which showed that the soil-pile stiffness under cyclic loading compared very favorably to the low amplitude dynamic loadings, but nonlinear response under large amplitude dynamic loads may reduce the apparent stiffness to a relatively

large extent. Figure 2.4 shows that to match the results of cyclic vibration test data at 6.12 kips, the soil stiffness parameter (f) value is reduced up to 80%.

Blaney and O'Neill (1989) reported lateral dynamic loading tests on a 3x3 group of steel pipe piles driven into over-consolidated clay. The piles used were 0.237 m dia and 13.7 m long. The load was applied horizontally through a linear inertial mass vibrator. With the measured pile responses, authors tried to provide some insights to the pile group behaviour under dynamic loading. The results obtained, however, may be useful for small piles in a shallow clay layer.

As part of a foundation investigation for a pile-supported bridge spanning a peat-filled slough near Seattle, Kramer (1993) performed forced vibration, ringdown, and impact tests on an 8 inch diameter steel pipe pile. Unfortunately, the test results of different methods were inconsistent and in some cases ran contrary to expected trends of behavior. Radiation damping in excess of 25% was recorded in the free vibration tests, and average horizontal stiffness was interpreted from the forced vibration test results. The latter value correlated reasonably well to static lateral load test results, and was therefore used in deriving the design dynamic stiffness of the pile groups.

Snyder (2004) carried out some quasi-static lateral pile load tests in soft Salt Lake City clay. The results from his study showed that the soil stiffness degraded with repeated cyclic shearing and plastic deformation of soil surrounding the pile.

Finally, brief reference is made to other noteworthy experimental programs including Fuse et al. (1992) who dynamically tested a 8x8 pile group, and Mizuno and Iiba (1992) who reported on a well-documented

parametric study of pile cap embedment depth. It will be noted that the above literature related almost entirely to forced oscillations on pile. Overall, there is a lack of well-documented seismic soil-pile response case histories, and even fewer included piles that have been instrumented to record dynamic response during earthquakes. This very limited database of instrumented pile performance during earthquakes does not provide a good basis for validation of the available analytical methods developed for seismic soil-pile-superstructure interaction problems.

2.1.4 Small-Scale Model Tests

Due to the lack of field data on pile response during earthquakes, analytical and numerical methods are quite commonly validated using small-scale model tests results. These model tests were conducted mainly to investigate the load-deformation behavior of soil-pile systems both singly and in groups, at small to large strains, loaded statically (Wen, 1955), cyclically (Matlock, 1962; Prakash, 1962), dynamically (Novak and Grigg, 1976; Kana et al., 1987; Burr et al., 1997), or seismically (Christina et al., 1999; Finn and Gohl, 1999; Fukuoka et al., 1996), by exciting the pile head or the soil mass, and covering a variety of pile types and soil conditions. The dynamic model tests on piles are mainly classified in two groups:

i) 1-g shaking table tests,

ii) Centrifuge model tests.

2.1.4.1 1-g Shaking Table Tests

The shaking table test of model piles is a useful approach to understand soil-pile interaction effects. The principal disadvantage of shaking table tests, however, is that they are conducted in a 1-g environment, and therefore cannot achieve the elevated stress field. A summary of 1-g shaking table tests programs is given in Table 2.1.

Kubo (1969) was among the earliest to present shaking table tests results which considered scale model similitude. He installed a 3x3 steel pipe pile group (3 inch dia) in dry sand. The bending moment profiles and deflections obtained from the shaking table tests were compared with the computed quasi-static prototype behavior.

Kagawa and Kraft (1981) performed some shaking table tests on model piles in sand to validate their proposed p-y method. The measured fundamental resonance frequency of the soil-pile-structure system was found to decrease from 34 to 4 Hz, indicating an intense liquefaction during shaking events. The numerical model compared favorably with the experimental results in the early and late stages of the loading sequence, but underestimated the response during the onset of liquefaction.

Mizuno and Iiba (1982) were the first to subject their models to a real earthquake time history as base excitation. They attempted to fabricate an elastic soil medium with a mixture of polyacrylamide and bentonite to partially address the scale similitude issue, and used model piles of rectangular cross-section supporting single mode model structures. Parametric studies of three building models confirmed the effects of building frequency on dynamic interaction, with pile response dominated by kinematic interaction effects at

the relatively low levels of shaking in these tests. Korgi (1986) extended these tests to investigate the effects of different soil deposits and pile cap embedment on the system response. However, this method did not consider the stiffness degradation of soil under repeated shaking.

Liu and Chen (1991) tested large groups of model piles in liquefiable sands, and investigated the effects of pile installation on densification of the foundation soils. Excess pore pressure ratios were measured to be lower in the soil adjacent to the piles than in the free-field, but quantitative conclusions could not be drawn from the test results due to erroneous stress fields in this 1-g model. The authors also acknowledged that although driven piles might densify the immediate surrounding soil, global liquefaction mechanisms could still render such foundations susceptible to lateral or bearing capacity failures.

Sreerama (1993) tested small pile groups embedded in soft clays at different spacing subjected to small amplitude base excitations in order to investigate pile group dynamic interaction. Pile stiffness and damping were computed as a function of soil shear strain, to account for nonlinearity in the response. He proposed a dynamic group interaction factor as a function of pile spacing and number of piles in the group, but independent of frequency, and compared his results to methods proposed by other researchers (Figure 2.5). His tests, however, were confined to relatively small strain ranges and hence might not be representative of the response at higher strains.

To expand the database of pile performance during strong shaking, a series of scaled model 1g shaking table tests of model piles in soft clay was performed at University of California at Berkeley (Meymand, 1998) (Figure 2.6). Principles of scale model similitude were used to derive a set of model

scaling relationships that recognized the dynamic and nonlinear nature of soil-pile interaction. Figure 2.7 described the scale modeling approach, adopted by Meymand, in which the primary modes of system response were first identified and prototype values for the variables contributing to these modes were established. Scaling relations were derived and used to compute scale model parameters for the variables of interest. Scale model components were fabricated and tested to verify their actual behavior. Scaling relations were then used to determine whether the measured model behavior implies a reasonable prototype response. Based on this approach, the scaling factors for the different variables were established as shown in Table 2.2.

A specialized test container with a flexible wall was developed to allow the soil to respond in the same fashion as the free-field, unencumbered by boundary effects. The shaking table reasonably reproduced both one-directional and two-directional input motions and model site response were consistent with the free-field behavior. Site characterization included laboratory and in-situ testing to establish the undrained shear strength and shear wave velocity profiles. One-dimensional equivalent linear dynamic response analyses were successfully used to simulate the model's free-field response, indicating that the model's soil-container system adequately reproduced free-field site conditions. The single piles were observed to respond with components of inertial and kinematic interaction, with the inertial components producing upper bound bending moments. The influences of two-directional shaking were seen to be minimal, as structural inertial forces tended to resolve the motion to a strong axis for the simple single degree of freedom models tested. Although the method addressed 1-g scaling

similitude issues quite rigorously compared to previous studies, there are still issues related to the accurate description of viscosity scaling.

Tao et al. (1998) conducted large-scale shaking table tests at the new NIED facility in Tsukuba, Japan. The table was 15 m x 15 m, with a payload capacity of 500 tons at 0.5 g. A large-scale laminar shear box and full-size piles were tested, and the measured responses were compared to the results from finite element analyses. In 2004, as part of the joint research efforts between NIED and Wayne State University, another large-scale laminar shear box was designed and fabricated as shown on Figure 2.8 (Kagawa, et al. 2004). The height of this shear box is more than 6 m, and its plan dimensions are 11 m x 3.5 m. This was probably the first study that involved extensive comparisons between the results from large-scale and dynamic centrifuge tests on geometrically similar soil–pile-structure models.

Thus, the preceding discussion shows that the majority of 1-g shaking table test programs have examined the seismic response of piles in cohesionless soils, with few studies conducted in cohesive soils. Input motions have primarily consisted of sine waves, with a limited number of base excitations based on actual earthquake records, among which only a handful were associated with strong levels of shaking. Also, issues related to scale model similitude issue were highlighted, but were not rigorously addressed.

2.1.4.2 Centrifuge Model Tests

The principal advantage of centrifuge testing over 1-g shaking table tests is that the increased gravitational stress field in the model can replicate prototype conditions. This consideration is crucial when testing materials such

as cohesionless sands whose stress-strain behavior is a function of confining pressure. In clayey soils, where overburden stresses are not as significant, the centrifuge does offer the important capability of consolidating the deposit during spin-up, thereby achieving a more realistic soil strength profile (Meymand, 1998).

Since the late 1970s and early 1980s, many model earthquake tests on the centrifuge have been conducted using stacked ring or laminar containers, which were designed to permit the soil to propagate shear waves vertically with minimal reflection from the ends (Meymand, 1998). Most of such studies dealt with piles in sand or liquefiable soil (Scott, 1977; Ting and Scott, 1984; Finn and Gohl, 1987; Liu and Dobry, 1995; Abdoun et al., 1996). In practice, many prototype pile foundations supporting critical structures are also sited in soft clays, which may exhibit very different behavior from sands during seismic loading. The San Francisco-Oakland Bay Bridge sited on San Francisco Bay Mud is a prime example.

In comparison with model tests on sand, tests on clay were relatively few in number. Hamilton et al. (1991) reported static centrifuge tests of laterally loaded piles in clay (Figure 2.9). Much of their analysis was focused on the computation of ultimate soil resistance, incorporating mechanisms of soil-pile suction and adhesion in their model. Normalized experimental p-y curves were compared with curves constructed by Matlock's soft clay criteria (1970).

Some dynamic centrifuge model tests were also performed using the large servo-hydraulic shaking table on the 9 m-radius centrifuge at the University of California at Davis (Café, 1991; Wilson, 1998; Christina et al.,

1999). Cafe (1991) reported tests on a model of the Struve Slough Bridge founded on peaty soil, which suffered major damage in the Loma Prieta earthquake. The model of a single span bridge deck, supported on 8 model piles, was tested on the centrifuge. The test results indicated large kinematic loading from the soil to the supporting piles, inducing large bending moments at the pile heads. A simplified finite element model of the soil-pile response was analyzed, which yielded reasonable agreement with the observed response.

Using the same shaking table and centrifuge set-up, Wilson (1998) and Christina et al. (1999) tested various soil-pile models in a flexible shear beam (FSB) container (Figure 2.10). The FSB container consists of a series of stacked aluminum rings separated by soft rubber that enables the container to deform with the soil. The inside dimensions of the container are 1.7 m long, 0.7 m deep, and 0.7 m wide. The soil profile consisted of two horizontal soil layers (Fig. 2.8a). The lower layer was fine, uniformly graded Nevada sand (C_u = 1.5 and D_{50} = 0.15 mm) at a dry density of 1.66 Mg/m^3, which corresponds to a relative density D_r of about 75–80%. The sand was air-pluviated, flushed with carbon dioxide, and saturated under vacuum. The upper layer was reconstituted Bay Mud (liquid limit= 88%, plasticity index = 48%) placed as a slurry (water content= 140%) in four equal layers, with each layer separated by filter paper to accelerate consolidation. Each layer was individually preconsolidated under an applied vertical stress. The pore fluid used was water (rather than a higher viscosity pore fluid), and saturation was confirmed by measuring *p*-waves velocities before testing. The two single-pile-supported systems (SP1 and SP2) analyzed in this paper consisted of a

superstructure mass attached to an extension of the pile. The aluminum pile (including its aboveground extension) had a mass per unit length of 0.37 Mg/m and a flexural stiffness EI of 417 MN/m^2, which is approximately equivalent to a 0.67-m-diameter steel pipe pile with a 19 mm wall thickness. The piles were installed at 1*g* (prior to spinning the centrifuge) and remained elastic throughout all the earthquake events. The two single-pile-supported structures were subjected to nine different earthquake events with peak accelerations ranging from 0.02 to 0.7*g*. Reasonably good agreement was obtained with a simple theoretical model for both structural models in all earthquake events. The sensitivity of the results to dynamic *p-y* model parameters and site response calculations was also studied.

This study was subsequently extended to evaluate a dynamic beam on a nonlinear Winkler foundation (BNWF) analysis method. The centrifuge tests included a structure supported on a group of nine piles founded in soft clay overlying dense sand, as shown on Figure 2.10b (Christina et al., 1999). This structure was subjected to nine earthquake events with peak accelerations ranging from 0.02 to 0.7*g*. Good agreement was obtained between the calculated and recorded structural responses, including superstructure accelerations and displacements, pile cap accelerations and displacements, pile bending moments and axial loads, and pile cap rotations (Figure 2.11). The sensitivity of the dynamic *p-y* analysis analyses to the numerical model parameters and site response calculations were evaluated. These results provide experimental support for the use of dynamic *p-y* analysis methods in seismic soil-pile-structure interaction problems involving pile-group systems.

2.1.5 Field Monitoring: Measured Pile Response During Earthquakes

In addition to the laboratory full-scale or model tests, a limited amount of measured response of the pile foundations during earthquakes has been found in the literature. These measurements varied from the acceleration time histories recorded by seismograph at the pile cap, in the structure or in the adjacent free-field, to in some cases bending and axial strain time histories recorded from the strain gauges fixed to the piles.

Housner (1957) published one of the first case histories involving soil-structure interaction with his analysis of the Hollywood Storage Company building performance during the 1952 Kern County earthquake. The response spectra computed from the accelerograms revealed nearly identical basement and free-field spectra for the N-S direction, but 50% deamplification of the basement motion relative to the free-field in the EW component across the full frequency range. Evaluating the performance of the same building under 1987 Whittier Narrows earthquake, Fenves and Serino (1992) revisited Housner's work, asserting that their new analysis revealed no evidence of soil-structure interaction. Similarly Stewart (1997) analyzed the response of the same building during 1994 Northridge earthquake.

Esashi and Yoshida (1980) compared the response of instrumented pile foundations during recorded earthquakes and subsequent static and dynamic field tests. The 16 in diameter steel pipe piles were driven 33 ft deep into soft cohesive soils and grouped in a 1x2 pile cap partially embedded at the surface. Seismic observations during the Matushiro earthquake (1966) showed similar free-field and pile accelerations. The study was particularly unique as it

partially validates the use of dynamic tests for the characterization of the dynamic response of the pile foundations.

Hamada and Ishida (1980) reported the response of a pile group, supporting a spherical tank, driven through soft soils (SPT N<10) subjected to two distant earthquakes in 1978. Figure 2.12 suggested that the spectral amplification of the tank footing relative to the ground surface was recorded at the periods less than 0.3 secs. Furthermore, Tsujino et al. (1987) illustrated that the overall structural response and strain regime in the piles was significantly sensitive to the height of the liquid in the supported LNG storage tank (Figure 2.13).

A number of researchers have studied the response of instrumented Ohba-Ohashi bridge near Tokyo to a 1983 magnitude 6.0 earthquake and attempted to correlate their analytical models to the observed response (Ohira et al., 1984; Tazoh et al., 1987; Gazetas et al. 1993). The bridge was supported on 11 piers and each pier was supported by 64 steel pipe piles driven through extremely soft soil consists of humus and silt (N~0). Observations suggested that large bending strains developed at the upper and lower ends of piles. Gazetas et al. (1993) concluded that it is extremely difficult to model such a soft ground and hence emphasis should be given on the measured responses.

In a damage survey, Hadijan et al. (1990) reported a spectral amplification of over 200% at periods less than 0.48 secs at the Imperial County Service Building during the 1979 Imperial Valley earthquake (Figure 2.14).

Celebi and Safak (1992) studied the response of a 30 story building, supported on the precast concrete piles driven through California Bay Mud,

during 1989 Loma Prieta earthquake. The recorded predominant periods and spectral amplifications indicated strong soil-pile interaction. Stewart (1997) compared his numerical analysis with these recorded response and concluded that a simple soil-structure interaction model was able explain the field observations.

Makris et al. (1996) analyzed the response of the Painter Street Bridge (California) to the 1992 magnitude 7 Petrolia earthquake. The bridge suffered minor damage, despite of experiencing an acceleration of 0.92g at the superstructure compared to a free-field acceleration of 0.48g. The bridge was supported on piles driven through a moderately stiff clay layer (N~15 to 25).

A 14-storey reinforced concrete building and the underlying soil were instrumented with strong motion accelerographs to study the amplification of seismic waves, the soil-structure interaction and the structural response to earthquakes of buildings founded on soft clay, such as the lake-bed area of Mexico City (Meli et al., 1998). The instrumentation consists of 14 strong motion accelerographs, two of them underground, one in free-field and 11 in the building. The main features of the seismic response of the building and its interaction with the soil were derived from the analysis of seismic recordings. Ambient vibration tests were also performed to determine basic dynamic properties. From the measured data it was found that the vibration periods of the building were found to increase significantly with the intensity of the ground shaking, indicating the non-linear behaviour of the structure, even under small levels of excitation.

2.1.6 Criteria for the Evaluation of the Pile Response

In recent decades, considerable efforts, endeavors and researches have been made subject to the review of the dominant criteria for design of structures against earthquakes. However, most of the seismic design philosophies are documented on the super-structures. The available studies on the criteria for the evaluation of pile response under earthquakes are far fewer.

Bhattacharya and Bolton (2004) indicated several criteria that can be found in the literature to determine the failure of a pile under earthquake or lateral loads. Most commonly, the failure criteria refers to the load at which settlement continues to increase without any further increase of load, or the load causing a gross settlement of 10% of the least pile width. Essentially, these criteria are based on failure of soil surrounding and underlying the pile. The design criteria are obtained either by using an appropriate factor of safety on failure or are based on serviceability limit state (settlement) for the structure in consideration. Thus, the design method should safeguard the piles against:

i) Buckling failure due to unsupported pile in liquefied /soft soil.

ii) Formation of a collapse mechanism due to lateral spreading forces (transient and residual).

iii) Excessive settlement leading to failure due to serviceability limit state.

The US Bridge Design (ODOT) manual (2005) stated that the seismic design of pile foundations often relies on the ultimate axial capacity of the piles (both in compression and tension). The ODOT Gates Equation and the Wave Equation are the most commonly used methods to develop pile driving

resistance criteria. However, different factors of safety (FOS) are used with each of these methods. The Wave Equation method should be used for predicting ultimate pile capacity in areas where the pile design may be controlled by seismic loads. As a general rule of thumb, this is in areas where the site bedrock PGA is greater than 0.20g. For liquefiable ground, obtaining adequate lateral pile capacity is generally the main concern. Furthermore, the bending stresses along the pile length and settlements of the pile-raft structure due to soil densification are also to be kept within permissible limit to satisfy the serviceability criterion.

Shirato et al. (2005) discussed the seismic requirements for the deep foundations as mentioned in Japanese Bridge Design manual (2002) According to the manual, apart from lateral load carrying capacity, the pile head displacement should be within 1% of the pile diameter. However, if the pile displacement remains within a certain level and no notable residual displacement appears, it is expected that a steady horizontal soil resistance to piles is maintained and nothing is going to happen in service. Traditionally, an allowable horizontal pile bearing capacity is defined with a displacement at the design ground level. Before 1990, empirical threshold horizontal displacements were 10 mm in the "Normal Situation" and 15 mm in the "Frequent Earthquake Situation" in Japan. From 1990, the specifications have described that the allowable horizontal displacement is the larger value of 1% of the pile diameter or 15 mm in both "Situations". This is based on Okahara et al. (1991a, 1991b) in which they collected in-situ test data of piles subjected to horizontal loads, and examined the elastic limit displacements on the observed load-displacement curves. The relative lateral displacement of pile-

cap has also been chosen as an important factor in a naval pier design project at Washington DC, USA (Klusmeyer and Harn, 2006).

In Taiwan, all the design specifications require the checks of foundation capacities at ordinary and seismic times. The settlements and deformations of the foundation also need inspection to ensure not exceeding the limits. Both working stress design (WSD) and limit state design (LSD) are adopted in current design practice. The trends and developments of load and resistance factor design (LRFD) and performance based design (PBD) were firmly introduced to local engineers in 2006 by a special issue of *Sino-Geotechnics* on PBD methods (Chang 2006). According to their suggestions, the seismic performances of the pile foundations could be categorized into three levels with the concerns of foundation serviceability, rehabilitation and safety, respectively (see Tables 1~3). Performance Level I reflects the elastic responses of the foundation under small to medium earthquakes where soil liquefaction does not occur or occurs slightly. Conventional design methods are applicable in this case. Level II is applicable to nonlinear foundation responses, in which the ground tends to liquefy during medium to large earthquakes. Level III is amendable to nonlinear responses of the foundations that are affected by soil liquefaction and liquefaction induced lateral spread of the ground under very large earthquakes. Chen et al. (2008) suggested that nonlinear static and dynamic analyses could be applied to complexity of the problem.

Based on the method discussed by International Navigation Association in the published book "Seismic Design and Evaluation for Port Structures", Jang and Chein (2006) proposed a performance based design

approach for a pile supported wharf structure in Taiwan. Apart from the conventional criteria (Lateral load capacity, pile cap displacement etc.), they have included few additional factors such as,

i) displacement ductility factor

ii) permanent displacement

iii) length of plastic hinge

iv) energy index and

v) damage index.

In the paper they have discussed the definition and respective influence of these factors in the design method.

2.2 Behaviour of Soft Clay

It is well known that the mechanical behavior of soil under dynamic loading, such as sea waves, earthquakes and traffic loading, differs significantly from those under quasi-static loading. Extensive studies have, therefore, been made to investigate the dynamic behavior of cohesive soils in the laboratory using cyclic triaxial, resonant column, and cyclic direct shear testing (Sangrey, 1968; Wood, 1974; Nishimura and Jardine, 2005; Hazen and Penumadu 1999; Thiers and Seed, 1968; Kagawa, 1991; Kokushko et al., 1982). Research on the dynamic properties of cohesive soil includes observations on low-amplitude shear modulus, strain (or stress) dependency of modulus and damping, stiffness degradation and strength under cyclic loading.

2.2.1 Non-linear and Stiffness Degradation Behaviour

The effect of seismic shaking on sandy deposits has been studied extensively and it is well-known that loose sand tends to liquefy under cyclic loading (Casagrande, 1976; Seed, 1979). On the other hand, the behaviour of soft clay under cyclic loading and its implications on pile foundations are much less extensively studied. Degradation of soft clays such as those found in many marine deposits during cyclic loading has been well documented in studies involving element tests (Rao and Panda, 1997). Nonlinearity associated with soft clay under cyclic loading was first experimentally shown by Idriss et al. (1978), whose study on marine clay of San Francisco Bay Mud revealed nonlinear and degrading stress-strain behavior of soft clay (Figure 2.15a). Puzrin et al. (1995) also showed similar trends with Israeli soft clay under cyclic loading (Figure 2.15b).

Yashuhara et al. (1982) described strength and deformation characteristics of highly plastic marine clay by a series of repeated triaxial compression tests to examine the effect of loading frequency, anisotropy and drainage condition. According to them, cyclic strength and deformation modulus are not strongly influenced by loading frequency. Authors also found that cyclic strength of anisotropically consolidated clay became gradually smaller accompanying by accumulation of the shear strain more than that of an isotropically consolidated clay.

Vucetic and Dobry (1991) produced some ready-to-use charts showing the effect of plasticity index on modulus degradation and subsequent use for seismic response study for Mexico City.

More recently, Hazen and Penumadu (1999) reported a comprehensive study on kaolin clay, which suggests that there is a threshold cyclic stress amplitude governing the degradation behaviour of kaolin. They also proposed some curves of principal stress difference ($\sigma_1 - \sigma_3$) and excess pore pressure against residual strain to estimate mobilized strength for a soil element under an expected earthquake loading. Teachavorasinskun et al.'s (2001) data also showed non-linearity with secant Young's modulus reducing with axial strain increment. They reported that the secant Young's modulus at moderate strains was influenced by the stress rate: the faster the stress rate, the larger the secant Young modulus. When the effective stress at the starting of the stress cycle decreases, so does the secant Young's modulus at moderate strains. However, at large strain levels, the strain dependence characteristic of the secant Young's modulus overwhelms the effects of loading rate and effective stress change. The degradation of the secant Young's modulus at large strains was dependent almost entirely on the initial consolidation stress.

2.2.2 Damping

The conventional way of looking at the damping properties of soil is to use a damping ratio calculated as a ratio between the area of the hysteretic stress-strain loop and the maximum energy stored in a cycle (Figure 2.16). Hardin and Drnevich (1972) fitted a series of equations to their data to predict the damping ratios for various soils, but there is considerable scatter in the experimental data. Their equations also do not include the number of cycles as a variable. This may be so at small strain amplitudes wherein soil behaviour

can be reasonably approximated as viscoelastic, with ideal elliptical hysteresis loops. However, at larger strains, the stress-strain cyclic loops tend to collapse in shape as the number of cycles is increased (Wood, 1982). At this point, the soil is evidently not behaving in the assumed fashion. Hardin and Drnevich (1972) and Seed et al. (1986) showed that, for small strain amplitudes, damping ratio seemed to increase with strain amplitude. However, Andersen et al. (1980) found a deviation from this pattern of behaviour, caused by the development of S-shaped hysteretic loops at higher strain amplitudes. Taylor and Bacchus (1969) reported values of damping ratio determined from tests, which showed maximum damping ratio at strain amplitude of about ± 1% for any number of cycles. Hence a clearly accurate computation of damping may require determination of the area of rather irregular geometrical figures-precise measurements of stress and strain around the cycle are required and there must be no phase errors between the measuring systems for stress and strain. Teachavorasinskun et al. (2001) commented from series of continuous cyclic load test and staged cyclic loading test that both types of tests gave fairly similar strain dependence characteristics damping ratio. For a given initial consolidation pressure, strain was observed to be a more important factor than the effective stress change.

Apart from strain dependencies, some studies have also shown that damping is affected by frequency or strain rate changes as well. Aggour et.al. (1987) reported the use of varying cutoff frequencies to determine the effects of frequencies on dynamic soil properties. They demonstrated that damping decreases with as frequencies are increased. Cavallaro and Maugeri (2004) reported that at very small strain of 0.00087%, a very low strain rate of 0.001

Hz can decrease the damping ratio of the Nato clayey soil. Their experiments on clay using the cyclic torsional shear and compression loading triaxial tests were used to model the cyclic behavior of cohesive soils.

Teachavorasinskun et al. (2002) reported a decrease in damping ratio with increase of loading frequency which is in accordance with the observation made by Shibuya et al. (1995). However, there few reports available where damping ratio seems to be increased with loading frequency (Kim et al., 1991; Zanvoral and Campanella, 1994; Thammathiwat and Weeraya, 2004). Brennan et. al. (2005) also suggested that damping is increased by 1.5 times when frequency is increased from 1 Hz to 50 Hz in their centrifuge tests for clay dynamic properties. Hence, it can be inferred that the effect of the frequency on damping of clay is highly case-specific and inconclusive, as well.

2.2.3 Modeling Cyclic and Strain-Rate Dependent Behaviour of Soft Soil

Most of the work on time-dependent stress–strain behaviour of soils has concentrated on one-dimensional (1D) straining in oedometer tests (e.g. Bjerrum, 1967 and Leroueil et al. 1985). Some earlier models were based on the elastic-viscoplastic (EVP) framework of Perzyna (1963, 1966). Many researchers commented that structure is as important as void ratio and effective stress states in controlling the behaviour of natural soft clays in EVP modeling (Burland, 1990; Leroueil and Vaughan, 1990).

Researchers showed that assumption of linear elasticity below yield point tends to over predict the deformation and introduction of non-linearity can considerably improve the quality of prediction (Jardine et al, 1991; Dasari,

1996). In devising all such model to reproduce non-linear properties, writers have assumed the basic stress–strain curve to be bilinear (Thiers and Seed, 1968), hyperbolic (Duncan and Chang, 1970; Hardin and Drnevich, 1972; Pyke., 1979; Puzrin et al., 1995; Rao and Panda, 1999; Liu and Ling, 2006) or of Ramberg–Osgood type (Streeter et al., 1975; Idriss et al., 1978; Adrianopoulos, 2006). Apart from non-linear stress-strain curve, substantial decrease of shear modulus of soil with the progression of loading cycle had also been incorporated in some of those models (Idriss et al., 1978; Vucetic, 1988; Vucetic and Dobry, 1988). Idriss et al. (1978) proposed a simple degradation model for soft marine clay under cyclic and transient loading based on their experimental results. Cyclic degradation, as described by Idriss , depends on amplitude of cyclic shear strain and number of cycles. He then extended his model to simulate transient loading tests where the strains were varying randomly after certain number of cycles (Figure 2.17). Matasovic and Vucetic (1995) extended Idriss' concept of degradation index to incorporate effect of pore pressure generation.

Hyodo et al. (1994), based on serried of undrained cyclic triaxial tests on isotropic and anisotropic clay, proposed an semi-empirical model for evaluating the development of residual shear strain during cyclic loading. Puzrin et al. (1995) have considered the influence of the changing mean effective stress on the parameters of the Iwan's series–parallel model (Iwan, 1967) which leads to the concept of a normalised nondegrading backbone curve and predicts the cyclic shear softening behaviour of soft Nile clay consistent with the Masing rules.

Rao and Panda (1999) produced an one-dimensional nonlinear model to simulate cyclic behavior of soft marine clay, the prediction of which compares reasonably well with the experimental data of Idriss et al.(1978) and Vucetic and Dobry (1988).

2.3 Concluding Remarks

In the current chapter it was seen that stress-strain behavior of natural clay soils during shear is highly nonlinear and the elastic modulus generally decreases with increase in shear strain. Extensive studies based on both numerical analysis and field monitoring has shown that this degradation of shear modulus with shear strain, or shear stress, significantly influences the performance of a foundation system. This is particularly important when a pile is subjected to axial loading in which the shear strain in the surrounding soil gradually and progressively increases from a small strain to a large strain as the applied load increases (Zhu and Chang, 2002). Furthermore, it has been established that, during cyclic loading with stress/strain amplitude above a critical value, there is often a continuous loss of strength and stiffness of clay with the number of cycles (e.g. Matasovic and Vucetic, 1995; Rao and Panda, 1999). For pile problems, Snyder (2004) conducted a quasi-static full scale pile load test and reported that soil stiffness degraded due to successive shearing and plastic deformation of soil around the pile, see Figure 2.18. This is likely to influence the seismic response of pile foundations significantly.

Notwithstanding the above studies, physical data on the effect of soil-pile interaction on the dynamic response characteristics of pile-supported

structures in soft clay remain scarce. In such soft-ground conditions, the fundamental period of the structure may be significantly affected by the compliance of the pile foundation. In addition, pile head motion may differ significantly from the anticipated "free-field" ground surface motion.

Numerically, researchers fitted some non-linear backbone curves to Iwan's series-parallel model to predict free-field soil responses under earthquake condition (Joyner and Chen, 1975; Bonilla et al., 1998; Bonilla, 2000; Hartzel, et. al., 2004). None of this models, however, used for complex clay-pile interaction.

Although Snyder (2004) showed that the clay stiffness degraded around a single pile during cyclic lateral load tests in field, the study was restricted to quasi-static cyclic loading-unloading process (Figure 2.18). Hence physical modeling of the application of real earthquake to clay-pile system is yet to be examined. Moreover, Snyder (2004) did not consider the effect of inertial loading from the superstructure and relative stiffness of soil-pile materials on ground response. As in soft-ground conditions, the fundamental period of the structure and the intensity and extent of pile-soil interaction may be significantly affected by the flexibility of the pile as well as different superstructure inertial loading. So far, there has been little or no literature reporting on the effects of soil non-linearity and stiffness degradation on the response of the pile and surrounding soil under earthquake excitation with superstructure inertial loading.

The objective of this study is to investigate the interaction between soil behaviour, pile stiffness and superstructure inertial loading on pile response during earthquake. A centrifuge modelling approach is used to generate

experimental data which then provides a basis for validating and calibrating numerical analyses.

Table 2.1 List of 1-g shaking table tests on model piles (Meymand, 1998)

		pile	pile	pile			pile								max.	
		diameter	wall	length	pile	pile	head		structural						accel.	model
Reference	model pile material	(in)	(in)	(in)	group	spacing	fixity	pile cap	mass	pile installation	model soil	test container	input excitation	(g)	similitude
Prakash and Aggarwal (1965)	aluminum pipe	0.6	0.1	13	n.a.	n.a.	free	none	?	embedded	sand	rigid box	2 -10 Hz.	?	no
Tajime et al. (1965)	steel pipe	1 - 1.2	0.04 - 0.06	7.9	2x2	?	fixed	embedded	yes	fixed at base	sand/plaster/water	rigid box	1.4 - 8 Hz.	?	no
Kubo (1969)	steel pipe	3.9	0.1	118	3x7	?	fixed	above grade	yes	fixed at base	cinder sand/oil	rigid box	1 - 4Hz.	0.1	yes
Yamashita and Inatomi (1970)	steel bar	3.9x0.4	n.a.	45.3	2x2	50d	fixed	above grade	yes	inserted	dry sand	?	sine waves	0.15	no
Hakuno et al. (1977)	aluminum rod	0.8	n.a.	27.6	2x2, 2x3, 3x3	3d	fixed	above grade	yes	fixed at base	saturated loose sand	hinged box	10 - 20 Hz.	0.13	yes
Tatsuoka et al. (1978)	aluminum rod	0.8	n.a.	27.6	2x2, 2x3, 3x3	3d	fixed	above grade	yes	fixed/free at base	saturated loose sand	hinged box	5 - 45 Hz.	0.1	no
Sugimura (1980)	steel bar	2x0.2	n.a.	28.2	1x2	?	?	embed / above	yes	?	polyacrylamide/bentonite	?	3 - 15 Hz.	0.1	no
Yao (1980)	aluminum pipe	0.4	0.04	21.3	1, 3x3	?	free/fixed	above grade	yes	inserted	clayey silt	hinged box	4 - 45 Hz.	0.1	no
Kagawa and Kraft (1981)	steel bar	2.4x0.2	0.4x0.2	31.5	n.a.	n.a.	free	?	yes	?	saturated sand	hinged box	10 Hz.	0.1	no
Mizuno and Iiba (1982)	steel bar	2x0.2	n.a.	28.2	1x2	?	fixed	embedded	yes	pinned at base	polyacrylamide/bentonite	rigid cylinder	sine waves, Japan EQ	0.1	yes
Ranjan et al. (1982)	?	0.3	?	13	2x2, 3x3, 4x4	2 - 5d	?	?	?	inserted	saturated sand	rigid box	4 Hz.	0.3	no
De Alba (1983)	brass pipe	1	?	2.5	2x2	2.5d	fixed	above grade	n.a.	inserted	saturated medium sand	laminar cylinder	cyclic	?	no
Heng-Li (1985)	acrylic pipe	0.3	0.1	12.6	10	2 - 2.7d	fixed	above grade	yes	?	silicon gum	?	2 - 24 Hz., Japan EQ	?	yes
Korgi (1986)	steel bar	2x0.2	n.a.	28.1	2x7	?	fixed	embedded	yes	pinned at base	polyacryl./bentonite/fly ash	rigid cylinder	1 - 30 Hz., Japan EQ	0.12	no
Gohl and Finn (1987)	aluminum pipe	0.25	0.05	24	n.a.	n.a.	free	above grade	yes	inserted	dense dry sand	rigid box	5 - 50 Hz.	0.6	no
Mizuno et al. (1988)	steel bar	2x0.2	n.a.	28.1	1x2	?	fixed	embed / above	yes	?	polyacrylamide/bentonite	rigid cylinder	1 - 30 Hz., EQ	0.12	yes+
Stanton et al. (1988)	stainless steel pipe	1.2	0.19	45	n.a.	n.a.	free	?	?	embedded	dry sand	flexible cylinder	1 - 40 Hz.	?	no
Tamori and Kitagawa (1988)	steel bar	2x0.2	n.a.	28.1	2x7	?	hinged	embedded	yes	pinned at base	plasticine/oil, polyacr./ben.	rigid cylinder	0 - 30 Hz., EQ	0.8	yes
Yoshikawa and Arano (1988)	aluminum pipe	4	?	21	2x2	4.4d	?	embedded	yes	?	loose saturated sand	shear box	10 - 25 Hz. w/ vertical	0.1	yes
Gohl (1991)	aluminum pipe	0.25	0.05	16	1, 1x2, 2x2	2 - 8d	fixed	above grade	yes	inserted	dry sand	rigid box	5 - 70 Hz., Taft	0.69	yes+
Liu and Chen (1991)	aluminum pipe	0.4	?	11.8	3x9, 5x9, 8x9	3d	?	?	?	inserted	saturated sand	?	?	0.6	no
Nomura et al. (1991)	?	1.9 - 3	?	78.7	2x7	?	?	above grade	yes	embedded	saturated clean silica sand	shear box	Taft, El Centro EQ	0.3	yes
Yan et al. (1991)	aluminum pipe	0.25 - 0.5	?	13.8	n.a.	n.a.	free	none	yes	?	saturated uniform fine sand	hydraulic gradient	10, 20 Hz.	0.51	yes
Finn and Gohl (1992)	aluminum pipe	0.25	0.05	24	1x2, 2x2	3 - 8d	fixed	above grade	yes	inserted	dry sand	rigid box	7.5, 10 Hz.	0.45	no
Mori et al. (1992)	aluminum rod	2	n.a.	39.4	3x3	?	fixed	above grade	yes	fixed at base	saturated sand	shear box	EQ	0.14	yes
Taga et al. (1992)	aluminum bar	0.2x0.4	n.a.	15.7	3x3	22d	pin	partial embed	yes	?	dry sand	rigid box	1 - 10 Hz.	0.2	yes
Tazoh and Shimizu (1992)	aluminum pipe	1.2	0.04	35.4	3x3	2.5d	fixed	above grade	yes	fixed at base	dry sand	shear box	1 - 30 Hz.	0.25	no
Tokida et al. (1992)	PVC pipe	0.9	?	31.1	1 - 16	?	free	none	no	fixed at base	sloping saturated sand	rigid box	2 Hz.	0.25	no
Yamamoto et al. (1992)	brass pipe	0.8	0.12	28.3	8	?	free/fixed	above grade	yes	fixed at base	N-methytol propene, sand	shear box	El Centro EQ	?	no
Yao and Kobayashi (1992)	aluminum tube	1x2	0.08	68.9	2x2	15d	?	above grade	yes	embedded	saturated sand	shear box	1 - 7 Hz.	0.3	no
Sreerama (1993)	aluminum pipe	0.44	0.03	17.5	1, 1x2, 2x2	3 - 8d	free/fixed	above grade	yes	inserted	low plasticity remolded clay	rigid box	1 - 12 Hz.	?	no
Kagawa et al. (1994)	steel rod	2x0.24	n.a.	36.1	1x2	16d	fixed	above grade	yes	pinned at base	saturated sand	shear box	0 - 25 Hz.	0.16	no
Ohtomo and Hamada (1994)	polycarbonate, PE pipe	0.7 - 1	?	24.4 - 26	n.a.	n.a.	free	none	no	fixed at base	sloping saturated sand	rigid box	10 Hz.	0.68	no
Sakajo et al. (1995)	plastic pipe	1	0.1	35.4	6x6	2.5d	fixed	above grade	no	fixed at base	saturated sand/gravel	shear box	10 Hz.	0.1	no
Dou and Byrne (1996)	aluminum pipe	0.25	0.03	15	n.a.	n.a.	free	above grade	yes	inserted	saturated uniform fine sand	hydraulic gradient	17.5, 30 Hz	0.49	no
Hideto et al. (1996)	acrylic resin	1.2	0.08	23.6	n.a.	n.a.	free	n.a.	yes	embedded	dry sand	shear box	10 - 60 Hz., EQ	0.3	no
Ohtomo (1996)	aluminum, stainless pipe	1	?	27.6	1x2	10d	fixed	embedded	no	?	saturated sand	rigid box	10 Hz.	0.4	no
Makris et al. (1997)	aluminum pipe	0.8	0.04	38.2	n.a.	n.a.	fixed	embedded	yes	fixed at base	dry sand	shear box	frequency sweep	?	no
Tao et al. (1998)	steel pipe	12	0.25	240	n.a.	n.a.	free	n.a.	no	pinned at base	loose moist sand	laminar shear box	sweep 1-20 Hz., KPI EQ	0.45	no

Table 2.2 Scaling factors used by Meymand (Meymand, 1998)

Mass Density	**1**	**Acceleration**	**1**	**Length**	λ
Force	λ^3	**Shear Wave Velocity**	$\lambda^{1/2}$	**Stress**	λ
Stiffness	λ^2	**Time**	$\lambda^{1/2}$	**Strain**	**1**
Modulus	λ	**Frequency**	$\lambda^{-1/2}$	**EI**	λ^5

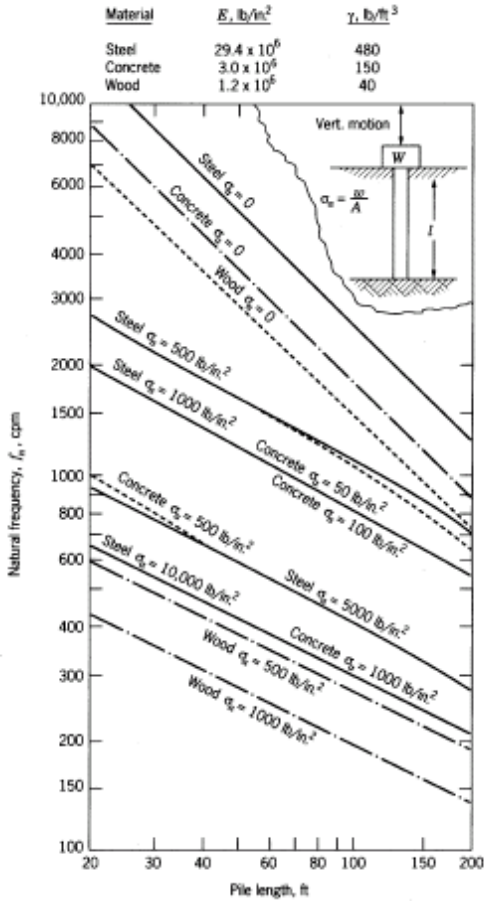

Figure 2.1 Resonant frequency of vertical oscillation for a point-bearing pile resting on a rigid stratum and carrying a static load W (after Richart, 1962)

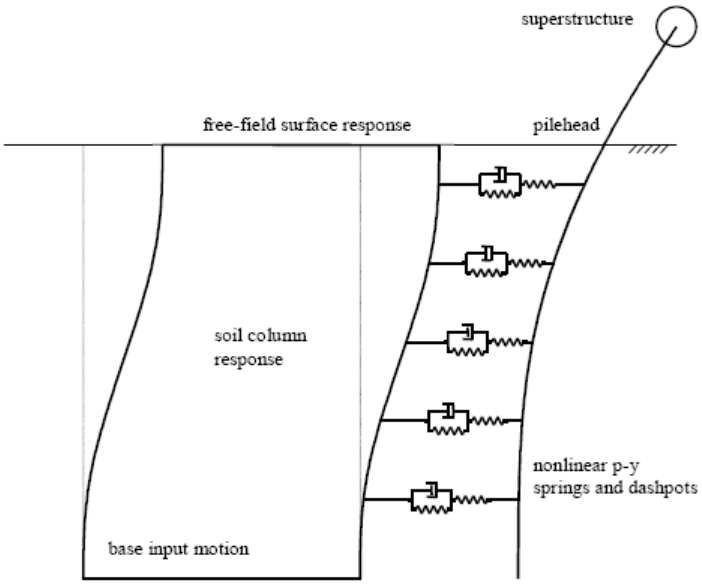

Figure 2.2 Nonlinear soil-springs (Wilson, 1998)

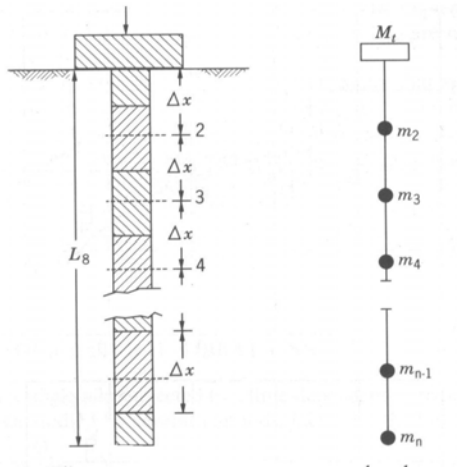

Figure 2.3 Lumped mass model

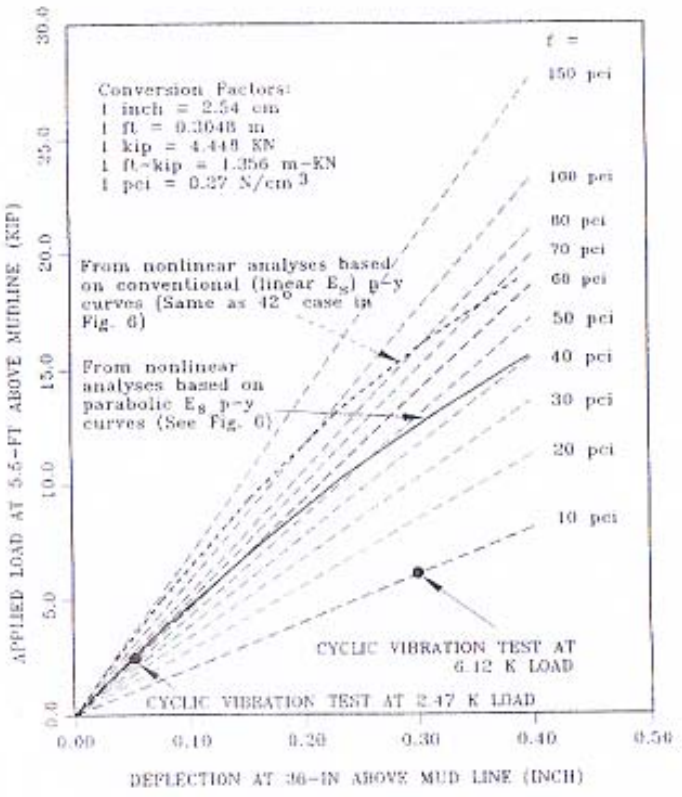

Figure 2.4 Load-deflection plot and equivalent p-y analysis of full-scale lateral pile load test (Lam and Cheang, 1995)

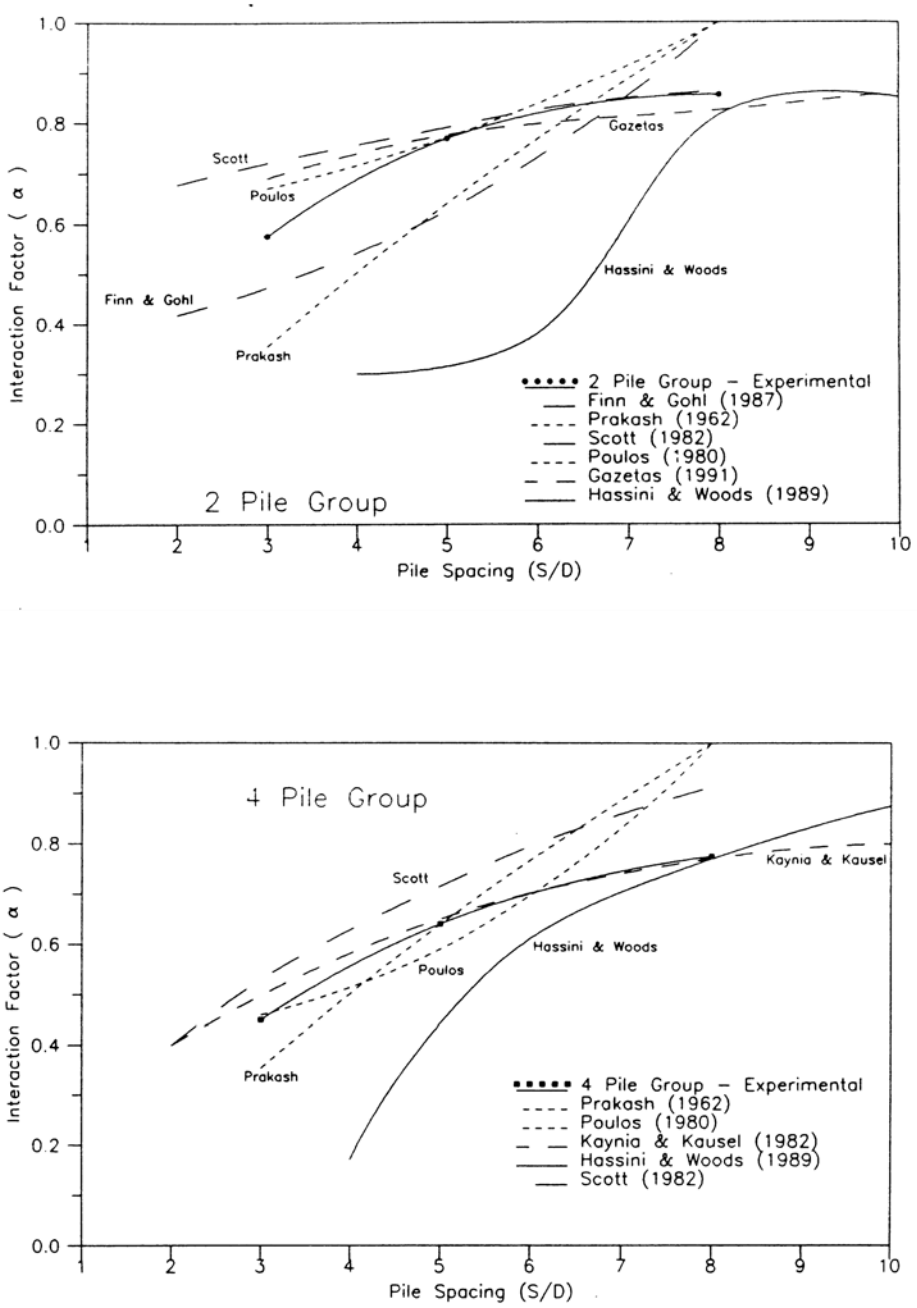

Figure 2.5 Shaking Table Model Pile Group Interaction Factor vs pile spacing (Sreerama, 1993)

(a)

(b)

Figure 2.6 (a) Small scale and (b) full scale shaking table at UCB (Meymand, 1998)

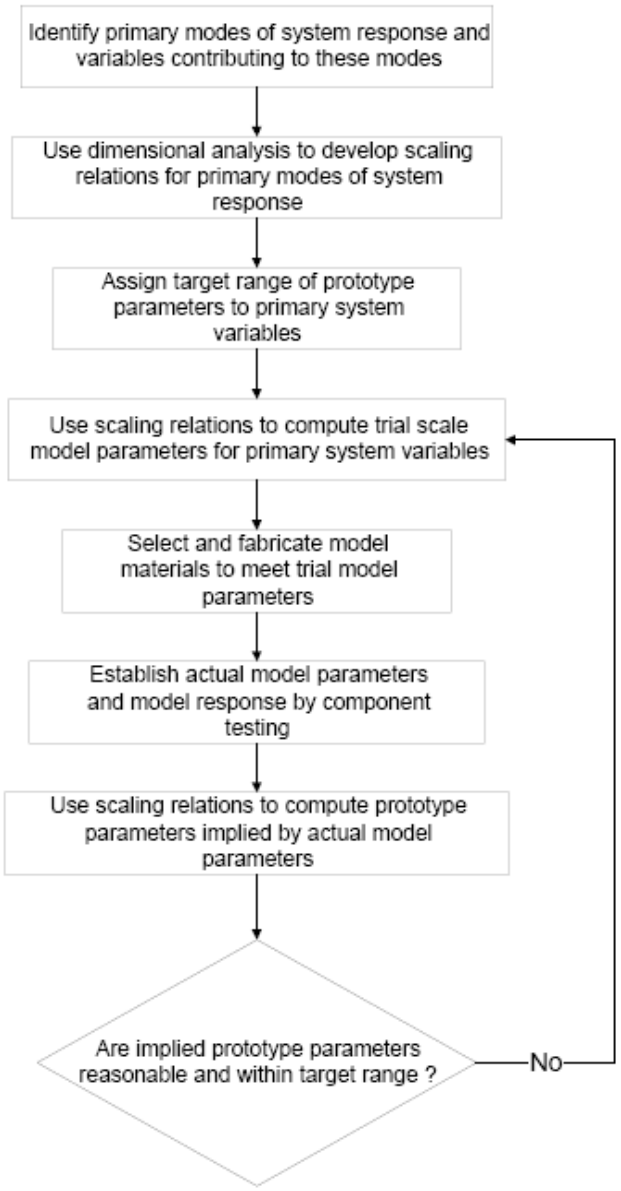

Figure 2.7 Similitude approach used by Meymand (Meymand, 1998)

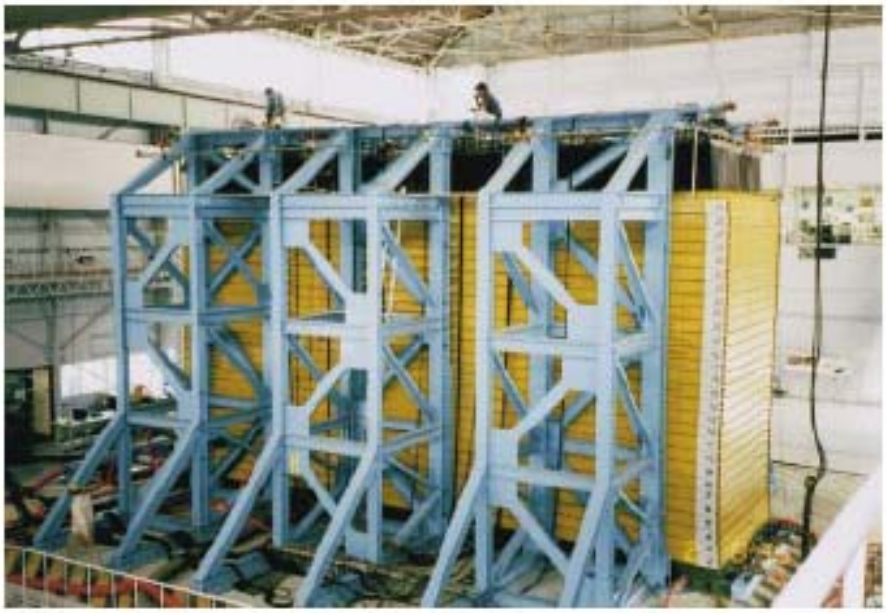

Figure 2.8 Large scale laminar box-shaking table assembly at NIED, Japan (Kagawa et al, 2004)

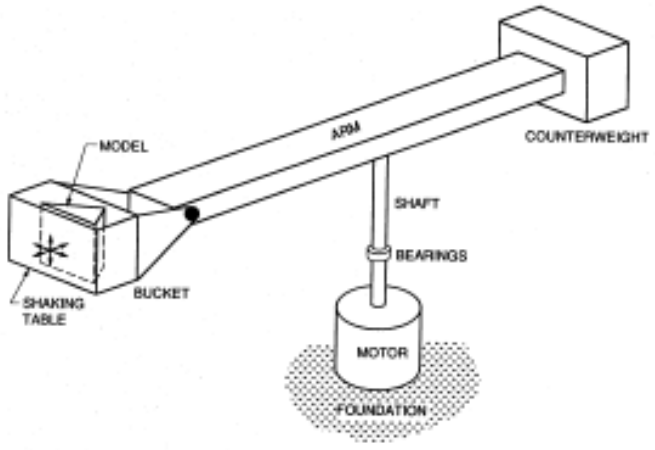

Figure 2.9 Simplified centrifuge test set-up

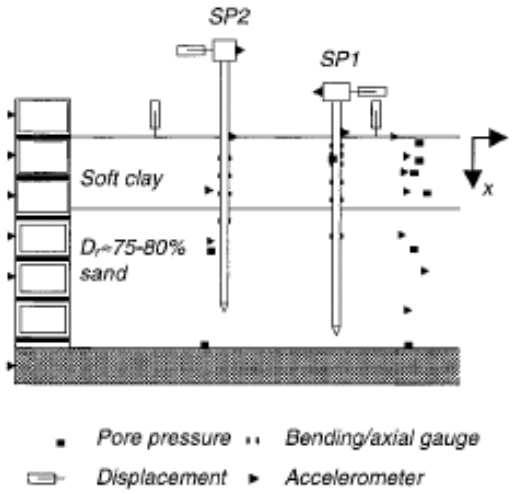

(a)

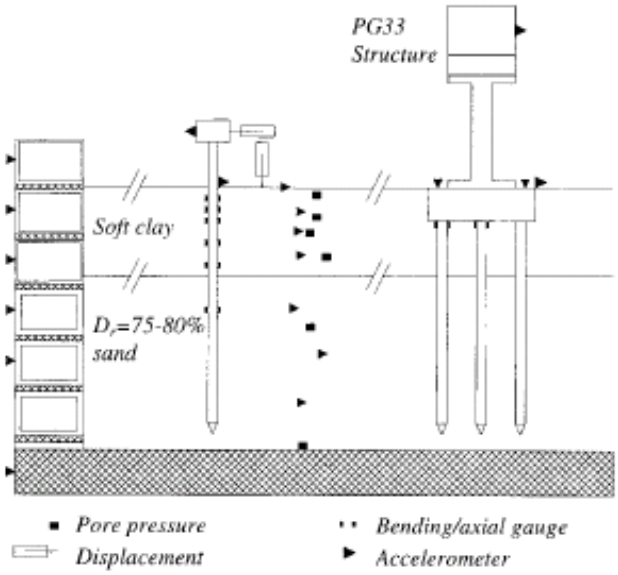

(b)

Figure 2.10 Models used in U.C. Davis for dynamic tests on clay (Christina et al., 1999)

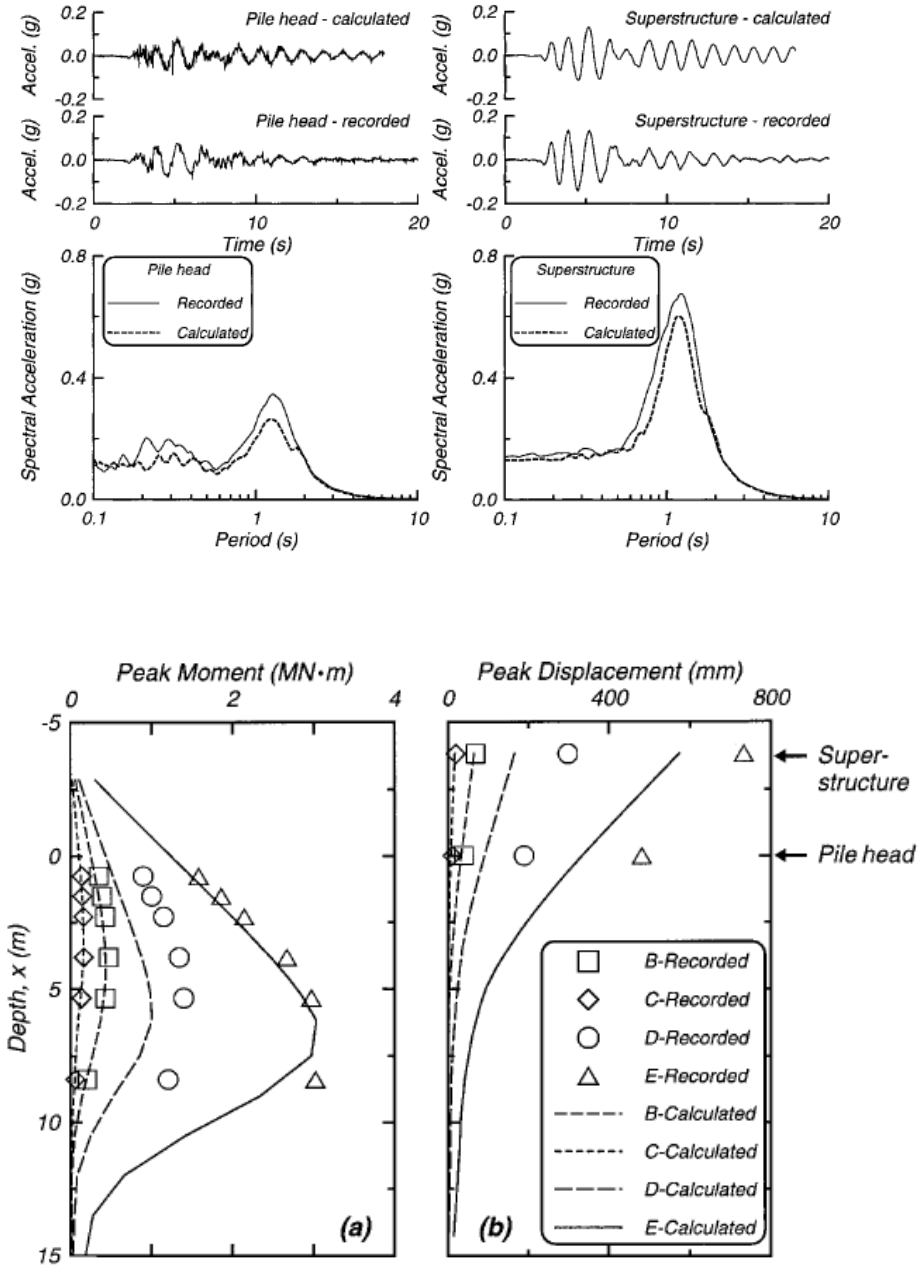

Figure 2.11 Calculated and recorded accelerations, peak bending moments and displacements (Christina et al., 1999)

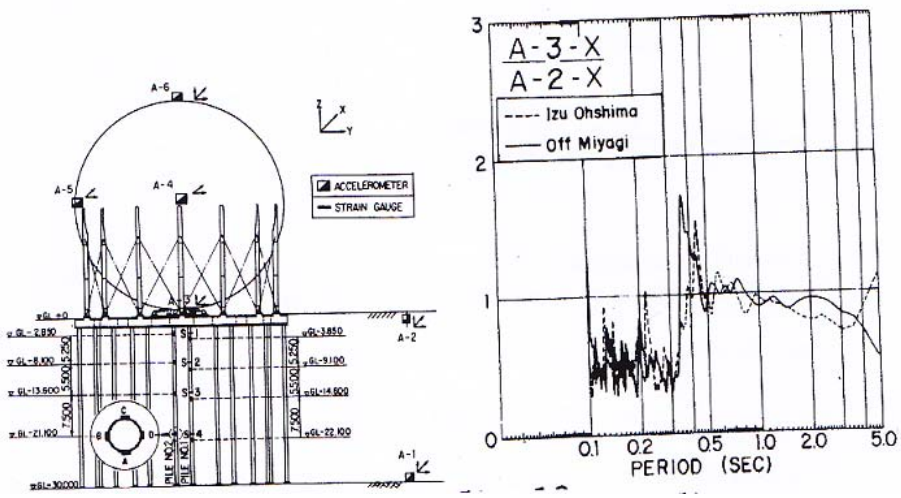

Figure 2.12 Spherical Tank structure instrumentation plan and pile cap to free field transfer function (Hamada and Ishida, 1980)

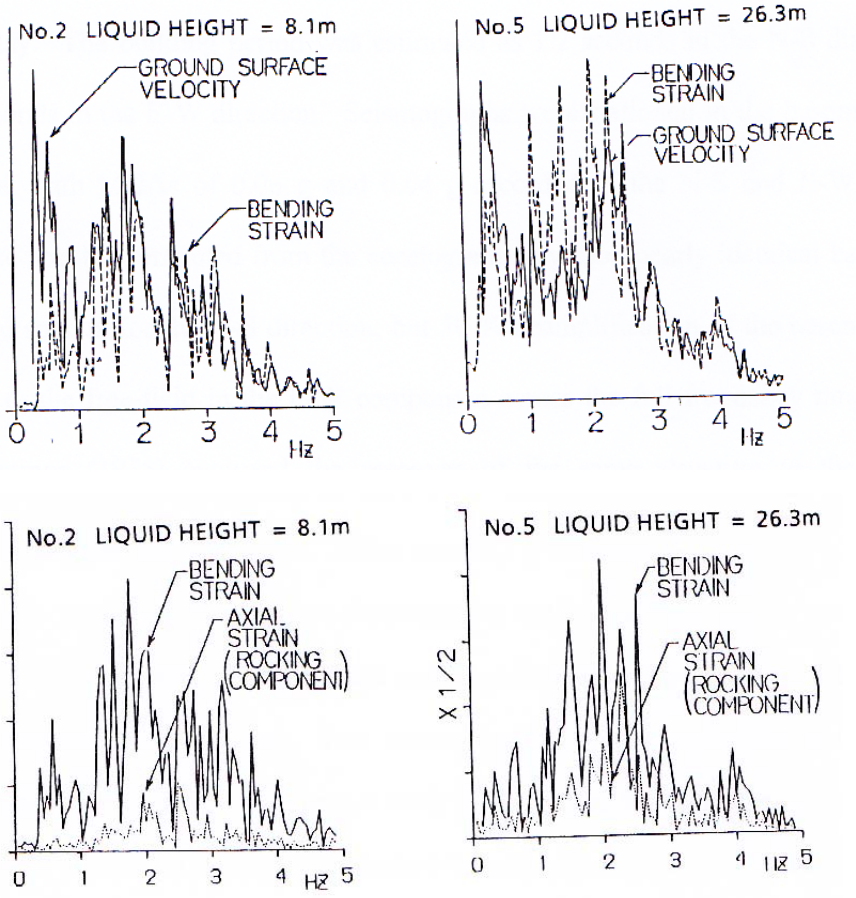

Figure 2.13 LNG Storage tank pile bending and axial strain spectra at two different liquid heights (Tsujino et al., 1987)

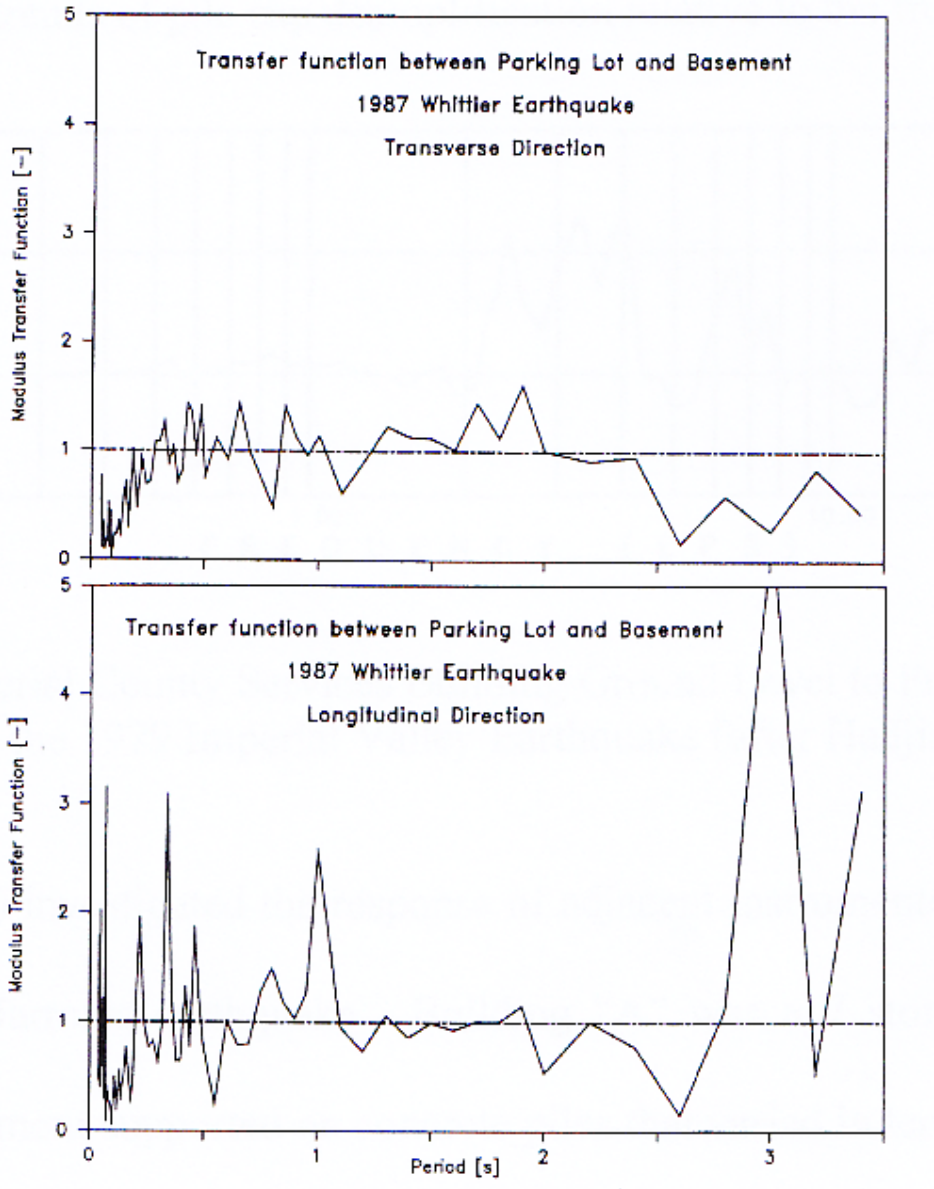

Figure 2.14 Hollywood Storage Building Parking Lot/ Basement transfer function during the Whitter Narrows earthquake (Fenves and Serino, 1992)

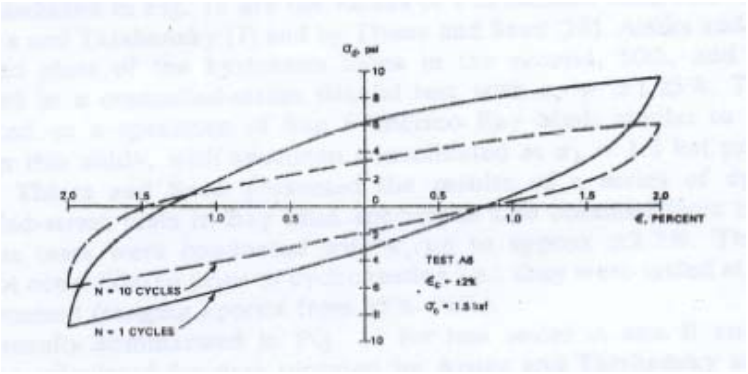

(a)

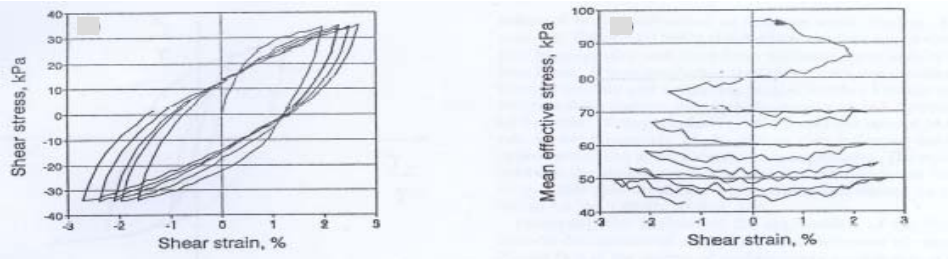

(b)

Figure 2.15 (a) Nonlinear stress-strain relation of San Francisco Bay Mud (Idriss et al., 1978) and (b) Cyclic test result on soft clay by Puzrin et al. (1995)

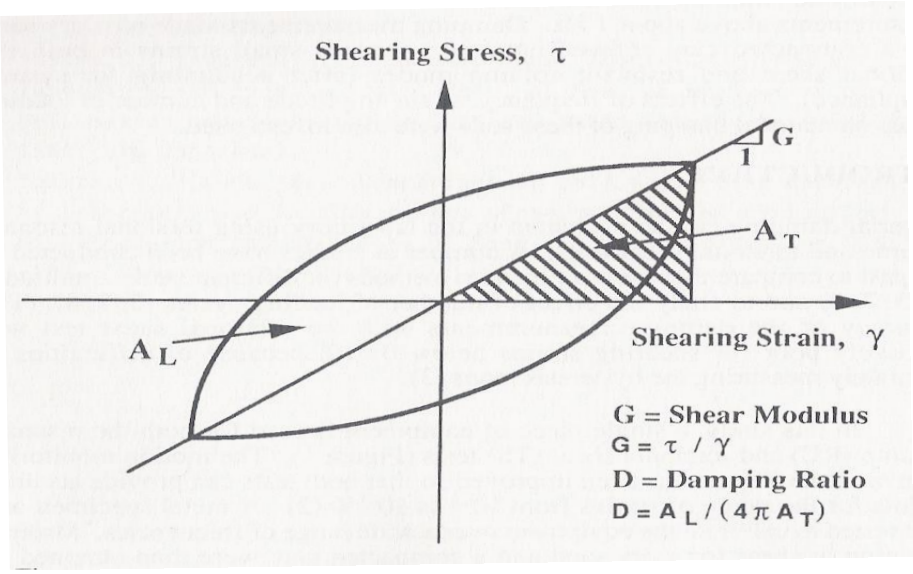

Figure 2.16 Determination of damping ratio from hysteretic loops. (Kim et. al. 1991)

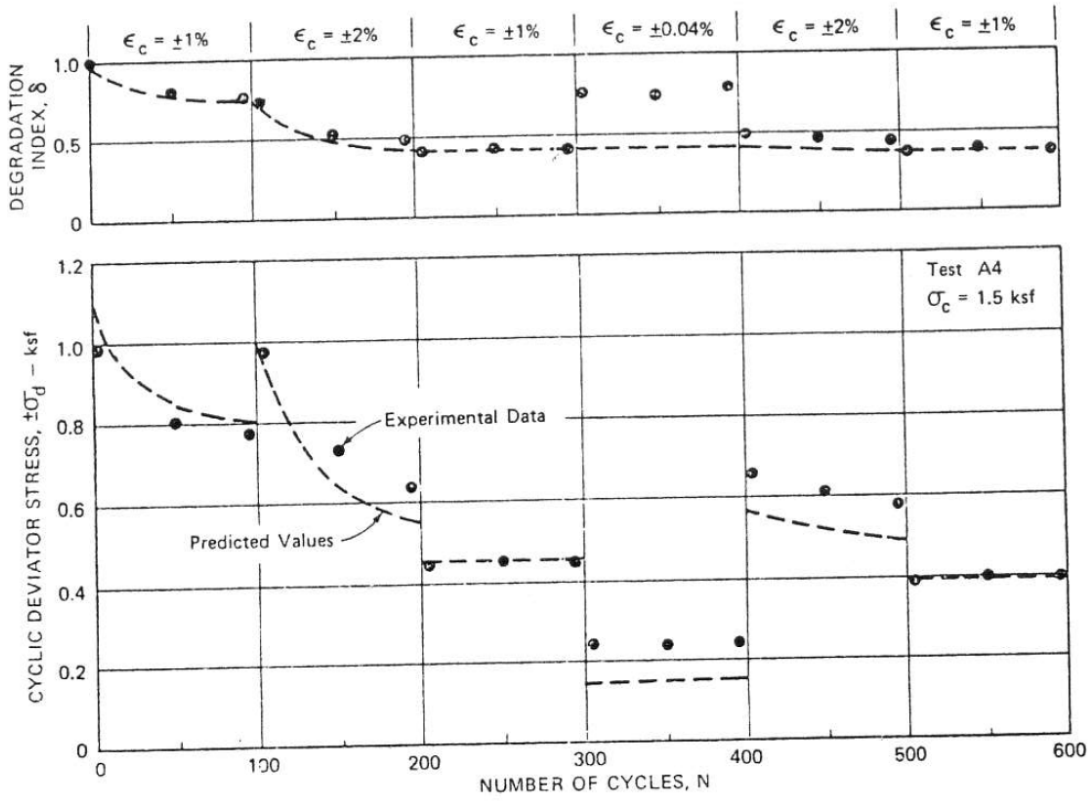

Figure 2.17 Stiffness degradation as modeled by Idriss et al., 1978

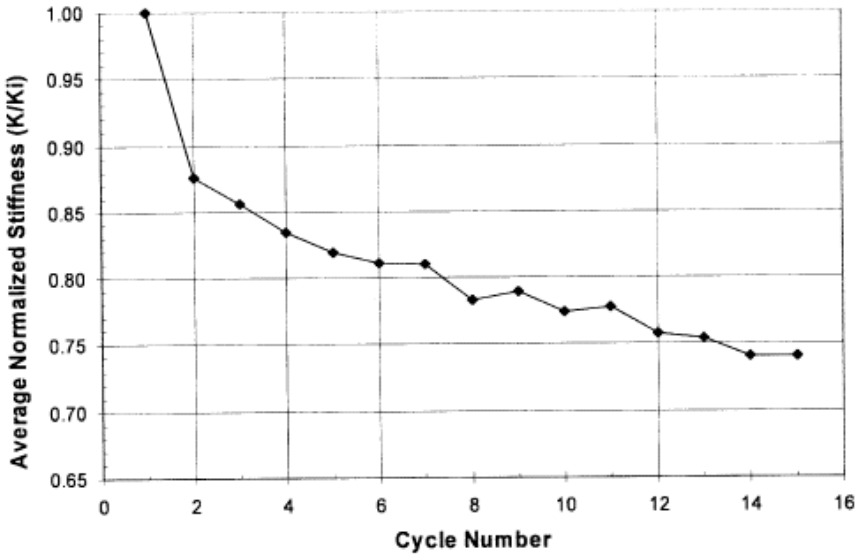

Figure 2.18 Stiffness degradation with cyclic loading in quasi-static pile load test (Snyder, 2004)

CHAPTER 3 DYNAMIC PROPERTIES OF KAOLIN CLAY

3.1 Introduction

From the preceding literature review, it is clear that the seismic performance of deep foundations is significantly affected by the non-linear dynamic properties of the soil in which they are installed in. For clayey soils, the shear modulus and the damping ratio are perhaps the two most common parameters considered in seismic soil behaviour characterization. For instance, variation in modulus and damping ratio with strain has been reported for various soils such as dry or saturated Toyoura sand (Kokusho, 1980), Fujisawa sand (Ishihara, 1996), San Francisco sand (Hardin and Drnevich, 1972b), normally consolidated San Francisco Bay Mud (Hardin and Drnevich, 1972b), Venezuelan clay (Vucetic and Dobry, 1991) and Israeli Dead Sea soft clay (Puzrin et al. , 1995). In addition, these changes have also been correlated to index properties such as the plasticity index for clays and the relative density for sands (Vucetic and Dobry, 1991; Ishihara, 1996).

The soil used in the centrifuge model tests in this study is Malaysian kaolin clay. Some engineering properties for this material, as reported by Goh (2003) based on static laboratory tests, are summarized in Table 3.1. The effect of strain-dependent stiffness and damping ratios were not considered in Goh's study. This chapter reports an investigation into the modulus and damping of Malaysian kaolin clay.

In this study, strain-controlled cyclic triaxial CIU tests (ASTM D3999-91) and resonant column tests (ASTM D4015-92) were performed to evaluate the dynamic properties of kaolin clay. The results were used to obtain modulus values and damping ratios for shear strains ranging from 10^{-3}% to 1%. Figure 3.1 shows the approximate strain range for which the various types of tests are applicable (Mair, 1993). The main shaking during earthquakes involves 10-20 times repetition of loads with differing magnitude (Ishihara, 1996). While the seismic loading is irregular in time history, the period of each impulse, is within the range between 0.1 to 3 secs depending on the near-field or far-field nature of the earthquake. As indicated in Chapter 1, the far-field earth tremors are often most common in Singapore. The typical range of the predominant period of those far-field earthquakes is approximately 0.8~2secs (Pan et al., 2007). The likely strain range for far-field earthquakes generally vary from 0.1 to 2% (Ishihara, 1996). However, Yu and Lee's (2002) back-analyses suggest that, in the earthquakes having peak ground acceleration of 0.1g, shear strain levels as high as 4-7% may be attained. The NUS traixial and resonant column tests set-up, however, are incapable of operating at strain level beyond 2%.

3.2 Cyclic Triaxial Test

3.2.1 Preparation of Test Specimens

The kaolin clay specimens were prepared by mixing kaolin powder with water in the ratio 1:1.2 by weight. The resulting slurry was then poured into pre-loading tubes of the same size as the test specimens, where they were left to pre-consolidate for at least a week. This step is crucial as it allows the

specimen to gain some shear strength prior to the consolidation process in the triaxial cell.

The pre-loading assembly consists of stainless steel tubes with 38 mm internal diameter, each fitted with a stand holder at its top through which loading plates can be added with minimal eccentricities (Figure 3.2). Weights of 6 and 10 kg were used to pre-consolidate the slurry to effective vertical stresses of 50kPa and 100kPa, respectively, prior to cyclic loading.

3.2.2 GDS Advanced Triaxial Test Set-Up

The GDS advanced triaxial apparatus shown on Figure 3.3 was used to perform the strain-controlled cyclic loading tests in this study. To set up, the pre-consolidated test specimen was first extracted from the steel tube and placed in the triaxial cell along with the membrane, filter paper and porous stones. Figure 3.4 shows the schematic of the test setup. To facilitate cyclic testing in the extension phase, an extension top cap and rubber sleeve assembly was used together with the standard triaxial top cap (Figure 3.5). During the extension phase, the suction developed within this sleeve couples the test specimen to the actuator.

When the test chamber is properly set up, the conical extension top cap would fit exactly into the sleeve. The narrow gap between the normal and extension top caps was maintained at the atmospheric pressure, so that the cell pressure confining the specimen would hold the two caps together. A photograph showing the coupled segments is shown on Figure 3.6.

3.2.3 Range of Cyclic Triaxial Test Conditions

Cyclic testing was carried out for six different frequencies ranging from 0.05 Hz to 1.5 Hz, which is the highest frequency the system can achieve. For each frequency, the specimen was subjected to several stages of cyclic loading, with strain amplitudes ranging from 0.137% to 1.37% (Table 3.2). Some preliminary tests showed that the first meaningful results were obtained at 0.137% strain level. In each stage, the specimen was subjected to 60 cycles of loading with constant strain amplitude.

3.2.4 Calculation of Shear Modulus and Damping

Following Kim et al. (1991) the secant modulus G is defined as follows:

$$G = \tau / \gamma \tag{3.1}$$

where τ is the shear stress experienced by the specimen and γ is the shear strain, as illustrated in Figure 3.7. As mentioned in Chapter 2, the material damping is determined by the ratio of the energy dissipated in one cycle and the energy stored during the loading. Following Kim et al. (1991), these quantities may be calculated from the areas of the stress-strain loop, as shown in Figure 3.7. Mathematically, the damping ratio D is given by

$$D = A_L / (4\pi A_T) \tag{3.2}$$

where A_T is the energy stored during loading phase and A_L is the energy dissipated in one cycle of loading.

3.2.5 Limitations

The main drawback of the cyclic triaxial test is its inability to measure shear modulus accurately, especially at very small strain levels. In standard triaxial testing, strains are not measured directly, but are usually obtained from displacement transducers located outside the triaxial chamber, which measure the average compression or extension of the entire specimen during loading. Owing to errors arising from non-uniformity at the specimen ends, the compression is likely to be over-estimated and the modulus underestimated, sometimes by as much as a factor of 10. However, Dupas et al. (1988) indicated that external strain measurement can be reasonably accurate down to 0.1% cyclic shear strain. Such an observation was also supported by Lacasse and Barre (1988).

3.3 Resonant Column Tests

In this study, the resonant column test is used to determine the shear modulus and damping ratio at very small strains (10^{-5}-10^{-3}). The excitation frequency applied in this test, which is typically about 30 to 40 Hz, is much higher than that achievable by cyclic triaxial tests.

3.3.1 Drnevich Long-Tor Resonant Column Apparatus

The Drnevich torsional resonant column apparatus is used in this study (Figure 3.8). It consists of a fixed pedestal at the base of the specimen, while the top is free to undergo torsion (Figure 3.9). The specimens were prepared in the same way as described in Section 3.2.1 for the triaxial tests. The clay specimen was first seated on the bottom platen. The top platen, together with

a large circular magnet, was then adjusted to make contact with the upper end of the specimen. The height of the bearing shaft and spring was pre-adjusted so as to support the weight of the magnet and platen while ensuring proper contact. To enhance the contact between specimen and platens, quick dry adhesives were added to all contact surfaces during mounting of the specimen.

The resonant column was found to be highly sensitive to small vibrations which had been observed to distort the Lissajous curves significantly as well as the free vibration response of the specimen during the decay stage. To minimize the effect of vibrations, isolation measures were implemented, including the placement of a 3-mm thick rubber mat at the base of the test apparatus to act as a vibration isolator. In addition, tests were conducted in the early mornings or late evenings as far as possible, when external activities are minimal.

The results from two series of resonant column tests performed in this study are summarized in Table 3.3.

3.3.2 Calculation for Small Strain Shear Modulus and Damping Ratio

Torsional excitation was applied to one end of the soil specimen and the frequency was varied until the lowest frequency at which resonance can be excited is reached. This is considered to the frequency of the fundamental mode of vibration. Once the fundamental mode of resonance frequency is established, the resonance frequency and amplitude of vibration were measured.

At the start of a typical resonant column test, a small voltage was used to generate a torque that produces small shear strains in the specimen. After

the voltage has stabilized, a slow frequency sweep was applied to the excitation voltage, starting from a very low frequency, until the Lissajous curve of acceleration against excitation voltage took on the form of an eclipse, indicating that the response (i.e. acceleration) is phase-leading the excitation voltage by 90°; this was taken to be the sign of resonance. The measured acceleration data is then used to calculate the corresponding strain and shear modulus of the kaolin clay specimen following the procedure described in ASTM D4015-92.

For torsional excitation,

$$\text{Shear modulus, } G_0 = \rho (2 \pi L)^2 (f_t / F_t)^2 \qquad (3.3)$$

where F_t = dimensionless frequency factor for torsional motion (Drvevich et. al., 1978).

f_t = system resonant frequency for torsional motion as observed during the test

Also,

$$\text{Shear strain, } \gamma = (RTO \times RCF) (SF) d / 2.5 L \qquad (3.4)$$

where RTO = rotational transducer output

RCF = rotational calibration factor

SF = strain factor

d = diameter of soil specimen

L = length of soil specimen

The damping ratio was calculated using the standard logarithmic decay method. During the test, the decay response was initiated by shutting off the power supply to the torsional excitation coils. This allows the specimen

motion to decay as it undergoes damped, free vibrations. Values of the initial amplitude, the final stabilized amplitude and the decay interval may be obtained from the free vibration history for calculating the damping ratio.

Using these information, the logarithmic decrement ζ for the whole system (inclusive of clay specimen, platens and oscillators) may be determined as follows, based on ASTM D4015-92:

$$\zeta = 1/n \, [\ln (A_1 / A_{n+1})] \tag{3.5}$$

where A_1 and A_{n+1} are the respective vibration amplitudes of the 1^{st} and $(n+1)^{th}$ cycle, after the power supply is shut off.

Following Drnevich et al. (1978), the specimen damping ratio is calculated as follows:

$$D (\%) = 100 / 2 \pi [\zeta_S (1 + S) - S \zeta_0] \tag{3.6}$$

where ζ_S = specimen logarithmic decrement for torsional vibration

ζ_0 = apparatus logarithmic decrement

S = system energy ratio

The system energy ratio, S, is defined as

$$S = (J_A / J) (f_{ot} F_T / f_T)^2 \tag{3.7}$$

where F_T = dimensionless frequency factors for torsional motion

J_A = rotational inertia of active-end platen system

J = Specimen rotational inertia

f_t = resonant frequency of torsional mode

By progressively increasing the applied voltage to the platens, the shear modulus and damping ratios were obtained for different strain levels using the procedure described above.

To assess the effects of air damping, a resonance column test was carried out with the clay specimen replaced by the calibration rod. Assuming negligible material damping of the rod, the resulting damping response may be attributed to the effects of air. This is plotted on Figure 3.10, which also shows the damping ratio response associated with the kaolin clay specimen. The results suggest that air damping does not contribute significantly to the overall damping response. Nevertheless, its contribution is deducted from all the kaolin clay results presented below.

3.4 Tests Results and Analysis

An overview of the cyclic triaxial tests carried out in this study is provided in Table 3.2. All the specimens were tested under a cell pressure of either 200 kPa (series CT1, CT3 amd TRS) or 150 kPa (series CT2). For series CT1 and CT2, each specimen was subjected to seven stages of cyclic loading, in which the strain amplitudes were progressively increased from 0.137% to 1.37% in seven increments, viz. 0.137%, 0.254%, 0.548%, 0.822%, 0.959%, 1.096% and 1.37%. Within each stage, the specimen was cyclically loaded for 60 cycles at constant strain amplitude. The same test procedure was repeated for six excitation frequencies ranging from 0.05 Hz to 1.5Hz.

In series CT3, two 'virgin' specimens were each subjected to a single stage loading of 60 cycles, with constant strain amplitudes of 0.789% and 1.37% respectively. Their results can be compared to those obtained from CT1-3, in which the specimen was subjected to prior stages of straining before the amplitudes of 0.789% and 1.37% were applied. In series CT4, the two

specimens were each tested under a higher frequency of 3 and 5 Hz respectively, at a constant strain amplitude of 1.37%.

Table 3.3 provides a summary of the resonant column tests, which were also carried out for the same confining cell pressures of 200 kPa and 150 kPa. However, these tests involve much smaller strain amplitudes ranging from 0.002% to 0.08% and higher frequency levels from 30 to 50 Hz.

Figure 3.11 shows the measured stress-strain and stress path responses for the stage when CT1-5 was cyclically loaded for 60 cycles at a constant strain amplitude of 0.789%. The gradual reduction in the peak deviator stress, q, is an indication of cyclic stiffness degradation. As shown on Figure 3.11b, the effect of cycling also reduces the mean effective stress (p') from the initial consolidation value ($p_c^{'}$) of 200 kPa to about 185 kPa. . This suggests that the reduction in mean effective stress is related to the shear modulus degradation, which would be consistent with the notion that modulus is dependent upon effective stress.

Figure 3.12 shows the corresponding results for test CT3-1, in which a virgin specimen was subjected to 60 cycles of constant strain amplitude 0.789%, without any prior loading at smaller strains. As shown on Figure 3.12a, the peak deviator stress measured in the first cycle was higher than the corresponding value of Figure 3.11a. This difference may be attributed to the cyclic degradation experienced by specimen CT1-5 due to the prior loading stages at smaller strain amplitudes. As for the stress path, Figure 3.12b shows a significant reduction in p' (from 200 kPa to 78 kPa) compared to Figure 3.11b (from 200 kPa to 185 kPa). The rate of decrease was higher during the

first 5~6 cycles, after which it gradually approached the final p' value of 78 kPa with additional cycling.

Similarly, another virgin specimen (CT3-2) was tested cyclically using a strain amplitude of 1.37%, with the same loading frequency of 1Hz. Figure 3.13 shows the stress-strain loops and corresponding stress paths of the test. The results indicate that the amount of cyclic degradation was significantly higher than that shown on Figure 3.12a. At the same time, the stress path also shows a greater reduction of p', compared to Figure 3.12b.

3.4.1 Shear Modulus

3.4.1.1 Calculation of G_{max}

There is considerable evidence that soil behaviour at very small strain is linear and elastic (Dasari, 1996; Jardine *et al.*, 1986). In both slow and dynamic cyclic loading tests involving very small strain amplitudes, the stress-strain loops show little or no hysteresis. This indicates that the soil behaviour is conservative and little or no energy is dissipated (Papa et al., 1988; Silvestri, 1991), so that volumetric and shear deformations are fully recoverable (Lo and Presti, 1989). The shear modulus also approaches a nearly constant value, which is usually referred to as the maximum shear modulus (G_{max}) of that soil (Dasari, 1996).

Figure 3.14 shows the variation in shear modulus obtained from the resonant column tests. Also plotted in this figure are values estimated using Viggiani *et al.*'s (1995) relation that

$$G_{\max} = C(p')^n (OCR)^m \qquad (3.8)$$

where,

n = effective stress exponent

OCR = over consolidation ratio

m = OCR exponent

C = a constant

For normally consolidated (i.e. R=1) speswhite kaolin, Viggiani et al. (1995) reported that C=1964 and n=0.653. Hence, Eq. 3.8 can be expressed as,

$$G_{max} = 1964(p')^{0.653} \tag{3.9}$$

As shown on Figure 3.14, the G_{max} values obtained from resonant column tests are about 5% higher than those calculated using Eq. 3.9, for p' values of 200 kPa and 150 kPa. Hence, for the kaolin clay used in this study, the value of the parameter C proposed by Viggiani has been increased by 5%, while keeping n constant. The corresponding relationship for kaolin clay is thus given by

$$G_{max} = 2060(p')^{0.653} \tag{3.10}$$

3.4.1.2 Effect of Shear Strain Amplitude

Figure 3.15 shows the stress-strain response of the first loading cycle, extracted from the same set of results shown in Figure 3.11. It is noted that the response is approximately linear at small strains of below 0.002%. Beyond this, the non-linear behaviour is characterized by a progressive reduction in the secant modulus with increasing strain.

For all the cyclic triaxial tests listed on Table 3.2, values of the secant shear modulus (G) were calculated at the peak deviator stress along the

loading phase of the first cycle, following the procedure of Section 3.2.4. These values of G were then normalized by the small strain shear modulus G_{max}, obtained from the resonant column tests for the corresponding consolidation pressure and shown in Figure 3.16. Figure 3.16 also shows the corresponding data for G obtained from resonant column tests. As can be seen, the resonant column and cyclic triaxial test results lie closely along an S-shaped trend with the shear modulus decreasing with shear strain. This S-shaped trend has been observed by numerous researchers in previous studies (Vucetic and Dobry, 1991; Kagawa, 1992; Hardin and Drnevich, 1972a,b; Ishibashi and Zhang, 1993; Kokusho, *et al.,* 1982). For the kaolin clay used in this study, it appears that there is negligible modulus degradation for very small shear strains of up to 0.01%. Beyond this, the effect of modulus reduction becomes significant, with the secant modulus decreasing quite rapidly to about $0.1G_{max}$ at a shear strain level of 1%.

Also plotted in the same figure are normalised modulus reduction curves reported in previous studies (Vucetic and Dobry, 1991; Kagawa, 1992; Hardin and Drnevich, 1972a,b; Ishibashi and Zhang, 1993; Kokusho, *et al.,* 1982) for different clays with plasticity index typically in the range of 30~40. The current test results, obtained using different strain amplitudes, loading frequencies and two consolidation pressures, fall within the lower bound reported by Hardin and Drnevich (1972) and the upper bounds reported by Kokusho et. al.(1982) and Ishibashi and Zhang (1993).

3.4.1.3 Effect of Frequency

While the strain-dependent nature of $\frac{G}{G_{max}}$ is quite well studied and understood, the effect of frequency on modulus reduction has not been conclusively stated in previous studies. Although an increase of shear modulus with the rate of loading has been reported by Stokoe et al. (1995), the effects of the number of loading cycles and frequency cannot be clearly distinguished. On the other hand, Shibuya et al. (1995) found that the loading rate has negligible effect on the shear modulus measured using the cyclic torsional shear test. Zanvoral and Campanella (1994), however, reported that shear modulus can increase with frequency, but the effect is relatively small compared to the strain contribution. Teachavorasinskun et al. (2002) also commented that at large strain levels, the effect of frequency on modulus degradation is quite negligible compared to that of strain.

The results shown in Figure 3.16 were compiled from resonant tests conducted at frequency ranging from 30Hz to 40Hz whereas the cyclic triaxial tests were conducted at frequency no higher than 1.5Hz. The fact that, in spite of the large frequency difference, they plot closely along a single S-trend suggests that the modulus is likely to be frequency independent. Figure 3.17 shows the $\frac{G}{G_{max}}$ ratios from the first load cycle of the cyclic triaxial tests conducted using a preconsolidation pressure of 200 kPa plotted against applied frequency, for different strain amplitudes. . As can be seen, for a given strain amplitude, the $\frac{G}{G_{max}}$ ratios remain largely constant. Thus, the results from the current tests suggest that the modulus degradation is largely frequency-

independent over the range of frequencies tested. In addition, since G_{max} is obtained under a high frequency of between 30Hz to 40Hz and is a constant value for a given preconsolidation pressure, the modulus at any strain level is also largely frequency-independent.

3.4.1.4 Effect of Cycles

Apart from the strain level, the shear modulus is also affected by the number of load cycles to which the specimen is subjected (Idriss et al., 1978). This is illustrated on Figure 3.18 for specimen CT1-5, which plots the stress-strain loops for only the first and the last (60^{th}) cycle of the stage when the applied strain amplitude was 0.789%. As can be seen from the figure, there is a degradation of the backbone curve, with the peak deviator stress reducing from 78 kPa to 63.4 kPa after 60 cycles of loading. This phenomenon of stiffness degradation under repeated loadings may be important when considering clay response to earthquake loading, as the latter often comprises numerous cycles of different strain amplitudes.

Matasovic and Vucetic (1995) introduced the concept of a threshold strain in relation to cyclic degradation, which states that there exists a minimum value of the shear strain below which stiffness degradation does not take place. Figure 3.19 shows the variation of degradation index with increasing strain amplitude for the three specimens CT1-1, CT1-3 and CT1-5, computed at the end of 60^{th} cycle. The general trend for all three samples suggests that initially, up to 0.137% strain, there is no considerable stiffness degradation. Additionally, Figure 3.20a shows two loops obtained from the 1^{st} and 60^{th} cycle of specimen CT1-5 for a cyclic strain amplitude of 0.137%.

There appears to be little or no change in the two backbone curves, which indicates the absence of any significant stiffness degradation under repeated loading at the given strain amplitude. On the other hand, as shown on Figure 3.20b, there is discernable degradation between the 1st and 60th cycle for a higher cyclic strain amplitude of 0.254%.

All these results from Figure 3.19 and 3.20 suggest that the threshold strain for the kaolin clay used in this study is between 0.137% and 0.254%. The value 0.137%, which may be considered a lower bound estimate of the threshold strain, is not too different from the value of 0.1% reported by Matasovic and Vucetic (1995) for normally consolidated and over-consolidated VNP marine clay.

The degradation index, δ, for transient loading conditions is defined by Idriss *et al*. (1978) as the ratio of the ordinate of the backbone curve at a specific strain level divided by the corresponding ordinate on the un-degraded first cycle backbone curve. In the present study, the strain level of 0.254% was used for calculating the degradation index, as this was the smallest amplitude at which degradation was observed. As an example, consider specimen CT1-1, which was subjected to six stages of constant strain amplitude loadings at a frequency of 0.05 Hz. Each stage comprised 60 cycles, thus giving rise to a total of 360 cycles. At any point during the test, the degradation index may be calculated as a ratio of the deviator stress at 0.254% strain measured during the current cycle to the peak deviator stress measured during the first un-degraded cycle. Figure 3.21 shows the variation of degradation index with increasing cycles for the three specimens CT1-1, CT1-3 and CT1-5, calculated at the end of each constant strain amplitude loading stage. The overall

responses for the three specimens are quite similar, which suggest that the degradation index is also likely to be frequency-independent. Such behaviour is in agreement with the observation made by Yasuhara *et al.* (1982).

3.4.1.5 Shear Modulus and Change in Effective Stress

As Figure 3.22 shows, the degradation index is reasonably well-correlated to the mean effective stress (p') for three strain levels (0.137%, 0.789% and 1.37%). It will be shown later in Section 3.5.1.5, that as G_{max} is calculated for very small strain, $\frac{G_{\max,N}}{G_{\max,1}} \approx \delta$ (Degradation index). Hence, Eq. 3.10 can also be used to compare the experimental trend. Figure shows that it can represent, at least to a certain extent, the experimental observations reasonably well. In addition, the reduction of p' appears to reach an insignificant level for a strain level of 0.137%, which is in line with the earlier postulates of threshold strain of 0.1%.

3.4.2 Damping ratio

3.4.2.1 Effect of Shear Strain Amplitude

Numerous studies in the literature have shown that the damping ratio in clay usually increases with strain level, forming a 'S'-shaped design curve (Vucetic and Dobry, 1991; Kagawa, 1992; Hardin and Drnevich, 1972a,b; Ishibashi and Zhang, 1993; Kokusho, *et al.*, 1982). As Figure 3.23 shows, the current results, obtained from both cyclic triaxial and resonant column tests, also showed also a similar trend in which the damping ratio increases with strain. It should be noted that, in processing the triaxial test results, the

damping ratios were calculated from the first cycle of loading. At low strain levels of about 0.01%, the damping ratio calculated from resonant column tests was about 3%. The damping ratio increases quite rapidly to about 20% at strain levels of about 1% or greater, as calculated using the first cycle of loading of the triaxial tests. Comparison of Figures 3.16 and 3.23 indicates the damping ratio data from the cyclic triaxial tests has a large scatter than the modulus, which may be explained by the difficulties in estimating the logarithmic decrement from the test data. As will be shown later, there is no discernible frequency-dependency in the cyclic triaxial test data. Nonetheless, the scatter in the damping ratio remains much smaller than the average damping ratio of about 17.5%. Furthermore, the current kaolin clay data generally fall between the reported results of Hardin and Drnevich (1972) and Kokusho et. al. (1982), which may be considered as the upper and lower bounds, respectively, of the damping ratio response.

For specimen CT1 (p'=200kPa), Figure 3.24 shows the individual components of the damping ratio, i.e. the energy stored during the loading and the energy dissipated in the first cycle, plotted against the shear strains. The results indicate that both the energy dissipated in one cycle and the energy stored during the loading stage increases nonlinearly with strain amplitude. However, the component of energy dissipation increases more rapidly with strain level compared to the energy stored during the loading stage. This trend is consistent with typical clay behaviour in which damping ratio increases with strain level.

3.4.2.2 Effect of Frequency

As discussed in Section 2.2.2, the influence of frequency on the damping ratio has been examined by other researchers. Shibuya et al. (1995) and Teachavorasinskun et al.(2002) reported a decrease in damping ratio with increase of loading frequency. On the contrary, there few reports available where damping ratio seems to be increased with loading frequency (Kim et al., 1991; Zanvoral and Campanella, 1994; Thammathiwat and Weeraya, 2004). Ishihara (1996) also suggested that "…*the energy dissipation in soils is mostly rate-independent and of a hysteretic nature*…".

In this study, the results from both triaxial and resonant column tests are combined to provide a database with which the damping ratios may be calculated over a fairly wide range of frequencies. The triaxial test series, CT1 and CT2, provide damping response information for specimens subjected to a maximum strain amplitude of 1.37% and loading frequencies of between 0.05 Hz and 1.5 Hz. On the other hand, resonant column tests involve significantly smaller strain levels (0.002% ~ 0.6%) and much higher frequencies of up to 40 Hz or more. For conditions involving high frequencies and relatively large strains (series CT4, see Table 3.2), an advanced GDS system was used in which the specimen was subjected to a maximum strain amplitude of 1.37% and a frequency of up to 5 Hz.

In Figure 3.25, the damping ratios obtained from the triaxial tests (CT1, CT2 and CT4) and the resonant column tests are plotted against the loading frequencies. For frequencies between 0.05 Hz and 40 Hz, there does not appear to be any clear correlation between the damping ratio and loading frequency. The resonant column results show much lower damping ratio in

spite of the higher frequency, primarily because of the lower strain amplitude imposed by the resonant column as shown in Figure 3.23. This indicates that the damping is much more dependent upon the strain amplitude rather than the frequency.

The effect of frequency on the individual damping components are also processed from the cyclic triaxial test results. Figure 3.26 is a plot showing how the energy dissipated in the first cycle varies with frequency. Figure 3.27 shows the corresponding plot for the energy stored during the loading phase. The results do not indicate any clear trend to suggest that either component varies with frequency.

3.4.2.3 Effect of Cycles

Figure 3.28 plots the damping ratio associated with the N^{th} cycle against the number of cycles (N) for test CT1-6. For the various strain amplitudes tested, there were significant reductions in the damping ratios over the first 10 cycles, from about 18% to 11% (based on averaged values). Beyond the first 10 cycles, the damping ratios did not change significantly. A similar trend was observed in Figure 3.29, which plots the energy dissipated within the N^{th} cycle versus the number of cycles (N).

3.4.2.4 Damping Ratio and Change in Effective Stress

Figure 3.30 shows that the hysteretic damping is not well well-correlated to changes in effective stress and therefore cannot be placed into a classical plasticity framework. In the existing well-known soil models which feature hysteresis (eg. Whittle, 1993; Puzrin et al. , 1995), the hysteretic

behaviour have been incorporated in a semi-empirical manner. Those models did not explain hysteresis in a more mechanistic point of view. Hence it can be argued, that the fundamental causes of hysteretic behavior in clay is still not well-known.

3.4.3 Summary of Tests Results

In the present study, resonant column and cyclic triaxial tests were carried out to evaluate the cyclic behavior of kaolin clay under a wide range of strains, frequencies and load cycles. The effects of strain amplitude on shear modulus and damping ratio are generally consistent with those reported in the literature for other clayey soils (Vucetic and Dobry, 1991; Kagawa, 1992; Hardin and Drnevich, 1972a,b; Ishibashi and Zhang, 1993; Kokusho, *et al.*, 1982).

As discussed earlier, the results from previous reported studies provide somewhat conflicting conclusions on the effect of frequency on the damping ratio. The results from the present study suggest that the damping ratio is relatively independent of frequency. This observation is consistent with the reported results of Vucetic and Dobry (1991) and Ishihara (1996). Hence, it may be inferred that, for the kaolin clay considered in this study, the damping ratio is independent of strain rate. In other words, it appears that viscous damping does not play a significant role in comparison to rate-independent hysteretic damping in the energy dissipation process. Phenomenological, hysteretic damping is similar to elasto-plastic damping. Lee's (2006) consideration of viscosity scaling in cement slurry suggests that, in a material with a sufficiently high Bingham yield stress, the Bingham yield stress (which

is related to hysteretic damping) can have a greater effect on slurry behaviour than the viscous stresses. In such cases, it may be more important to model the Bingham yield stress correctly, rather than the viscous stress. In light of this possibility, one can surmise that hysteretic damping may be much larger than the viscous damping for the kaolin clay tested in this study.

The degradation of shear modulus of kaolin clay is affected by the shear strain and the number of cycles of loading. Within each cycle of loading, the modulus reduction is quite negligible for small strains up to about 0.01%. Beyond this, the secant modulus reduced quite significantly with increasing strain. For example, at a shear strain of 1%, the secant modulus was about 0.1 G_{max}. Moreover, there exists a threshold strain of about 0.137% below which there was no significant degradation of the backbone curve under repeated cycles of loading.

3.5 A Strain Dependent Hyperbolic Hysteretic Soil Model

The following section introduces a soil model that will be used in the numerical analyses in this study. This model incorporates the features discussed in the preceding sections of this chapter, namely the modulus reduction with increasing strain, and stiffness degradation of the backbone curve under repeated cycling.

3.5.1 Theoretical Formulation of the Proposed Model

The model proposed herein encompasses the concepts of small strain non-linearity (Dasari, 1996; Puzrin 1998), hysteretic stress-strain behaviour (Pyke, 1979; Liu and Ling, 2006) and cyclic degradation of backbone curve

(Idriss, 1978; Rao and Panda, 1999) for the application to dynamic problems. The non-linear elasticity was modelled by varying the shear and bulk moduli as a function of the mean effective stress, the overconsolidation ratio and the corresponding strain increment since the last strain reversal (Viggiani et al., 1995; Dasari, 1996). The hysteretic stress-strain behaviour for unloading and reloading is modelled using the Masing rule (Masing, 1926). The progressive degradation of the backbone curve under repeated loading was modeled using Idriss's concept of degradation index (Idriss, 1978).

3.5.1.1 Hyperbolic Backbone Curve

As shown on Figure 3.16, the normalized shear modulus G/G_{max} decreases with increasing strain amplitude. In devising a model to reproduce such non-linear properties, the basic stress–strain curve was described using a hyperbolic relationship (Nasim, 1999) of the form

$$q = q_f - \frac{1}{\frac{S_{\max}}{q_f}}\left[\frac{S_{\max}}{1+\frac{(S_{\max})|\varepsilon_s|}{q_f}}\right] \tag{3.11}$$

where

q = deviator stress

S = tangent modulus of stress-strain curve

S_{max} = tangent modulus at very small strain

ε_s = generalized shear strain

q_f = deviator stress at failure

If $\varepsilon_s > 0$, then Eq. 3.11 may be written as,

$$q = q_f - \frac{1}{\frac{S_{\max}}{q_f}}\left[\frac{S_{\max}}{1+\frac{(S_{\max})\varepsilon_s}{q_f}}\right] \tag{3.12}$$

Denoting $$S = \frac{dq}{d\varepsilon_s} \tag{3.13a}$$

and $$A = \frac{S_{nax}}{q_f} \tag{3.13b}$$

then

$$S = \frac{dq}{d\varepsilon_s} = \frac{S_{nax}}{(1+A\varepsilon_s)^2} \tag{3.14}$$

For a three-dimensional stress state, the deviator stress q can be defined as

$$q = q' = \frac{1}{\sqrt{2}}\sqrt{(\sigma_x' - \sigma_y')^2 + (\sigma_y' - \sigma_z')^2 + (\sigma_z' - \sigma_x')^2 + 6(\tau_{xy}{}^2 + \tau_{xy}{}^2 + \tau_{xy}{}^2)} \tag{3.15}$$

The generalized Hooke's law for an elastic material may be written as

$$\sigma_x' = (K' + \frac{4}{3}G)\varepsilon_x + (K' - \frac{2}{3}G)\varepsilon_y + (K' - \frac{2}{3}G)\varepsilon_z \tag{3.16}$$

$$\sigma_y' = (K' - \frac{2}{3}G)\varepsilon_x + (K' + \frac{4}{3}G)\varepsilon_y + (K' - \frac{2}{3}G)\varepsilon_z \tag{3.17}$$

$$\sigma_z' = (K' - \frac{2}{3}G)\varepsilon_x + (K' - \frac{2}{3}G)\varepsilon_y + (K' + \frac{4}{3}G)\varepsilon_z \tag{3.18}$$

$$\tau_{xy} = G\gamma_{xy} \tag{3.19}$$

$$\tau_{yz} = G\gamma_{yz} \tag{3.20}$$

$$\tau_{zx} = G\gamma_{zx} \tag{3.21}$$

The generalized shear strain, ε_s, is defined as

$$\varepsilon_s = \frac{2}{3}\sqrt{\frac{1}{2}\left\{(\varepsilon_x^{'} - \varepsilon_y^{'})^2 + (\varepsilon_y^{'} - \varepsilon_z^{'})^2 + (\varepsilon_z^{'} - \varepsilon_x^{'})^2\right\} + \frac{3}{4}(\gamma_{xy}{}^2 + \gamma_{xy}{}^2 + \gamma_{xy}{}^2)} \tag{3.22}$$

Substituting Eqs. 3.15 to 3.20 into Eq. 3.14 and simplifying leads to

$$q = 3G\varepsilon_s \tag{3.23}$$

Hence $$\frac{dq}{d\varepsilon_s} = 3G \tag{3.24}$$

Comparing Eqs. 3.13a and 3.24 leads to

$$S = \frac{dq}{d\varepsilon_s} = 3G \tag{3.25}$$

and $$S_{\max} = 3G_{\max} \tag{3.26}$$

Substituting Eq. 3.26 into Eq. 3.11 leads to

$$q = q_f - \frac{1}{\dfrac{3G_{\max}}{q_f}}\left[\frac{3G_{\max}}{1 + \dfrac{(3G_{\max})|\varepsilon_s|}{q_f}}\right] \tag{3.27}$$

which describes the sub-yield behavior of the kaolin clay.

Substituting Eqs. 3.25 and 3.26 into Eq. 3.14 yields

$$G = \frac{G_{\max}}{\left[1 + \frac{3(G_{\max})|\varepsilon_s|}{q_f}\right]^2} \tag{3.28}$$

where,

$G_{\max}$ is taken as the shear modulus at very small strains (Eq. 3.10)

ε_s is the current generalized shear strain.

The deviator stress at failure (q_f) is calculated as,

$$q_f = \frac{Mp'}{2^n} \tag{3.29a}$$

where *p*' is the mean effective stress, and the friction coefficient M is given as,

$$M = \frac{6\sin\varphi}{3 - \sin\varphi} \tag{3.29b}$$

The secant shear modulus (G_{sec}) can be expressed as,

$$G_{sec} = \frac{q_r}{3\varepsilon_r} \tag{3.30}$$

where, q_r is the deviator stress at strain amplitude ε_r.

From Eq. 3.12,

$$q_r = q_f - \frac{1}{\frac{S_{\max}}{q_f}}\left[\frac{S_{\max}}{1 + \frac{(S_{\max})\varepsilon_r}{q_f}}\right] \tag{3.31}$$

Using Eq. 3.26,

$$q_r = q_f - \frac{1}{\frac{3G_{\max}}{q_f}}\left[\frac{3G_{\max}}{1+\frac{3G_{\max}\varepsilon_r}{q_f}}\right] \tag{3.32a}$$

Denoting $\frac{G_{\max}}{q_f} = \mathrm{R}$,

$$q_r = q_f - \frac{1}{3R}\left[\frac{3G_{\max}}{1+3R\varepsilon_r}\right] \tag{3.32b}$$

Combining Eq. 3.30 and Eq. 3.32 leads to

$$\mathrm{G_{sec}} = \frac{q_r}{3\varepsilon_r} = \frac{1}{3\varepsilon_r}\left[q_f - \frac{1}{3R}\left(\frac{3G_{\max}}{1+3R\varepsilon_r}\right)\right] = \frac{G_{\max}}{1+3R\varepsilon_r} \tag{3.33}$$

Hence , $\frac{\mathrm{G_{sec}}}{G_{\max}} = \frac{1}{1+3R\varepsilon_r}$ (3.34)

Figure 3.31 plots the values of $\frac{G_{\sec}}{G_{\max}}$ computed from Eq. 3.33 for different ε_r, together with the experimental data from Figure 3.16. The comparison suggests that the stress-strain relationship represented by Eq. 3.12 can characterize the nonlinear modulus degradation response of the kaolin clay considered in this study reasonably well.

From Eq. 3.29 and Eq. 3.33 ,

$$G_{\sec} = \frac{G_{\max}}{1+\frac{3G_{\max}\varepsilon_r}{Mp'}} \tag{3.35}$$

Eq. 3.35 may be used to check the measured performance of specimens CT3-1 and CT3-2. Figure 3.32 shows the plot of $\frac{G_{sec}}{G_{max}}$ against $\frac{p'}{p'_c}$, in which the solid symbols are the measured values at the end of every 10th cycle. The continuous lines are calculated from Eq. 3.35 for two strain levels of 0.789% (CT3-1) and 1.37% (CT3-2), in which G_{max} = 66.59 MPa for a consolidation stress p'$_c$ = 200 kPa, and M = 0.9 , corresponding to ϕ = 25° for kaolin clay. The mean effective stress, p', was obtained from the triaxial tests at the end of every 10th cycle. As can be seen from the figure, the values of $\frac{G_{sec}}{G_{max}}$ calculated using Eq. 3.35 can replicate the experimental trends reasonably well.

3.5.1.2 Modeling the Hysteretic Behaviour of Soils: Masing's Rules

In this study, Masing's rule (1926) was adopted to model the hysteretic behavior of the soil during the unloading and reloading phases of each load cycle. Accordingly, the shape of the unloading and reloading curves is similar to that of the backbone curve, except that (i) the scale is enlarged by a factor of 2 and (ii) the shear modulus on each loading reversal assumes a value equal to the initial tangent modulus of the initial loading (backbone) curve.

Eq. 3.11 can be simplified as,

$$q = q_f - \frac{1}{\frac{3G_{max}}{q_f}}\left[\frac{3G_{max}}{1+\frac{3G_{max}\varepsilon_s}{q_f}}\right] \qquad (3.36a)$$

Denoting $\frac{G_{\max}}{q_f} = \mathrm{R}$,

$$q = q_f - \frac{1}{3R}\left[\frac{3G_{\max}}{1+3R\varepsilon_s}\right] \tag{3.36b}$$

According to Masing's rule,

$$\text{Unloading path: } q = -2q_f + \frac{2}{3R}\left[\frac{3G_{\max}}{1+\frac{3R}{2}(\varepsilon_{r1}-\varepsilon_s)}\right] + q_{r1} \tag{3.37a}$$

$$\text{Reloading path: } q = 2q_f - \frac{2}{3R}\left[\frac{3G_{\max}}{1+\frac{3R}{2}(\varepsilon_s-\varepsilon_{r2})}\right] - q_{r2} \tag{3.37b}$$

where, q_{r1} and q_{r2} are the deviator stresses at the point of reversal as shown in the Figure 3.33.

As shown previously in Section 3.5.1.1, the tangent shear modulus can be obtained as:

$$G = \frac{G_{\max}}{\left[1+\frac{3(G_{\max})|\varepsilon_s-\varepsilon_{ur}|}{2q_f}\right]^2} \tag{3.38}$$

where ε_{ur} is the unloading-reloading shear strain at the point of reversal

There are several approaches available to determine if stress path reversal has occurred. Stallebrass (1990) defined the reversal angle as the angle of rotation between the previous and current stress path direction. She further commented that, for the reversal angle of 180°, a complete reversal would occur if the soil stiffness was at a maximum. On the other hand, Dasari (1996) defined the reversal angle in the strain space. The directions of the

previous and current strain increment vectors are calculated and the angle between these vectors is determined. If the angle is larger than 90°, the stress path is deemed to have reversed. A similar concept was also adopted by Whittle (1993) in the MIT-E3 model. In the current constitutive relationship, the reversal angle was formulated using Dasari's approach as follows:

$$\text{Reversal angle, } \theta = \cos^{-1}\frac{\overline{X}.\overline{Y}}{\sqrt{\overline{X}\,\overline{X}}\sqrt{\overline{Y}\,\overline{Y}}} \qquad (3.39)$$

where,

$\overline{X}$ = strain increments for all six strain components between (*i-1*)-th step and (*i-2*)-th step and

$\overline{Y}$ = strain increment for all six strain components between *i*-th step and (*i-1*)-th step

Eq. 3.39 is derived from the standard expression for the angle between two vectors in three dimensional space which states that, if A and B are two vectors in 3-D space, then the angle α between A and B can be formulated by the dot product as follows (Kreyszig, 2006),

$$\alpha = \cos^{-1}\frac{\overline{A}.\overline{B}}{\sqrt{\overline{A}\overline{A}}\sqrt{\overline{B}\overline{B}}} \qquad (3.40)$$

Accordingly, if the reversal angle θ computed from Eq. 3.39 is larger than 90°, stress path reversal is deemed to have occurred.

Pyke (1979) pointed out that the original Masing's rules could not adequately describe the stress–strain behaviour of soft clays under irregular or non-uniform cyclic loading. The stresses that may be generated under arbitrary loadings are not necessarily bounded by the conditions assumed in the Masing-type model. For example, the shear stresses under irregular cyclic

loadings may exceed the maximum shear stress experienced by the soil during the first cycle. To account for such situations, Pyke proposed two additional rules:

1. Figure 3.34a shows that if a reloading curve (for smaller loop) is carried past the previous limit of cyclic loading, it can be seen that the reloading curve is tangential to the initial loading curve at that point (point A) and hence diverges from initial loading curve. Therefore, to account for this problem, the first additional rule stated that the unloading and reloading curves should follow the backbone curve if the previous maximum amplitude of the shear strain is exceeded.
2. Secondly, it can be observed in Figure 3.34b that, even though the initial loading is bounded for this model, the stresses beyond point A that can be generated under arbitrary loadings are not necessarily bounded by a simple Masing-type model. Hence there is a need for another additional rule which states that, if the current unloading and reloading curve intersects the curve described by a previous unloading and reloading curve, the stress–strain relationship follows that of the previous curve as shown by path B in Figure 3.34b.

The preceding rules proposed by Pyke (1979), together with the original Masing's rules, constitute the generalised Masing criteria adopted in this study.

3.5.1.3 Damping Characteristics of the Proposed Model

According to Ishihara (1996), the area of hysteresis loop can be expressed as

$$\Delta W = 8\left[\int_0^{\varepsilon_r} f(\varepsilon)d\varepsilon - W\right] \tag{3.41}$$

in which W is the energy stored in the loading phase:

$$W = \frac{1}{2}\varepsilon_r f(\varepsilon_r) \tag{3.42}$$

where, $f(\varepsilon)$ describes the basic stress strain relationship given by Eq. 3.36

From the definition of damping ratio given by Eq. 3.2,

$$D = \frac{\Delta W}{4\pi W} = \frac{2}{\pi}\left[\frac{2\int_0^{\varepsilon_r} f(\varepsilon)d\varepsilon}{\varepsilon_r f(\varepsilon_r)} - 1\right] \tag{3.43}$$

Substituting $f(\varepsilon)$ as q from Eq. 3.36, D can be expressed as

$$D = \frac{2}{\pi}\left[\frac{2 + 3R\varepsilon_r - \frac{2(1+3R\varepsilon_r)}{3R\varepsilon_r}\ln(1+3R\varepsilon_r)}{3R\varepsilon_r}\right] \tag{3.44}$$

where, R=$\frac{G_{\max}}{q_f}$.

The damping response given by Eq. 3.44 is graphically plotted on Figure 3.35, together with the present experimental data and previously published damping curves from other researchers. The results indicate that, for strains of up to 1%, the proposed model can reasonably capture the strain-dependent damping characteristics of kaolin clay.

For large strains, that is, as $\varepsilon_r \to \infty$,

$$D=D_{max}=\frac{2}{\pi}=0.637=63.7\% \quad (3.45)$$

This theoretical limiting value of the damping ratio, D_{max}, is consistent with the value obtained by Ishihara (1996).

3.5.1.4 Correlation of Modulus Degradation and Damping Ratio with Plasticity Index

The modulus degradation and damping ratio of clayey soils are usually correlated to the plasticity index (PI) (e.g. Vucetic and Dobry, 1991; Ishibashi and Zhang, 1993). These semi-empirical correlations are typically established by a curve fitting approach using different sources of published experimental data from soils with different PI. However, as can be seen from Eq. 3.34 and Eq. 3.44, the modulus degradation and damping ratio responses are both expressed as functions of $\frac{G_{max}}{q_f}$, and not the PI. To account for the effect of PI in the proposed model, Eqs. 3.34 and 3.44 may be modified using the procedure presented below.

Vucetic and Dobry (1991) proposed an empirical correlation of G_{max} as a function of void ratio, mean effective stress and OCR,

$$G_{max} = 625\frac{OCR^k}{0.3+0.7e^2}\sqrt{P_a \cdot p'} \quad (3.46)$$

where, e = void ratio

P_a = atmospheric pressure = 1atm. = 100 kPa

p' = mean effective stress

By substituting OCR = 1 and P_a = 100 kPa,

$$G_{\max} = 6250 \frac{1}{0.3 + 0.7e^2} \sqrt{p'} \tag{3.47}$$

The void ratio, e, can be expressed as

$$e = e_0 - \lambda \ln p' \tag{3.48}$$

where, λ and e_0 are the compression index and the void ratio at a mean effective stress of 1kPa.

The compression index has been widely correlated to the plasticity index (e.g. Schofield and Wroth 1968, Wroth and Wood 1978, Nakase et al. 1988). Using Schofield and Wroth's (1968) relationship for e_0 with Wroth and Wood's (1978) relationship for compression index in Eqs. 3.47 and 3.48 leads to

$$G_{\max} = 6250 \frac{1}{0.3 + 0.7\{0.25 + (5.399 - 0.585 \ln p')PI\}^2} \sqrt{p'} \tag{3.49a}$$

Using Nakase et al.'s (1978) relationships for e_0 and compression index lead to

$$G_{\max} = 6250 \frac{1}{0.3 + 0.7\{0.612 - 0.02 \ln p' + (3.96 + 0.45 \ln p')PI\}^2} \sqrt{p'} \tag{3.49b}$$

As can be seen, both. Eqs 3.49a & b suggest that, for a given mean effective stress, the small strain shear modulus decreases with plasticity index.

Combining Eqs. 3.29a and 3.49a leads to

$$R = 6250 \frac{1}{0.3 + 0.7\{0.25 + (5.399 - 0.585 \ln p')PI\}^2} \sqrt{p'} \frac{2^n}{Mp'} \tag{3.50a}$$

Combining Eqs. 3.29a and 3.49b leads to

$$R = 6250 \frac{1}{0.3 + 0.7\{0.612 - 0.02 \ln p' + (3.96 + 0.45 \ln p')PI\}^2} \sqrt{p'} \frac{2^n}{Mp'} \tag{3.50b}$$

The parameter n can be determined if the recompression index κ is known. Nakase et al. (1988) also suggested that

$$\kappa = 0.\ 084\ (\mathrm{PI} - 0.046) \tag{3.51}$$

The friction angle ϕ' can also be correlated to the plasticity index through Kulhawy and Mayne's (1990) relationship; this leads to

$$M = \frac{4.8 - 56.4PI}{2.2 + 9.4PI} \tag{3.52}$$

Substituting Eqs. 3.51 and 3.52 into Eqs. 3.50a & b leads to

$$R = 6250 \frac{1}{0.3 + 0.7\{0.25 + (5.399 - 0.585 \ln p')PI\}^2} \sqrt{p'} \frac{2^{\left\{\frac{0.501PI + 0.003864}{0.084(PI - 0.046)}\right\}}}{\left\{\frac{4.8 - 56.4PI}{2.2 + 9.4PI}\right\} p'} \tag{3.51a}$$

$$R = 6250 \frac{1}{0.3 + 0.7\{0.612 - 0.02 \ln p' + (3.96 + 0.45 \ln p')PI\}^2} \sqrt{p'} \frac{2^{\left\{\frac{0.366PI + 0.0238}{0.084(PI - 0.046)}\right\}}}{\left\{\frac{4.8 - 56.4PI}{2.2 + 9.4PI}\right\} p'} \tag{3.51b}$$

As shown in Figure 3.36, the normalized modulus deduced from Eqs. 3.51a & b is relatively insensitive to the mean effective stress for high and medium-plasticity clays. For low plasticity clays, changes in the normalized modulus are more marked but is still proportionately much less than the change in effective stress. This trend is also reflected in the damping ratio as shown in Figure 3.37.

Moreover, as shown in Figure 3.38, the trend of the computed variation in damping ratio with cyclic shear strain agrees well with experimental results from previous studies for shear strain below 0.1%. The increased divergence between the predicted and measured damping ratio for shear strain above 0.1% is consistent the earlier observation that Masing's rules appear to over-predicting the damping ratio at large strains. Thus the variation of the damping ratio with plasticity index, as well as its relative insensitivity to the effective stress, can be explained in terms of the effects of these factors on the normalized modulus.

As shown in Figure 3.39a and b, the modulus ratio deduced for a low-, medium- and high-plasticity clays using Eqs. 3.51a & b, shows a trend which is consistent with the experimental results of Vucetic and Dobry (1991) and Ishibashi and Zhang (1993). For medium- and high-plasticity clay, the agreement with the results of all two previous experimental studies is remarkably good. For low-plasticity clays, the mean effective stress has a more effect and the modulus ratios fall into a band. Furthermore, as shown in Figure 3.40, Vucetic and Dobry's (1991) results match closely with the hyperbolic relationships for a p' of 50 kPa. On the other hand, for a p' of 600 kPa, hyperbolic relationships appears to agree well with the Ishibashi and Zhang's (1993) results.

Ishihara (1996) also used a hyperbolic-Masing formulation to carry out an analytical study of modulus degradation and damping ratio. His relationships, however, did not explicitly consider the plasticity index of the soil. Figure 3.41 shows Ishihara's prediction of the damping ratio and $\frac{G_{sec}}{G_{max}}$,

together with the results obtained from the present hyperbolic-Masing formulation for PI between 1 to 100%. It appears that Ishihara's results are well-bounded by the curves obtained from the present study, and correspond to a PI of about 30 to 40%, which is typical of many clays.

3.5.1.5 Modeling of Stiffness Degradation of Backbone Curve

For strain-controlled triaxial tests, Idriss et al. (1978) characterized the degradation of the backbone curve using the degradation index δ (defined earlier in Section 3.4.1.4) and the damage parameter t. The degradation index may be mathematically expressed as

$$\delta = \frac{G_{sN}}{G_{s1}} = \frac{\frac{\tau_{cN}}{\gamma_c}}{\frac{\tau_{c1}}{\gamma_c}} = \frac{\tau_{cN}}{\tau_{c1}} \tag{3.52}$$

where,

G_{sN} and G_{s1} are the secant shear modulus associated with the peak stress of the Nth and 1st cycle, respectively,

τ_{cN} and τ_{c1} are the cyclic shear stress amplitude of the Nth and 1st cycle, respectively, and

γ_c is the cyclic shear strain amplitude.

The damage parameter, t, is defined as

$$t = -\frac{\log \delta}{\log N} \tag{3.53a}$$

which may be rearranged to yield

$$\delta = N^{-t} \tag{3.53b}$$

In cases where a specimen is subjected to a complex loading sequence comprising variable strain amplitudes and number of cycles, the above formulation may be extended to calculate the change in degradation index from cycle number m to cycle number n, where the applied strain amplitude is constant from cycle m to n. This is done via the incremental form of the degradation index (Idriss et al., 1978):

$$\delta_n = \delta_m [1 + |m - n| \delta_m^{1/t}]^{-t} \tag{3.54}$$

Eq. 3.54 relates the degradation index at the end of cycle n to the value at the end of cycle m, where n > m and the applied strain amplitude is constant from cycle m+1 to cycle n. This form of the degradation index is particularly useful for earthquake loadings, in which the strain amplitudes and number of cycles vary in a random manner.

The damage parameter, t, depends on the cyclic shear strain amplitude (Idriss et al., 1978). In Idriss et al. (1980), a hyperbolic relationship between t and the strain amplitude was presented for clay of plasticity index 15-20%. The transient loading test data reported in Idriss et al. (1980) is replotted in Figure 3.42, together with their proposed hyperbolic fit shown as a dashed line. It appears that Idriss et al. (1980) did not take into consideration a threshold strain level below which no degradation would occur.

Figure 3.43 shows the damage parameter t plotted against the shear strain amplitude, using kaolin clay data obtained from the cyclic triaxial tests carried out in this study. The points describe a non-linear trend similar to that reported by Idriss et al. (1980), and can be reasonably fitted by a logarithmic function of the form

$$t = 0.0536 \log(\varepsilon) + 0.1285 \tag{3.55}$$

In Eq. 3.55, the value of t becomes negative for strain levels smaller than 0.1%. In other words, 0.1% is the threshold strain level below which no degradation or damage takes place, which is consistent with the value reported by Matasovic and Vucetic (1995).

From Eq. 3.32,

$$G_{sec} = \frac{G_{max}}{1 + 3R\varepsilon_r} \tag{3.56}$$

Using Eq. 3.52, $G_{sN} = \delta G_{s1}$ (3.57)

Hence from Eq. 3.56 and Eq. 3.57 ,

$$\frac{G_{max,N}}{1 + 3R_N\varepsilon_r} = \delta \frac{G_{max,1}}{1 + 3R_1\varepsilon_r} \tag{3.58}$$

For a given strain, δ is constant. As G_{max} is calculated for very small strain,

$$\frac{G_{max,N}}{G_{max,1}} \approx \delta$$

Hence, for Eq. 3.58 to be valid at any strain,

$$R_N = R_1 \tag{3.59}$$

In other words, cyclic degradation of the backbone curve does not affect $\frac{G_{max}}{q_f}$. Recall from Eq. 3.44 that the damping ratio at a given strain depends only on $\frac{G_{max}}{q_f}$. As $\frac{G_{max}}{q_f}$ remains constant throughout the degradation process, it follows that the damping ratio is also independent of the degradation of the backbone curve if the unloading-reloading relationship is described by Masing's rule.

3.5.2 Numerical Simulation of Triaxial Test

3.5.2.1 3D Triaxial Modelling using ABAQUS

Three-dimenisonal (3-D) numerical models of the cyclic triaxial tests described in this chapter were set up and analyzed using the general purpose finite element program ABAQUS 6.7.1. From symmetry considerations, a quadrant of the standard triaxial specimen (38mm dia and 76mm long) was discretized using eighty 20-noded brick (C3D20) elements (Figure 3.44). An isotropic stress state was obtained by applying uniform pressures on the cylindrical and top surface. The strain-controlled cyclic loading is applied at the nodes on the top face, by prescribing time-dependent sinusoidal displacements with the desired frequency and amplitude.

The hyperbolic stress-strain relationship and generalized Masing's rules of Section 3.5 were coded into a user-defined subroutine HyperMas, which was then compiled and linked to ABAQUS.

3.5.2.2 Model Performance for Test Series CT1 and CT2

Figure 3.45 shows the measured and computed loops for the 1st and 60th cycle of selected specimens tested at different frequencies and strain amplitudes. The results indicate that, for all cases, stiffness degradation observed in the numerical analysis are consistent with the experimental trends. Figure 3.45 also shows that the size of the computed loops increased from the low strain amplitude tests (0.254%) to high strain amplitude tests (1.37%). In other words, the amount of energy dissipated in the first cycle of loading, which is related to the damping ratio, increased with the applied strain level.

This trend is consistent with the strain-dependent damping characteristics of clay discussed in Section 3.4.2.1.

The measured degradation indices shown on Figure 3.21 are replotted on Figure 3.46, along with the computed degradation trend (solid line) obtained using Eq 3.56 and 3.57. The results indicate that the proposed semi-empirical relationship between damage parameter t and strain level ε (Eq. 3.57) is reasonable for characterizing the cyclic degradation behaviour of the kaolin clay used in this study.

3.5.2.3 Model Performance for Test Series TRS1, TRS 2 and TRS 3

Up to now, the CT1 and CT2 specimens tested in this study were subjected to controlled strain amplitudes that were progressively increased during the course of cycling. However, this may not be representative of field conditions, in which the strains are likely to vary randomly throughout the earthquake loading history. Hence, another series of laboratory cyclic triaxial tests, TRS, was carried out to study the response of specimens subjected to more general loading conditions. In series TRS, three specimens were each subjected to two stages of cyclic straining, in which the applied strains in the first stage were higher than those in the second (Table 3.2). For example, in test TRS-1, the specimen is first cyclically loaded for 60 cycles under a strain amplitude of 0.789%, followed by another 60 cycles under a smaller strain amplitude of 0.254%. Throughout this process, the frequency of the loading is maintained at 0.25 Hz. Similarly, for TRS-2, the specimen is subjected to 60 cycles of strain amplitude 1.37%, followed by another 60 cycles of a smaller strain amplitude 0.789%, both at a frequency of 0.25 Hz. The loading cycles

and strain amplitudes of test TRS-3 are similar to those of TRS-1, except that the frequency was increased to 1 Hz.

The solid symbols on Figure 3.47 show the degradation index computed from the laboratory cyclic triaxial tests, plotted against the number of cycles. On the same figure, the continuous trend lines show the degradation index back-calculated from the numerical analyses. As indicated in section 3.4.1.4, the experimental degradation indices are evaluated from the measured cyclic loops assuming that the threshold strain level for initiation of degradation is 0.137%. In the numerical analyses, the degradation index is calculated using Eqs. 3.33 and 3.34 which is then applied in the subroutine HyperMas to calculate the peak deviator stress. The comparison shows that the computed degradation trends are generally consistent with those obtained from the laboratory testing.

Figure 3.48 plots the computed peak deviator stresses (shown as dashed lines) and the corresponding measured values (solid symbols) from the laboratory tests, as a function of the number of cycles. The sudden jumps (or drops) that occur at cycle number 60 correspond to the abrupt change in applied strain amplitude from one stage to another. Overall, there is good agreement between the computed and measured peak stresses.

3.5.2.4 The Modulus Reduction and Damping Characteristics

The modulus reduction and damping characteristics were back-calculated from the numerical analyses for different strain amplitudes, and plotted on Figures 3.48 and 3.50 respectively. The red line in Figure 3.49 represents the numerically computed trend of the modulus reduction

ratio $\frac{G}{G_{\max}}$ for different strain levels associated with the initial backbone curve. Also reproduced on the same figure are the modulus reduction curves from previous studies, as well as the laboratory cyclic triaxial and resonant column tests conducted in the present study. The back-calculated modulus reduction curve from the present numerical analyses exhibits the typical reverse S-shape trend, while appearing to upper-bound the measured data. However, the computed curve does fall within the range covered by the previous data. For small strains between 0.01% and 0.1%, the numerical model appears to overpredict the $\frac{G}{G_{\max}}$ ratios slightly.

The red line in Figure 3.50 plots the damping ratios back-calculated from the numerical analyses, for different strain amplitudes associated with the initial backbone curve. Also reproduced in the figure are the strain-dependent damping curves from previous studies, as well as the laboratory cyclic triaxial and resonant column tests conducted in the present study. As mentioned Sec. 3.5.1.2, the computed damping ratios from the present numerical analyses exhibit over-prediction at higher strain level. However, the computed values up to 1% strain fall within the range covered by the triaxial data, indicating that, within the small to moderate strain range, reasonable agreement is obtained.

3.5.3 Concluding Remarks

The preceding comparisons between the numerical and experimental results from cyclic triaxial tests indicate that the proposed phenomenological

soil model can reasonably capture the non-linear modulus reduction and stiffness degradation response of soft soils under cyclic loading. Nevertheless, it should be noted that this model is based on the total stress approach, and hence is unable to fully model a dual-phase coupled system with generation and dissipation of excess pore pressures.

Table 3.1: Geotechnical properties of kaolin clay (Goh, 2003)

Properties	Range
Bulk unit weight (kN/m^3)	16
Water content	66%
Liquid limit	80%
Plastic limit	40%
Compression index	0.55
Recompression index	0.14
Coefficient of permeability (m/s)	$1.36x10^{-8}$
Initial void ratio	1.76
Angle of friction	25°

Table 3.2: Details of cyclic triaxial tests

Name	Pre-consolidation pressure (kPa)	Cyclic strain level (%)	Frequency (Hz)	No. of cycles/each strain level
CT1-1	200	0.137% to 1.37%	0.05	60
CT1-2	200	0.137% to 1.37%	0.1	60
CT1-3	200	0.137% to 1.37%	0.25	60
CT1-4	200	0.137% to 1.37%	0.5	60
CT1-5	200	0.137% to 1.37%	1	60
CT1-6	200	0.137% to 1.37%	1.5	60
CT2-1	150	0.137% to 1.37%	0.05	60
CT2-2	150	0.137% to 1.37%	0.1	60
CT2-3	150	0.137% to 1.37%	0.25	60
CT2-4	150	0.137% to 1.37%	0.5	60
CT2-5	150	0.137% to 1.37%	1	60
CT2-6	150	0.137% to 1.37%	1.5	60
CT3-1	200	0.789%	1	60
CT3-2	200	1.37%	1	60
CT4-1	200	1.37%	5	60
CT4-2	200	1.37%	3	60
TRS-1	200	a. 0.789%	0.25	60
		b. 0.254%	0.25	60
TRS-2	200	a. 1.37%	0.25	60
		b. 0.789%	0.25	60
TRS-3	200	a. 1.37%	1	60
		b. 0.254%	1	60

Table 3.3 Details of resonant column tests

Name	Pre-consolidation pressure (kPa)	Cyclic strain level (%)	Frequency (Hz)
RC-1	200	0.002% to 0.04%	40 to 48
RC-2	150	0.003% to 0.08%	30 to 42

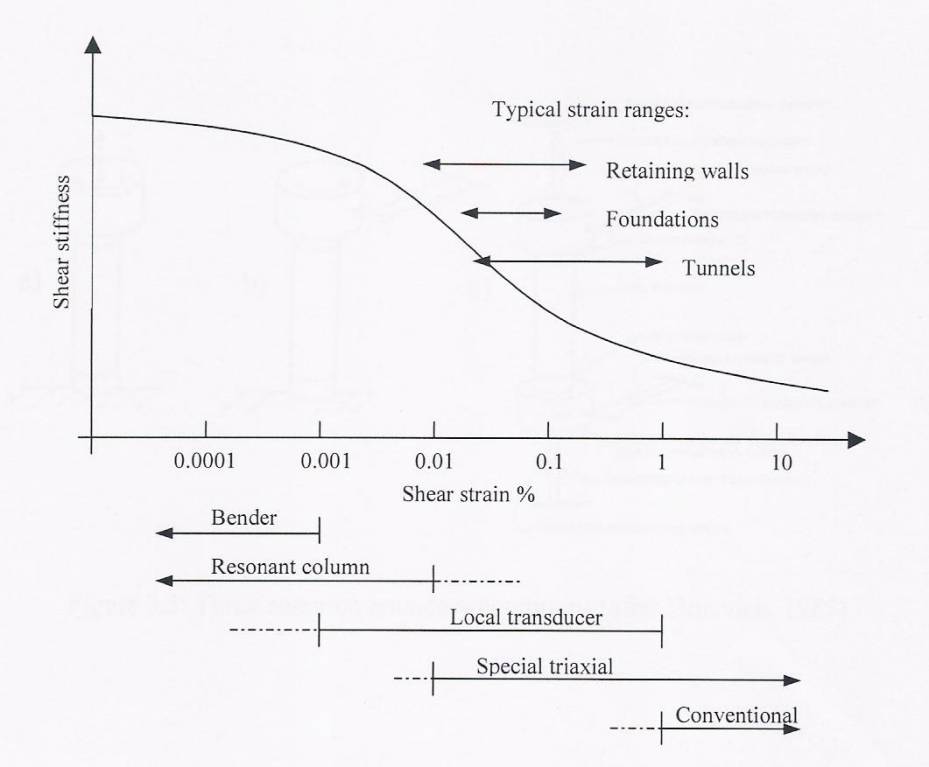

Figure 3.1 Strain range applicable for different test methods (Mair, 1993)

Figure 3.2 Preparation of kaolin clay specimens

Figure 3.3 GDS advanced triaxial apparatus

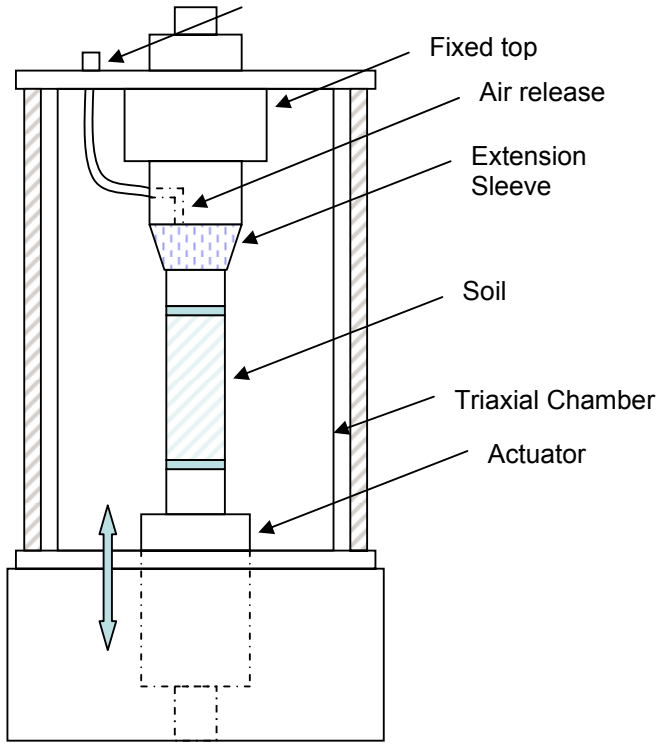

Figure 3.4 Schematic diagram of the cyclic triaxial set-up

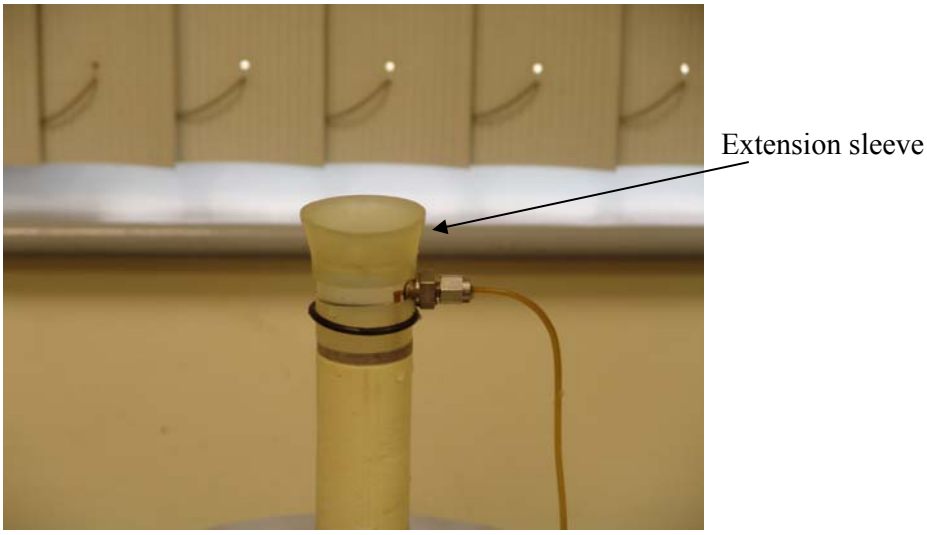

Figure 3.5 Sleeve component used for cyclic triaxial tests

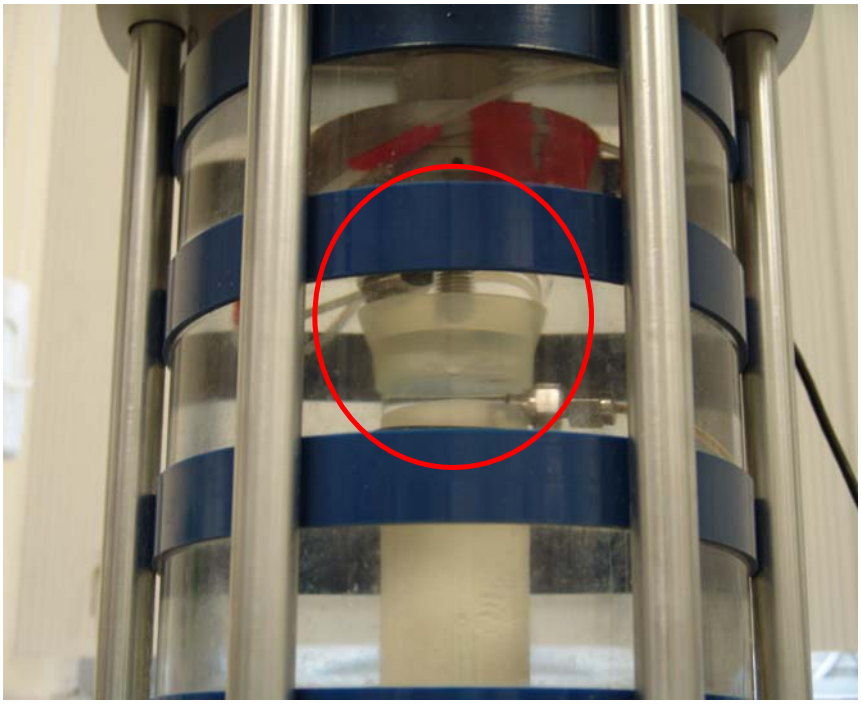

Figure 3.6 Coupling connection between top cap and loading ram

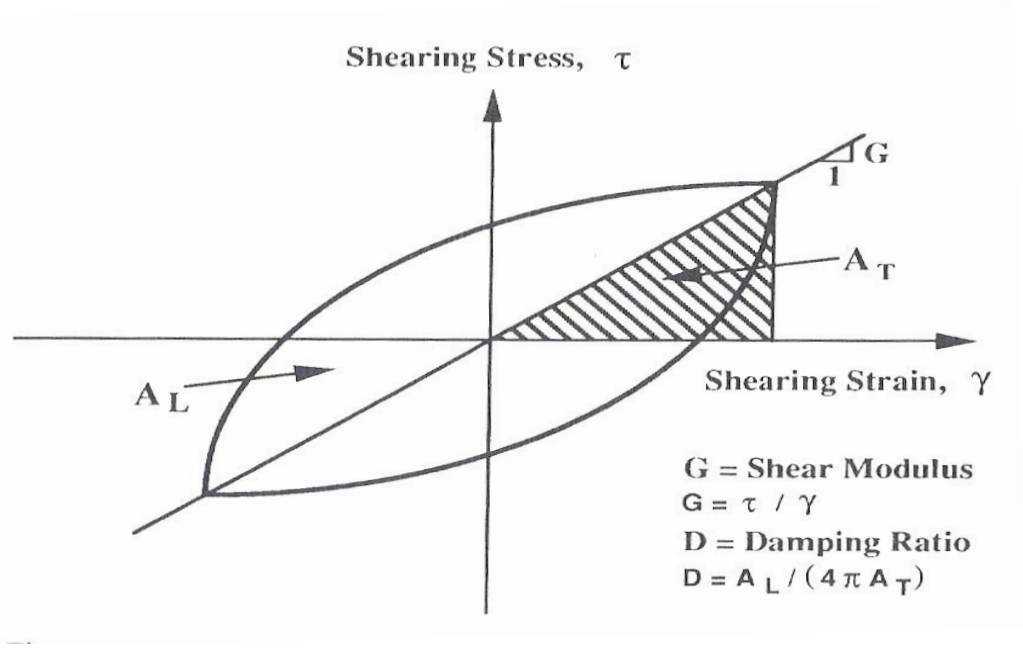

Figure 3.7 Determination of G and D from hysteretic loops. (Kim et al. 1991)

Figure 3.8 Hardin- Drnevich resonant column apparatus

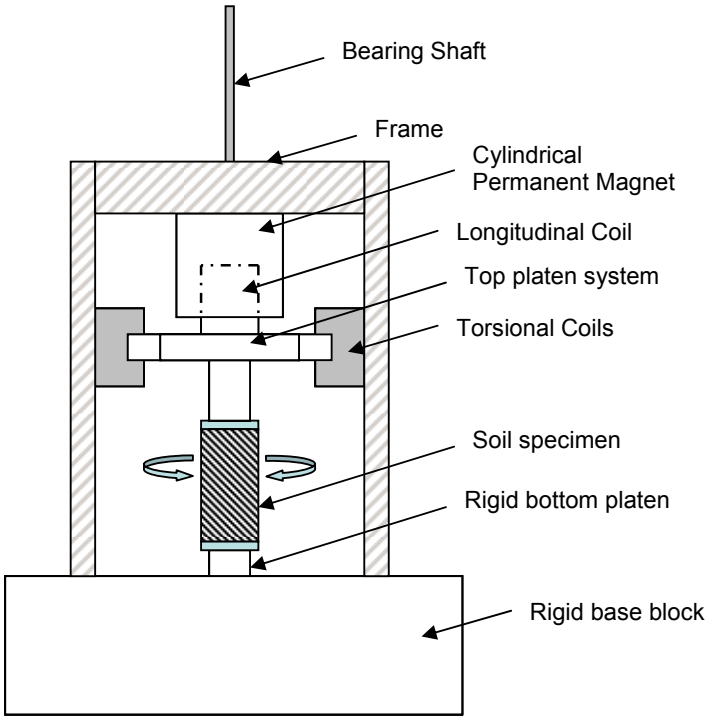

Figure 3.9 Schematic diagram of the resonant column apparatus

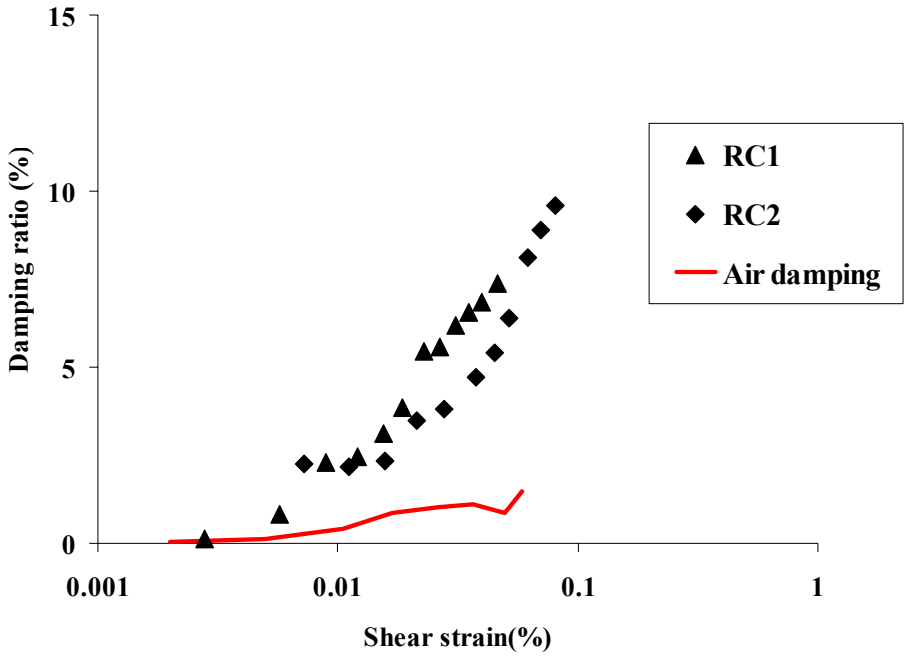

Figure 3.10 Comparison of soil and air damping ratio

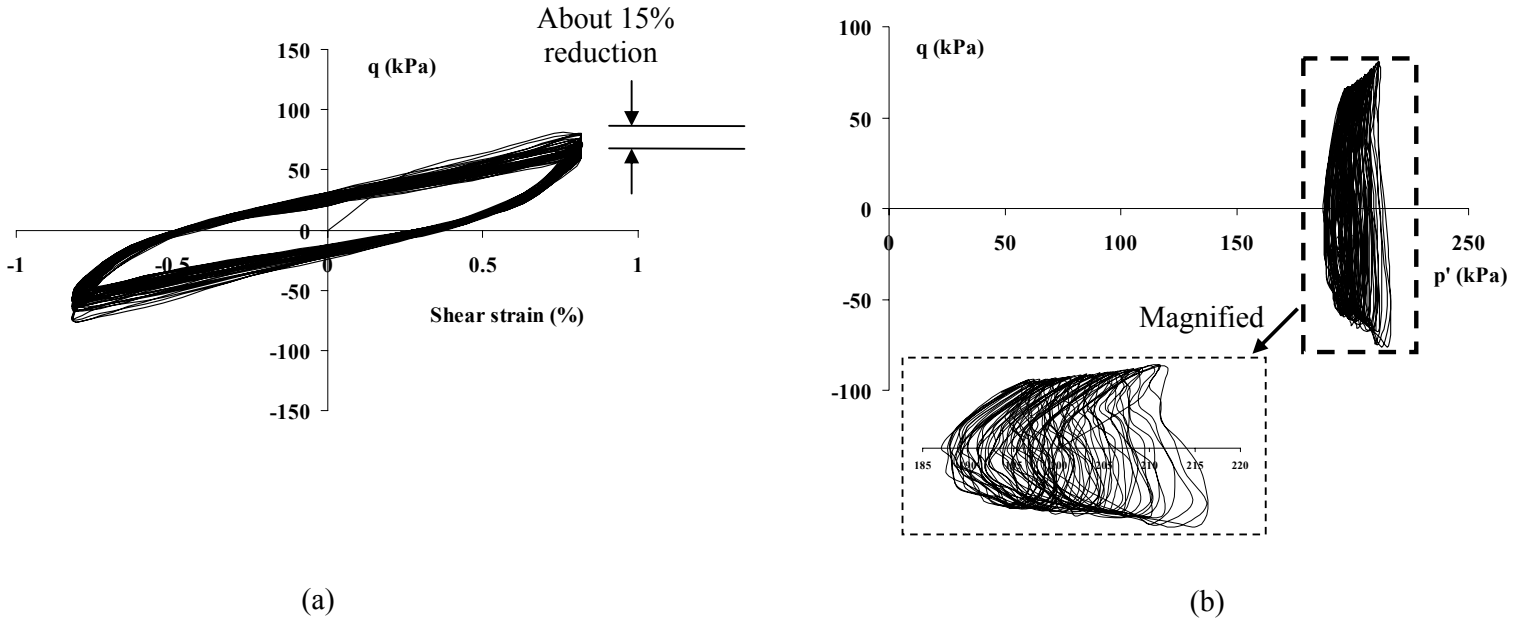

(a) (b)

Figure 3.11 Typical (a) stress-strain loops and (b) stress-paths from CT1-5 (cyclic strain = 0.789%, cell pressure = 200kPa and frequency=1Hz)

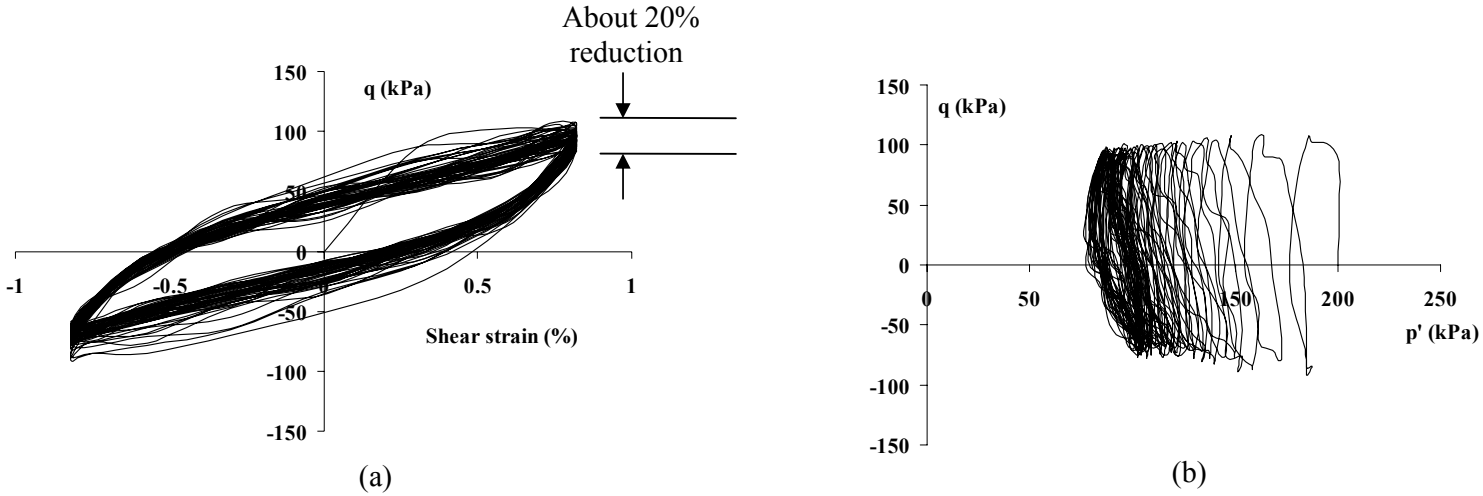

Figure 3.12 (a) Stress-strain loops and (b) stress-paths from CT3-1 (Virgin sample, cyclic strain=0.789%, cell pressure = 200kPa and frequency = 1 Hz)

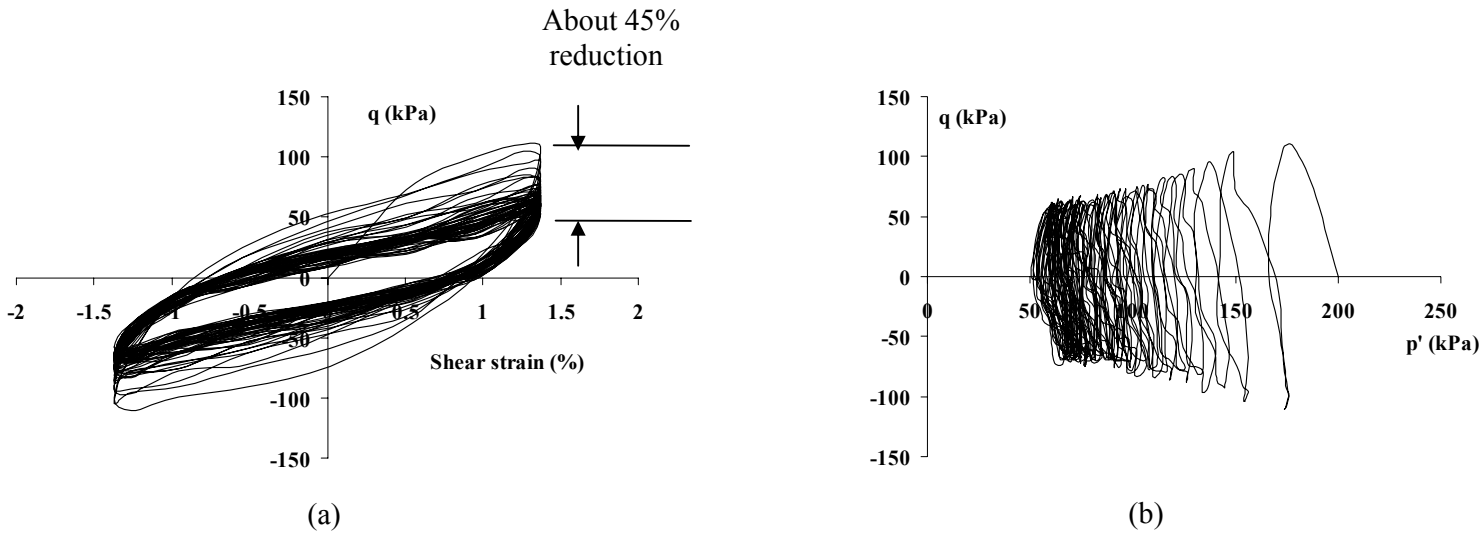

Figure 3.13 (a) Stress-strain loops and (b) stress-paths from CT3-2 (cyclic strain = 1.37%, cell pressure = 200kPa and frequency = 1 Hz)

(a)

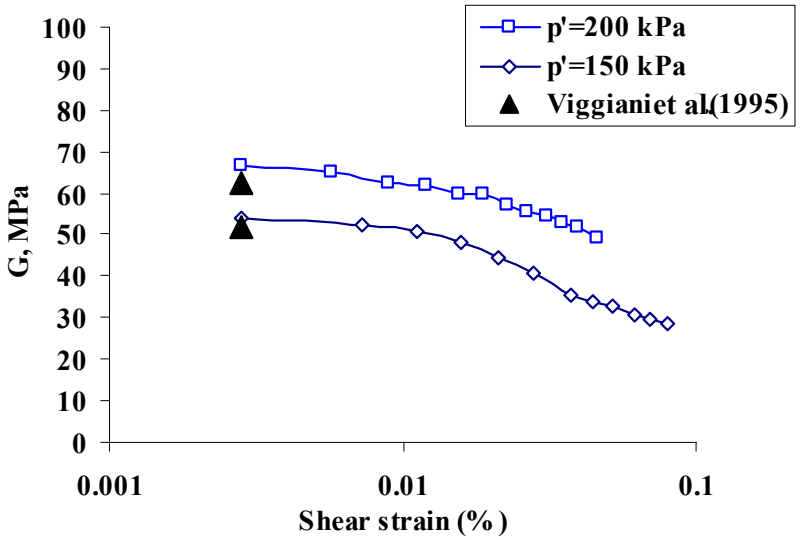

Figure 3.14 Small strain shear modulus values from RC tests

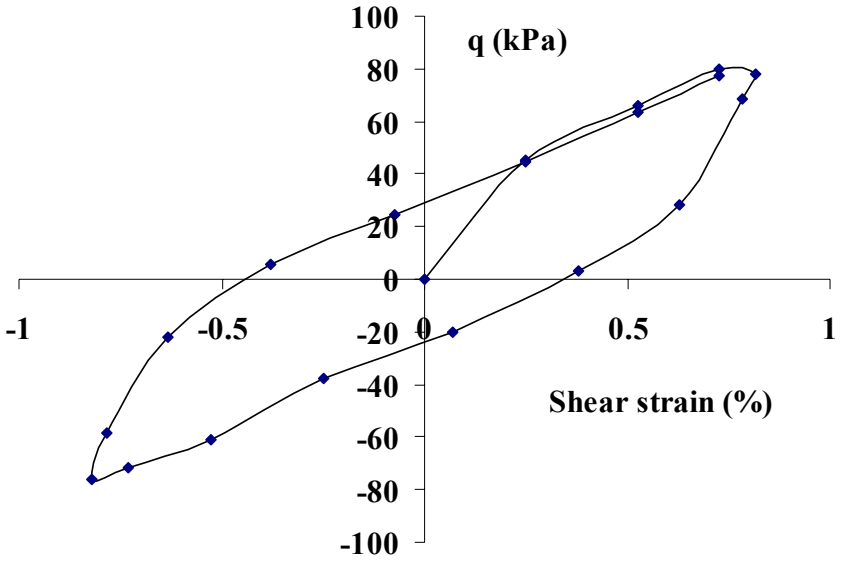

Figure 3.15 Typical stress-strain loop as obtained from CT1-5 (cyclic strain = 0.789%, cell pressure = 200kPa and frequency = 1.0Hz, 1st cycle)

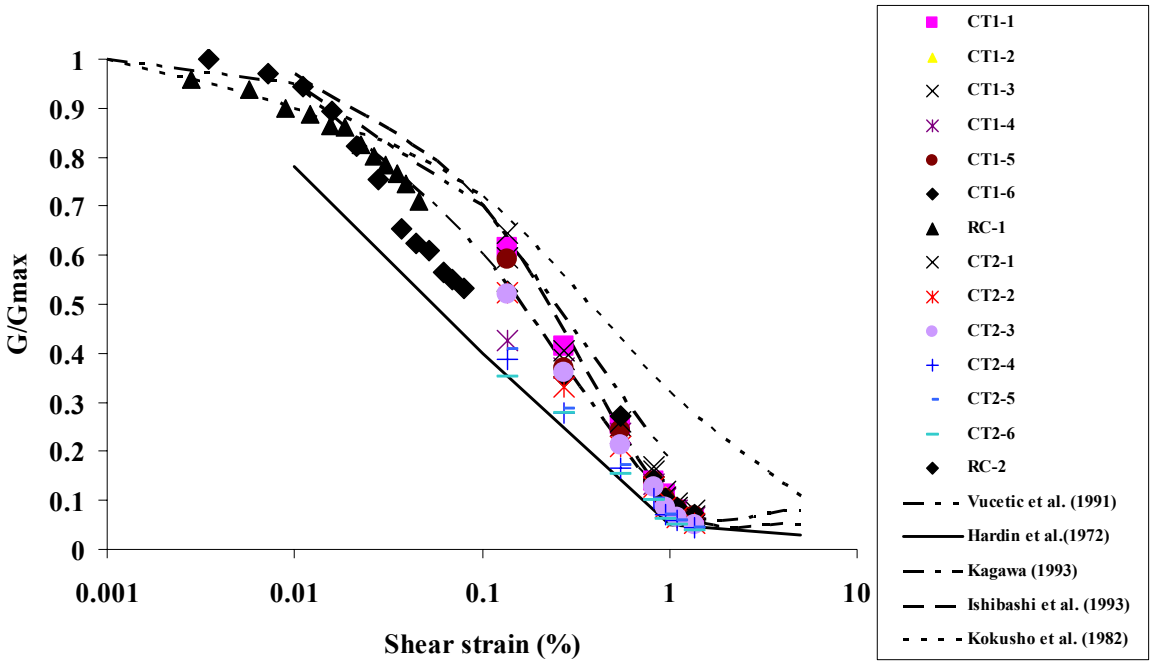

Figure 3.16 Variation of G/G_{max} with shear strain from cyclic triaxial tests and resonance column tests (present study) and reported trends (from published literature)

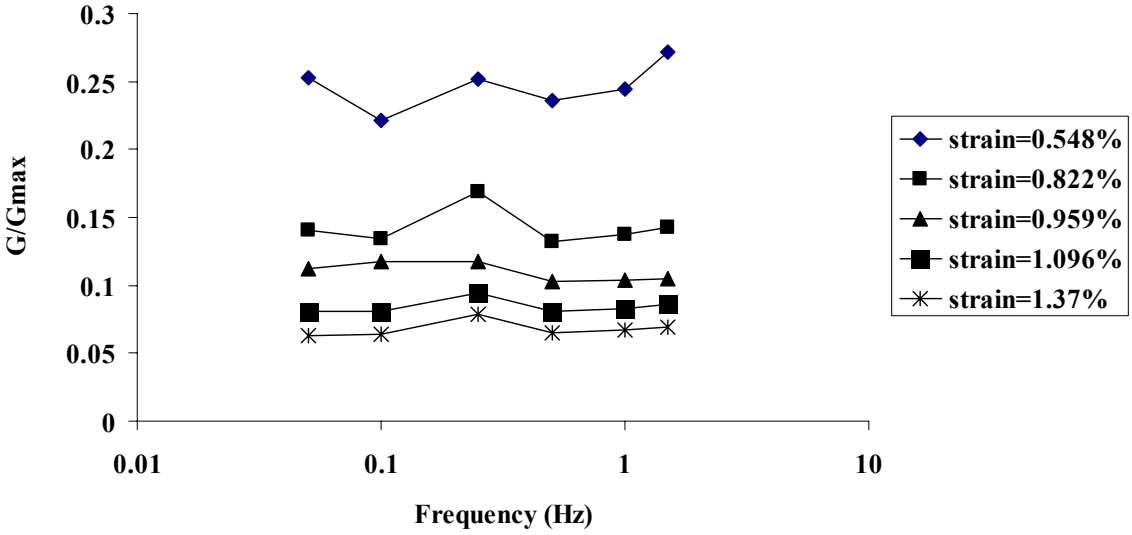

Figure 3.17 Variation of G/G_{max} with frequency

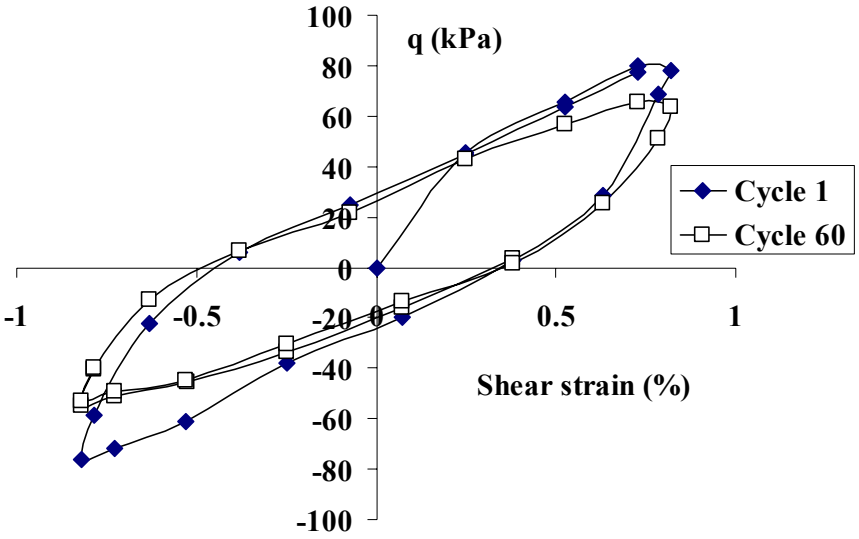

Figure 3.18 1st and 60th stress-strain loop as obtained from CT1-5 (cyclic strain = 0.789%, cell pressure = 200 kPa and frequency = 1.0Hz)

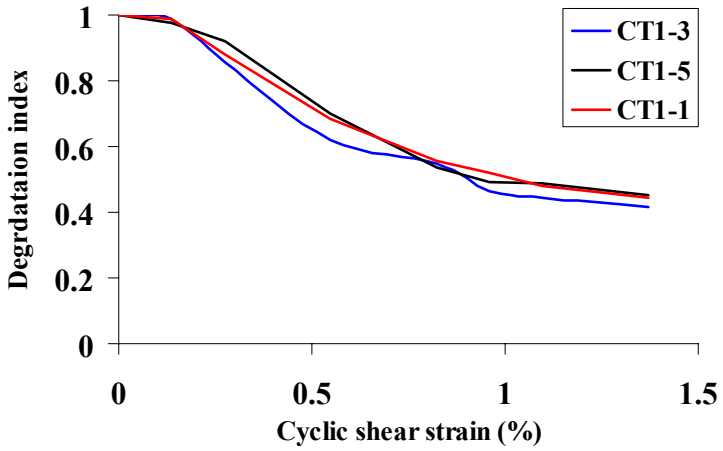

Figure 3.19 Variation of degradation index with shear strain during the loading phase of 60th cycle

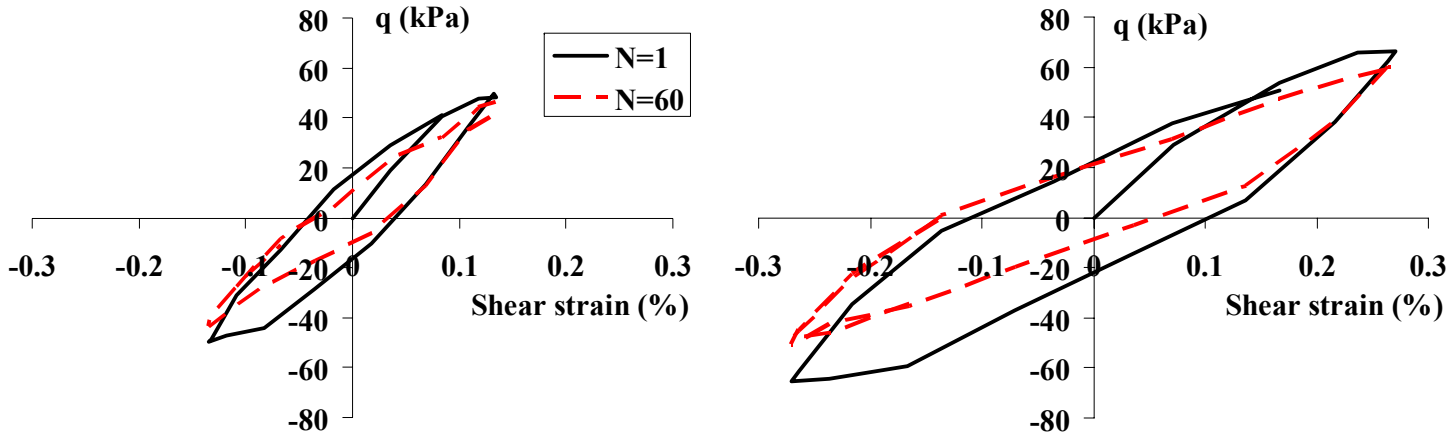

Figure 3.20 For test CT1-6, 1st and 60th stress-strain loops for cyclic strain amplitude of (a) 0.137% and (b) 0.254%

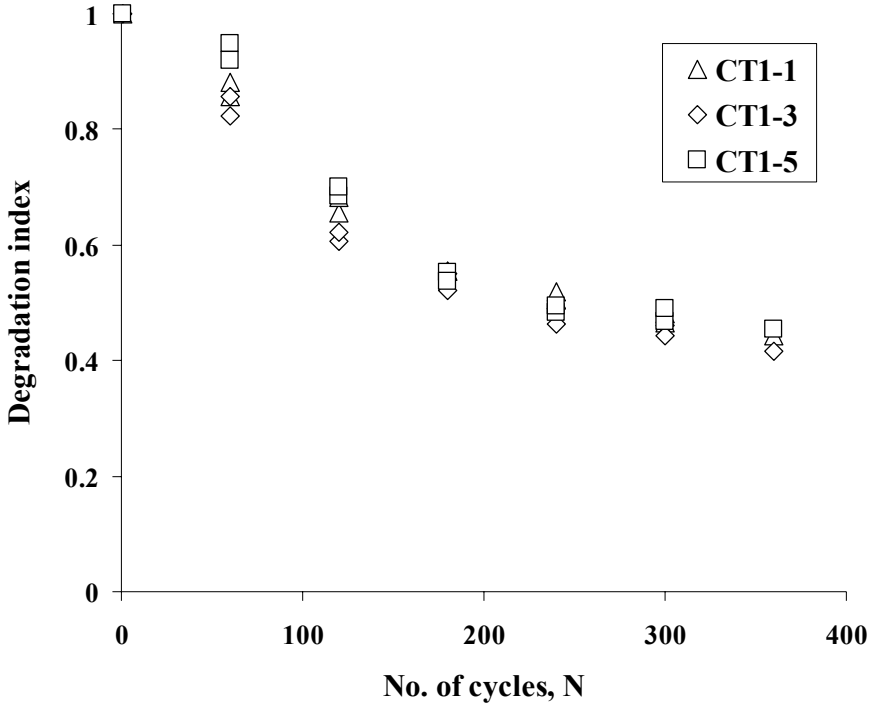

Figure 3.21 Degradation index for Test CT1-1 (0.05Hz), CT1-3 (0.25Hz) and CT1-5 (1Hz)

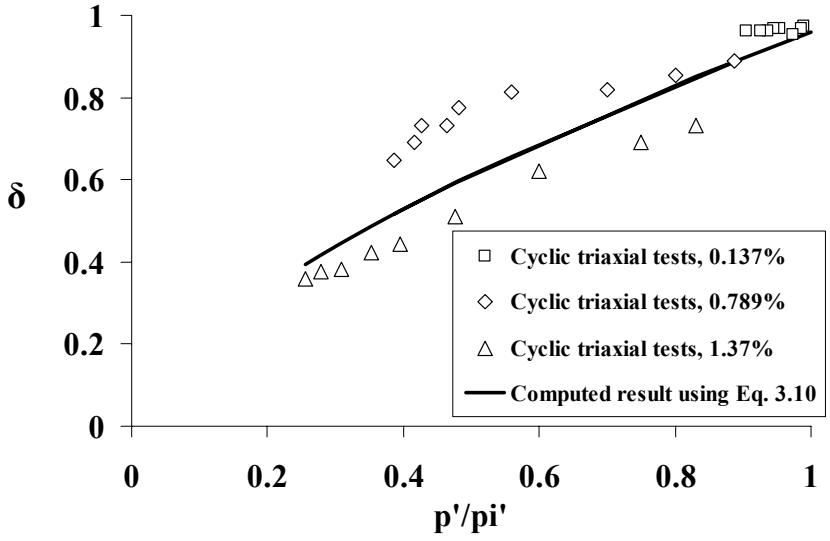

Figure 3.22 Degradation of the shear modulus to change in effective stress

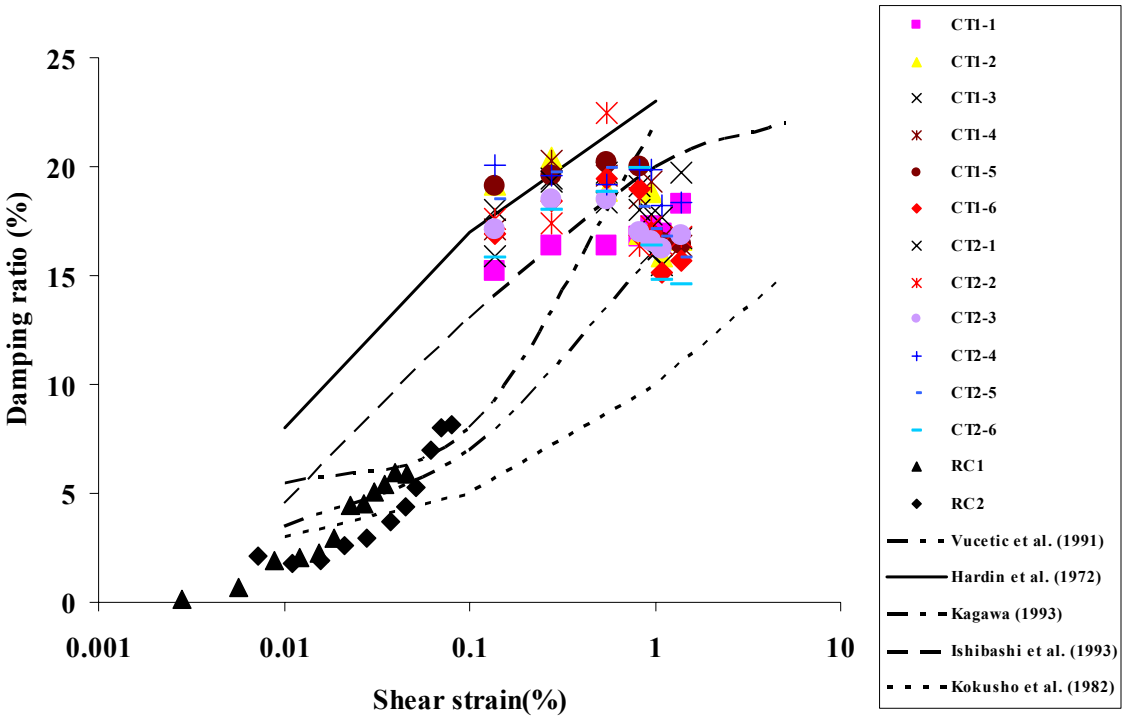

Figure 3.23 Variation of damping ratio with shear strain from cyclic triaxial tests and resonance column tests (present study) and reported trends (from published literature)

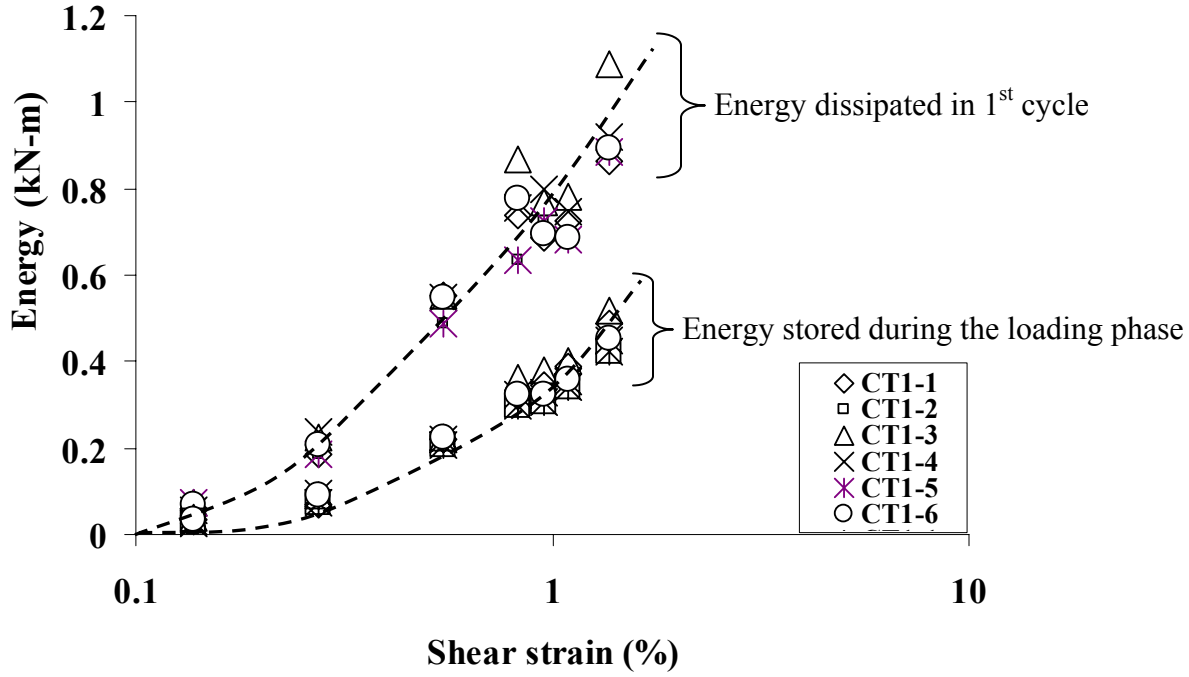

Figure 3.24 Increase in energy components with shear strain

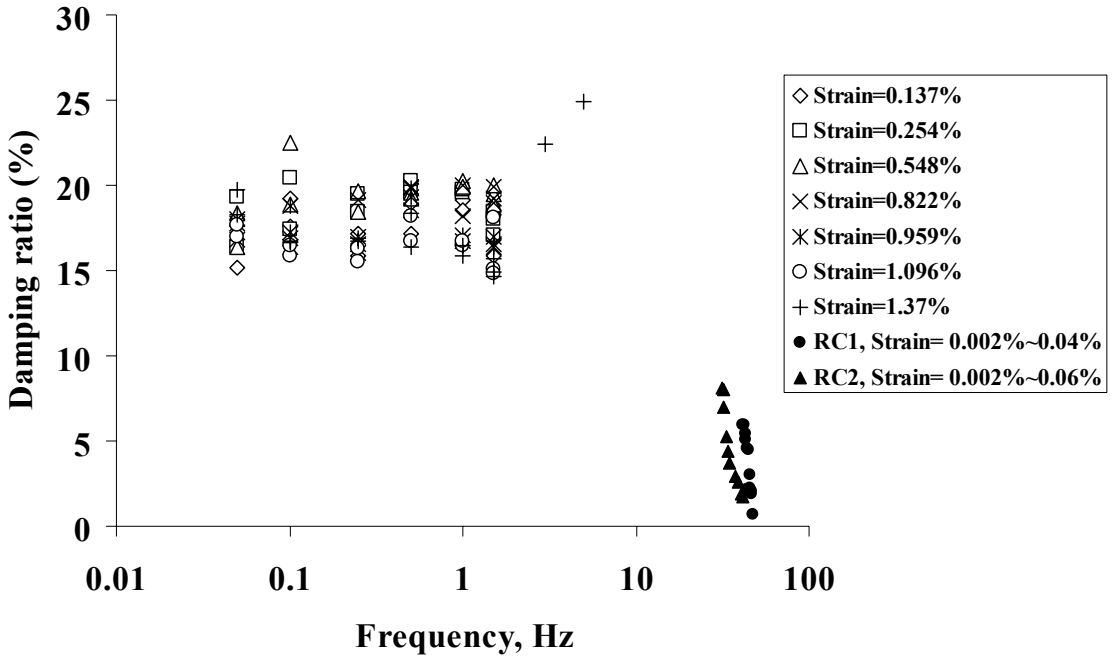

Figure 3.25 Variation of damping ratio with frequency, from cyclic triaxial tests and resonance column tests

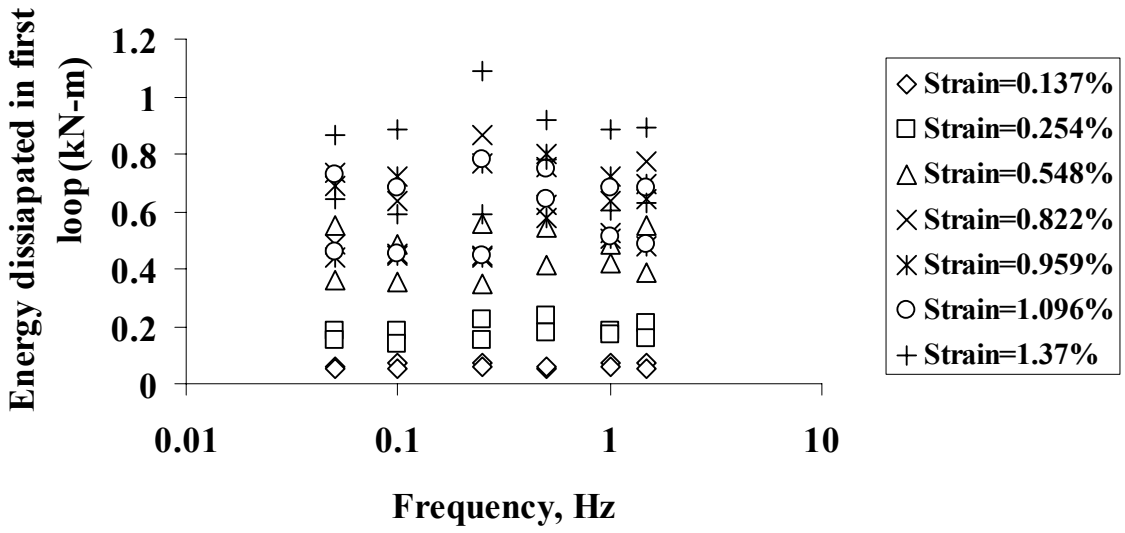

Figure 3.26 Energy dissipated in first loop for different frequencies

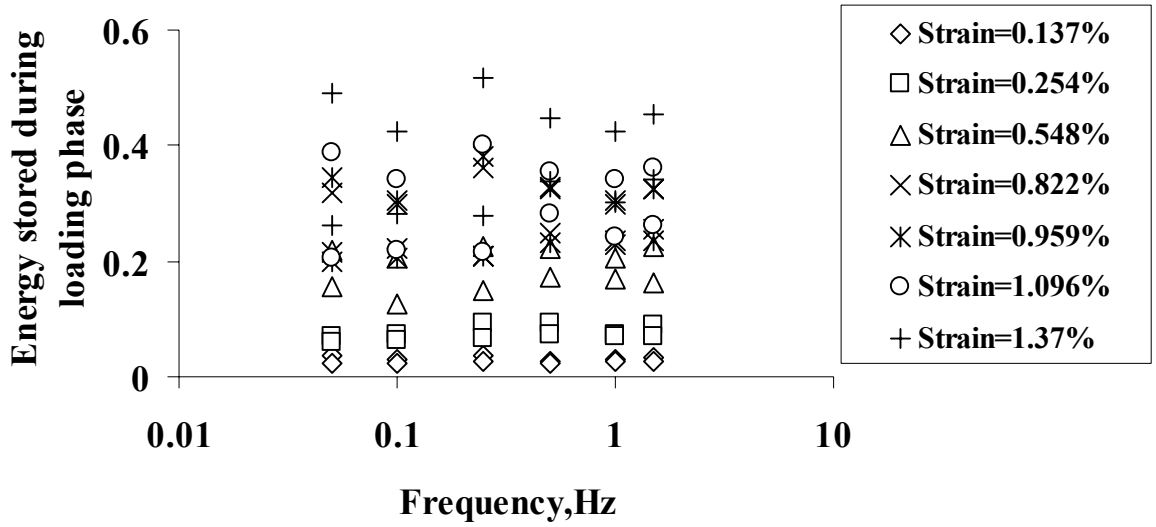

Figure 3.27 Energy stored during loading phase for different frequencies

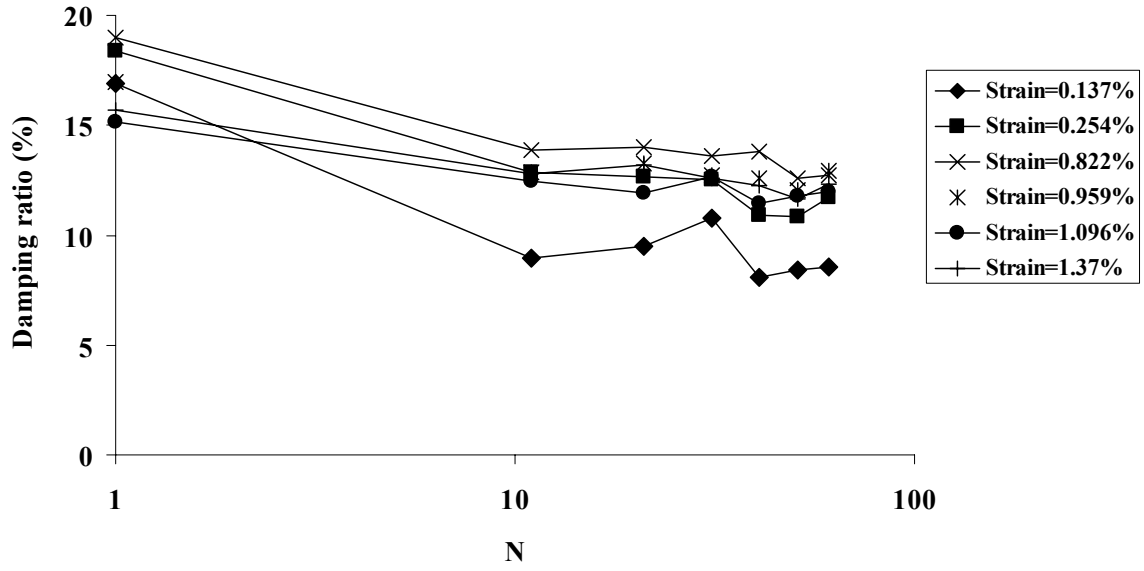

Figure 3.28 Variation of damping ratio with increasing number of load cycles (Test CT1-6)

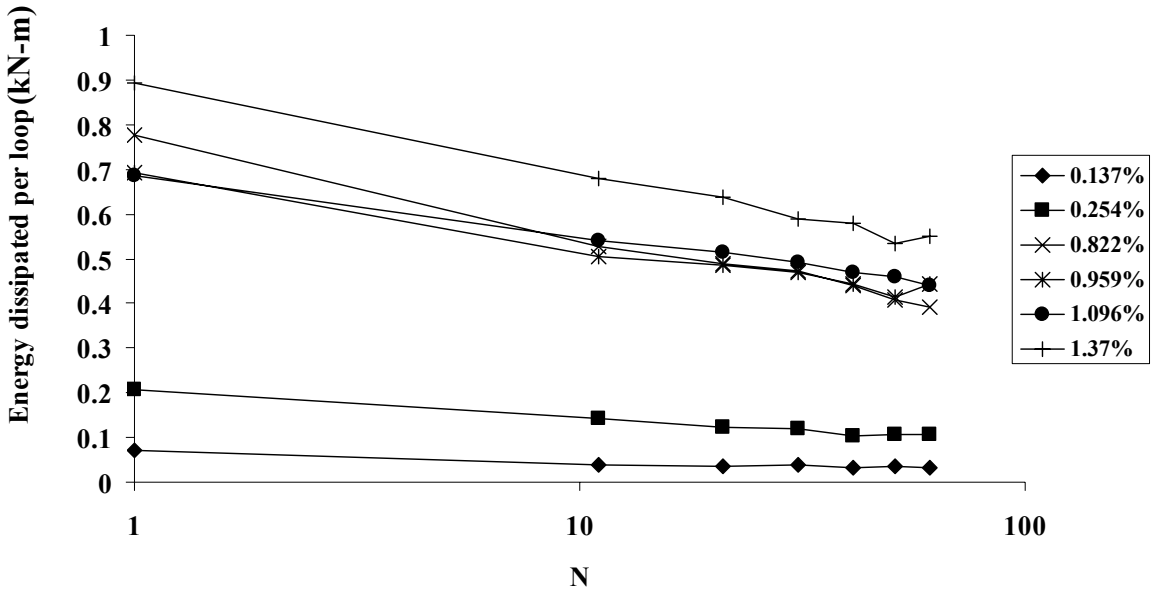

Figure 3.29 Energy dissipation with increasing number of load cycles

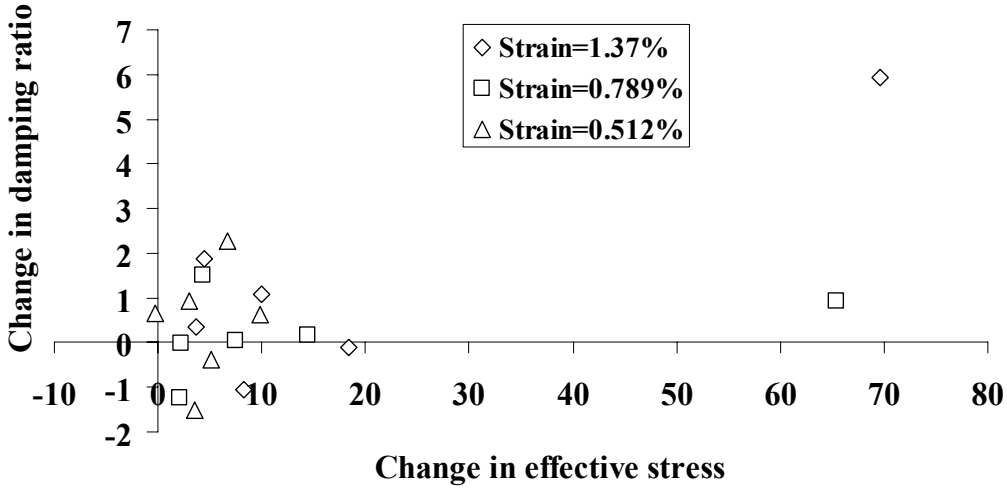

Figure 3.30 Effect of change in effective stress on damping ratio

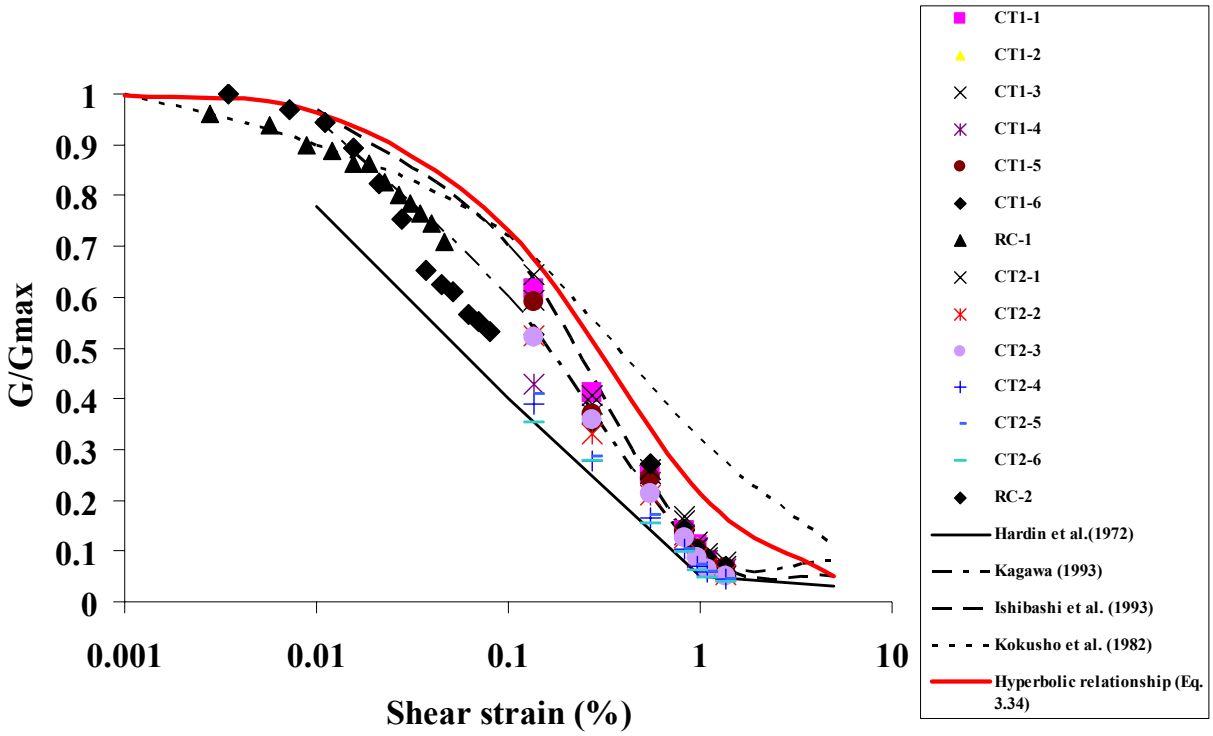

Figure 3.31 Comparison of G/G_{max} computed from Eq. 3.33 with test data

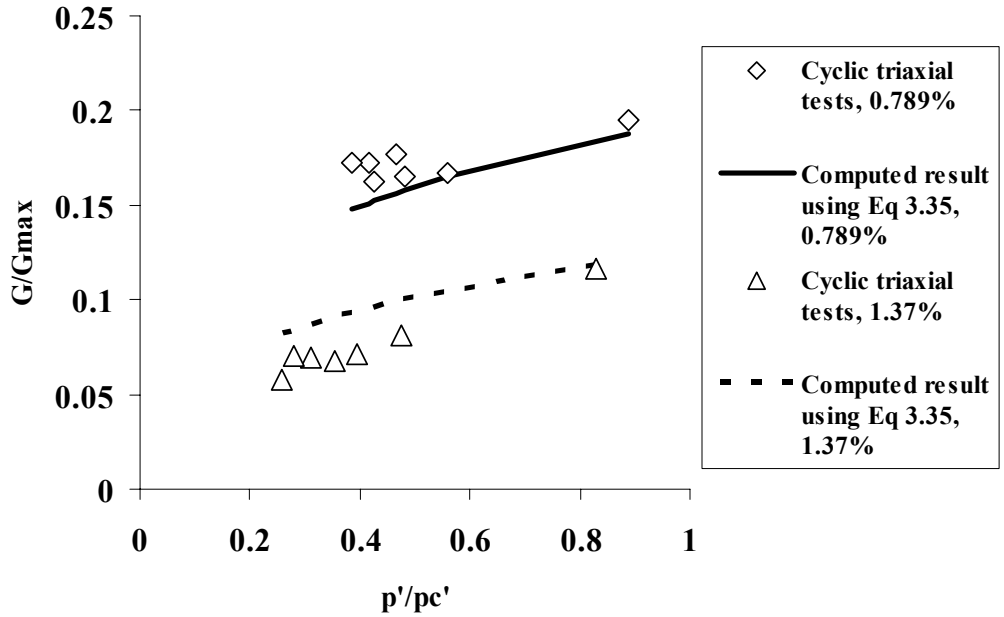

Figure 3.32 G-p' trend obtained from the proposed backbone curve (Eq. 3.29) plotted with the cyclic triaxial test results for virgin samples

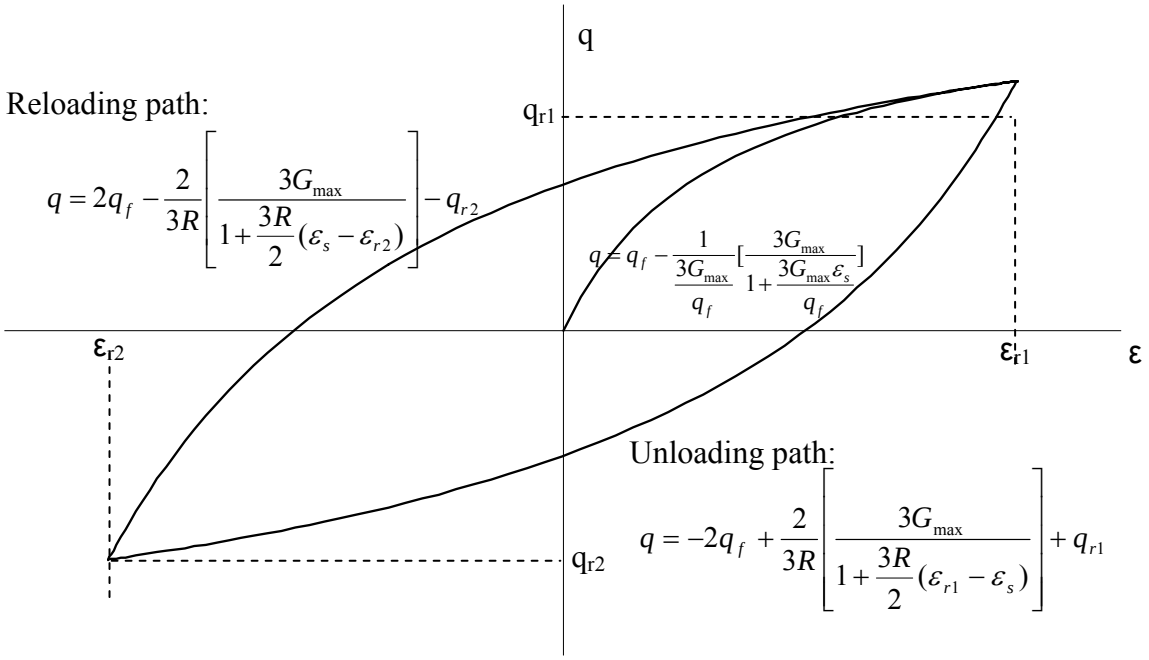

Figure 3.33 Unloading-reloading relationship based on Masing's rule

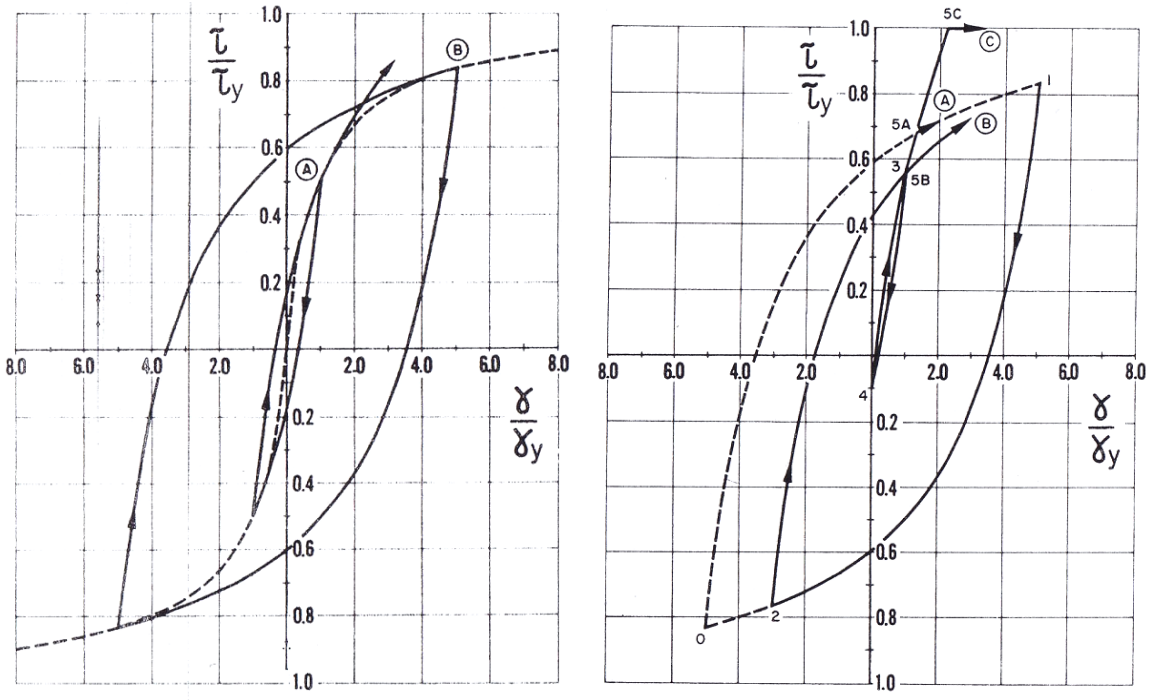

Figure 3.34 Pyke's extension of original Masing's rule (Pyke, 1979)

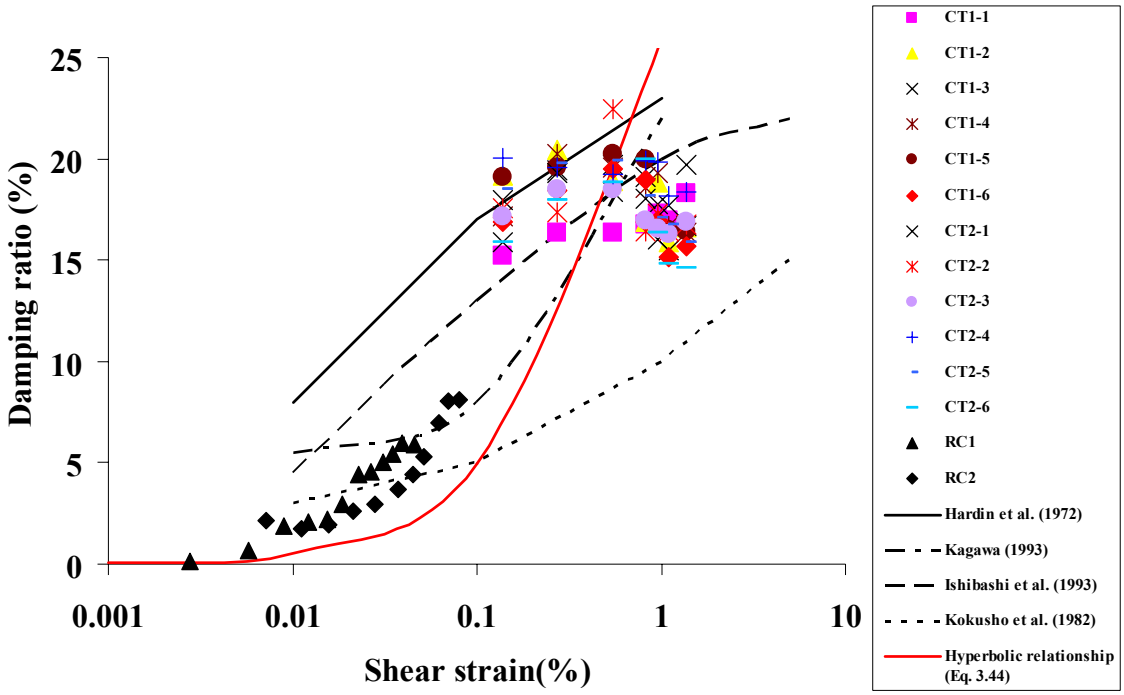

Figure 3.35 Comparison of damping ratios computed from Eq. 3.43 with test data

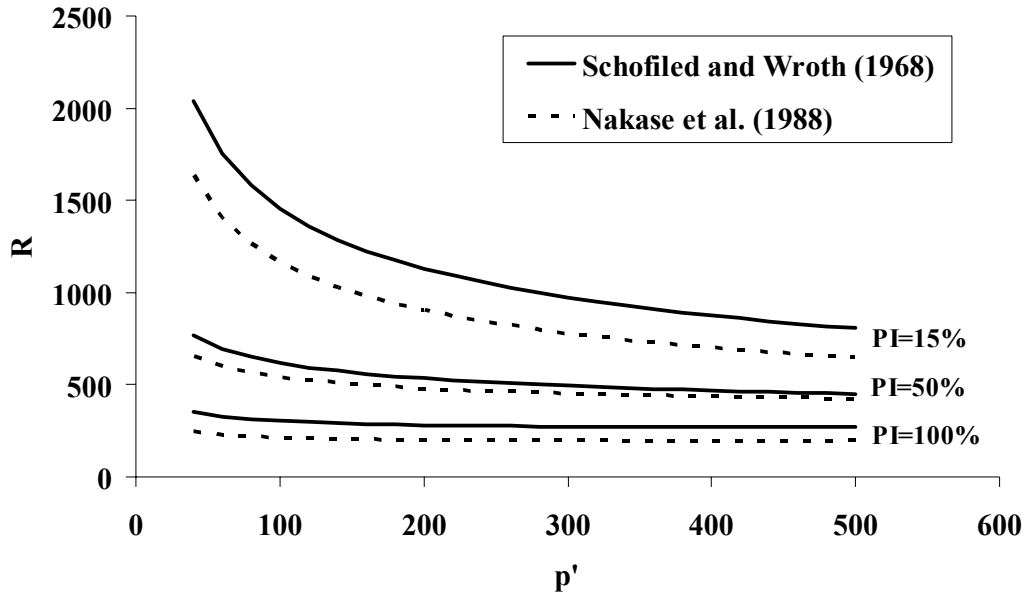

Figure 3.36 Normalized modulus (R) vs. confining stress (p')

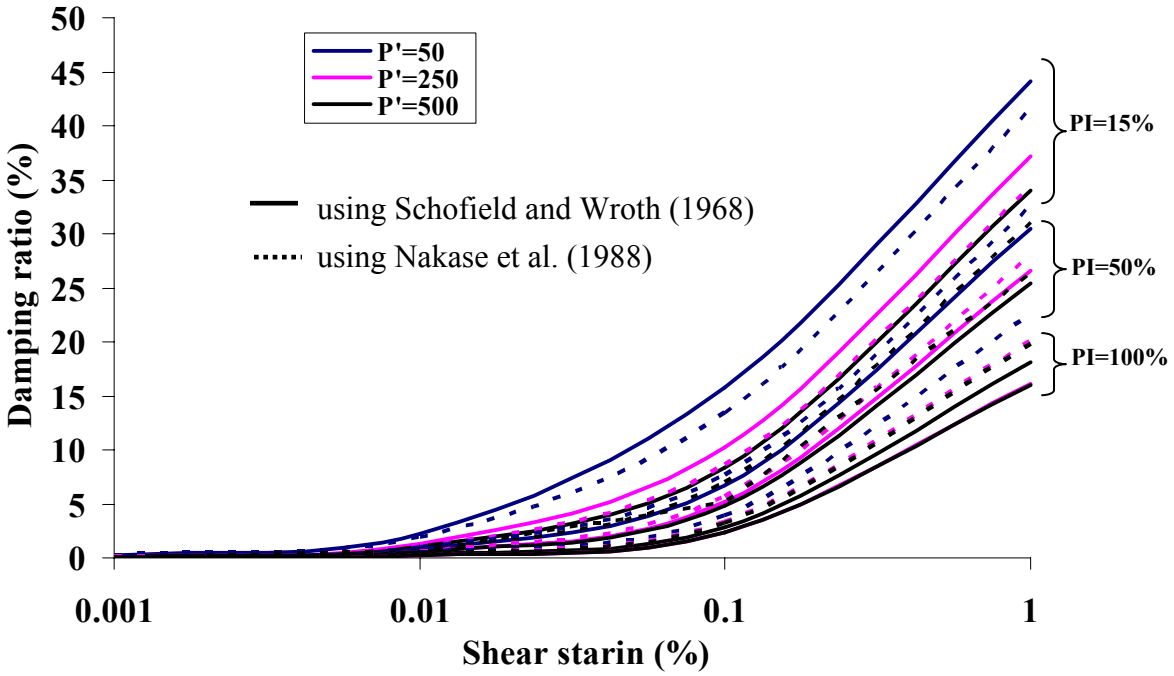

Figure 3.37 Damping ratio vs. shear strain for different confining stress and PI

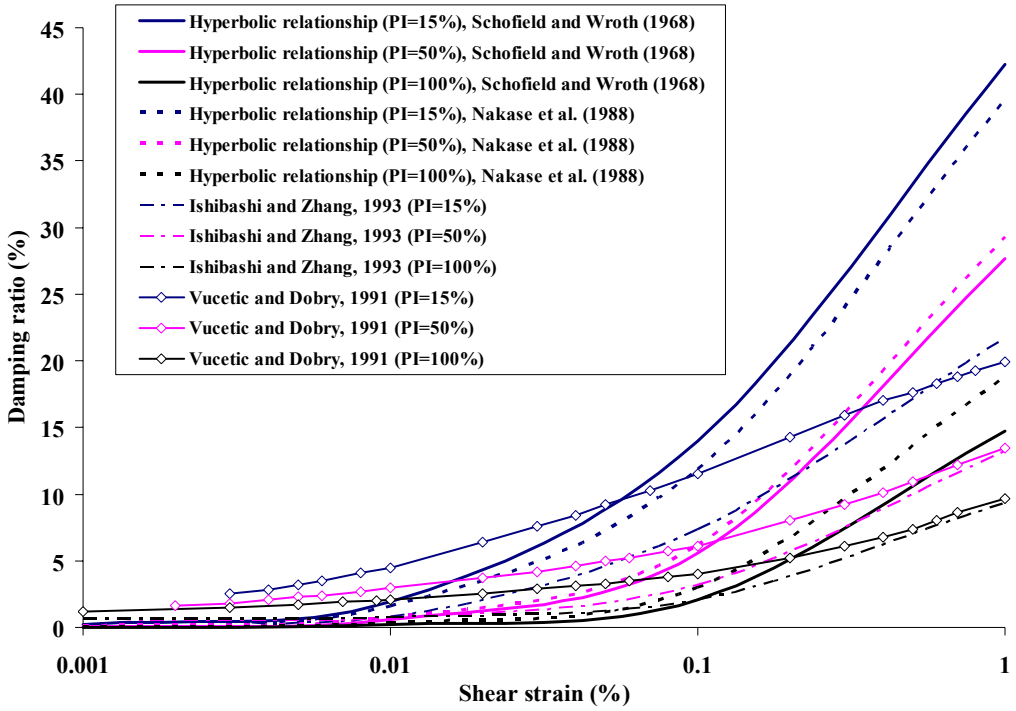

Figure 3.38 Comparison of damping ratio computed for different PI with published trends

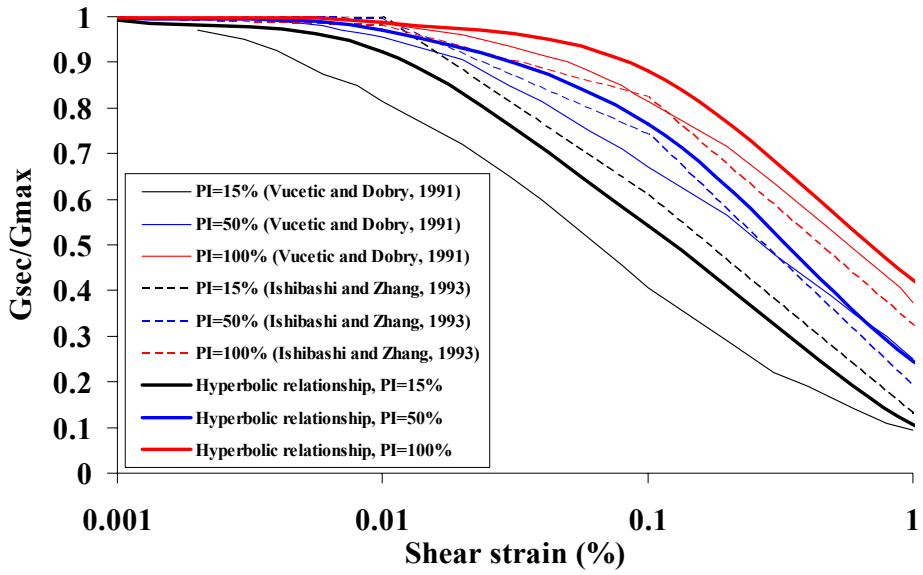

(a) Hyperbolic relationship using Nakase et al (1988)

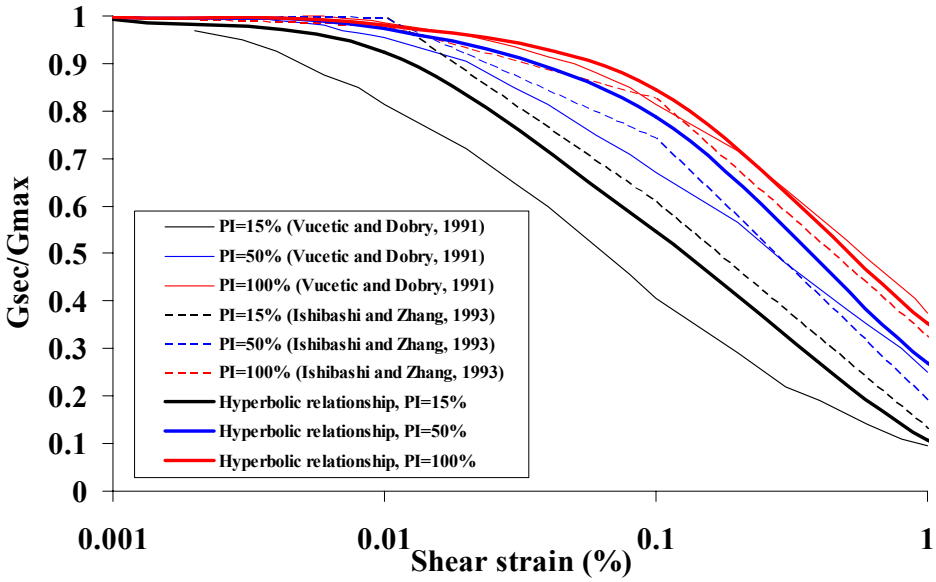

(b) Hyperbolic relationship using Schofield and Wroth (1968)

Figure 3.39 Comparison of G_{sec}/G_{max} computed for different PIs with published trends

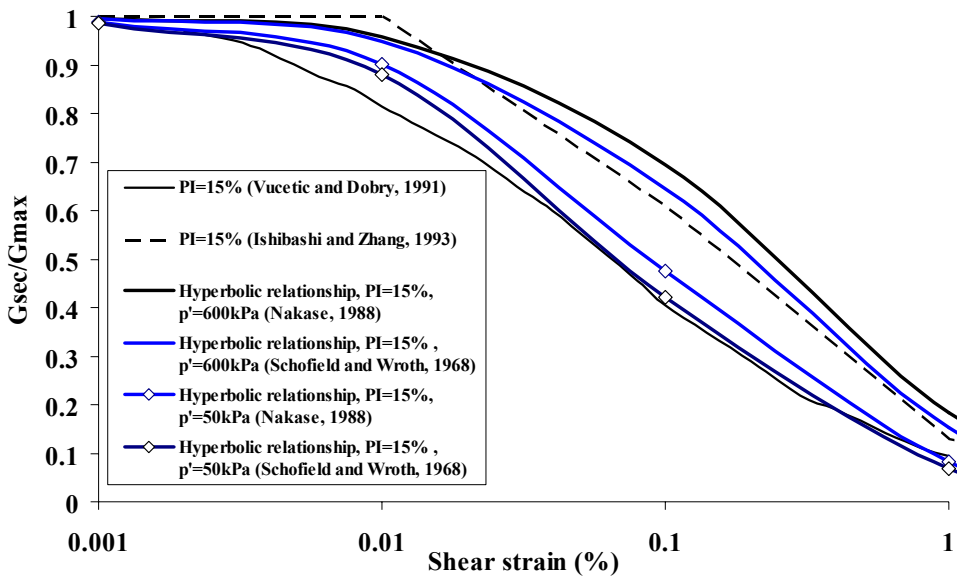

Figure 3.40 Comparison of G_{sec}/G_{max} for low-plasticity soil (PI=15%) at different confining stresses with published trends

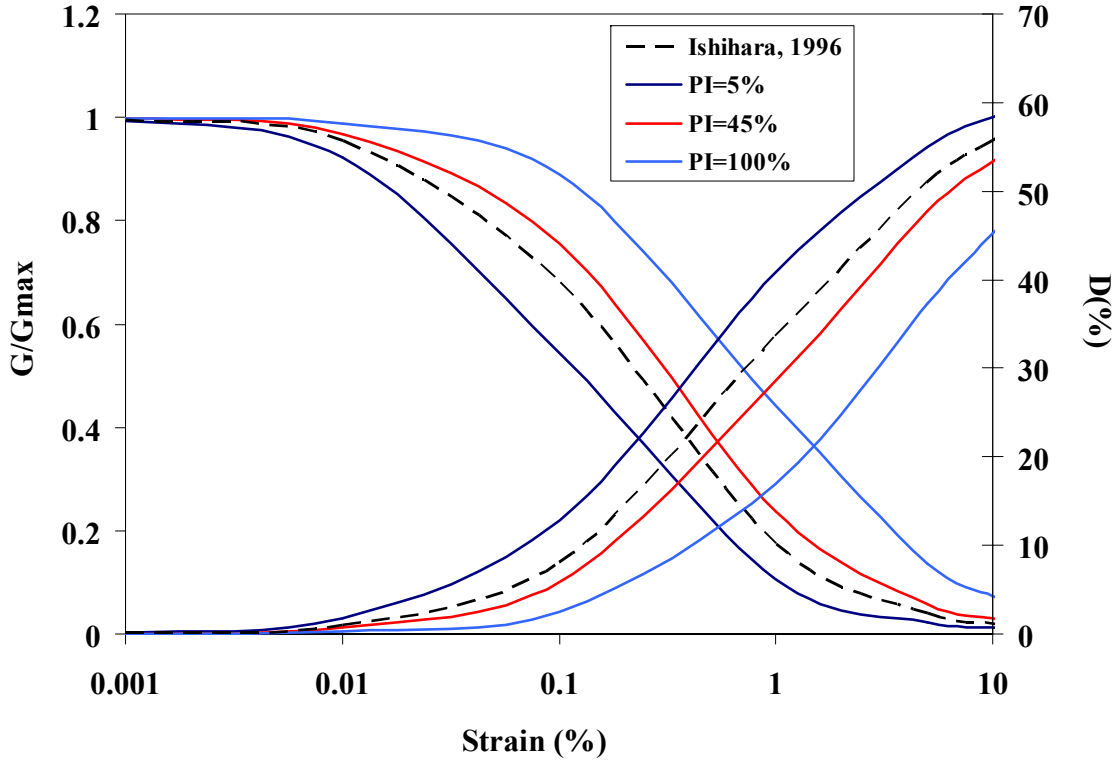

Figure 3.41 Comparison of G/G_{max} and damping ratio with Ishihara's relationship (Ishihara, 1996)

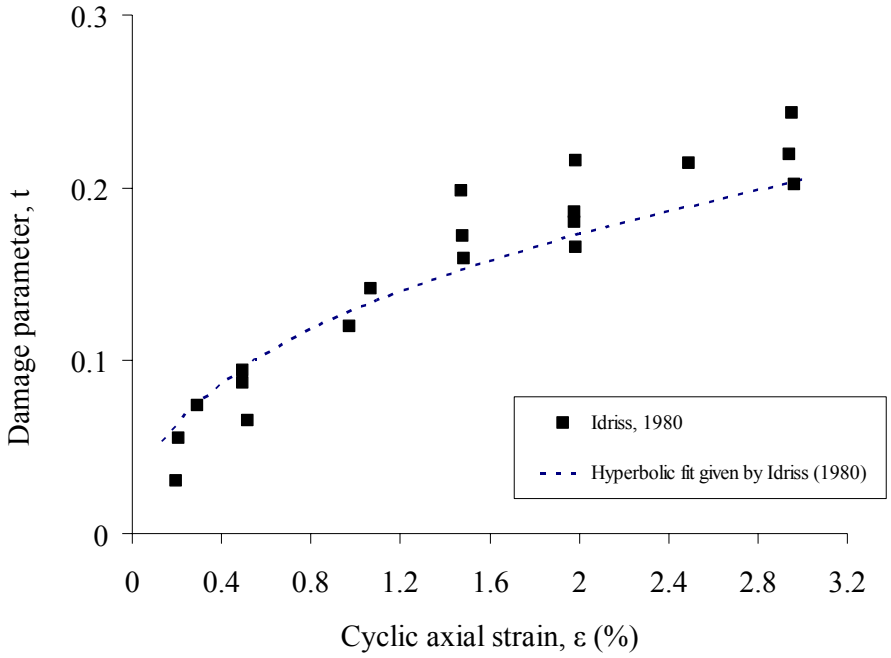

Figure 3.42 Idriss' (1980) hyperbolic fit between damage parameter (t) and cyclic strain amplitude

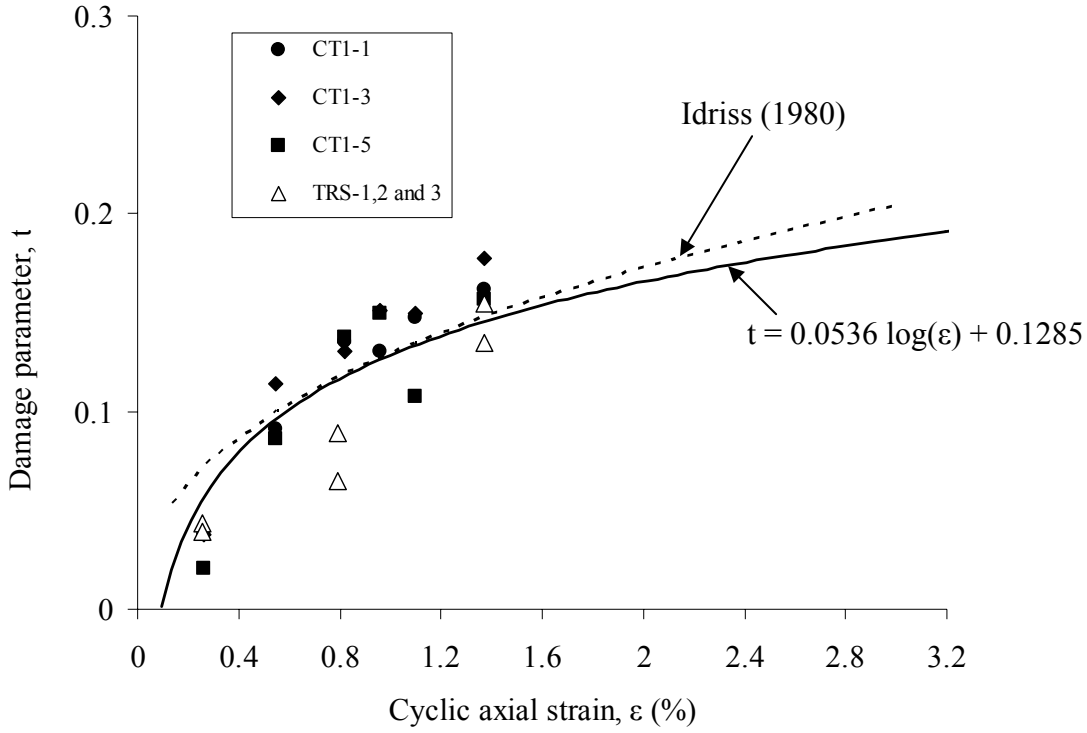

Figure 3.43 Proposed relationship between damage parameter (t) and cyclic strain amplitude

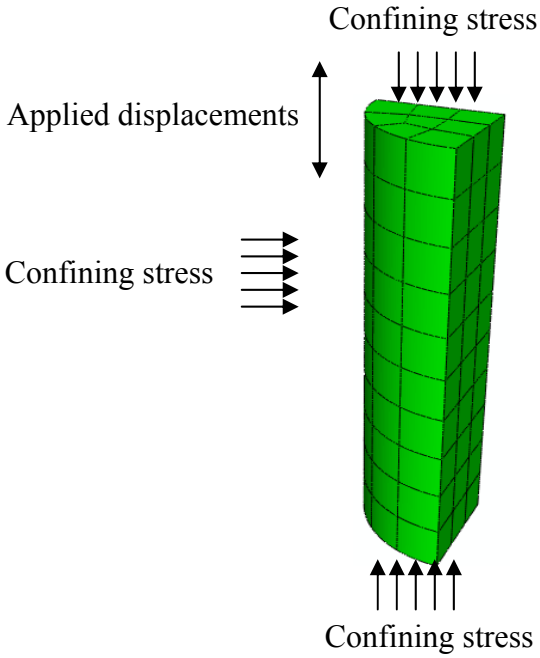

Figure 3.44 ABAQUS 3D quarter model for cyclic triaxial tests

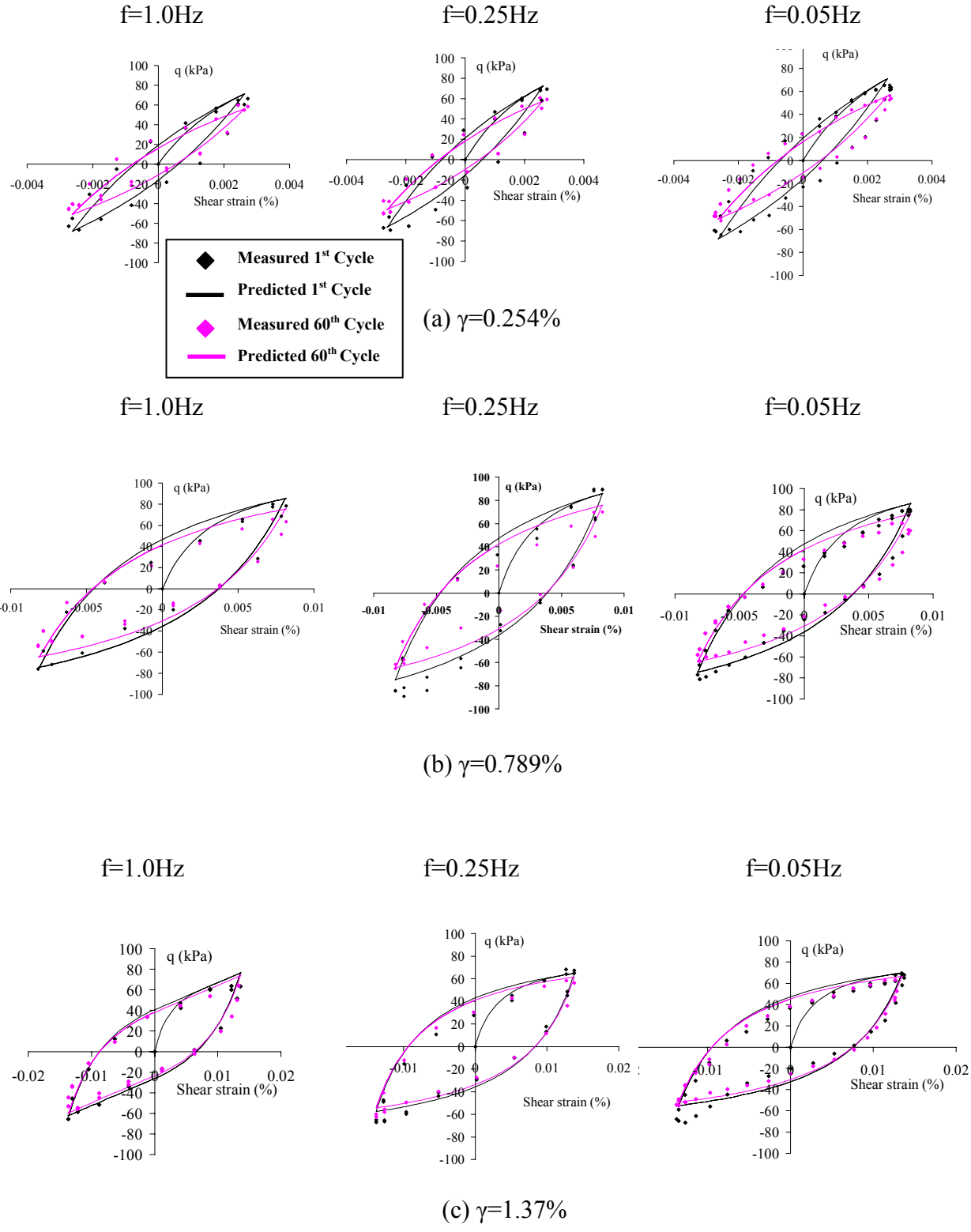

Figure 3.45 Comparison of measured and predicted stress-strain loops for three different strains and three different frequencies

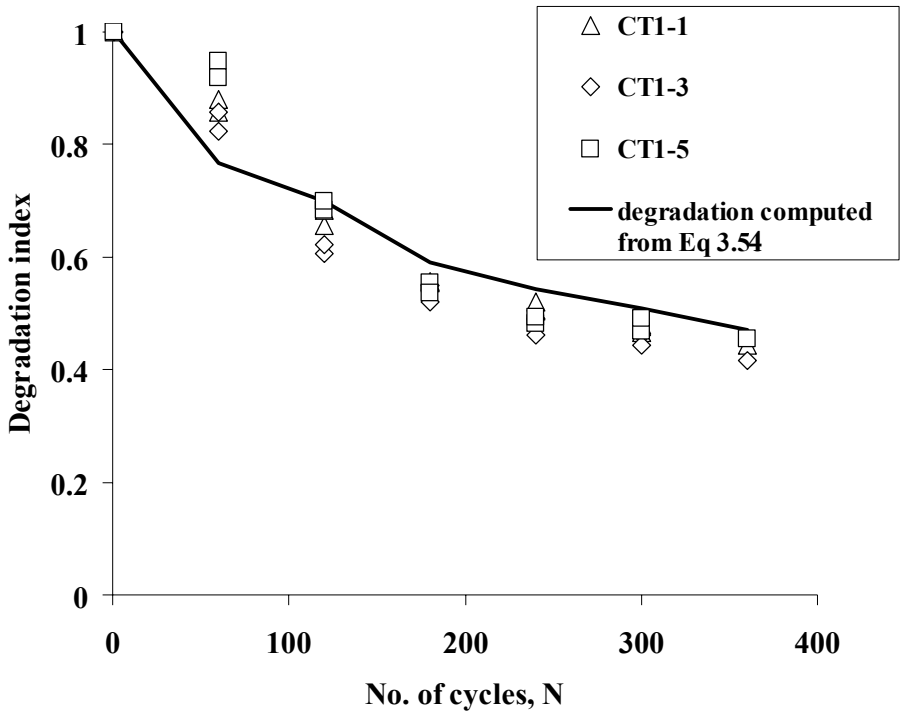

Figure 3.46 Comparison of proposed degradation relationship (Eq. 3.54) with test series CT1-1, CT1-3 and CT1-5

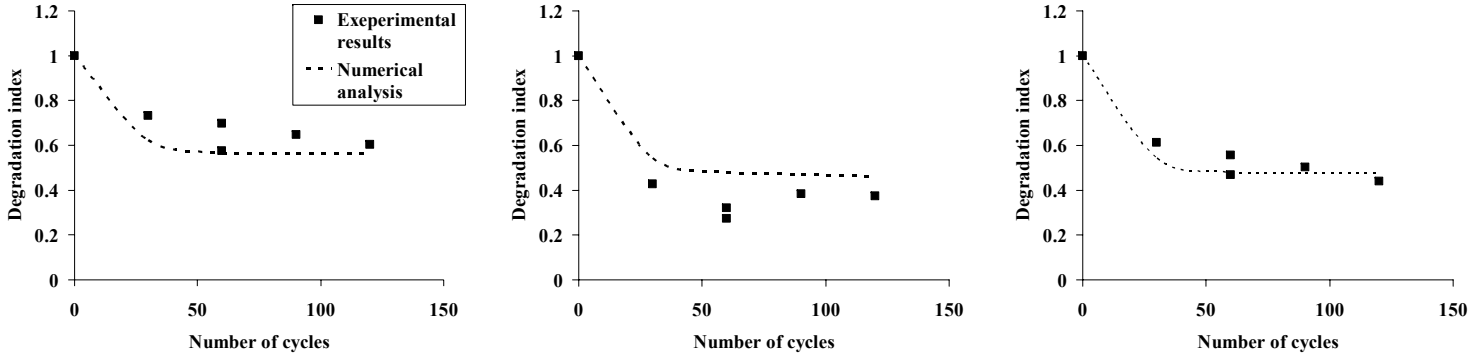

(a) TRS-1 (b) TRS-2 (c) TRS-3

Figure 3.47 Comparison of computed and experimental degradation index for test series TRS

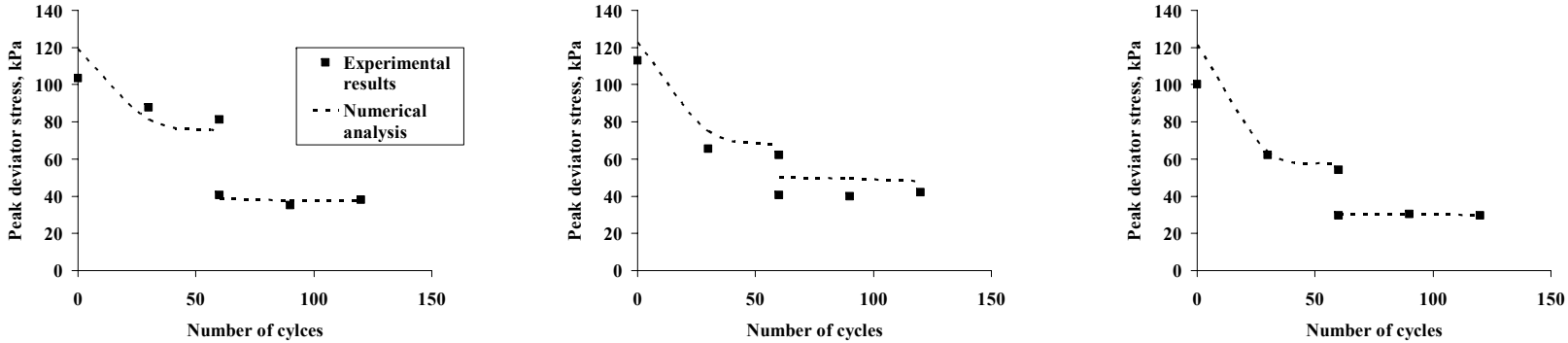

(a) TRS-1 (b) TRS-2 (c) TRS-3

Figure 3.48 Comparison of computed and experimental peak deviator stress for test series TRS

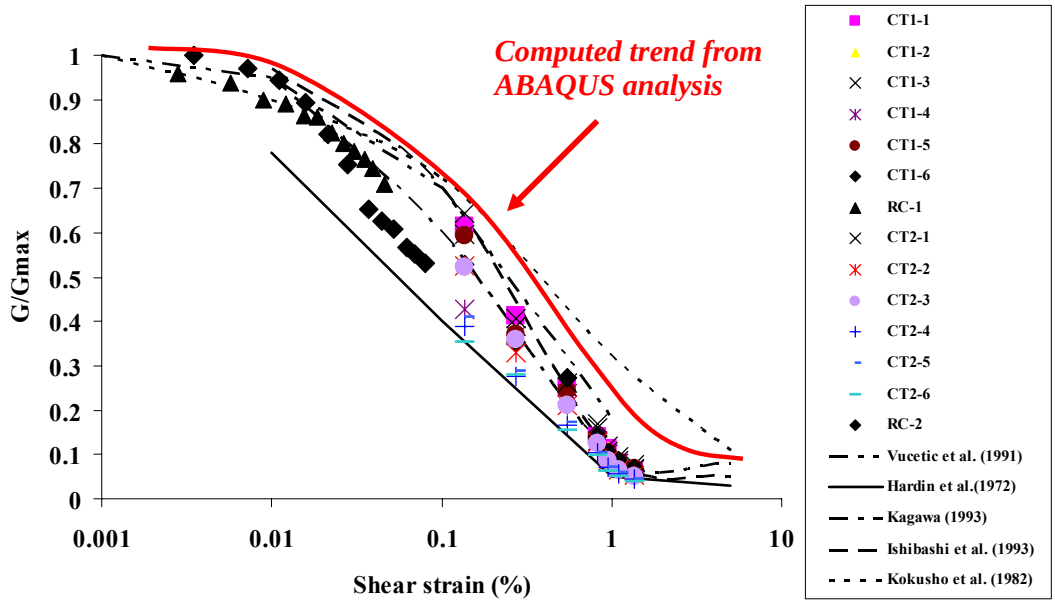

Figure 3.49 Measured and predicted G/G_{max} values at different strains

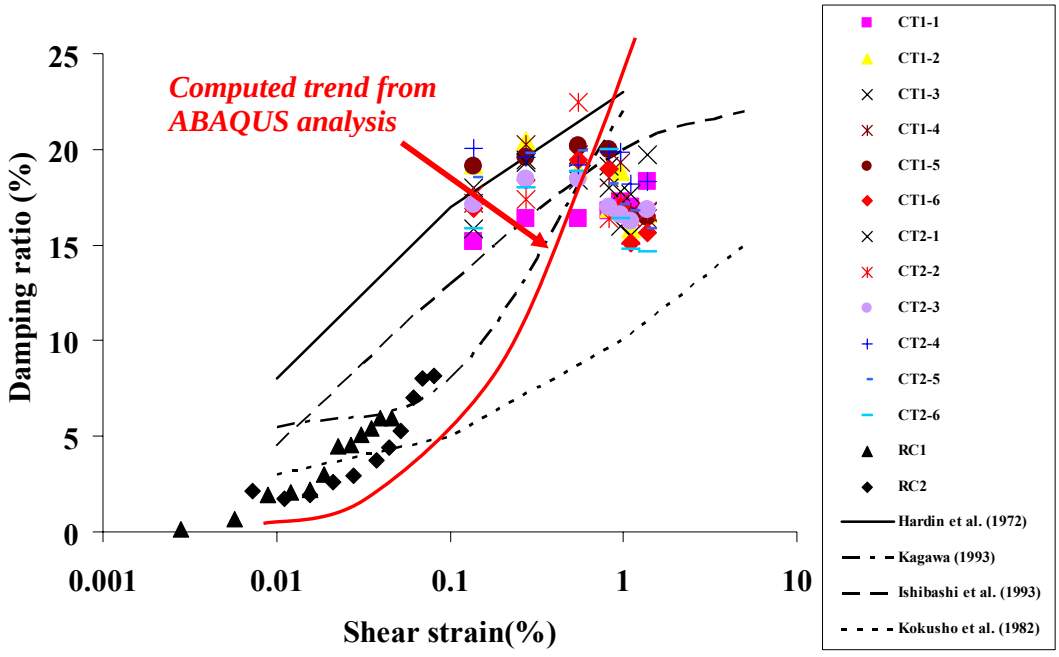

Figure 3.50 Measured and computed damping ratio values at different strains

CHAPTER 4 CENTRIFUGE MODEL TEST SET-UP AND CALIBRATION RESULTS

4.1 Introduction

Seismic soil-pile interaction is a complex phenomenon involving linear and nonlinear behavior of the soil and the pile, frequency content and amplitude of the seismic excitation, as well as the natural frequency and damping characteristics of the soil-foundation unit. To better understand the various mechanisms and how they affect the soil-pile system, it is helpful to begin by examining the seismic response of the soil in the absence of any structure. This chapter first discusses the centrifuge model set-up for performing shake table tests under high-g conditions, and then presents some results which highlight the key features of clay behaviour under earthquake loading. The insights gleaned from such a study serve as a valuable baseline reference against which soil-pile interaction effects can be assessed and analyzed in the following chapter.

4.2 Centrifuge Tests Set-Up

4.2.1 Structure of Centrifuge

The 2-m radius NUS geotechnical centrifuge has a payload capacity of 40,000 g-kg and a maximum working g-level of 200g (Lee et al., 1991). It rotates about a vertical rotor shaft which is driven by a hydraulic motor located at its base. The shaft has an outer diameter of 250 mm and a wall

thickness of 50 mm (Figure 4.1). The driving torque is transmitted from the shaft through a welded steel cage to the rotor arm. The centrifugal force is carried by four parallel steel plates which form the main elements of the rotor arm. These plates are held together by connecting and stiffener plates. A steel swing platform is hinged onto each end of the rotor arm. Each platform has a working area of about 750 mm x 700 mm and model headroom of about 1200 mm. When the platforms are fully swung up under operating conditions, the radial distance from the centre of rotation to the base of the model container is approximately 1960 mm. There is a small difference in length between the two arms of the centrifuge, as the swing platform for the model container is slightly deeper than that of the counterweight.

4.2.2 Viscosity Scaling Issue

In order to ensure that the behaviour of soil elements in a reduced-scaled model are consistent with those of the prototype, the stress levels in both systems should be identical. To achieve this, small scale models are often tested in the centrifuge where they are subjected to increased gravitational fields which modify the stress levels in the soil accordingly. The model results can then be scaled to the prototype values in a self-consistent and rigorous manner.

The scaling relations between the small scale model and full scale prototype are usually derived in two ways, namely by dimensional analysis (Hoek, 1965) and by considering the equations of equilibrium of the forces acting on the two phases of a soil element (Roscoe, 1968). A list of commonly

used scaling relations is summarized in Table 4.1 (Leung et al., 1991), in which N is the scale factor for the length.

As Table 4.1 shows, the time scaling factors for different events are not identical. Seepage and consolidation events are speeded up by N^2 times, whereas dynamic events, or events in which inertial effects feature significantly, are speeded up by N times. This leads to the well-known discrepancy between consolidation and dynamic scaling in experiments wherein both consolidation and dynamic events feature strongly, e.g. excess pore pressure generation and dissipation during earthquake shaking (Lee and Schofield, 1988; Ng and Lee, 2002; Zhang, 2006). The usual approach to resolving this conflict is to replace water in the centrifuge experiements with another pore fluid which is N times as viscous. For instance, Lee and Schofield (1988), Ng and Lee (2002) and Zhang (2006) used silicone oil as the pore fluid instead of water. By so doing, seepage and consolidation events are slowed down by a factor of N times compared to tests in which water is used; relative to the prototype, they are speeded up by N times rather than N^2 times. This ensures consistency between seepage, consolidation and dynamic scaling. In the case of clay experiments, it is difficult to replace water by another pore fluid without affecting the clay-water chemistry and soil behaviour. However, in many dynamic clay model tests, the dynamic event occurs so rapidly that little or no consolidation takes place during the event. In such cases, consolidation events are often assumed to be insignificant and not modeled.

As shown on Table 4.1, the duration of viscous events in the centrifuge should be properly scaled to that of the prototype in order that the contribution of viscous forces are properly accounted for. In the case of model tests

involving sand, this effect is often assumed to be unimportant and viscous scaling is therefore ignored (Lee and Schofield, 1988). However, for clay tests, viscous effects may be significant. Since such effects cannot be easily altered in a fine-grained material by using a different pore fluid, there is no known way of resolving the conflict between viscosity and dynamic scaling. The effect of this discrepancy can be deduced from the differential forms of the governing equations of a dynamic event. The equation of motion at any point in a continuum can be expressed as

$$\sigma'_{ij,j} + p_{,j}\,\delta_{ij} + \rho\, f_i = \rho\, \ddot{u}_i \qquad (4.1)$$

where

σ'_{ij} = effective stress tensor

p = pore pressure

ρ = bulk density of soil

u_i = displacement vector

f_i = gravity vector

and δ_{ij} = the Kronecker Delta.

Subscripted commas represent differentiation with respect to the i^{th} dimension while dots represent differentiation with respect to time. Range and summation conventions are applicable (Frederick and Chang, 1965).

If we assume that the effective stress tensor σ_{ij}' is the sum of a non-rate-dependent component σ^{o}_{ij}'(which is a function of stress state and the strain component ε_{ij}) and a perfectly viscous component that is proportional to strain rate $\dot{\varepsilon}_{ij}$, then

$$\sigma'_{ij} = \sigma'^{o}_{ij}\,(\sigma'^{o}_{ij}, \varepsilon_{ij}) + c\,\dot{\varepsilon}_{ij} \qquad (4.2)$$

in which the parentheses denote a functional dependence and c is a constant. Substituting Eq. 1.2 into 1.3 leads to

$$\sigma'^{o}_{ij,j} + c\ \dot{\varepsilon}_{ij,j} + p_{,j}\,\delta_{ij} + \rho\, f_i = \rho\ \ddot{u}_I \tag{4.3}$$

In the case of the prototype, we can write Eq. 4.3 as

$$\sigma'^{op}_{ij,j} + c^p\ \dot{\varepsilon}^p_{ij,j} + p^p_{,j}\,\delta_{ij} + \rho^p\, f^p_i = \rho^p\ \ddot{u}^p_i \tag{4.4}$$

As Table 4.1 shows, rate-independent stresses and strains are preserved in the centrifuge model and the prototype. Thus,

$$\sigma'^{om}_{ij} = \sigma'^{op}_{ij} \tag{4.5a}$$

$$p^m = p^p \tag{4.5b}$$

$$\rho^m = \rho^p \tag{4.5c}$$

$$f^m_i = N\, f^p_i \quad \text{since gravity is scaled up N-times} \tag{4.5d}$$

$$\ddot{u}^m_i = N\,\ddot{u}^p_i \quad \text{since acceleration is scaled up in the same way as gravity} \tag{4.5e}$$

and $$\varepsilon^m_{ij} = \varepsilon^p_{ij} \tag{4.5f}$$

in which the superscripts p and m denote prototype and model quantities. Furthermore, since linear dimensions are down-scaled by N times, the derivatives with respect to linear dimensions will be scaled up by N times, i.e.

$$\sigma'^{om}_{ij,j} = N\,\sigma'^{op}_{ij,j} \tag{4.5g}$$

$$p^m_{,j} = N\,p^p_{,j} \tag{4.5h}$$

and $$\varepsilon^m_{ij,j} = N\ \varepsilon^p_{ij,j} \tag{4.5i}$$

We also know that, in order to preserve inertial effects

$$t^m = t^p/N \tag{4.6}$$

The model strains can be expressed as

$$\dot{\varepsilon}^{m}_{ij,j} = \frac{\partial \varepsilon^{m}_{ij,j}}{\partial t^{m}} = N^2 \frac{\partial \varepsilon^{p}_{ij}}{\partial t^{p}} = N^2 \dot{\varepsilon}^{p}_{ij,j} \tag{4.7}$$

in view of Eqs. 4.6 and 4.5i.

Thus, Eq. 4.3 for the centrifuge model can be expressed as

$$N\sigma'^{op}_{ij,j} + N^2 c^p \dot{\varepsilon}^{p}_{ij,j} + Np^p_{,j} \delta_{ij} + N\rho^p f^p_i = N\rho^p \ddot{u}^p_i \tag{4.8}$$

or $$\sigma'^{op}_{ij,j} + N c^p \dot{\varepsilon}^{p}_{ij,j} + p^p_{,j} \delta_{ij} + \rho^p f^p_i = \rho^p \ddot{u}^p_i \tag{4.9}$$

In other words, the behaviour of a centrifuge clay model is equivalent to that of a prototype wherein the damping factor of the clay has been increased by N times. In view of this, one can expect the effects of mis-scaling viscosity to be non-trivial if viscous effects are indeed significant.

Brennan et al. (2005) calculated the shear modulus and damping ratio of a sand, a normally consolidated clay and a municipal solid waste from centrifuge accelerometer data. Earthquake motion is applied using the mechanical stored angular momentum actuator described by Madabhushi et al. (1998). The shear modulus values appeared to agree well with published degradation curves for all three different soils. However, their measured damping values were somewhat higher than those typically obtained from conventional laboratory tests. They attributed this to rate-dependent effects arising from the above mis-scaling in the centrifuge tests.

On the other hand, the present laboratory test results presented in Chapter 3 for Malaysian kaolin clay indicate that, while the damping ratio is highly strain-dependent it is also relatively rate-independent. This suggests that, for the kaolin clay used in this study, the hysteretic strain-dependent damping is likely to be much larger than the rate-dependent viscous damping. Hence, scale distortion arising from viscosity mis-scaling is likely to be

insignificant. Moreover, for numerical back-analyses of the centrifuge tests, it is not necessary to up-scale the damping ratio in order to simulate the centrifuge conditions under the high-g environment.

4.3 Shake Table

As shown in Figure 4.4, the shake table assembly consists of a laminar box seated on top of a sliding platform driven by a hydraulic actuator controlled by twin servo-hydraulic valves.

4.3.1 Laminar Box

The laminar box is constructed from hollow aluminum alloy sections to minimize both the payload mass and the inertial loading imposed by the laminar rings onto the model clay bed (Figure 4.2). The laminar box, whose inner dimensions are 526 mm long by 300 mm wide by 310 mm high, comprises nine rectangular laminar rings (Figure 4.2b) of 38 mm thickness each. On the top and the bottom surfaces of each rectangular ring, 10 grooves, each 22 mm wide, 1.25 mm deep and 80 mm long, were machined along the two long sides for the placement of bearings. Each linear bearing contains eight rollers.

The laminar model box was mounted onto a shaking platform constructed of aluminum alloy, which slides on another set of linear bearings. The flexural stiffness of the platform was enhanced using ribbed construction on its underside. The bearings were, in turn, mounted on top of a grillage constructed from welded stainless steel sections and machined to a fine

tolerance. The linear bearings were specially selected to provide enhanced resistance against rocking, yawing and pitching of the payload.

To prevent leakage, a rubber bag was placed inside the laminar box (Figure 4.3) prior to sample preparation. The rubber bag is made of a cotton cloth painted with several layers of liquid latex, and specially sewn to fit the inner dimensions of the laminar box.

4.3.2 Shaking Apparatus

The key components of the shaker are the slip table, servo-actuator, servo-valves and built-in displacement transducer (Figure 4.4). The servo-controlled actuator connected to the base plate actuates the shaker based on the incoming control signal. To minimize any rocking tendency and to maximize the stiffness along the path of force transfer, the actuator shaft was connected directly to the end of the sliding platform, thereby minimizing the vertical offset between the lines of action of the motion and inertial forces. The reaction mass used to develop the motion force is provided by the swing platform and the fixed base of the shaking table. The mass of the moving payload is typically 200kg or less, whereas the combined mass of the swing platform and fixed base is about 700kg.

One unique feature of the shaker is the placement of the hydraulic power source on the arm of the centrifuge (Figure 4.5), which obviates the need for expensive high-pressure rotary joints whilst allowing an almost unlimited number of tests to be performed without swing-down. In order to ensure sufficient energy supply for long-duration earthquakes, two 20-litre accumulators were incorporated into the hydraulic system. The low-friction

servo-actuator is controlled by two Moog4679 servo-valves which maintain a relatively flat frequency response up to about 100Hz (Figure 4.5). At 50g model gravity, this translates to a prototype upper frequency limit of 2Hz, which is well above the main frequency band of Singapore earthquakes.

A multi-channel data acquisition system installed with the DasyLab ver. 3 software was used to send in the earthquake input signal to excite the model, and to record the transducer output data for the accelerations and pore pressures. The typical data sampling rate used was 5 kHz. Closed-loop control was implemented using the feedback from a built-in displacement transducer.

4.4 Transducers

Two types of transducers were used in the centrifuge models for measuring accelerations and pore pressures. The accelerations were measured using PCB Piezotronics 352C66 quartz piezoelectric accelerometers, which have an operating frequency range of 1 to 10000 Hz (Figure 4.6). Each accelerometer has a diameter of 7mm, a height of 12.2 mm and a mass of 2 g. In-house calibration of the accelerometers, performed using a calibrator and amplifiers, showed good agreement with the manufacturer's chart. The nominal calibration constant is approximately 100 mV/g. The accelerometer's reading was believed to be accurate up to 3rd order decimal places.

There were two difficulties initially encountered when using these accelerometers. First, it was found that the transducers could not work properly under high-g conditions due to short circuit caused by ingress of water. Second, the density of the accelerometer is significantly higher than

that of the surrounding soil, causing it to sink in the soft clay. These problems were overcome by waterproofing each accelerometer with a coat of silicon rubber, which also reduces its overall density to a value close to that of the soil.

A pore pressure transducer (PPT) was also placed at the middle of the soil to monitor pore pressure build-up during earthquake shaking, as well as its dissipation during the post-event consolidation. The PPT was saturated with water in a saturation chamber, as shown the Figure 4.7, before embedment in the soil model.

Two types of amplifiers were used for signal conditioning. The accelerometer readings were amplified by a factor of 2 using the signal-cum-power conditioners manufactured by PCB Piezoelectronics Inc. On the other hand, the LVDT and PPT signals were amplified 100 times using NEC6L02DC amplifiers.

The locations and depths of the accelerometers and pore pressure transducers are shown on Figure 4.8.

4.5 Preparation of Soft Clay Bed Model

4.5.1 Preparation of Clay Slurry

The clay bed used in the centrifuge model tests were prepared using kaolin powder. The geotechnical properties of the kaolin clay used in this study are given in Table 4.2. White kaolin powder was first mixed with water in a ratio of 1: 1.2 to form the clay slurry. The total mass of kaolin slurry required to fill the laminar box was about 82 kg, comprising 37 kg of kaolin powder and 45 kg of water. Mixing of the slurry was carried out in a deairing

chamber for about 5 hours. After mixing, the clay slurry was transferred into the rubber-lined laminar box in several pours, so that the transducers could be placed at the desired locations and depths.

Before transferring the slurry into the laminar box, a thin plastic hose perforated with holes along its length was taped to the inside bottom of the rubber bag to provide a drainage path during the consolidation phase. The hose was then embedded within a 10 mm layer of sand, which was air-pluviated to form a thin drainage layer at the bottom of the clay bed.

4.5.2 Consolidation of Clay Slurry

The completed slurry mixture was then subjected to both 1-g and 50-g consolidation processes to develop the representative strength profile and stress history. The 1-g consolidation was carried out first to pre-compress the clay beds, so as to reduce the time required for the subsequent in-flight consolidation. Dead weights were applied in stages, up to a total load of about 100 kg, which corresponds to an effective overburden stress of about 5 kPa at the top of the clay bed. To ensure a uniform pressure distribution acting on the clay bed, the weights were applied on a thick Perspex platen resting on a geotextile layer placed over the surface of the clay slurry. This 1-g loading condition was maintained for 7 days (Figure 4.9).

After one week of 1-g consolidation, the dead weights and the Perspex plate were removed, following which the laminar box was mounted on the centrifuge together with the shaker and other accessories. It was then subjected to in-flight centrifuge consolidation under 50 g until the degree of consolidation along the entire depth was 70% or more. Based on Terzaghi's

1-D consolidation theory, the consolidation time was expected to take about 10 hrs.

4.6 Input Ground Motions

The prototype earthquake motions considered in this study are characteristic of far-field events measured at rock site in Singapore from previous Sumatran earthquakes, which typically have long periods and long durations. Using the typical response spectra of such earthquakes, the synthetic ground motions shown on Figure 4.10 were generated for this study, in which the low frequency components with prototype periods exceeding 20s were removed (Yu and Lee, 2002). The frequency content and duration of the three earthquake events shown on the figure are identical, except for the peak ground accelerations (PGA) that were scaled to 0.1g, 0.07g and 0.022g respectively.

The accelerations of Figure 4.10 were double-integrated and drift-corrected to obtain the displacement histories shown on Figure 4.11. These displacements were then scaled down by a factor of 50, and converted into digital signals that were fed into the servo-actuator to prescribe the base motion for the centrifuge tests under a 50-g acceleration field.

Figures 4.12 and 4.13 show the typical acceleration and displacement time-histories recorded at a rock site in Singapore, from the Great Sumatra-Andaman Islands and Great Nias-Simeulue earthquakes, respectively (Pan et al. 2007). The time histories are shown for the three directions of East-West (E), North-South (N) and Up-Down (Z). For the Great Sumatra-Andaman Islands earthquake, the largest of the peak acceleration and peak displacement

in the three directions are 4 mm/s^2 and 19 mm, respectively. For the Great Nias-Simeulue earthquake, the largest of the peak acceleration and peak displacement in the three directions are 9 mm/s^2 and 33 mm, respectively. Hence, it can be acknowledged that the input motions used for the current study are significantly higher than the usual records and the probability of occurrence of earthquakes with such a high PGA is relatively less.

In each centrifuge experiment, the model was subjected to nine earthquake events over three cycles. Each cycle comprised a small, a medium and a large earthquake that were triggered sequentially. Figure 4.14 shows the sequence of earthquake events for a typical centrifuge experiment.

4.7 Results and Observations

4.7.1 Medium Earthquake (PGA=0.07g), 1st Cycle

Figures 4.15a and b show the measured prototype acceleration histories at the base and the surface of the clay layer respectively, recorded during the medium earthquake event of the 1st cycle. As these are plotted to the same scales, the measurements clearly indicate amplification of the seismic wave as it propagated from the base to the surface of the clay layer.

Figure 4.15c shows the response spectra corresponding to the measured acceleration histories of (a) and (b). These spectra depict the maximum response of a single-degree-of-freedom (SDOF) system to the prescribed earthquake motions as a function of the natural period (or natural frequency) and damping ratio of the SDOF system. By providing the amplitude and frequency content of the prescribed excitations, such spectra

serve as useful indicators of the ground motion characteristics at the base and at the surface of the clay bed.

As shown on Figure 4.15c, the response spectrum of the surface motion shows a significant increase in amplitude for natural periods of between 1 and 2 seconds, compared to the response spectrum of the base motion. By taking the ratio of the surface to base spectral amplitudes for each natural period, the amplification response shown on Figure 4.15d is obtained. The maximum amplification is about 1.85, and is associated with a natural period of about 1.5 secs. In the following discussion, the natural period associated with the maximum amplification is termed hereafter as the 'resonance period' of the soil (or soil-structure) system under consideration.

4.7.2 Large Earthquake (PGA = 0.1g), 1st Cycle

Figure 4.16 shows, in a similar format, the corresponding acceleration histories, response spectra and amplification response for the large earthquake event of the 1st cycle. For this earthquake, the maximum amplification is about 2.7, corresponding to a resonance period of about 1.9 seconds. Hence, compared to the medium earthquake, the large earthquake results in an increase in both the amplification and the resonance period.

4.7.3 Large Earthquake (PGA = 0.1g), 2nd cycle

In a similar manner, the centrifuge data are processed for the small, medium and large earthquakes triggered in the second and third cycles. Figure 4.17 shows, in a similar format, the corresponding acceleration histories, response spectra and amplification response for the large earthquake event of

the 2nd cycle. For this earthquake, the maximum amplification is about 3, corresponding to a resonance period of about 2.3 seconds. It appears that, compared to the large earthquake of the 1st cycle, the corresponding earthquake of the 2nd cycle resulted in further increases in both the amplification and the resonance period.

4.7.4 Summary of the Test Data

Figure 4.18 shows the resonance periods plotted against the peak ground accelerations for all nine earthquake events. Within each cycle of three earthquakes, the measured resonance period increased as the clay model was subjected to successively larger earthquakes. For a given earthquake intensity, the resonance period also increased with successive cycles of earthquakes. The observed increase in the resonance periods are indicative of a reduction in the clay stiffness. Strain softening is likely to be the dominant mechanism causing the observed changes within each earthquake in any given cycle, as the clay was subjected to increasingly higher peak ground accelerations.

4.8 Numerical Analysis on Seismic Behaviour of Soft Clay

This section presents the details and results of 3-D numerical analyses that were performed to back-analyze the centrifuge experiments. The analyses were carried out using ABAQUS ver 6.7, and incorporated the hyperbolic-hysteretic clay behaviour described in Chapter 3 via the user-defined subroutine HyperMas.

4.8.1 Model Description

In principle, a two-dimensional (2-D) plane strain model is adequate for analyzing the clay bed response associated with shaking under laminar box conditions. Nevertheless, a three-dimensional (3-D) model was set up for this purpose, which was later modified to include piles and raft for the soil-pile-raft interaction study of Chapters 5 and 6. The discretized mesh of the 3-D half-model, shown on Figure 4.19, was made up of 4720 20-noded brick elements.

To simulate laminar box movements, linear multi-point constraints were applied to the two vertical faces normal to the earthquake motion, so that nodes at opposite ends of the domain and at the same depth move in unison with each other (Figure 4.20). In addition, the nodes on the vertical plane of symmetry were restrained against any horizontal displacements in the direction normal to this plane. The remaining three vertical faces, as well as the base of the mesh, were restrained vertically.

The soft clay behaviour was characterized using the hyperbolic-hysteretic model with degradation described in Chapter 3, which was incorporated into ABAQUS via the user-defined subroutine HyperMas. The material parameters adopted for the following ground response analyses were based on the laboratory tests and FE model calibration results described in Section 3.5.2.

The results in Chapter 3 suggest that rate-independent hysteretic damping effects arising from the non-linear stiffness behaviour are more significant than those associated with conventional Newtonian viscous damping. Hence, the effects of viscous damping was not considered in the

numerical analyses. The effects of damping are naturally incorporated in the analyses through the energy dissipation process arising from the hysteresis loops.

Just as in the centrifuge test, the earthquake input motion was fed in through the base of the mesh as a prescribed acceleration history. The measured acceleration at the base of the clay layer from the centrifuge test was used as the input motion. As Figure 4.21 shows, the accelerations deduced by double-differentiating the feedback displacement time histories from the internal LVDT and the measured accelerations at the base of the model are reasonably consistent. The standard Newmark's integration scheme was used in the dynamic time-stepping computations. The computed accelerations at selected nodal locations, which correspond to the accelerometer positions in the centrifuge model, were then compared with the experimental observations.

4.8.2 Comparison of Centrifuge and FEM Results

Figures 4.22a and c show the measured vs computed time histories at the mid-depth of the clay bed (accelerometer A2) and at the clay surface (accelerometer A3) respectively, for the medium earthquake of the first cycle. Despite some discrepancies at the surface, the computed responses were in reasonable agreement with the measured accelerations at both locations.

Figures 4.22b and d plot the computed and measured response spectra corresponding to the acceleration histories of Figures 4.22a and c respectively. As can be seen, there is good agreement between the computed and measured responses, with both showing a dominant period of about 1.5 secs.

Figure 4.23 shows the computed and measured amplification response of the clay bed, obtained by dividing the response spectrum at the soil surface by the corresponding spectrum at the base of the layer. In both cases, the maximum amplification is about 1.8, and occurs at a resonance period of about 1.2 secs. However, the computed case shows a distinct but smaller secondary peak below 1sec.

Figure 4.24 shows the computed and measured resonance periods of the clay bed associated with the three earthquakes of different scaled intensities. Both the experiments and the analyses indicate a similar trend in which the resonance period increases from about 0.8 secs to 2 secs as the peak ground accelerations increases from 0.22 m/s^2 to 1 m/s^2. The reason for this trend was discussed earlier in Section 4.7.

4.9 Concluding Remarks

The foregoing centrifuge tests on kaolin clay beds indicate that the resonance period of clay layers increases with the peak ground acceleration. Moreover, for a given earthquake, the resonance period also increased with successive cycles of earthquakes. The observed increases in the resonance periods are indicative of a reduction in the clay stiffness. As shown by the stress-strain response of Figure 2.15, the reduction may be brought about by (i) strain softening under monotonic loading, and (ii) stiffness degradation under repeated load cycling. Strain softening is likely to be the dominant mechanism causing the observed changes within each earthquake in any given cycle, as the clay was subjected to increasingly higher peak ground accelerations. Yu and Lee's (2002) back-analyses suggest that, in the large

earthquakes, shear strain levels as high as 4-7% may be attained. Cyclic stiffness degradation of the backbone curve, on the other hand, accounts for the increasing resonance period for earthquakes of similar magnitude across successive cycles.

The results from the numerical analyses show that the proposed phenomenological soil model of Chapter 3, despite its relatively simple total stress framework, can satisfactorily capture the acceleration histories and spectral response of the clay bed under seismic excitation. In the subsequent chapters, the same soil model will be used for the analysis of more complex soil-pile-raft interaction problems.

Table 4.1 Centrifuge scaling relations (Leung et al., 1991)

Parameters	Prototype	Centrifuge model at N-g
Linear dimension	1	1/N
Area	1	$1/N^2$
Density	1	1
Mass	1	$1/N^3$
Frequency	1	N
Acceleration	1	N
Velocity	1	1
Displacement	1	1/N
Strain	1	1
Energy density	1	1
Energy	1	$1/N^3$
Stress	1	1
Force	1	$1/N^2$
Time (viscous flow)	1	1
Time (dynamic)	1	1/N
Time (seepage and consolidation)	1	$1/N^2$

Table 4.2 Geotechnical properties of the kaolin clay (Goh, 2003)

Properties	Range
Bulk unit weight (kN/m^3)	16
Water content	66%
Liquid limit	80%
Plastic limit	35%
Compression index	0.55
Recompression index	0.14
Coefficient of permeability (m/s)	$2x10^{-8}$
Initial void ratio	2.54
Angle of friction	25°

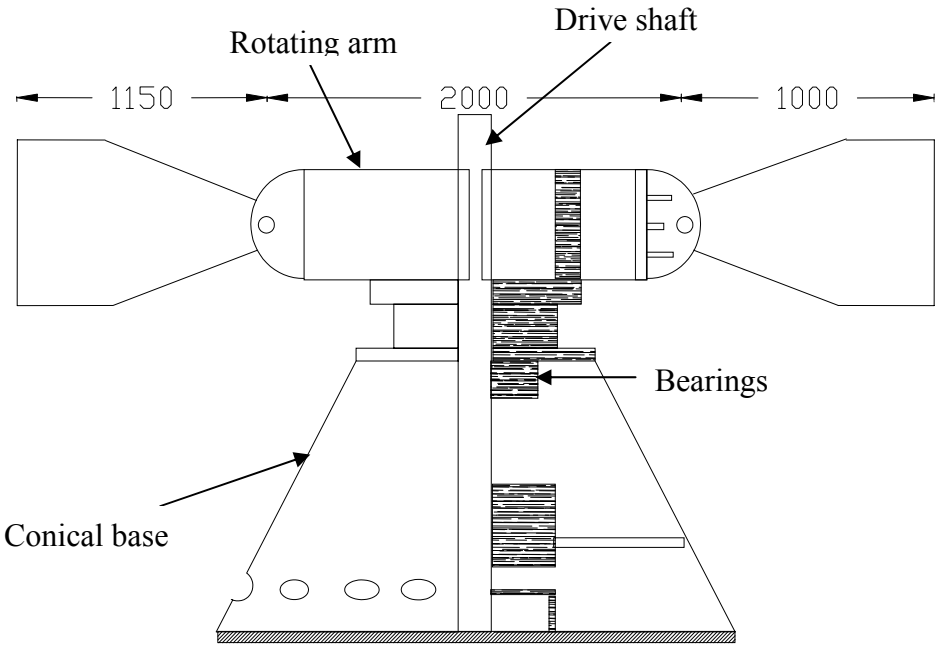

Figure 4.1 Schematic views of NUS Geotechnical Centrifuge

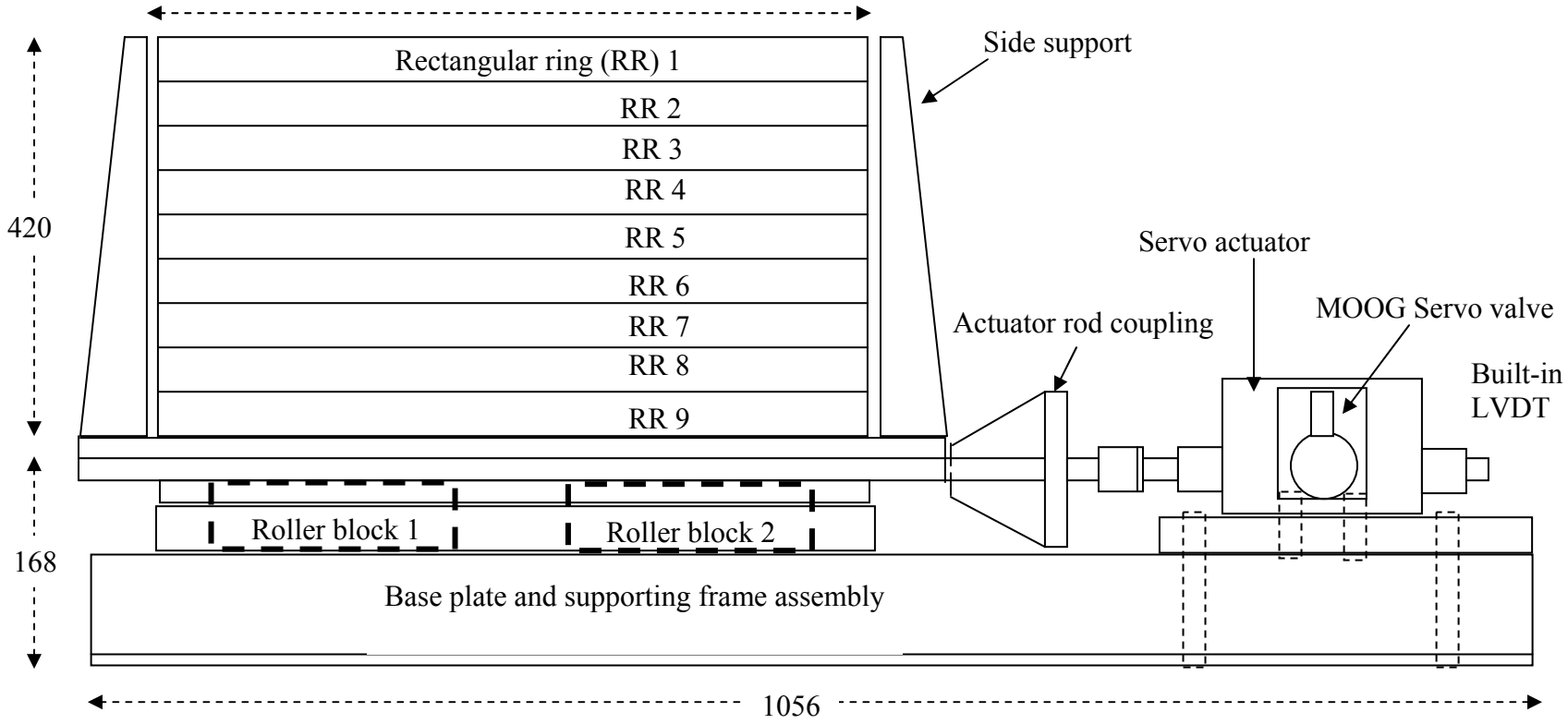

(a)

Figure 4.2 Sectional views of (a) Laminar box + shaking table assembly and (b) Rectangular hollow ring

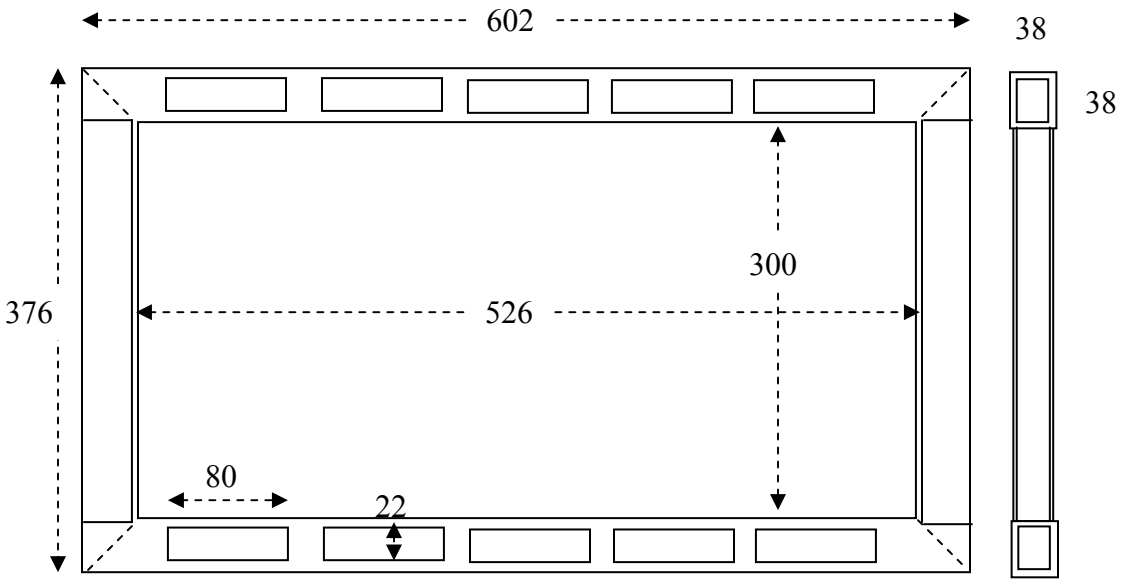

Figure 4.2 Sectional views of (a) Laminar box + shaking table assembly and (b) Rectangular hollow ring *(continued)*

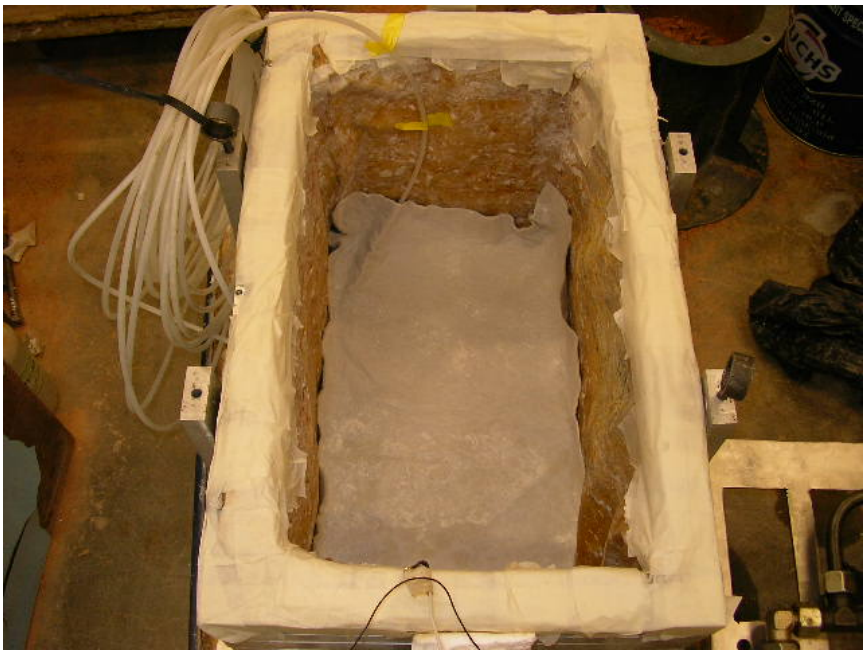

Figure 4.3 Laminar box without soil

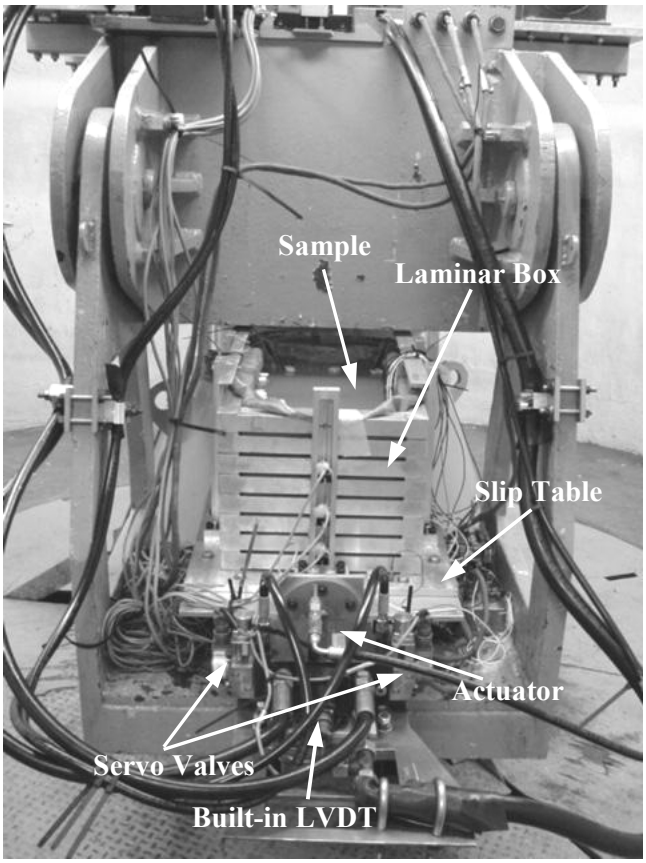

Figure 4.4 Set-up of shaking table with test model on swing platform

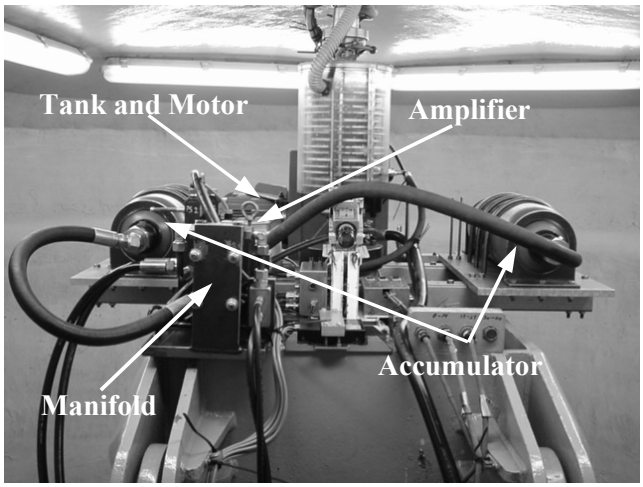

Figure 4.5 Hydraulic power equipment and motion command amplifier

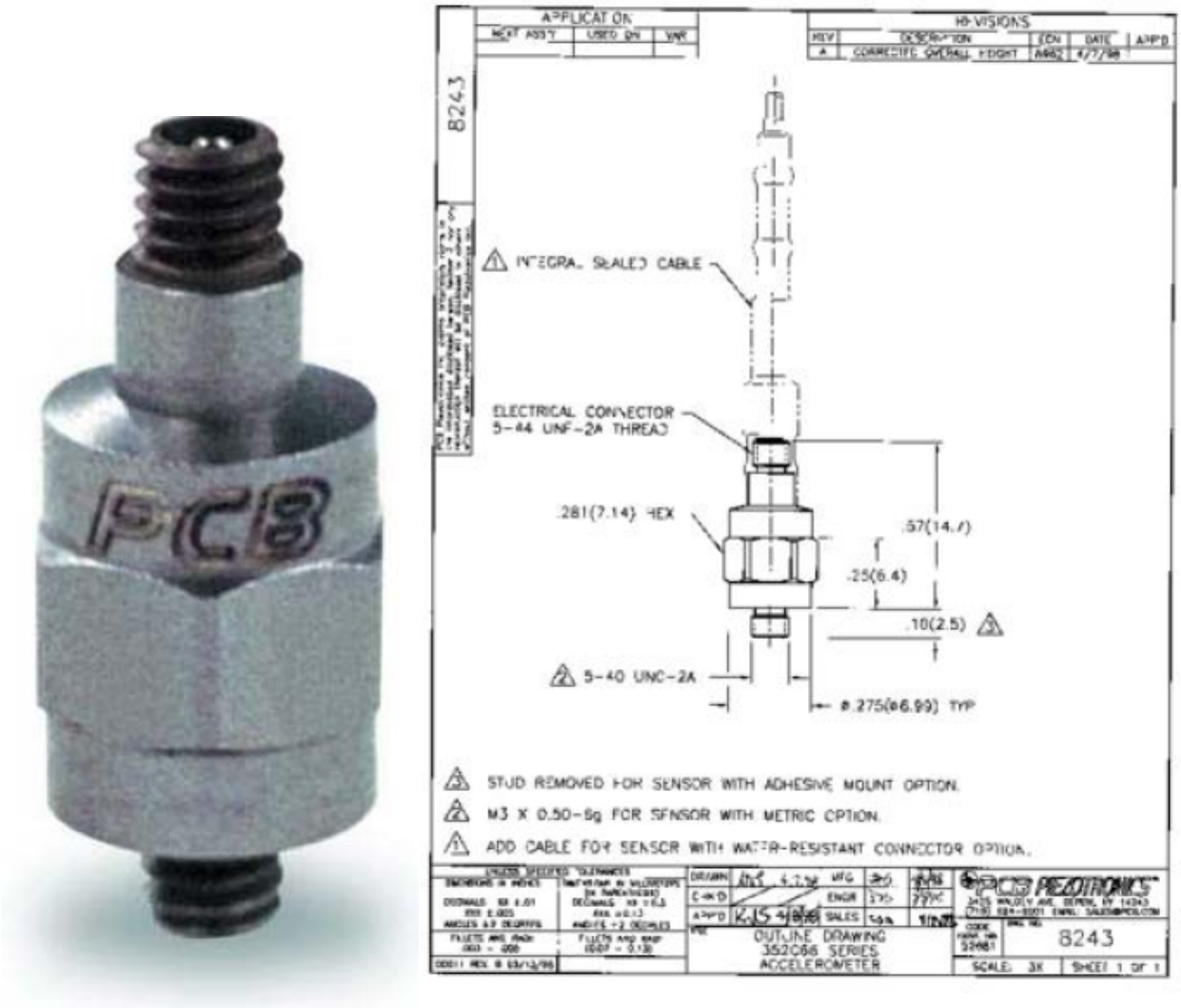

Figure 4.6 PCB Piezotronics model 352C66 quartz piezoelectric accelerometers

Figure 4.7 Saturation of pore pressure transducer (PPT)

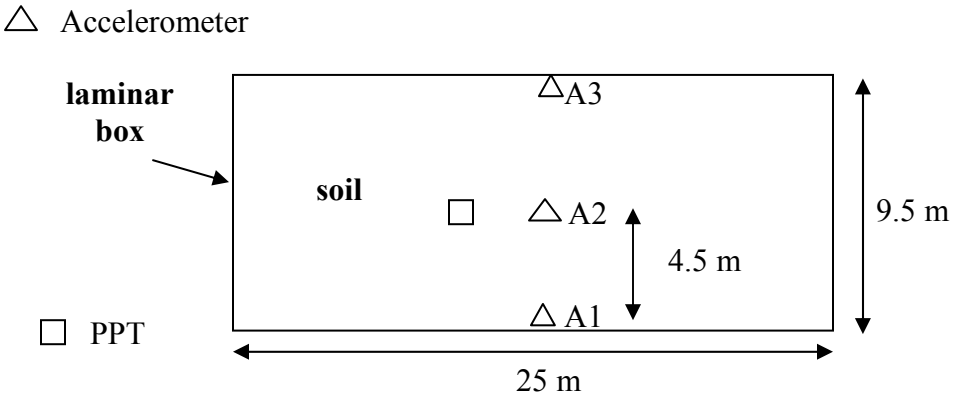

Figure 4.8 Instrumentation lay-out in the pure clay bed models (longitudinal side view of laminar box)

Figure 4.9 1-g consolidation of clay model under dead weights

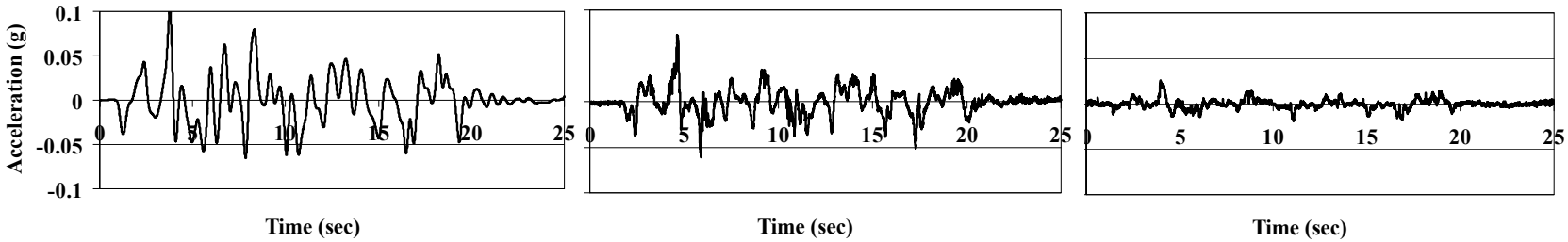

Large Earthquake Medium Earthquake Small Earthquake

Figure 4.10 Time histories of earthquake accelerations used in the centrifuge tests

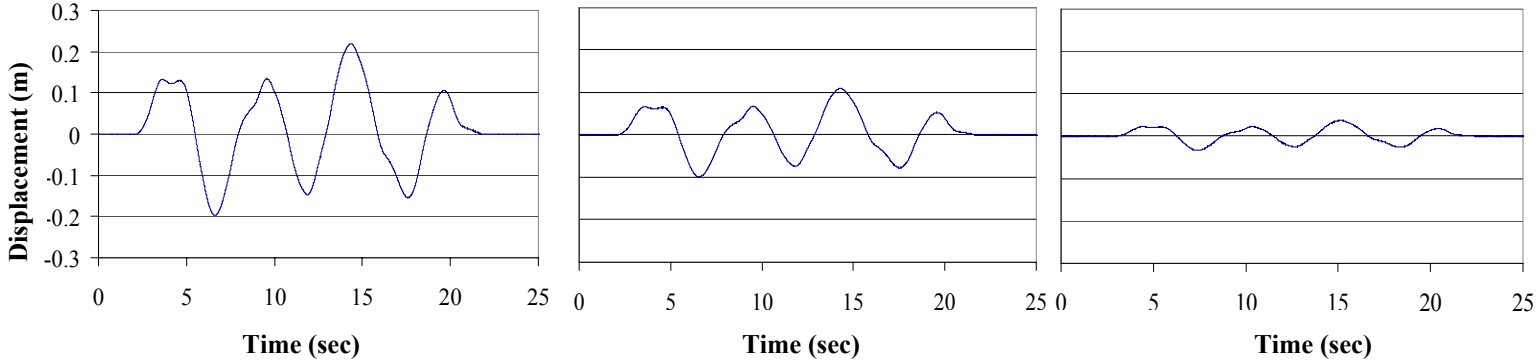

Large Earthquake Medium Earthquake Small Earthquake

Figure 4.11 Time histories of prototype displacements for use as centrifuge input motions

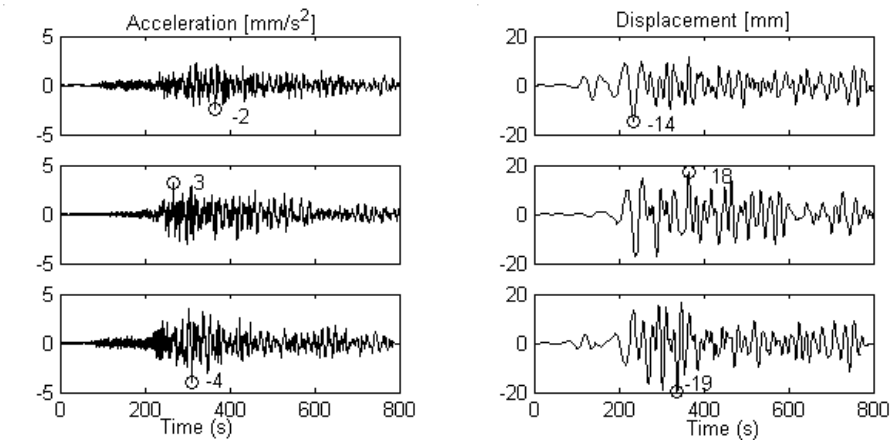

Figure 4.12 Acceleration and displacement of the Great Sumatra-Andaman (2004) Islands earthquake, recorded at the BTDF station.(Pan et al. 2007)

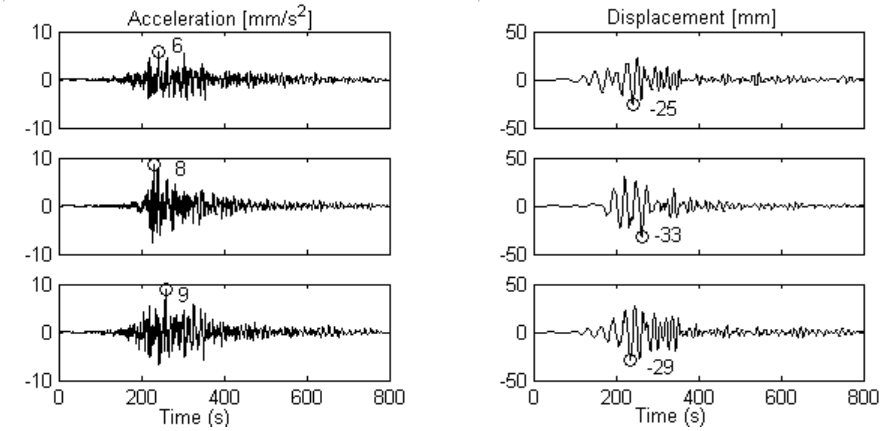

Figure 4.13 Acceleration and displacement of the Great Nias-Simeulue (2005) earthquake, recorded at the BTDF station. (Pan et al. 2007)

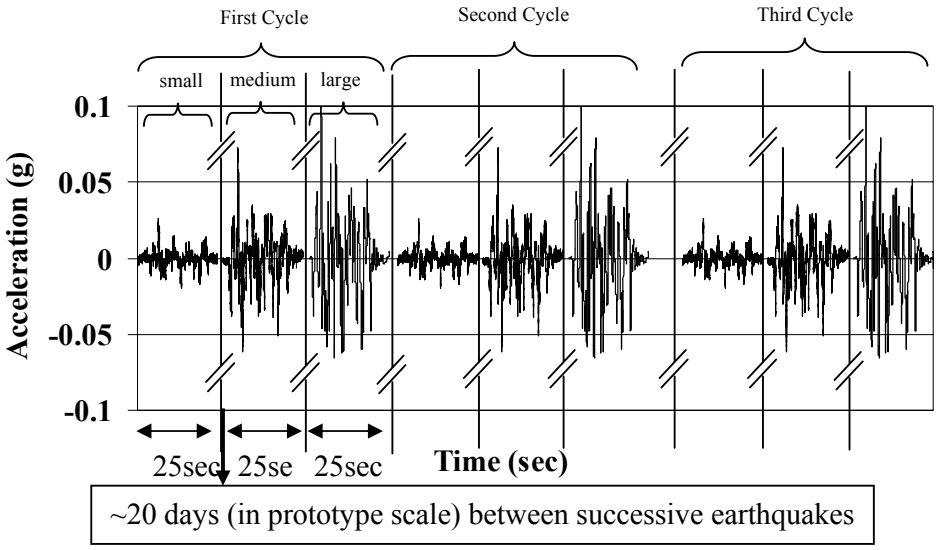

Figure 4.14 Three cycles of nine earthquakes triggered in each centrifuge test

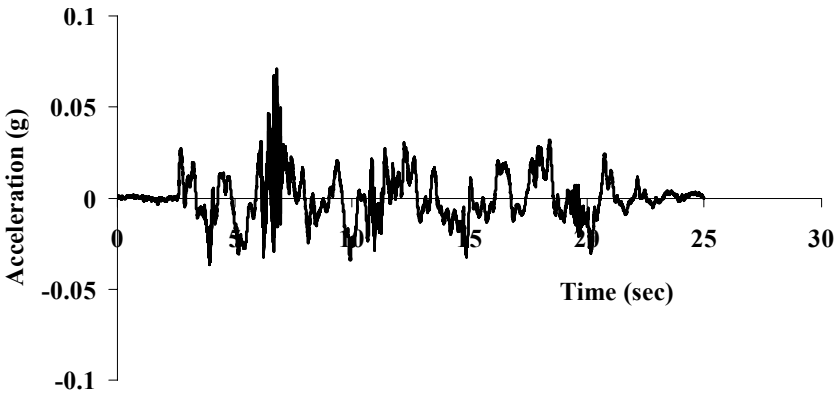

(a) Measured sccelerations at base of clay layer (*Accelerometer A1*)

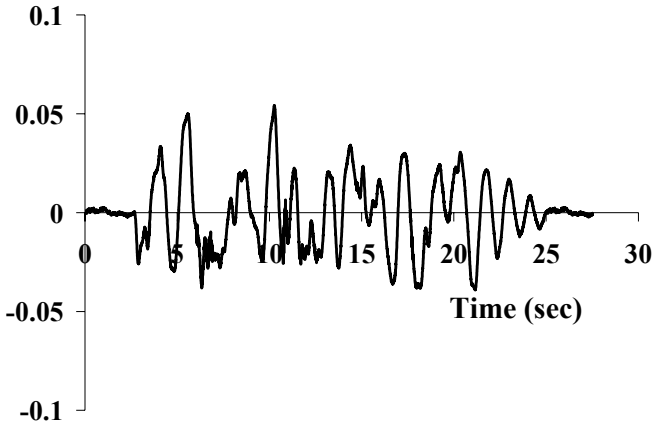

(b) Measured accelerations at surface of clay layer (*Accelerometer A3*)

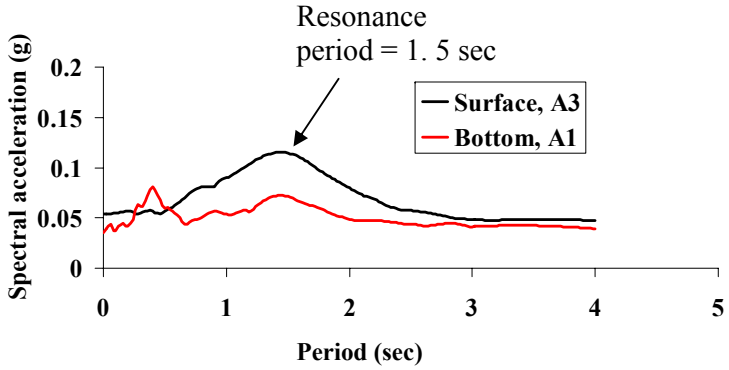

(c) Response spectra for the base and surface acceleration time histories

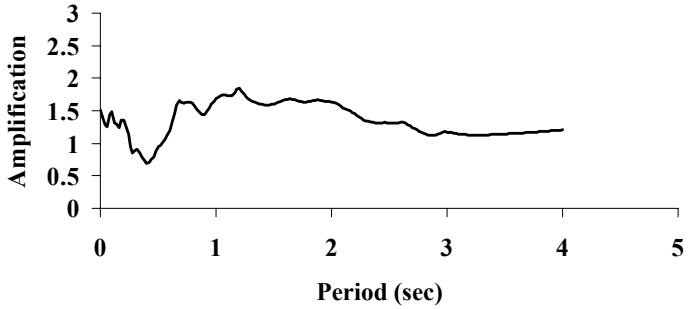

(d) Surface amplification response

Figure 4.15 Time histories, response spectra and amplification for medium earthquake, first cycle

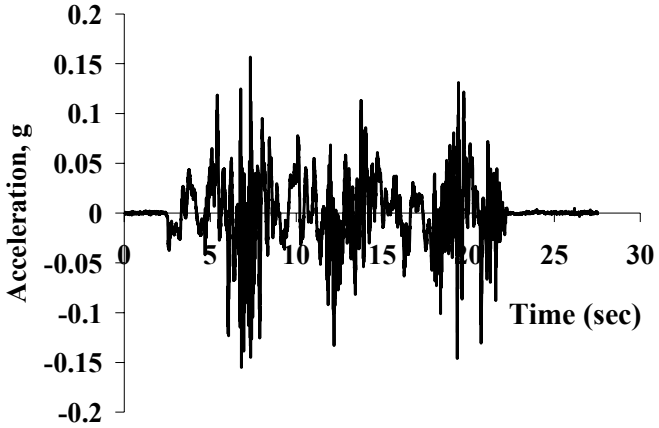

(a) Measured accelerations at base of clay layer *(Accelerometer A1)*

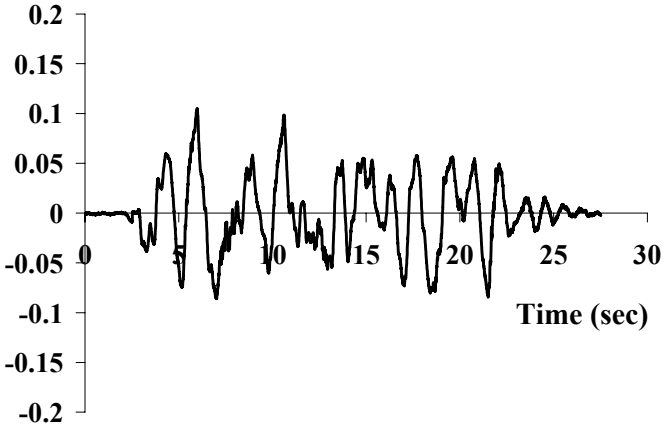

(b) Measured accelerations at surface of clay layer *(Accelerometer A3)*

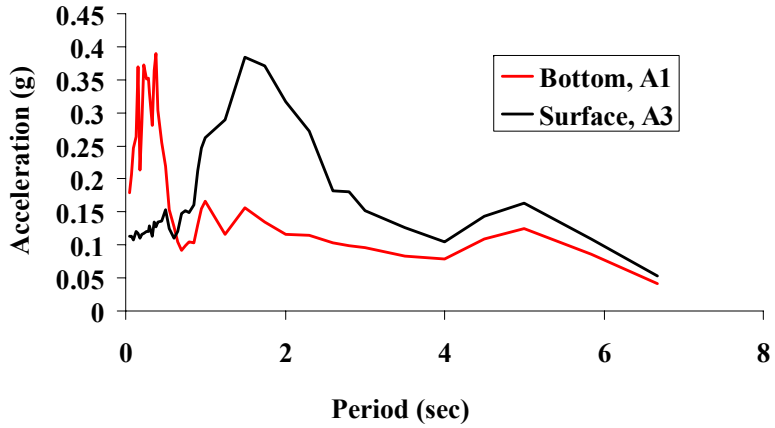

(c) Response spectra for the base and surface acceleration time histories

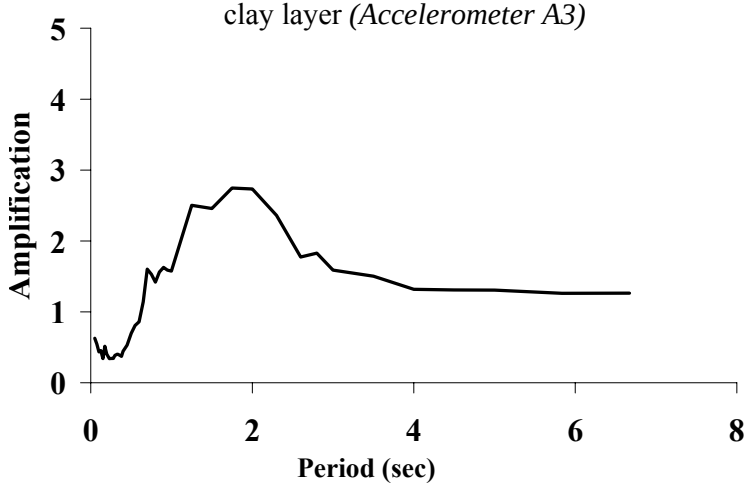

(d) Surface amplification response

Figure 4.16 Time histories, response spectra and amplification for large earthquake, first cycle

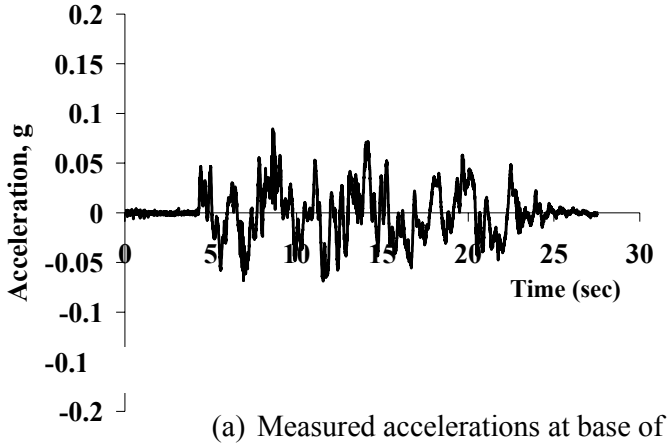

(a) Measured accelerations at base of clay layer *(Accelerometer A1)*

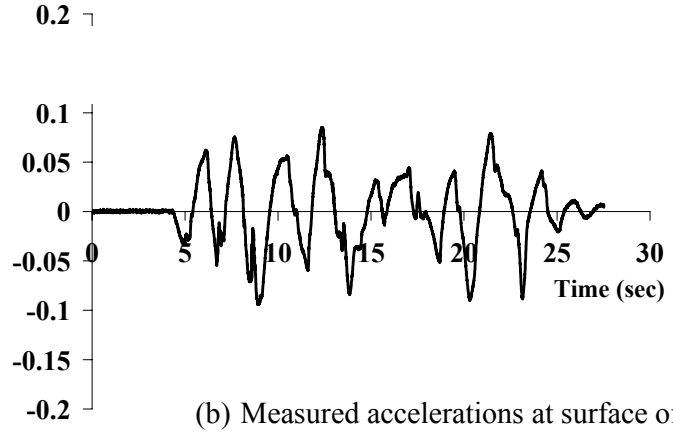

(b) Measured accelerations at surface of clay layer *(Accelerometer A3)*

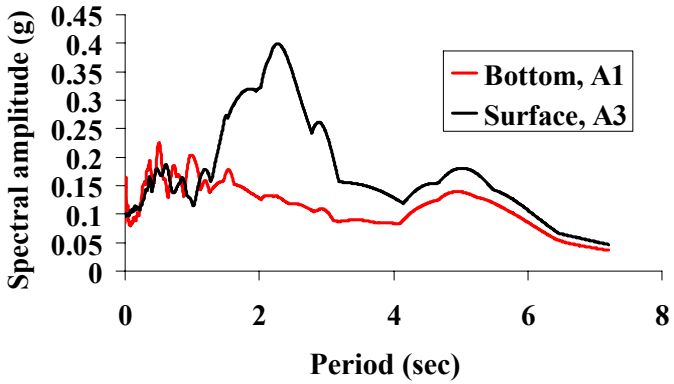

(c) Response spectra for the base and surface acceleration time histories

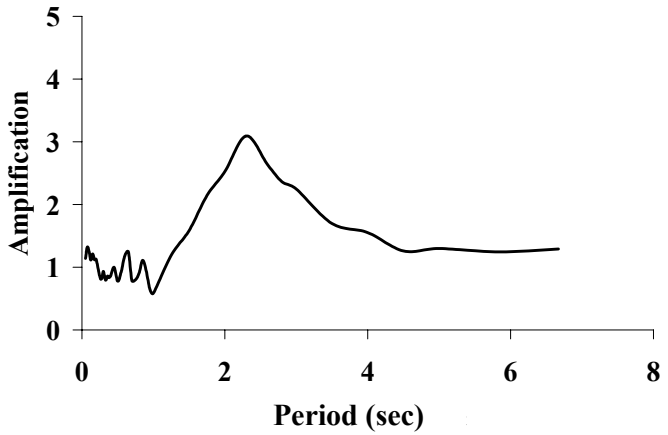

(d) Surface amplification response

Figure 4.17 Time histories, response spectra and amplification for large earthquake, second cycle

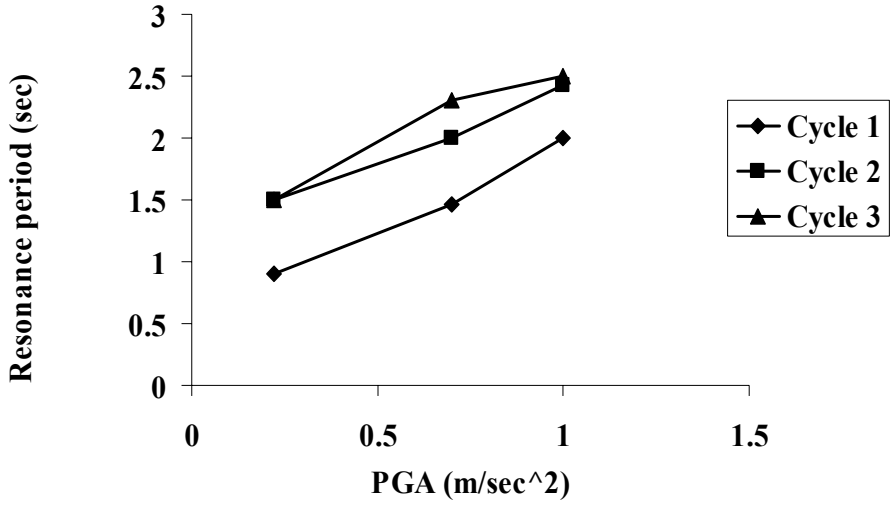

Figure 4.18 Resonance periods of the measured surface ground motions associated with different input peak ground accelerations for the 9 Events over three earthquake cycles

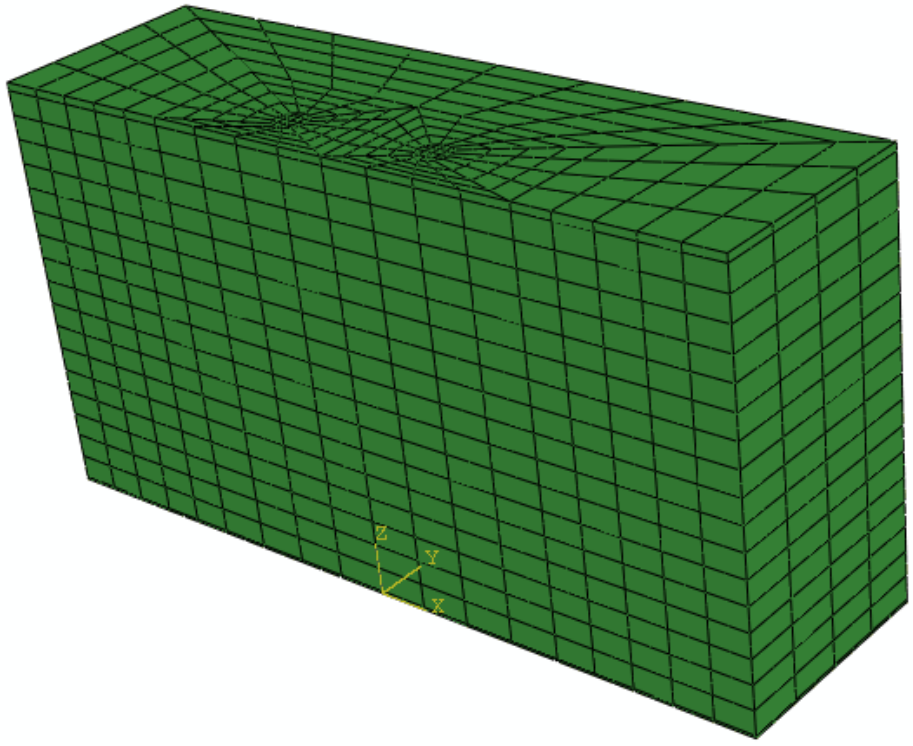

Figure 4.19 ABAQUS half-model of the centrifuge clay-bed tests

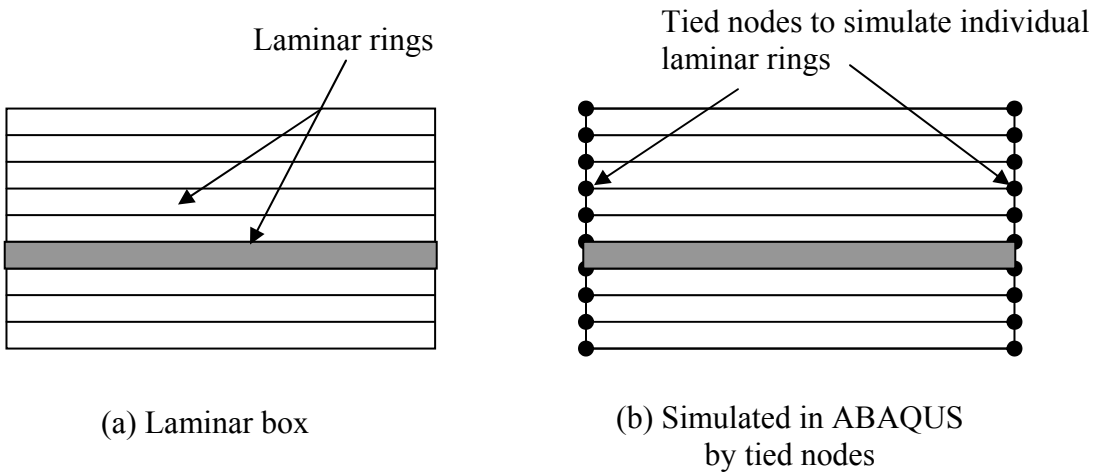

Figure 4.20 Modeling of laminar box motion in the ABAQUS finite element analyses

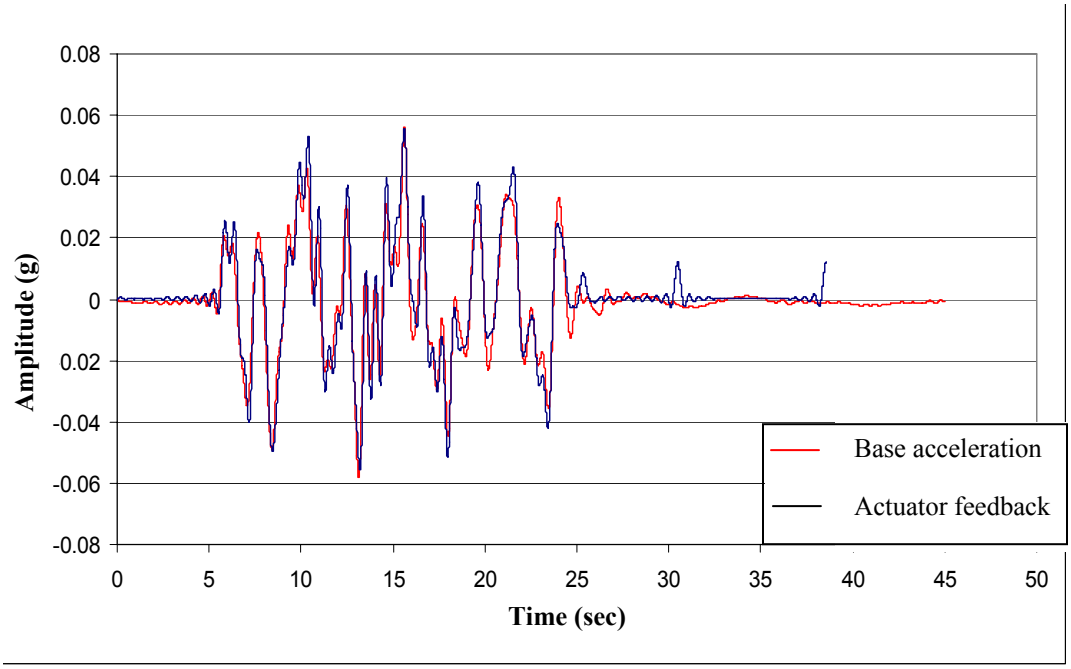

Figure 4.21 Comparison of feedback from the actuator and base acceleration

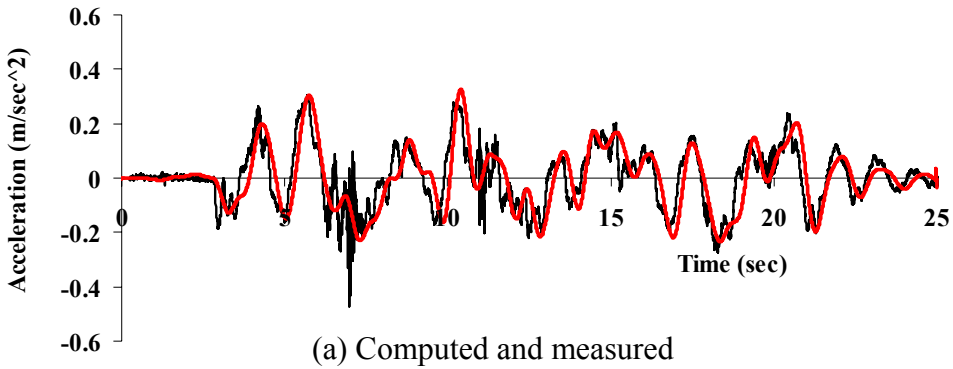

(a) Computed and measured accelerations at Mid-depth of Clay Layer (A2)

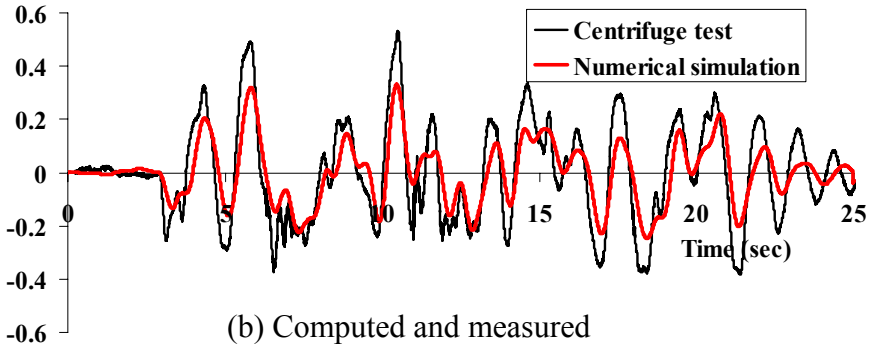

(b) Computed and measured response spectra at Mid-depth of Clay Layer (A2)

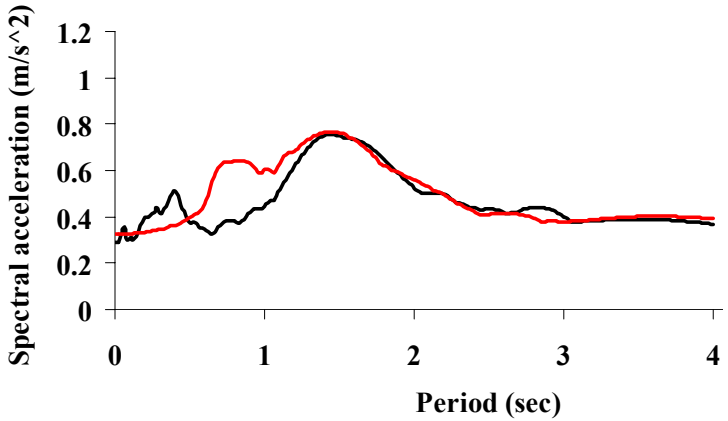

(c) Computed and measured accelerations at Surface (A3)

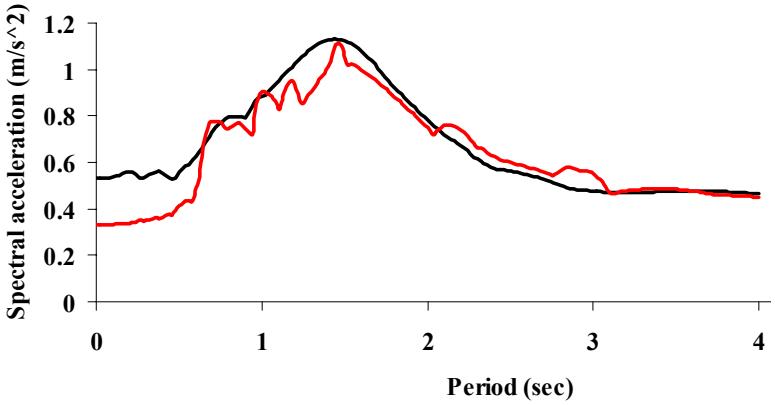

(d) Computed and measured response spectra at Surface (A3)

Figure 4.22 Comparison of typical ground response recorded in centrifuge tests with the results from numerical simulations

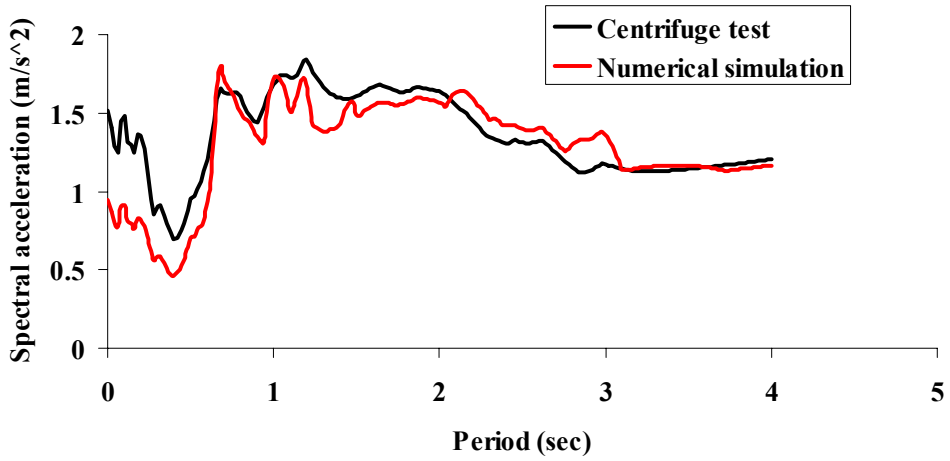

Figure 4.23 Comparison of measured and computed surface amplification response

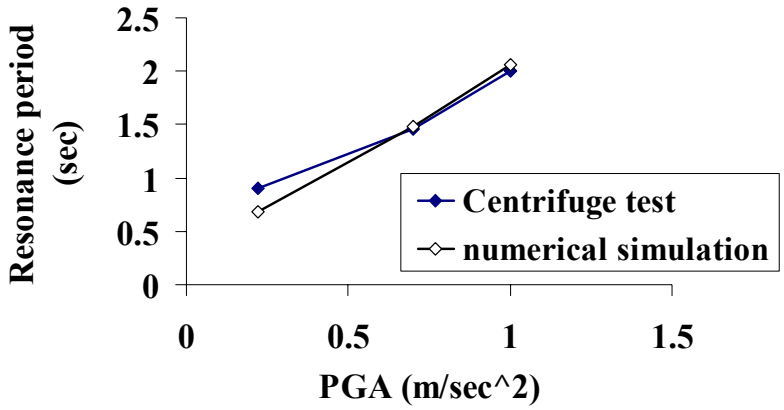

Figure 4.24 Resonance period of the surface ground motion associated with different peak ground acceleration applied at the base.

CHAPTER 5 CENTRIFUGE MODELLING OF SEISMIC SOIL-PILE-RAFT INTERACTION AND ITS NUMERICAL BACK ANALYSES

5.1 Introduction

In the preceding chapters, it was observed that the stress-strain behaviour of a clay was affected in two main ways under the action of cyclic and/or earthquake loadings. Firstly, there was progressive modulus degradation with increasing strain within the loading, unloading and reloading phase of each cycle, resulting in a nonlinear, hysteretic backbone curve. Secondly, there was progressive degradation of the backbone curve with repeated or cyclic loading. For the clay bed models studied in Chapter 4, these effects resulted in the lengthening of the resonance period of the clay layer from small to medium to large earthquake. Additionally, while travelling through the soft clay layer, all three input base excitations, that is, small, medium and large, were found to be amplified. In this chapter, the response of a pile-raft system embedded in soft clay under earthquake loading will be investigated. In the discussion below, prototype-equivalent dimensions will be used unless otherwise stated.

In the present study, centrifuge tests were conducted using three different types of piles. These were to simulate prototype piles of the following:

a) solid stainless steel pile of diameter 0.9 m,

b) hollow stainless steel pile of outer diameter 0.9 m and thickness 50 mm, and c) stainless steel pile of outer diameter 0.9 m and thickness 50 mm with concrete in-fill. The flexural rigidities of the different piles are given in Table 5.1.

Figure 5.1 shows the test layout and prototype dimensions of the centrifuge soil-pile-raft model. The raft, with prototype dimensions of 12.5 m × 7.5 m ×0.5 m, was supported on four piles, each with a prototype diameter of 0.9 m and a length L of 13 m. The pile-to-pile spacing, s, was chosen so that the s/d ratios are approximately 11 in the direction of shaking and 6 in the direction normal to the shaking, in order to minimize the interaction between piles within the space constraints of the model container. In the centrifuge tests, the pile-raft system was modeled using four 1.8 cm diameter and 26 cm long (model dimensions) bars, connected to a rigid steel plate of model dimensions 25 cm× 15 cm×1 cm. The raft was partially embedded in the ground so that there was direct contact between raft and soil. This is a commonly used foundation system for soft clays in Singapore.

The masses due to superstructural mass were simulated by adding steel plates on top of the base plate (raft), as shown on Figure 5.2. These plates, each weighing 1.9 kg, were added in two stages, up to a total of 6 plates. Under 50-g conditions, the equivalent prototype masses associated with the different added plate masses are summarized in Table 5.2. The maximum vertical load on the raft was selected to ensure that there was a factor of safety of at least 2.5 against structural pile failure.

The input earthquake motions considered in this study are the same as those described in the previous chapter (Sec. 4.6). Figure 4.11 showed the displacement time histories used as the prescribed base motion for the centrifuge tests. In each centrifuge experiment, the model was subjected to six earthquake events over two cycles. Each cycle comprised a small, a medium and a large earthquake that were actuated sequentially.

In this study, the centrifuge tests were carried out to study the effect of different pile types and added masses over two cycles of the small, medium and large earthquakes. A summary of all the tests is provided on Table 5.3.

Four accelerometers were used in each experiment, the locations of which are shown on Figure 5.1. Accelerometers A1 and A2 were placed in the clay near the bottom of the laminar box and at the mid-depth of the clay layer, respectively. Accelerometer A3 was located at the surface of the clay layer, while A4 was installed on the raft.

Apart from accelerations, the flexural response of piles is also an important design consideration. To measure the bending moment arising from seismic soil-pile interaction, strain gauges were installed at five levels along the length of an instrumented pile (Figure 5.3a). The strain gauges, labeled S1 to S5, are spaced 50 mm apart in the model scale. S1 is about 35 mm from the pile head, and S5 is 15 mm from the tip of the pile. The pile was coated with a protective layer of epoxy to prevent water leakage and possible short-circuiting. The response from the strain gauges was recorded in terms of volts in a 12-bit Data Acquisition System. The piles were pre-calibrated by fixing the pile-raft system on a rigid platform as shown in Figure 5.3b. Assuming a

cantilever-type condition, the bending moments, induced by different dead weights hanged at the tip, were calculated at different points along the pile and subsequently correlated with the strain gauge response in volts as shown in Figure 5.3c. The fitted relationship between bending moments in kNm and electrical signal (V) could be found as,

$$\text{Bending moment (kNm)} = 8.215 \times \text{Reading (Volt)} \qquad (5.1)$$

Eq. 5.1 had a quite satisfactory R^2 value of 0.9472. It was then used as the calibration factor for the strain gauges to convert readings in volt to bending moments. The calibration was done up to 3rd order decimal places. Hence the computed bending moments were also believed to be accurate up to 3rd order decimal places.

The accuracy of the sensors also depends on the accuracy of the data acquisition system. The 12-Byte data acquisition system with voltage range of +/- 10V has an accuracy of 2.441×10^{-3} Volt/bit. Hence from the correlation with bending moment (kNm) it translates into a accuracy of 2×10^{-2} kNm/bit. Similarly from calibration factor of accelerometers, the accuracy can be estimated as 2.441g/bits.

5.2 Centrifuge Tests Results

5.2.1 Acceleration Response of Clay-Pile-Raft System

Figure 5.4 shows the time histories recorded by different accelerometers from a small earthquake event generated in the centrifuge. For this experiment, solid stainless steel piles were attached to the raft (or base plate), on which three steel plates were attached to provide the added mass.

The recorded time histories correspond to the measured accelerations at the base (A1), mid-depth (A2) and surface of the clay layer (A3), as well as those measured at the top of the raft (A4). By comparing the A2, A3 and A4 peak ground accelerations with those of A1, it is clear that amplification of ground motion occurred in both the clay and the structure as the seismic waves propagate upwards. Moreover, the recorded time histories indicated that the soil-pile-raft system also helped to filter out the higher frequency components that were present in the input signal recorded by A1. However, despite being at the same elevation, there are differences noted between the A3 (clay) and A4 (raft) acceleration histories, which suggest that the raft does not move in tandem with the ground. This will be further examined below.

Figure 5.5 (a) shows the response spectra for the A1, A3 and A4 time histories. The response spectrum for A1, at the bottom of the clay layer, is similar to that obtained for the clay bed model without any piles present (Section 4.7, Figure 4.16). At the surface, the response spectrum for A3, which measures accelerations in the clay adjacent to the raft (3 m distance in prototype), shows a resonance period of about 1.84 sec. This is significantly higher than the resonance period of 1.0 sec at the ground surface for the corresponding earthquake in the clay bed model without the pile-raft system (Figure 4.16).

The response spectrum for A4, as shown on Figure 5.5a, indicates that the resonance period at the surface of the embedded raft is about 1.64 sec. This is about 0.2 sec lower than that measured in the adjacent soil. The difference in the measured resonance period between the soil and the structure

provides another indicator, besides the time history plots, that the soil motion may not be representative of the raft motion, that is, the two do not necessarily move in tandem. This suggests that there is interaction between pile and soil.

Additionally, a series of centrifuge tests done on the pile-raft structure (Figure 5.6), in the absence of any soil. To secure the pile-raft from sliding during the shaking events, the pile tips were rigidly fixed at the bottom of the container. The measured resonance periods of the structure are found to be 0.98, 1.14 and 1.22 sec for the solid, hollow and concrete in-fill piles, respectively. These values are considerably smaller than the resonance period associated with the response spectrum of A4, which is for the pile raft with the surrounding soil in place. The results suggest that the surrounding soil imposes an additional inertial load onto the piles, which results in an increase in the natural period of the pile-raft system.

Figure 5.5b shows the spectral amplification responses corresponding to the A3 and A4 acceleration histories, which indicate that the maximum amplification is higher in the raft (about 4.75) than in the clay (about 3.23). As shown in Section 3.5.1.4 (Figure 3.37) this is due to the fact that, at a given shear strain, the damping ratio decreases with the increase in stiffness. Therefore the damping ratio of the steel raft, which is much stiffer than the surrounding soil, is considerably lower compared to the soft kaolin clay.

5.2.2 Resonance Periods of Different Pile Systems and Super-structure Masses

As mentioned earlier, three different pile types were considered in this study. Figure 5.7 summarizes, for the three earthquakes, the resonance periods of the three pile types for different added masses on the pile raft in the 1st cycle. The results indicate that the resonance period of a pile-raft system increases when it is more heavily loaded. This is to be expected, since the additional plate loads increases the inertia of the pile-raft system. Figure 5.7 also shows that the hollow piles generally have the largest resonance period, which is not surprising given that it possesses the smallest flexural rigidity among the different pile types. The said difference is most prominent at small to medium earthquakes. However, in all cases, the measured resonance periods are much higher than the natural periods of the pile-raft system in the absence of any soil mentioned in Section 5.2.1.

In a similar way, Figure 5.8 plots the resonance periods at the clay surface (adjacent to the raft) for different levels of added masses. By comparing with Figure 5.7, it is clear that, in almost all cases, the resonance periods in the adjacent clay are higher than those calculated for the embedded pile-raft, which in turn are higher than that of the pile raft without any soil. As discussed earlier, this indicates that the soil and the pile-raft do not move in tandem. It also indicates that the effect of the soil around the pile is predominantly one of imposing additional inertial loading on the pile-raft structure. As shown in Figure 5.8, the type of piles has little effect on the

resonance period of the adjacent soil although there seems to be a slight increase in period for large earthquake on the heavily loaded raft.

The data of Figure 5.8 are re-plotted in Figure 5.9 to show how the resonance periods of the adjacent clay vary with peak ground acceleration (PGA), for different pile types and added masses on the raft. As can be seen, in each case, the soil surface adjacent to the pile group shows a significant increase in the resonance period with PGA. In addition, the resonance period further increases with the second cycle of earthquake loadings. The trend is similar to that shown on Figure 4.16.

Comparison of Figure 5.9 with Figure 4.16 shows that resonance period of the clay around the structure increases much more significantly with peak ground acceleration than that of the clay bed without structure. This may be caused by the relative motion between the pile, raft and soil, leading to the development of shear strains in the clay. The magnitude of such shear strains may be quite large in the pile-raft vicinity, especially for larger earthquakes with stronger ground motions. This in turn results in significant strain softening and stiffness degradation of the clay, as reflected in the increase in the resonance period of the ground around the structure compared to that of the pure clay bed. Previous field studies involving quasi-static pile load tests (Snyder, 2004) have shown that the presence of piles will cause significant stiffness degradation of the clay, especially in the vicinity of the piles.

5.2.3 Amplification

Figure 5.10 summarizes, for the three added masses, the amplification of ground motion at the clay surface during the first cycle of three earthquakes. The results indicate a progressive reduction in amplification from the small to medium to large earthquake, which may be explained by the increase in damping in the soil with strain amplitude. This is consistent with the fact that successive earthquakes of greater magnitude subject the soil to increasingly large shear strains which, as discussed in Section 3.4.2.1, increases the damping ratio in the soil. A similar trend has also been reported by Yu and Lee (2002).

Figure 5.11 compares the amplification response between for the first and second cycles of earthquake loading, for the solid piles with different added masses on the raft. For all the added masses, the amplification during the second cycle is significantly lower than the first cycle. Again, this can be attributed to the increase in material damping over the two cycles of earthquakes. Similar observations can be made for other two types of piles as well.

As shown on Figure 5.12, there is no obvious trend on how the PGA affects the amplification response of the raft. Successive cycles of earthquake loading also do not appear to affect the amplification response of the raft. In all cases, the raft supported on solid stainless steel piles experienced the largest amplification.

5.2.4 Bending Moment Response of Pile

The bending moments along the pile were measured using strain gauges mounted at different locations along the pile length, as shown on Figures 5.1 and 5.3. Figure 5.13 shows a typical set of bending moment time histories obtained for a small earthquake. In this particular case, no added masses were placed on the raft. Figure 5.13 shows that the largest bending moments were recorded at location S1, which is 1.75 m below the base of the raft. This observation is consistent with the pile being subjected to a fix-headed connection between the pile top and the raft, while the pile-tip is lightly embedded in a thin layer of sand underlying the clay. Hence, the largest moments are expected to develop near the pile head, and progressively reduce along the pile length.

From the design aspect, it is useful to obtain the maximum bending moment envelope along the pile length. To identify the maximum bending moments at each location and the time at which they occur, all the time histories were plotted together on Figure 5.14 . It is observed that, for all five levels, the maximum bending moments occur approximately at the same time of 6.82~6.84 secs. The respective magnitudes of the maximum moment were then plotted against the pile length (Figure 5.15). The resulting envelope shows that the maximum moment occurs near the pile head, and reduces along the pile length. At a depth of about 7.5 m (or about 8.4D), the moment envelope becomes negative. At the strain gauge location near the pile tip (S5), the maximum bending moment reaches its largest negative value, although this is still much smaller than the positive value near the fixed pile head. The

negative moment at the lower segment of the pile suggests that below this depth, the restraining effect of the soil on the pile becomes significant.

5.2.4.1 Effect of Different Earthquakes

Figure 5.16 shows the maximum bending moment envelopes for the concrete in-fill pile for the small, medium and large events of the first cycle of earthquake loadings. For all three earthquakes, no added masses were placed on the raft. The results clearly indicate that the bending moment near the pile head (S1) increases from the small, medium to large earthquake. The increase is not very significant at the intermediate locations (S2, S3 and S4). Near the pile tip (S5), the maximum negative moment again shows a similar increasing trend with increasing earthquake magnitude.

Figure 5.17 shows the maximum bending moment envelope plotted against the peak ground acceleration, for each strain gauge location. The results indicate that the effect of increasing earthquake magnitude is significant near the fixed end (S1), where the moment magnitude increases roughly linearly with the increase in peak ground acceleration.

Figure 5.18 plots the maximum bending moment envelopes for both the first and second cycles of earthquake loadings. In all cases, the bending moments did not change significantly between the first and second cycle of earthquake loadings. This suggests that the maximum bending moment in a fix-headed pile is predominantly governed by the flexural rigidity of the pile-raft system, and that the cyclic degradation of the backbone curve does not significantly affect the moment response.

5.2.4.2 Effect of Different Added Masses

Figure 5.19 shows how the maximum bending moment envelopes of concrete in-fill piles vary with the different levels of added masses, for the small, medium and large earthquakes. For all three earthquakes, the maximum bending moment increases with the added masses, the effect being more significant for the medium and large earthquakes.

Figure 5.19 is now normalized by the respective maximum moment of the smallest load case (368 tonne in prototype) to Figure 5.20. Again, Figure 5.20 shows that, for medium and large earthquakes, there are significant increase in the maximum bending moments with the added mass. However, the increments in the maximum moment are not in proportion. Hence the raft with 6 plates attached produced the largest bending moments in all cases. The results suggest that super-structural or building loads may play a key role in affecting seismic lateral pile response, especially during large earthquakes.

Figure 5.21 shows the variation of the maximum bending moments near the pile head (S1) with added mass on the pile raft, for the small, medium and large earthquakes. The bending moment at this location increases very sharply with the added masses for the medium and large earthquakes, while the effect is not that significant for the small earthquake.

5.2.4.3 Effect of Different Pile Material

The bending moment envelopes for the small, medium and large earthquakes under different levels of added masses are shown on Figure 5.22 for the three pile types. The results indicate that the solid steel piles developed

the largest bending moment, which is due to its higher flexural rigidity compared to the other two pile types. This is consistent with the trends shown on the Tabesh and Poulos (2007) design charts for the seismic analysis of piles. Overall, the results and trends shown on Figure 5.22 indicate that, for each pile type, the maximum bending moment envelopes generally increase with the level of added masses and the earthquake magnitude.

Figure 5.23 plots the maximum bending moment near the pile head (S1) versus the pile flexural rigidity (EI) for the small, medium and large earthquakes, for different levels of added masses. The results indicate that, for any given added mass, the maximum bending moments appear to increase almost linearly with the pile flexural rigidity.

5.3 Numerical Analysis of Seismic Soil-Pile Interaction

In this section, three-dimensional finite element analyses will be carried out to back-analyze the measured pile-raft and soil responses obtained from the centrifuge experiments. As in Chapter 4, these analyses will be carried out using ABAQUS v6.8.

By considering geometrical and loading symmetry, it is possible to simulate the soil-pile-raft system in the centrifuge experiment using a half-model. The model was discretized using 20-noded brick elements, as shown on Figure 5.24, resulting in 20765 nodes and 4720 elements. The brick elements associated with the piles were chosen as "Reduced integration-type" to avoid probable shear locking. The boundary conditions, including the linear

multi-point constraints similar to those discussed in Section 4.8 and shown on Figure 4.18, were prescribed to simulate one-dimensional shaking.

The input parameters for the hyperbolic-hysteretic soil model (HyperMas) are also identical to those adopted in Chapter 4 for the kaolin clay bed without structure (Section 4.8.1). The flexural rigidities are shown on Table 5.1 for the different pile types. The earthquake input motion was applied at the bottom of the model. The computed acceleration time histories were tracked at the locations where accelerometers were placed in the centrifuge tests (Figure 5.1).

In addition to the acceleration responses, it is required to compute bending moments along the pile length. As the piles were modeled using solid elements, the bending moments could not be directly obtained from the ABAQUS output. This limitation may be overcome by adding a column of very flexible beam elements along the discretized pile axis, as shown on Figure 5.25. The flexural rigidity of these elements may be prescribed a value obtained by scaling down the actual pile stiffness by a factor of 10^6, so that they will freely adopt the deformed pile shape without interfering with its structural response. In this way, the bending moments along the actual pile may be obtained by simply multiplying the computed beam moments by the same scaling factor of 10^6. The flexible beams are modeled using 3-noded quadratic space beam elements. The total number of nodes and elements along each beam are 57 and 19 respectively.

5.3.1 Effect of Joint Flexibility

In the pile-raft, the piles are connected to the raft via a through bolt system. This connection may have a certain degree of flexibility which needs to be characterized. To investigate this issue, the pile-raft system was fixed on a rigid platform to simulate a cantilever-type condition as shown in Figure 5.26. The dead weights were gradually hanged at the tip of pile and the resulting deflection at the tip was measured by the attached dial gauge.

Theoretically, deflection at the tip is given by,

$$d_{max}=\frac{Pl^3}{3EI}, \tag{5.2}$$

where, P is the weight attached at the tip of cantilever

l is the length of the cantilever arm

EI is the flexural rigidity of the cantilever

Equation 5.2 can be written as,

$$\frac{d_{max}}{l}=\frac{Pl^2}{3EI} \tag{5.3}$$

For a case where the end support of the cantilever is not perfectly rigid, assuming the principal of superposition is valid for structural members Equation 5.3 can be generalized to,

$$\frac{d_{max}}{l}=\frac{Pl^2}{3EI}+\theta \tag{5.4}$$

where, θ is the angle of rotation of the flexible joint (Figure 5.26b).

Now θ can be expressed as,

$$\theta=\frac{Pl}{k_\theta} \tag{5.5}$$

where k_θ is the equivalent angular rigidity at the flexible joint.

Hence from equation 5.4 and 5.5,

$$\frac{d_{\max}}{l} = \frac{Pl^2}{3EI} + \frac{Pl}{k_\theta} \tag{5.6a}$$

$$\text{or, } \frac{d_{\max}}{Pl} = \frac{l^2}{3EI} + \frac{l}{k_\theta} \tag{5.6b}$$

Hence for perfectly rigid joint, $k_\theta \sim \infty$,

$$\frac{d_{\max}}{Pl} = \frac{l^2}{3EI} \tag{5.7}$$

Hence from equation 5.6 and 5.7,

$$\left(\frac{d_{\max}}{Pl}\right)_{rigid} - \left(\frac{d_{\max}}{Pl}\right)_{flexible} = \frac{l}{k_\theta} \tag{5.8}$$

Figure 5.27 shows the plot of $\frac{d_{\max}}{Pl}$ vs $\frac{l^2}{3EI}$ for the theoretical and observed tip deflection. The results suggest that the observed deflections were higher compared to the theoretical values for perfectly rigid case and an average $\frac{l}{k_\theta}$ can be computed as,

$$\frac{l}{k_\theta} \approx 0.001$$

For l=0.26m, k_θ=260 kN-m

Now, considering the joint flexibility as shown, a 3-D finite element model of the pile-raft structure (Figure 5.28), in the absence of any soil, was set up and analyzed using ABAQUS v6.8. The computed resonance periods of the structure were found to be 0.99, 1.10 and 1.16 sec for the solid, hollow

and concrete in-fill piles, respectively. These values are quite close to the centrifuge results mentioned in Section 5.2.1 .

Hence, for the soil-pile model (Figure 5.24), the flexibility of joints seems to be small and do not play a major role. Figure 5.29 describes the pile bending moment results with and without considering joint flexibility. The analysis shows almost identical results. This may be due to the presence of soil around pile-raft connection.

5.3.2 Comparison of Centrifuge and FEM Results: Acceleration Responses

Figure 5.30 (a) and (c) plot the measured vs computed time histories at (i) the top of pile raft, corresponding to accelerometer A4 and (ii) the clay surface, corresponding to accelerometer A3 for small earthquake. The pile under consideration is solid steel, with three added masses. Despite some discrepancies, the computed responses provide generally good fits to the measured accelerations at both locations, and are able to capture the maximum values quite well.

As Figures 5.30 (b) and (d) show, the agreement between the computed and the measured raft and ground surface response also shows good general agreement. However, the computed raft response shows a local peak around 0.8sec period, which is likely to be due to raft resonance. The main resonance period, on the other hand, is similar to that shown by the clay and is likely to be due to inertial loading from the clay. In particular, the resonance period (as discussed in 4.7.1) and the maximum amplification of both the clay

and the raft are reasonably well replicated in the numerical analyses, as shown on Figure 5.31. The computed results also indicate that both the clay and pile-raft structures are not moving in unison.

The 3-D finite element analyses were carried out for all the centrifuge tests discussed in the previous sections, covering the small, medium and large earthquakes, different added masses and different pile types. The computed resonance periods of the raft are plotted on Figure 5.32 for different added masses. It is observed that the numerical results reflect the experimental trends (discussed and shown earlier on Figure 5.7, Section 5.2.2) quite well. Figure 5.33 shows the corresponding trends computed at the surface of the clay layer adjacent to the raft, for different levels of added masses. The computed trends are also similar to those obtained from the centrifuge experiments (discussed and shown earlier on Figure 5.8, Section 5.2.2).

In Figure 5.34, the computed resonance periods at clay surface are plotted against the peak ground accelerations for the three levels of added masses. The trend is reasonably similar to that shown on Figure 5.9 of Section 5.2.2

Figure 5.35 shows the computed amplification at the clay surface, plotted against the peak ground accelerations, for different levels of added masses. The decrease in amplification with increasing earthquake magnitude is consistent with the earlier postulate that larger shear strains develop with stronger ground motion, which in turn leads to larger damping ratio.

5.3.3 Comparison of Centrifuge and FEM Results: Bending Moment

Figure 5.36 plots the measured and computed bending moment time histories at the five levels where strain gauges were mounted on the pile. The pile under consideration is concrete in-filled, with no added masses. Despite some discrepancies towards the later part of the time histories, the measured maximum moment at location S1 (near the pile raft) at time ≈ 7 secs is reasonably well predicted by the numerical results.

Figure 5.37 plots the computed maximum moment envelope along the pile length, together with the centrifuge measurements at the five strain gauge locations. . Both the measured and computed results show maximum moment just below the pile-raft connection and a reverse minima near the pile tip. In contrast to lateral loadings applied at the raft, significant bending moments persists almost right down to the tips of the piles. Thus, earthquake loadings may cause significantly different bending moment profiles in the piles from lateral loads on the raft.

Figure 5.38 plots the computed versus measured maximum moment envelopes for the small, medium and large earthquakes. In all cases, the maxima is well-replicated. However, there is significant differences in the magnitude of the minima with the computed results consistently over-predicting the measured results.

Figure 5.39 plots the maximum moment envelopes for different added masses, corresponding to the small, medium and large earthquakes (similar to Figure 5.19, Section 5.2.4.2). In all cases, the maxima are reasonably well-captured. For the small earthquakes and the largest added mass, the minimas

are also reasonably captured. For other cases, the magnitude of the minima appears to be over-predicted. This is attributable to the rocking of the piles about their tips which may occur under conditions of large earthquake, especially when the overburden load on the piles is low. This issue will further be investigated in the next section.

The computed and measured maximum moment envelopes for different pile types are shown on Figure 5.40. For the most part, there is good agreement between the numerical and measured responses. The largest computed moments are obtained in the solid stainless steel piles, which is consistent with the measured centrifuge trends. However, once again the magnitudes of the minima are over-predicted.

5.3.4 Pile Tip Fixity Issue

As can be seen in Figure 5.30, although the time history is replicated reasonably by the analysis, the computed raft motion seems to possess a significant amount of a higher harmonic, showing a local peak around 0.8sec period (Figure 5.30 b). Similarly, in Figure 5.36, the bending moment history also indicates presence of some higher harmonics. The response spectra of the bending moment, shown in Figure 5.41, also shows a local peak around 0.7~0.8 sec. In addition to these, Figures 5.39 and 5.40 show that, although the maxima of the moment envelope was well-predicted, the magnitude of the minima is grossly over-predicted.

Investigation showed that these are due to the way in which the bottom sand layer was modelled. In the initial analysis, the layer was modelled as an

elastic material since it is unlikely to yield under the applied shaking intensity. However, the stress concentration around the pile tip may be sufficiently high to cause local yielding when the pile rocks and sways during the earthquake event. This will not be modeled by an elastic sand layer which will over-predict the boundary constraint to the pile tip movement causing very large negative moment near the tip.

To study this, the sand was re-modelled as Mohr-Coulomb material. The angle of friction for dense sand is chosen as 35°. The pile under consideration is a solid steel pile, excited by small earthquake with no extra plate added on the raft. The Figure 5.42 and 5.43 indicate that the higher harmonics at the acceleration time history are now absent and the local peak in the response spectra also disappears. In addition, Figure 5.44 shows that much better agreement is also obtained for the bending moment profiles. The computed results show a significantly lower minima at the pile tip. There is an increase in the maxima of the bending moment profile, of not more than 10%. Figure 5.45 shows the comparison of measured and computed bending moment results for different earthquakes and added masses for solid piles. For comparison, the bending moment results for solid piles with elastic sand layer are also plotted in Figure 5.46. As Figures 5.45 and 5.46 show, by modelling the sand layer as a Mohr-Coulomb material, the agreement at the minima are substantially improved for all different earthquakes and added masses.

5.4 Concluding Remarks

The foregoing discussion shows that strain softening and stiffness degradation affect soft clay and pile-raft foundations in several ways. There are significant soil-structure effects which causes the resonance period of the ground motion and pile-raft structure to differ from their respective resonance periods. The results of the study show that the effect of the surrounding soil is largely one of imposing inertial loading onto the pile and raft. This leads to a lengthening of the resonance period of the pile-raft structure. The resonance period of the surrounding ground is also lower than that a corresponding clay bed with equal thickness but without pile-raft. This is attributed to the larger shear strains arising from the relative motion between pile, raft and soil.

For the pile response, the maximum bending moment is recorded near the relatively rigid connection between the pile and raft. The bending moment is found to increase almost linearly with the increase in peak ground acceleration. It is also observed that bending moment increases with the increase in flexural rigidity of pile material, as well as with increasing added masses on the raft.

From the numerical simulations, it can be inferred that the proposed hyperbolic-hysteresis soil model can be used to analyze complex 3D problems such as the seismic response of clay-pile-raft system. Although the model has some limitations in modeling real clay behaviour, it can capture pile bending moments reasonably well.

The engineering implication arising from this study is that, for the case of piles in soft clays, ground surface motions may not be representative of pile-raft motion. Furthermore, a pile in soft clay under earthquake excitation is likely to behave differently from the same pile loaded dynamically from the pile top. In the latter case, the soil around the pile has a restraining effect on it. In the former, the foregoing centrifuge test results show that the soil actually applies an inertial loading onto the pile. In view of this, it seems highly questionable as to whether conventional dynamic or cyclic pile load tests will shed any significant light on the response of such piles to earthquake loading. The test results, however, is only valid for relatively short and rigid piles rested on the hard base. More study needed on longer and more flexible piles with different end conditions such as socketed or floating types.

Table 5.1 Different piles used for the study

Pile material	Model flexural rigidity, kN-m^2	Prototype flexural rigidity , kN-m^2
Solid stainless steel	1.65	10308351
Hollow stainless steel	0.57	3545002
Hollow stainless steel filled with plain cement concrete	0.685	4285785

Table 5.2 Mass of the added plates

Added mass	Model mass, kg	Prototype mass, tonne
only base plate	2.95	368
base plate + 3 added plates	4.84	605
base plate +6 added plates	6.90	863

Table 5.3 Summary of test program for kaolin clay with pile

Test no.	Name	Cycle	Earthquake	Maximum acceleration produced	Pile type	Prototype load on the pile-raft, kN
1	SS10	1	Small	0.022g	Solid steel	3680
	SM10		Medium	0.07g	Solid steel	3680
	SL10		Large	0.1g	Solid steel	3680
	SS20	2	Small	0.022g	Solid steel	3680
	SM20		Medium	0.07g	Solid steel	3680
	SL20		Large	0.1g	Solid steel	3680
2	SS13	1	Small	0.022g	Solid steel	6050
	SM13		Medium	0.07g	Solid steel	6050
	SL13		Large	0.1g	Solid steel	6050
	SS23	2	Small	0.022g	Solid steel	6050
	SM23		Medium	0.07g	Solid steel	6050
	SL23		Large	0.1g	Solid steel	6050
3	SS17	1	Small	0.022g	Solid steel	8630
	SM17		Medium	0.07g	Solid steel	8630
	SL17		Large	0.1g	Solid steel	8630
	SS27	2	Small	0.022g	Solid steel	8630
	SM27		Medium	0.07g	Solid steel	8630
	SL27		Large	0.1g	Solid steel	8630
4	HS10	1	Small	0.022g	Hollow steel	3680
	HM10		Medium	0.07g	Hollow steel	3680
	HL10		Large	0.1g	Hollow steel	3680
	HS20	2	Small	0.022g	Hollow steel	3680
	HM20		Medium	0.07g	Hollow steel	3680
	HL20		Large	0.1g	Hollow steel	3680
5	HS13	1	Small	0.022g	Hollow steel	6050
	HM13		Medium	0.07g	Hollow steel	6050
	HL13		Large	0.1g	Hollow steel	6050
	HS23	2	Small	0.022g	Hollow steel	6050
	HM23		Medium	0.07g	Hollow steel	6050
	HL23		Large	0.1g	Hollow steel	6050
6	HS17	1	Small	0.022g	Hollow steel	8630
	HM17		Medium	0.07g	Hollow steel	8630
	HL17		Large	0.1g	Hollow steel	8630
	HS27	2	Small	0.022g	Hollow steel	8630
	HM27		Medium	0.07g	Hollow steel	8630
	HL27		Large	0.1g	Hollow steel	8630
7	CS10	1	Small	0.022g	Concrete in-fill	3680
	CM10		Medium	0.07g	Concrete in-fill	3680
	CL10		Large	0.1g	Concrete in-fill	3680
	CS20	2	Small	0.022g	Concrete in-fill	3680
	CM20		Medium	0.07g	Concrete in-fill	3680
	CL20		Large	0.1g	Concrete in-fill	3680
8	CS13	1	Small	0.022g	Concrete in-fill	6050
	CM13		Medium	0.07g	Concrete in-fill	6050
	CL13		Large	0.1g	Concrete in-fill	6050
	CS23	2	Small	0.022g	Concrete in-fill	6050
	CM23		Medium	0.07g	Concrete in-fill	6050
	CL23		Large	0.1g	Concrete in-fill	6050
9	CS17	1	Small	0.022g	Concrete in-fill	8630
	CM17		Medium	0.07g	Concrete in-fill	8630
	CL17		Large	0.1g	Concrete in-fill	8630
	CS27	2	Small	0.022g	Concrete in-fill	8630
	CM27		Medium	0.07g	Concrete in-fill	8630
	CL27		Large	0.1g	Concrete in-fill	8630

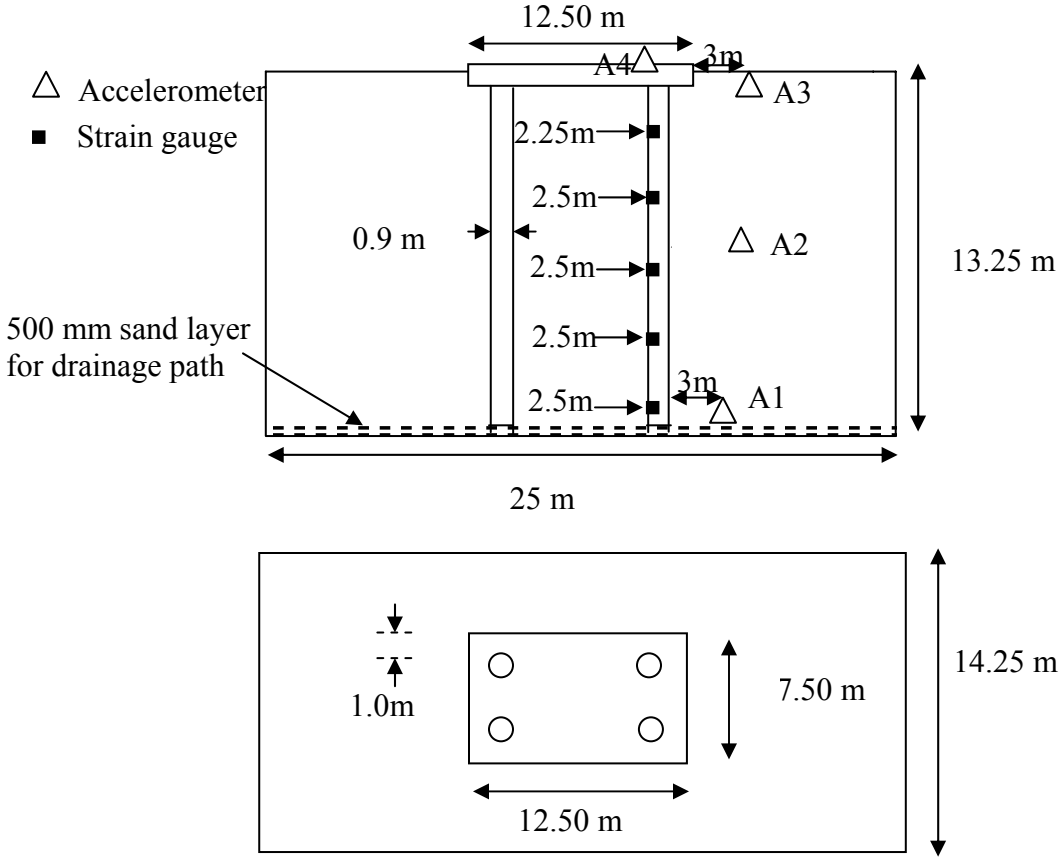

Figure 5.1 Centrifuge model views and instrumentation lay-out for tests with embedded pile-raft structure

Figure 5.2 Steel plates to simulate added masses

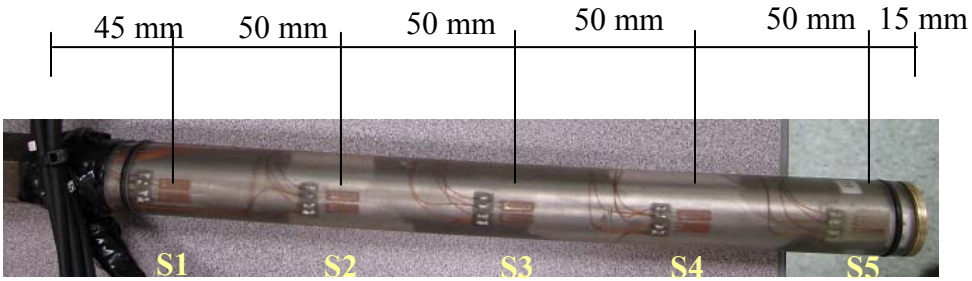

(a)

(b)

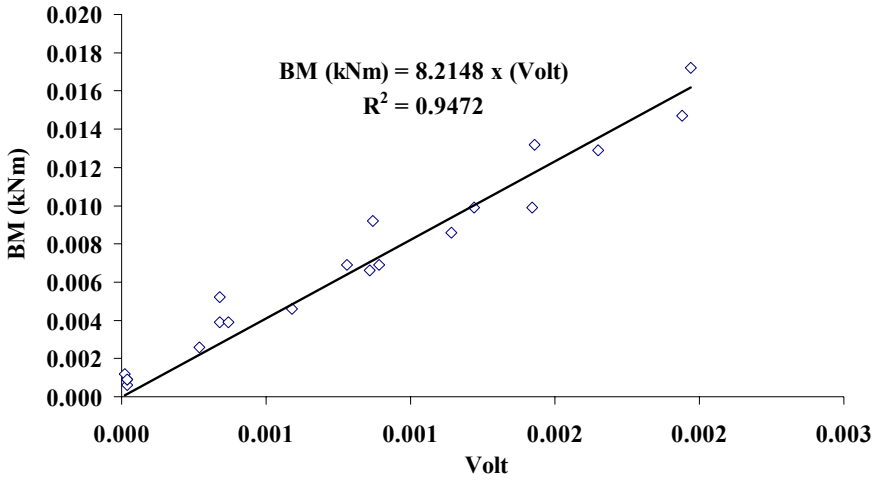

(c)

Figure 5.3 (a) Strain gauge positions on the instrumented pile, (b) Pile calibration set-up, and (c) Pile calibration result

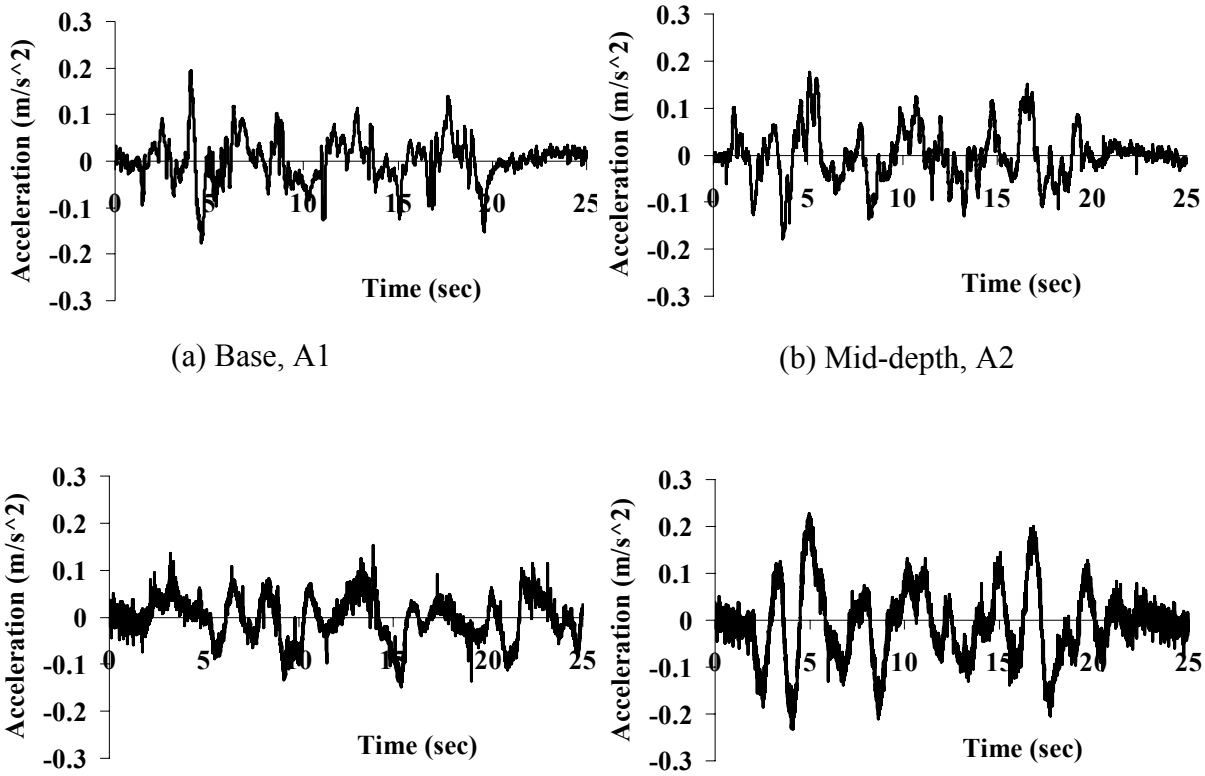

(a) Base, A1

(b) Mid-depth, A2

(c) Clay surface, A3

(d) Top of the Raft, A4

Figure 5.4 Typical acceleration time histories measured in test with pile-raft structure (small earthquake)

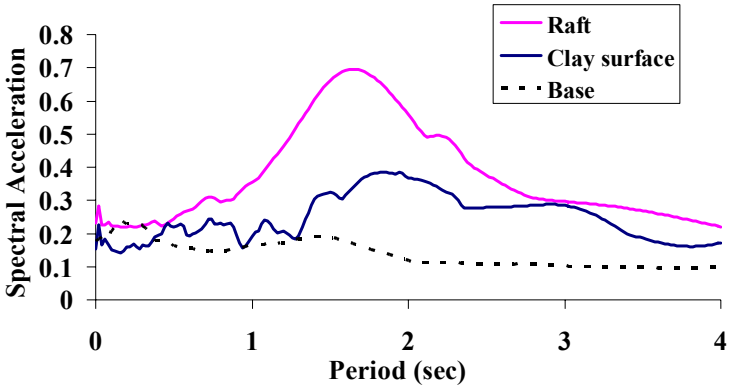

(a)

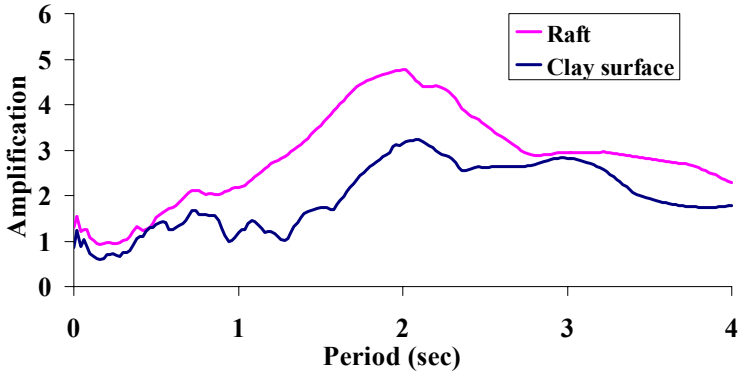

(b)

Figure 5.5 (a) Response spectra and (b) Amplification at clay surface (A3) and at top of the raft (A4) (small earthquake)

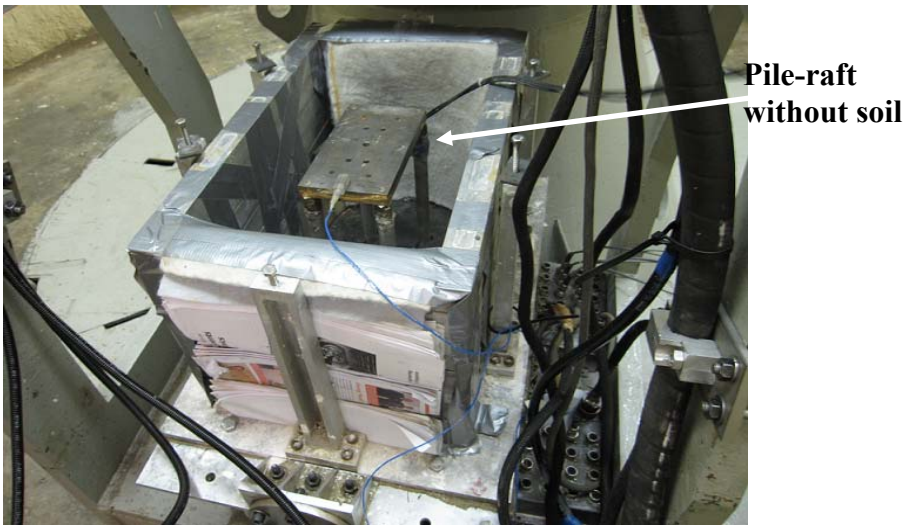

Figure 5.6 Centrifuge test of pile-raft structure without soil

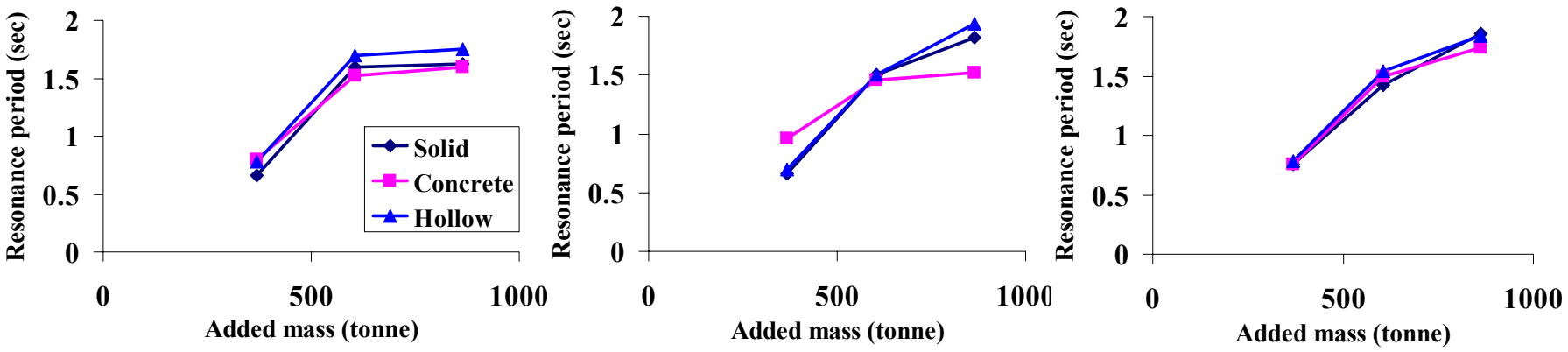

(a) Small earthquake (PGA=0.022g)

(b) Medium earthquake (PGA=0.07g)

(c) Large earthquake (PGA=0.1g)

Figure 5.7 Resonance period of the pile raft (A4) associated with a) Small, b) Medium and c) Large Earthquake

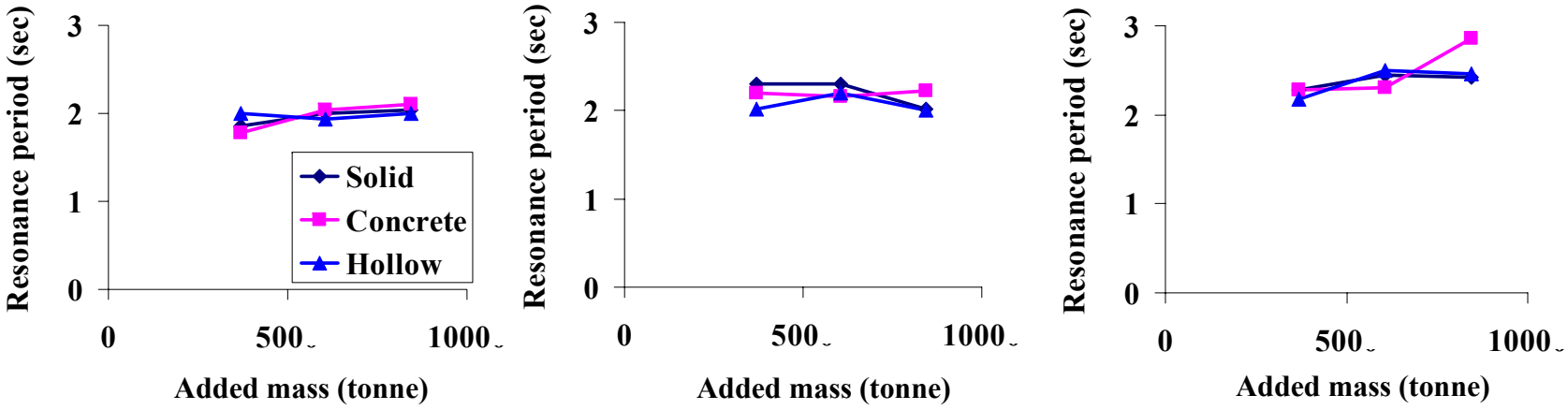

(a) Small earthquake (PGA=0.022g)

(b) Medium earthquake (PGA=0.07g)

(c) Large earthquake (PGA=0.1g)

Figure 5.8 Resonance period of the clay surface (A3) associated with a) Small, b) Medium and c) Large Earthquake

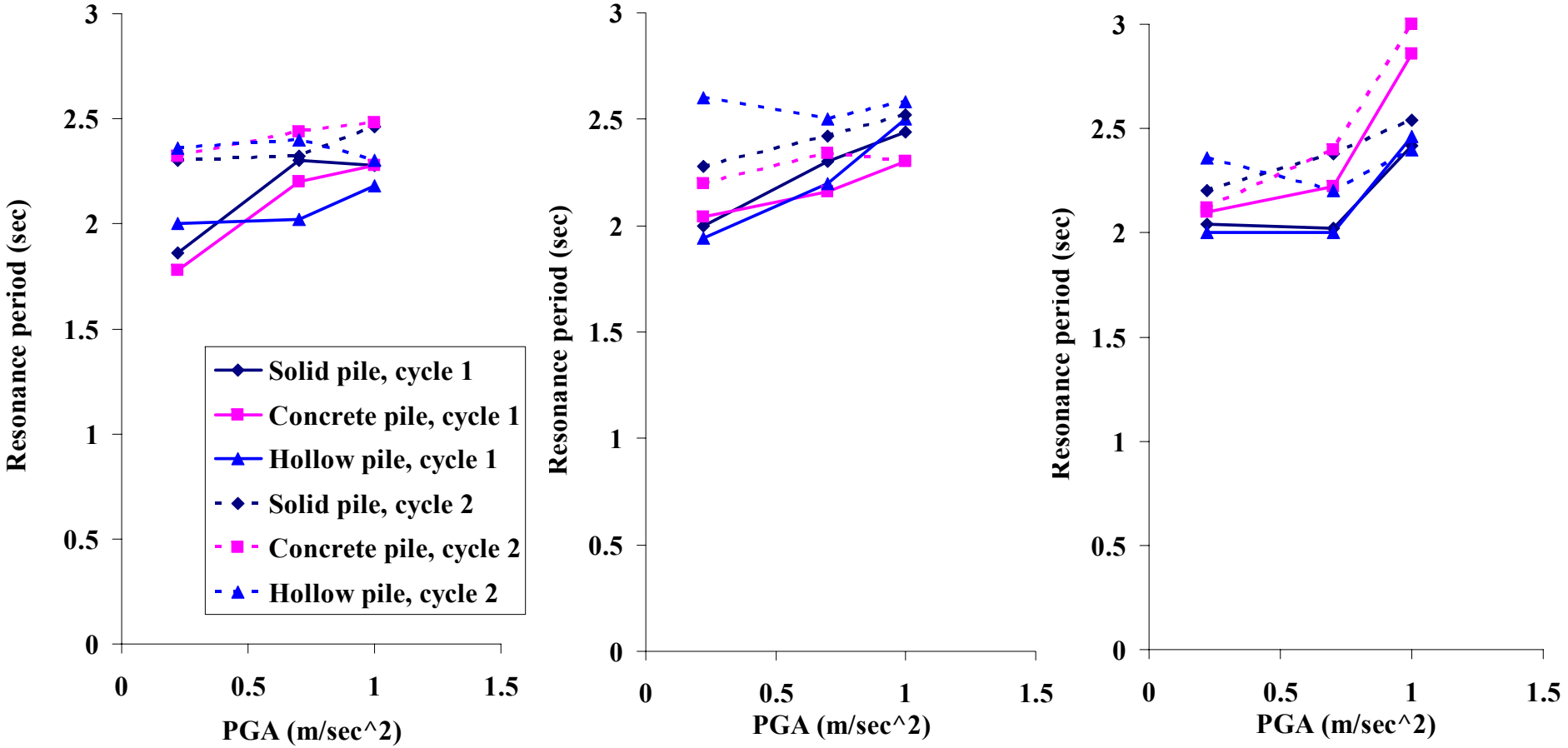

(a) Added mass = 368 tonne

(b) Added mass = 605 tonne

(c) Added mass = 863 tonne

Figure 5.9 Raft resonance periods derived from centrifuge tests for different peak ground accelerations and different added masses

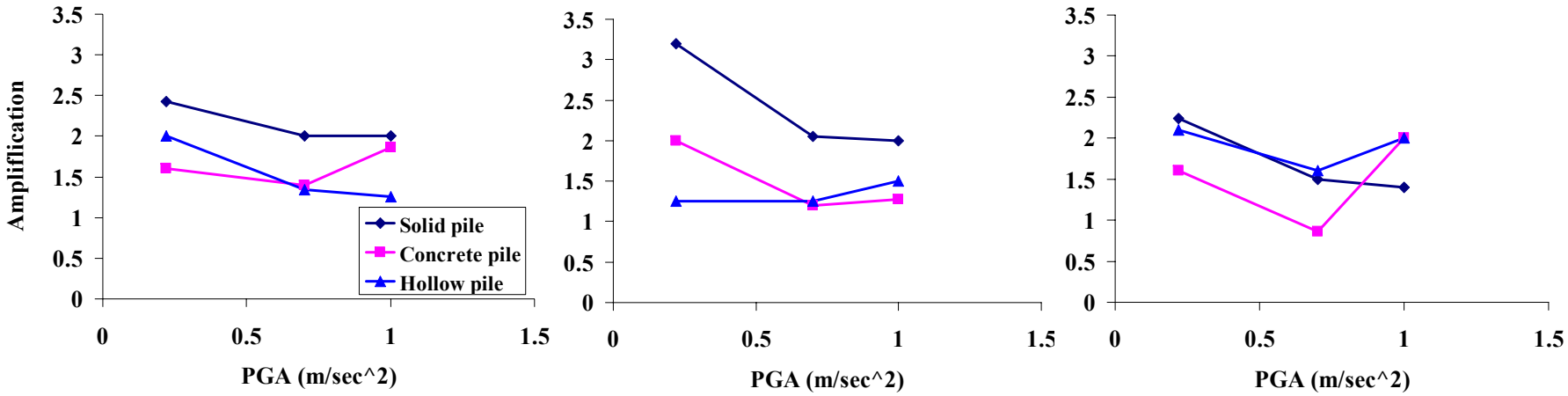

(a) Added mass = 368 tonne (b) Added mass = 605 tonne (c) Added mass = 863 tonne

Figure 5.10 Amplification at clay surface derived from centrifuge tests for different peak ground accelerations of cycle 1 and different added masses

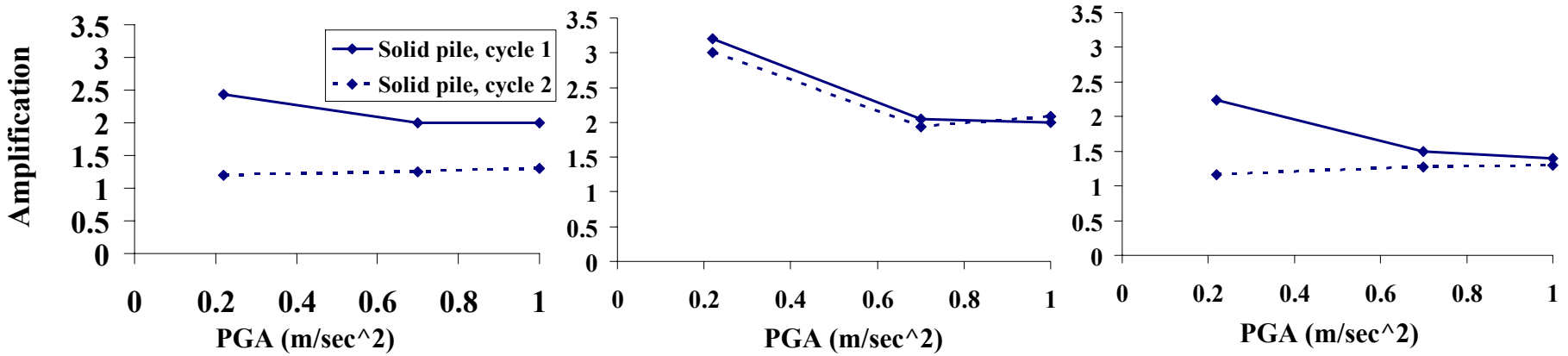

(a) Added mass = 368 tonne (b) Added mass = 605 tonne (c) Added mass = 863 tonne

Figure 5.11 Amplification at clay surface derived from centrifuge tests for different peak ground accelerations of cycle 1 and 2 for different added masses

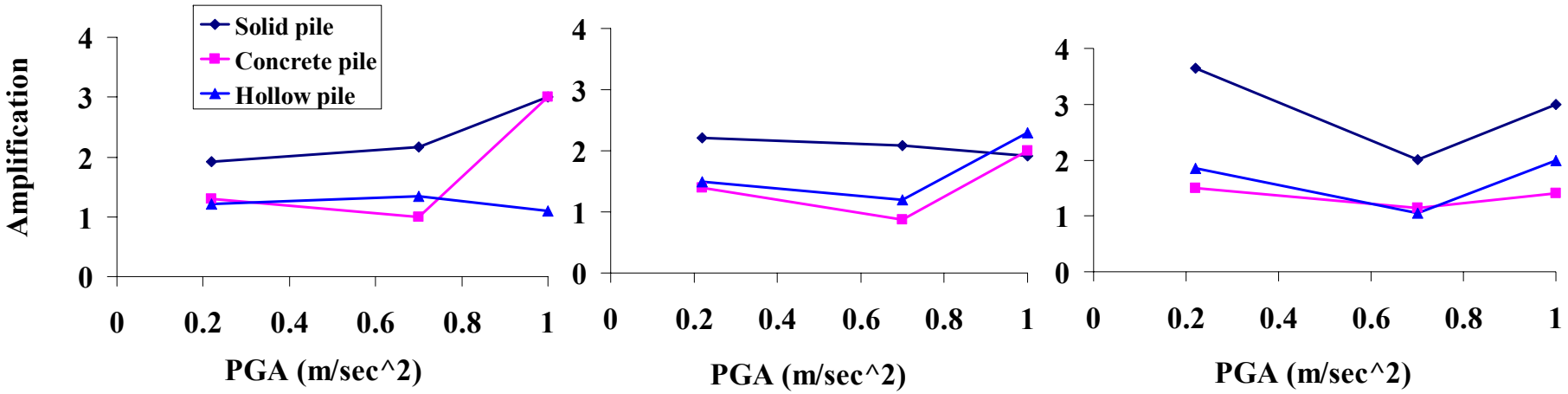

(a) Added mass = 368 tonne (b) Added mass = 605 tonne (c) Added mass = 863 tonne

Figure 5.12 Amplification at the raft top derived from centrifuge tests for different peak ground accelerations of cycle 1 and different added masses.

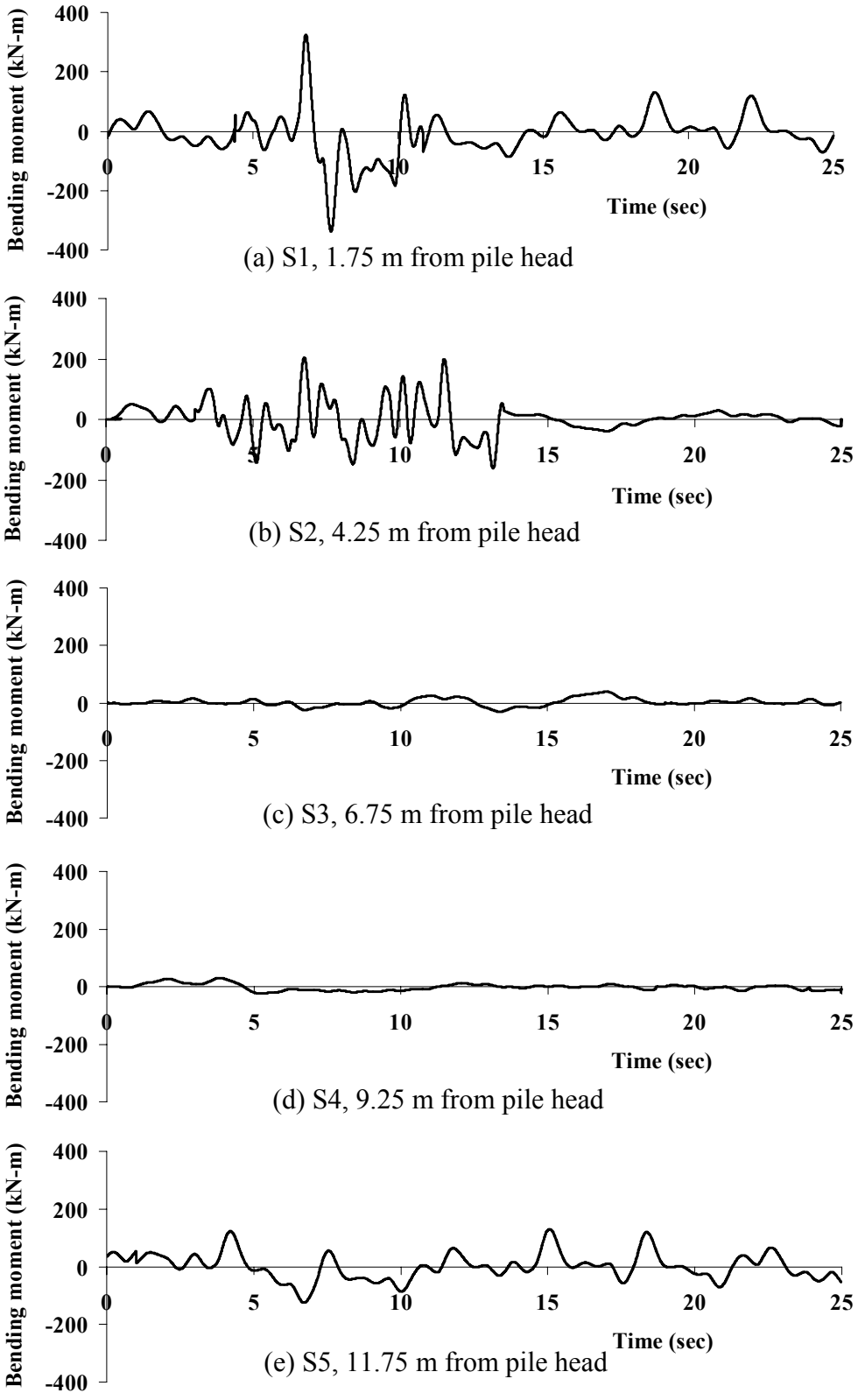

(a) S1, 1.75 m from pile head

(b) S2, 4.25 m from pile head

(c) S3, 6.75 m from pile head

(d) S4, 9.25 m from pile head

(e) S5, 11.75 m from pile head

Figure 5.13 Typical bending moment time histories measured in centrifuge test with pile-raft structure (concrete in-filled pile)

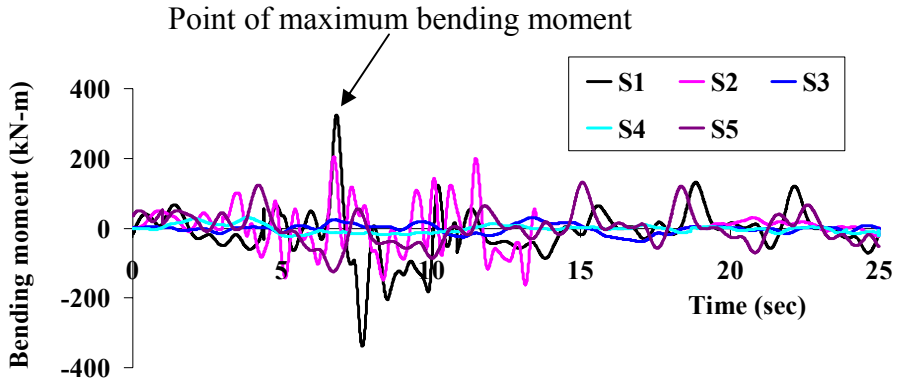

Figure 5.14 Bending moment time histories at all five strain gauge levels, plotted on the same axes(concrete in-filled pile)

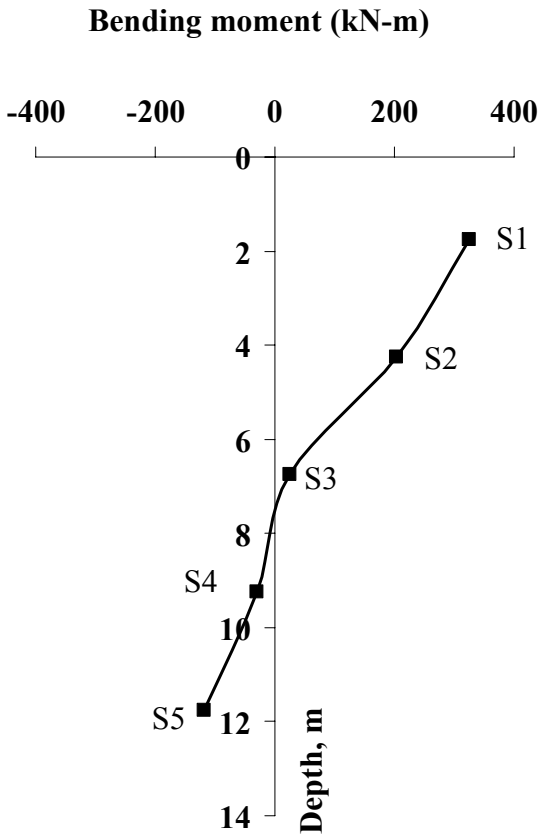

Figure 5.15 Maximum bending moment envelope for the concrete-infilled pile

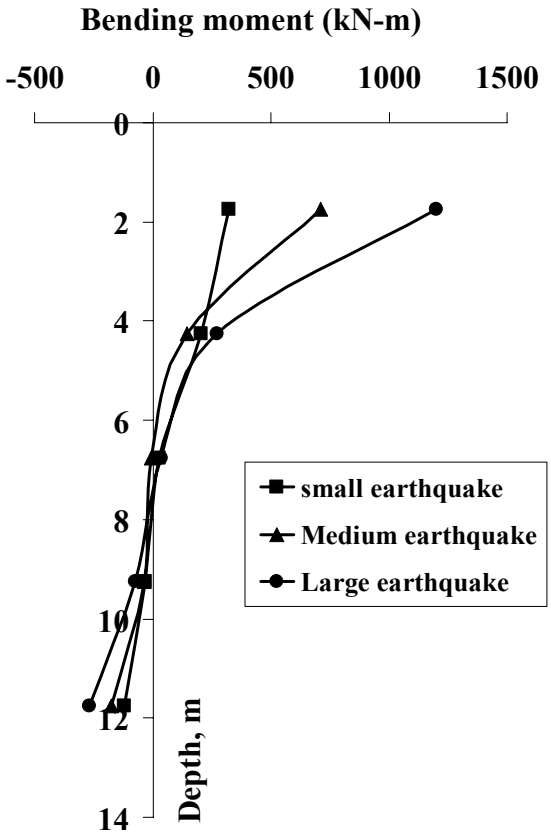

Figure 5.16 Maximum bending moment envelopes for three scaled earthquakes for the concrete-infilled pile.

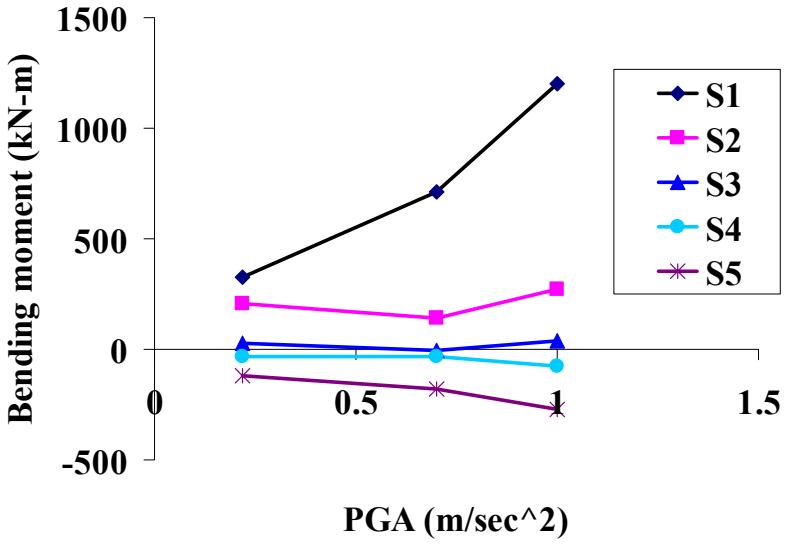

Figure 5.17 Variation of maximum bending moments with peak ground acceleration at different strain gauge positions

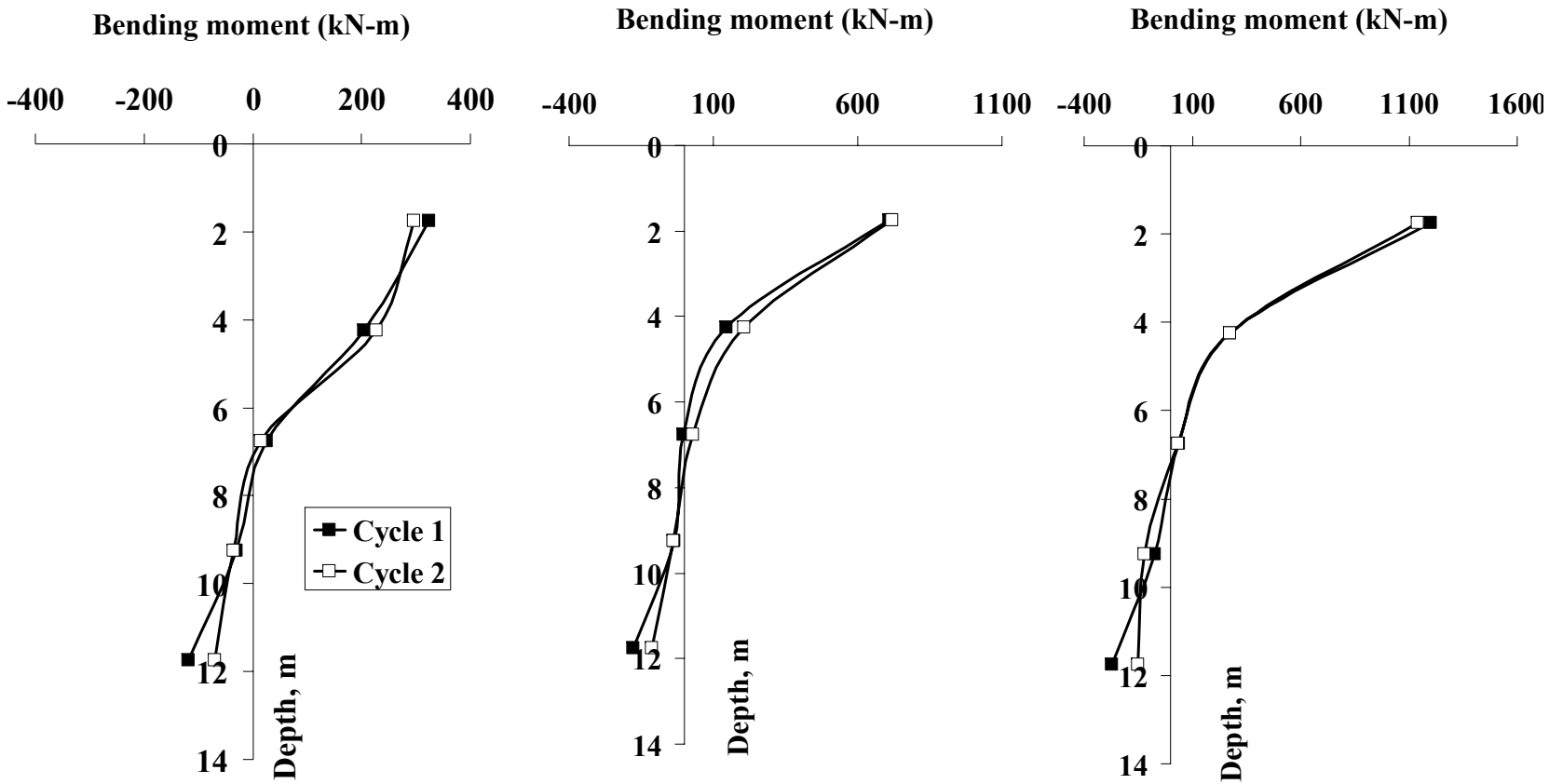

(a) Small earthquake (PGA=0.022g)

(b) Medium earthquake (PGA=0.07g)

(c) Large earthquake (PGA=0.1g)

Figure 5.18 Maximum bending moment envelopes during cycle 1 and 2 for three scaled earthquakes

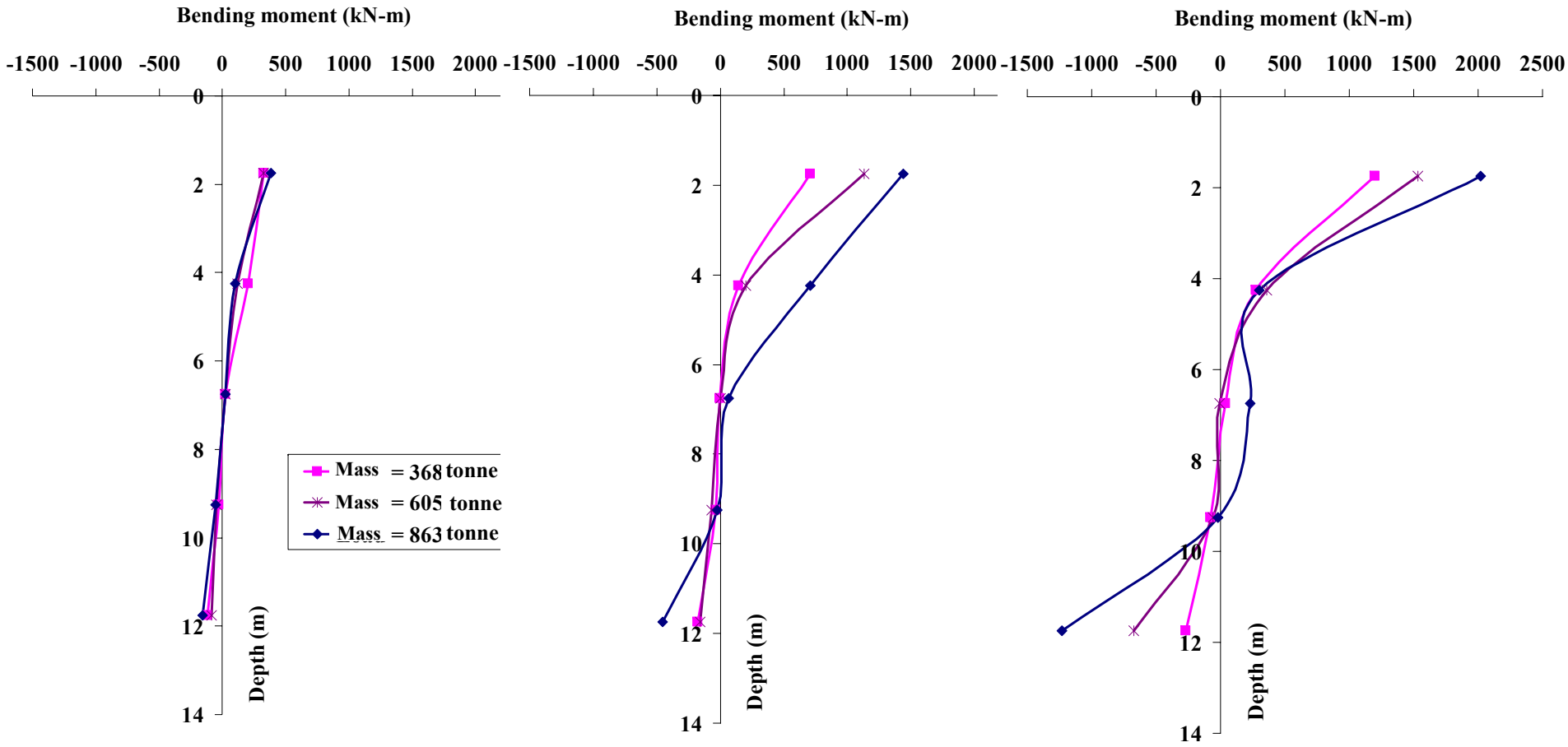

(a) Small earthquake (PGA=0.022g)

(b) Medium earthquake (PGA=0.07g)

(c) Large earthquake (PGA=0.1g)

Figure 5.19 Maximum bending moment envelopes for three scaled earthquakes at different added masses

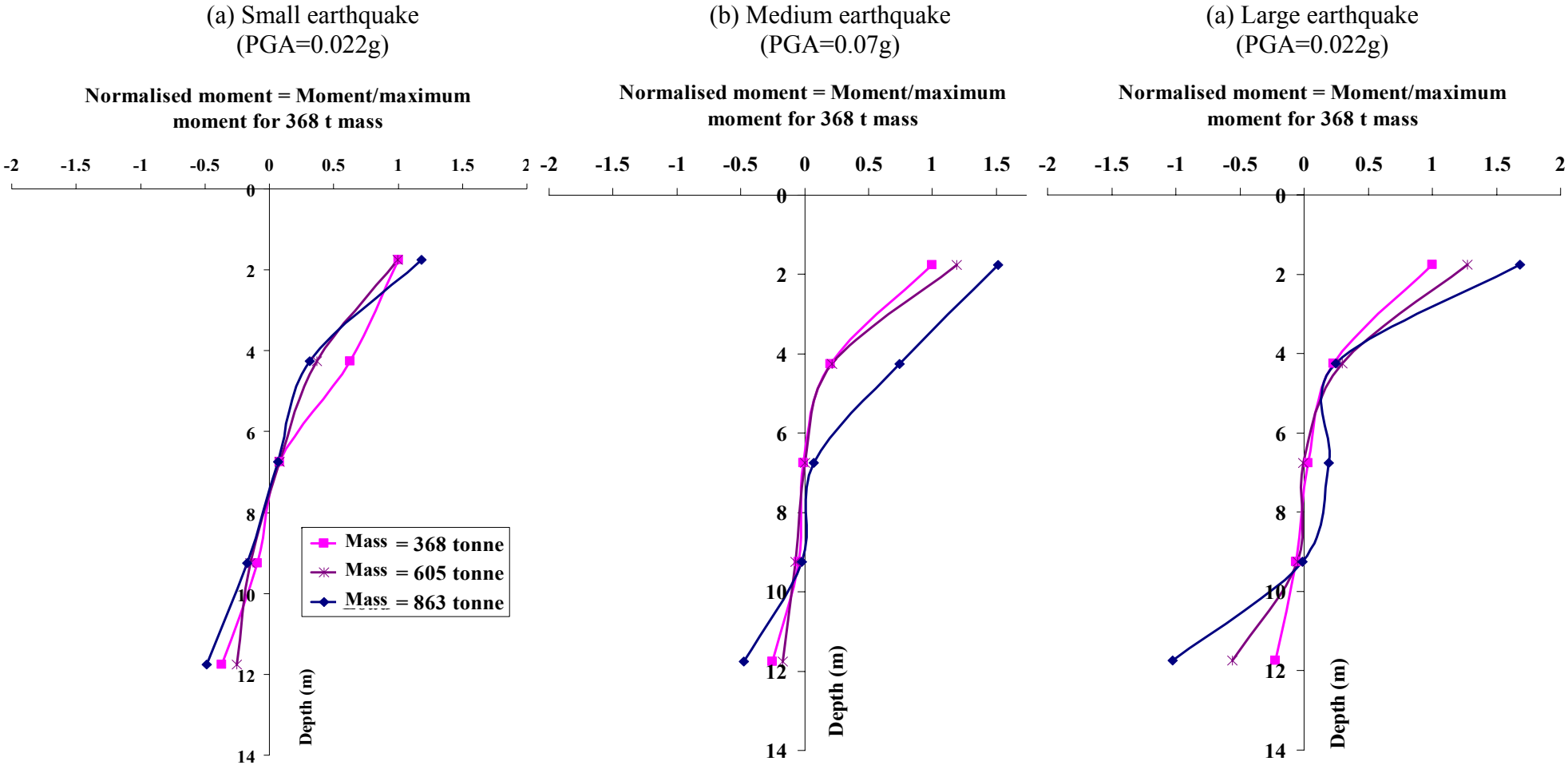

Figure 5.20 Normalised bending moment envelopes for three scaled earthquakes at different added masses

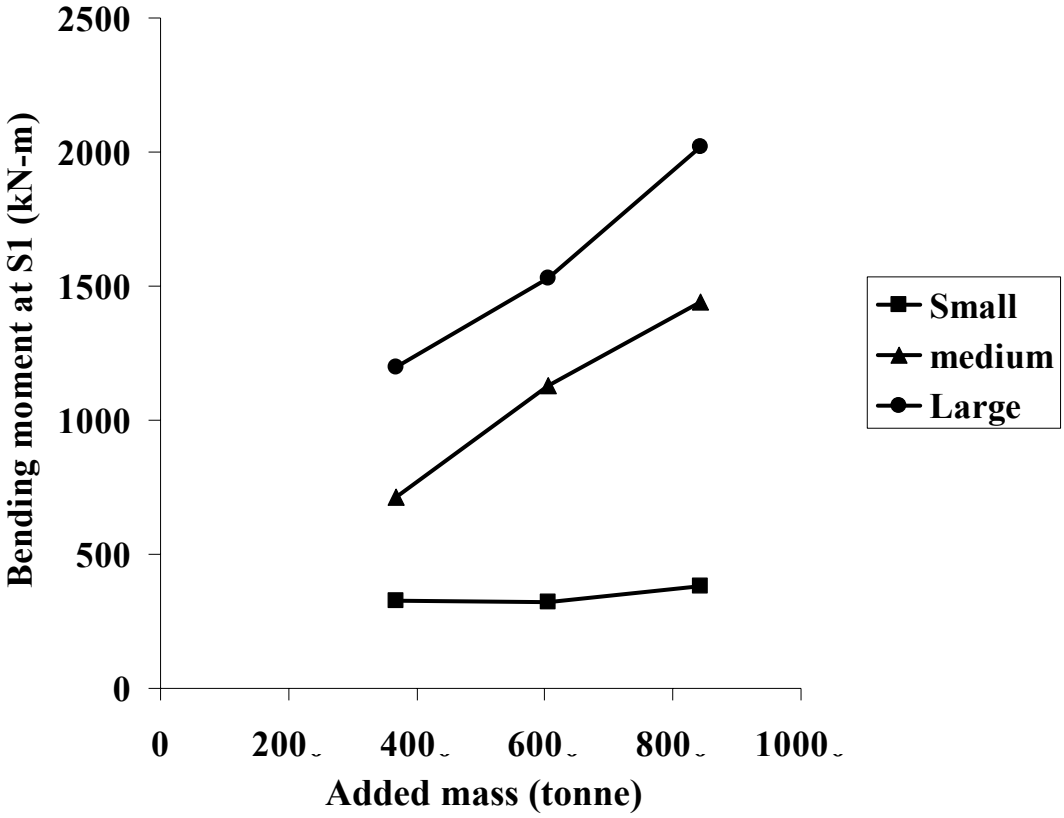

Figure 5.21 Bending moment at S1 vs. added masses for three scaled earthquakes

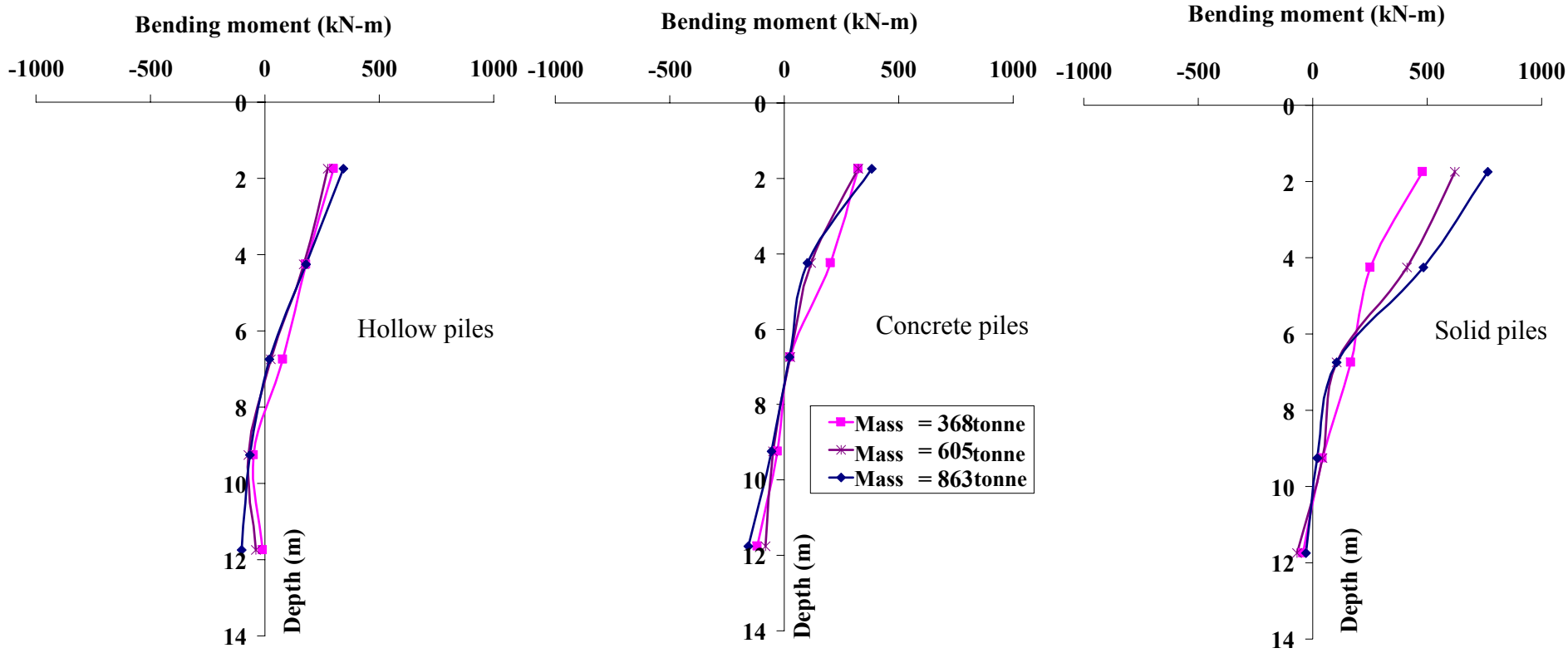

(a) Small earthquake
(PGA=0.022g)

Figure 5.22 Maximum bending moment envelopes for three scaled earthquakes for three different pile types

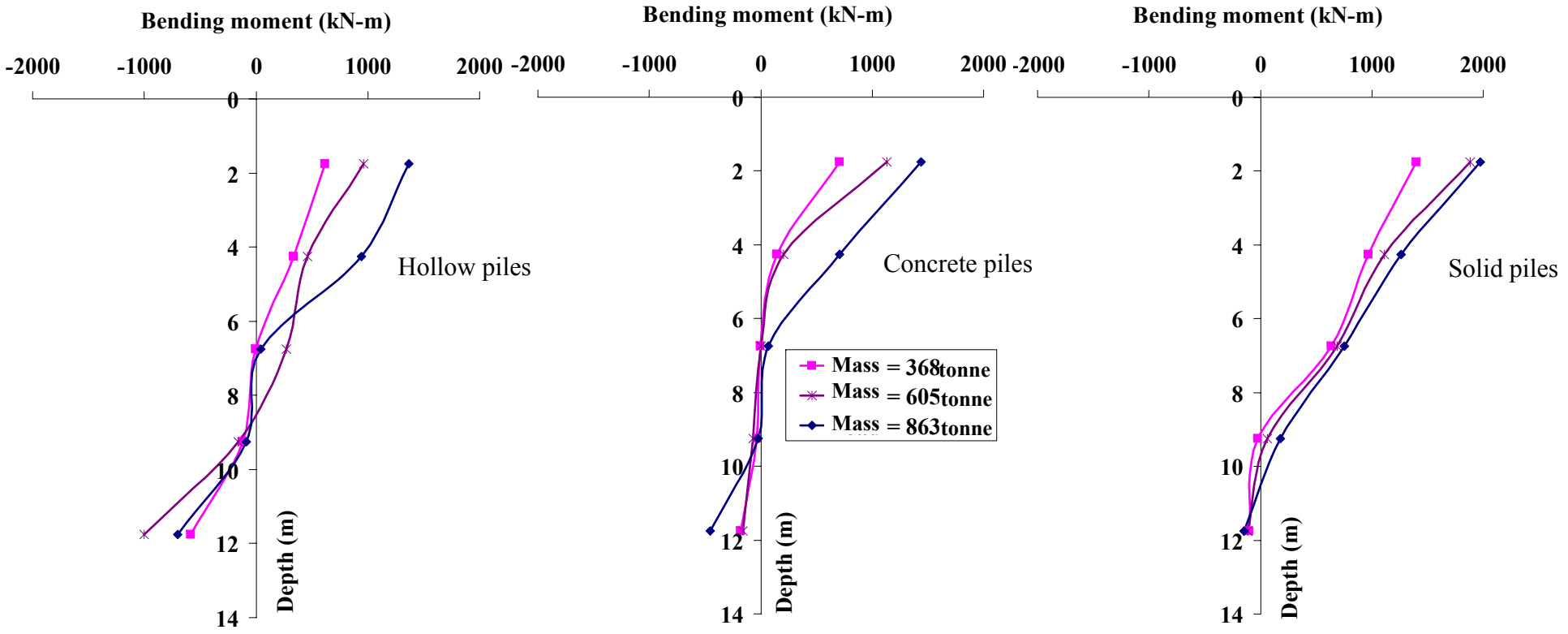

(b) Medium earthquake
(PGA=0.07g)

Figure 5.22 Maximum bending moment envelopes for three scaled earthquakes for three different pile types *(continued)*

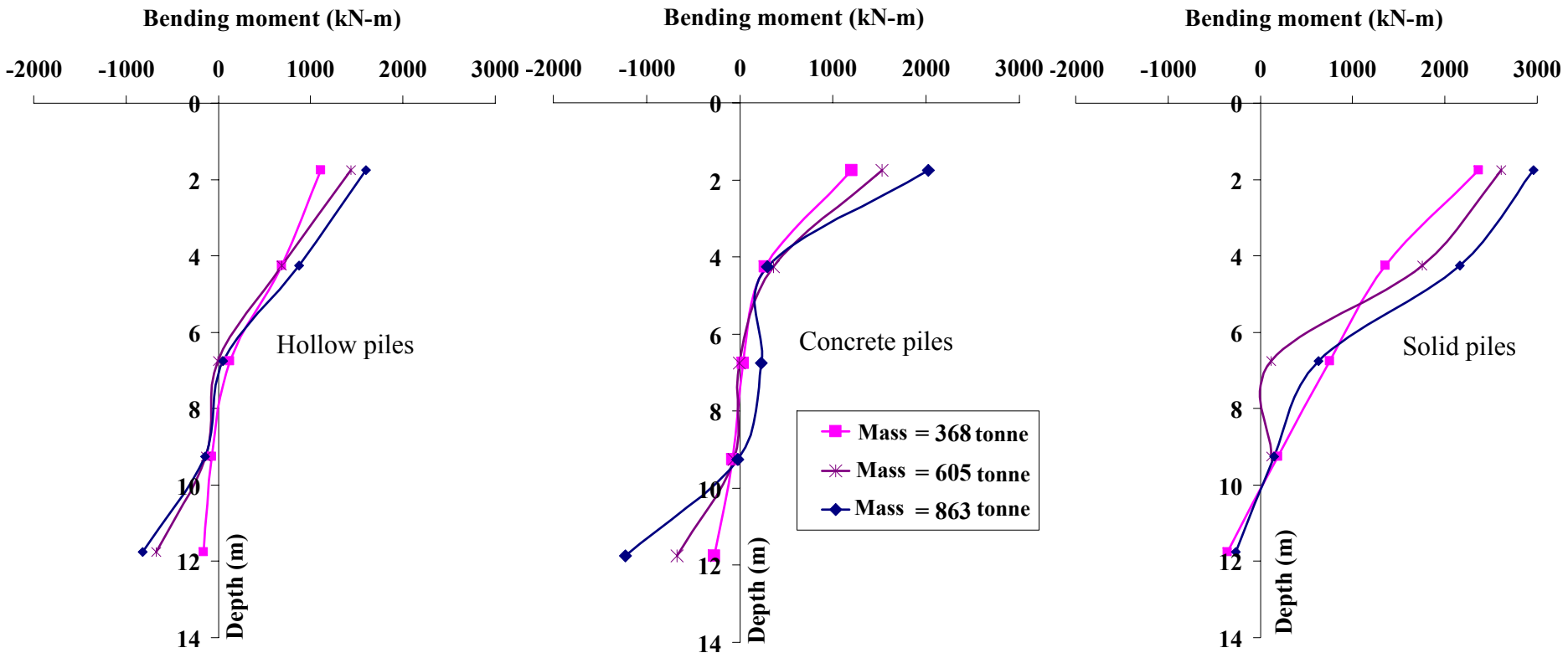

(c) Large earthquake (PGA=0.1g)

Figure 5.22 Maximum bending moment envelopes for three scaled earthquakes for three different pile types *(continued)*

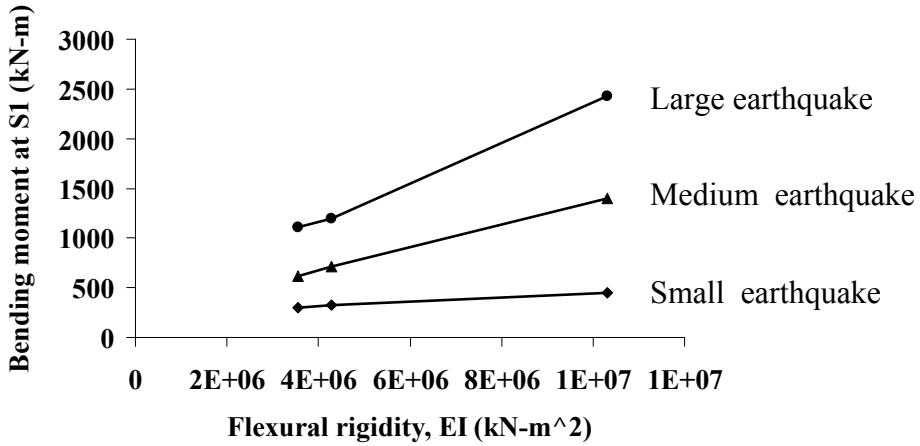

(a) Added mass = 368 tonne

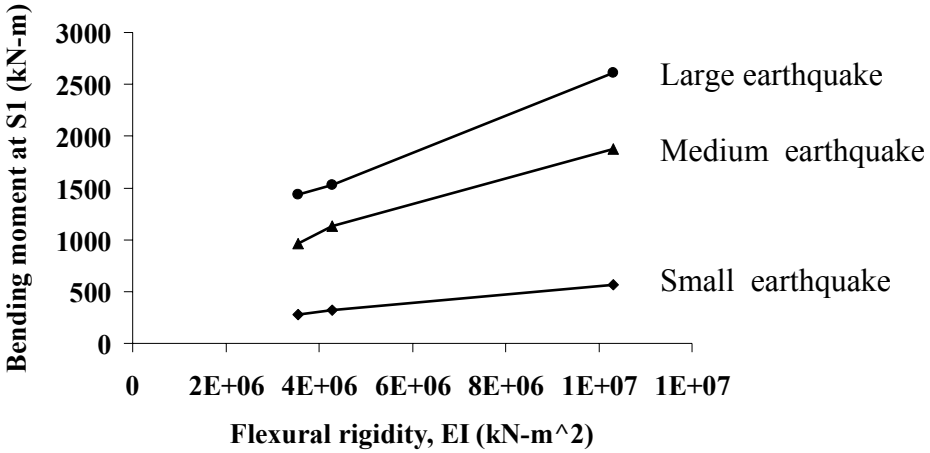

(b) Added mass = 605 tonne

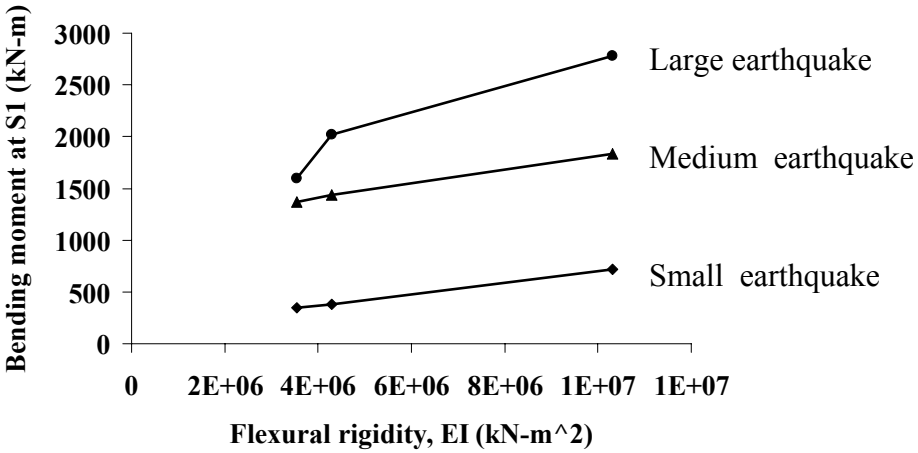

(c) Added mass = 863 tonne

Figure 5.23 Bending moment at S1 vs. EI of piles for three different earthquakes and three different added masses

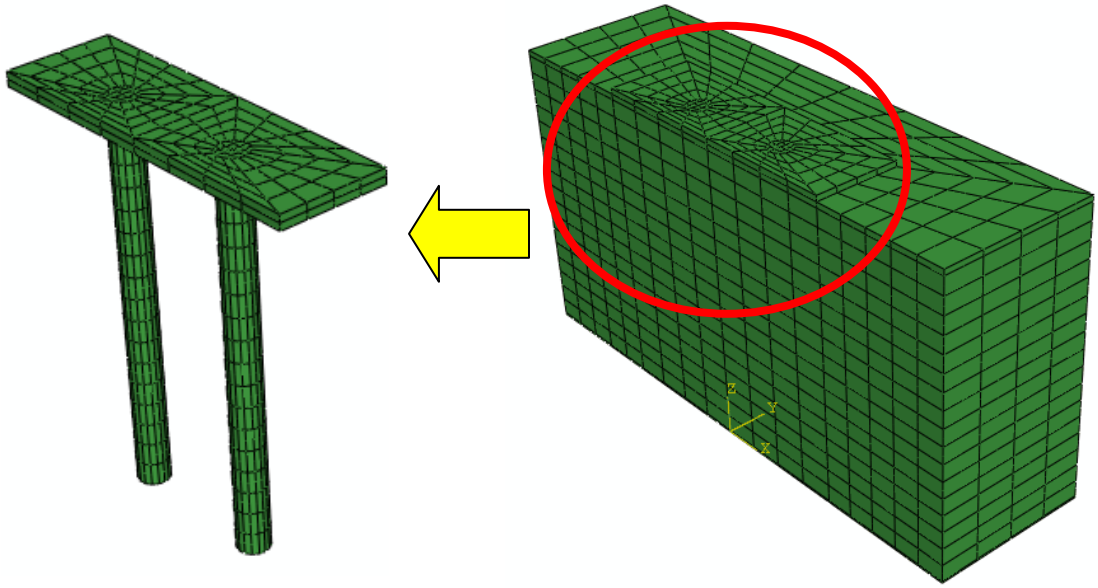

Figure 5.24 ABAQUS half-model for clay-pile-raft test

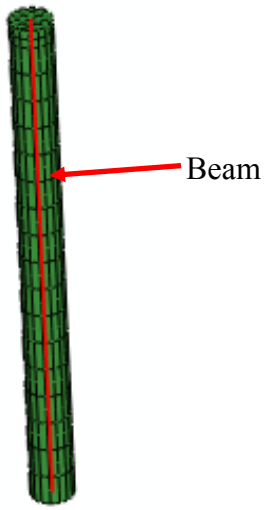

Figure 5.25 Flexible beam along the pile central axes to measure bending moments

(a)

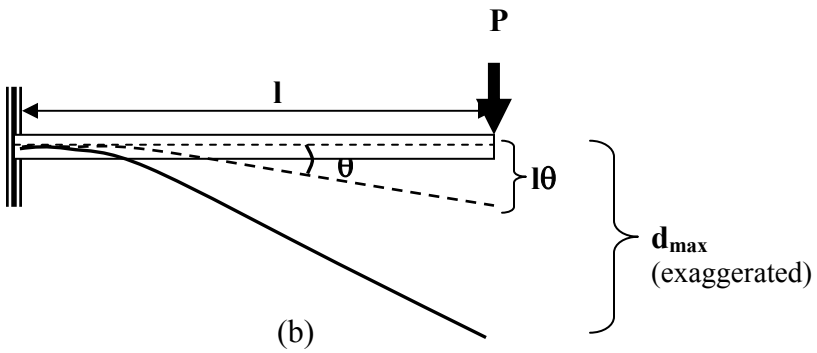

(b)

Figure 5.26 Calibration of pile-raft joint: (a) Measurement of pile deflection and (b) Assumed cantilever mechanism

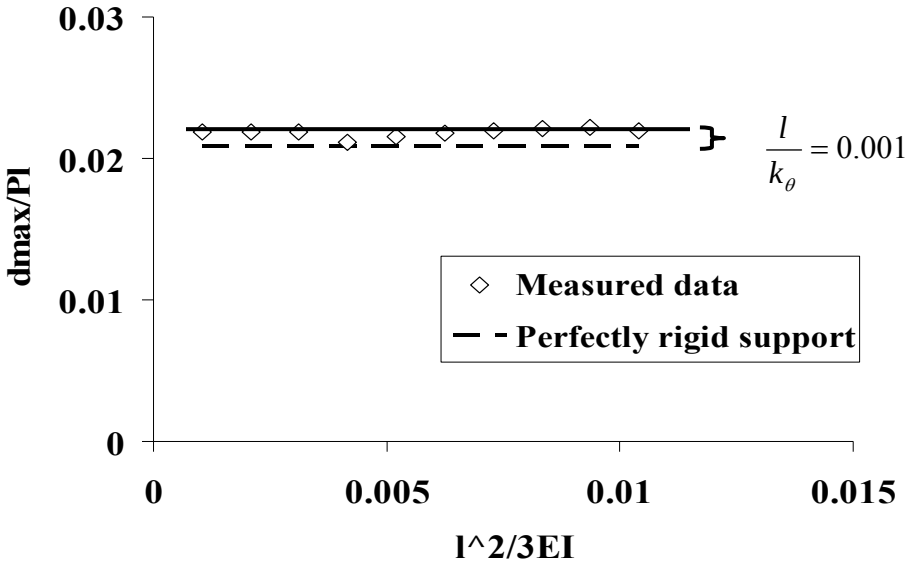

Figure 5.27 Comparison of measured and theoretical pile tip deflection

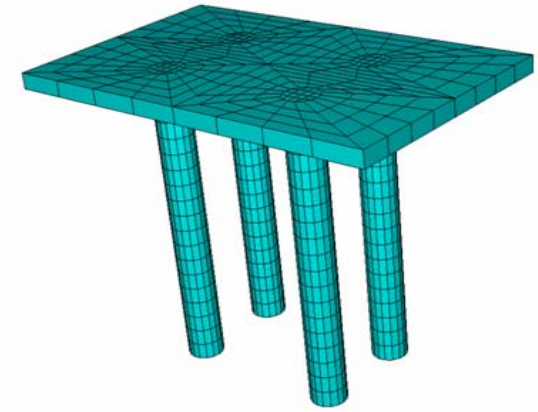

Figure 5.28 ABAQUS 3D model for pile-raft structure

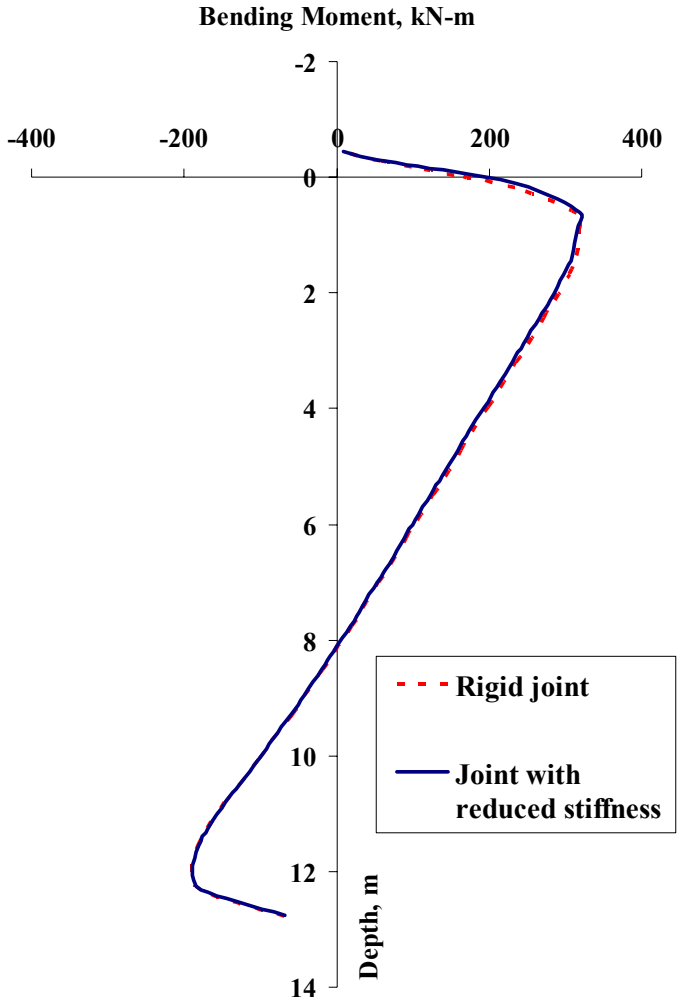

Figure 5.29 Comparison of the bending moment profiles with rigid joints and joints with reduced stiffness

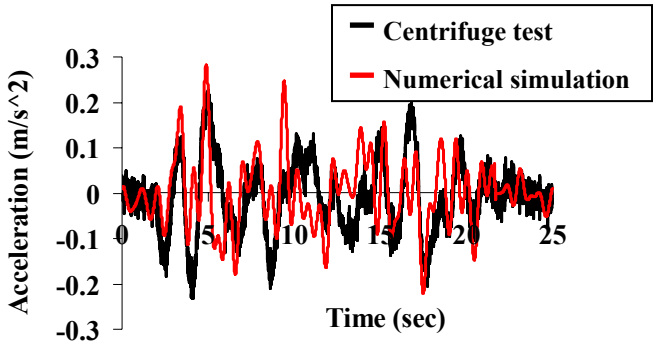

(a) Computed and measured accelerations at Top of the Raft (A4)

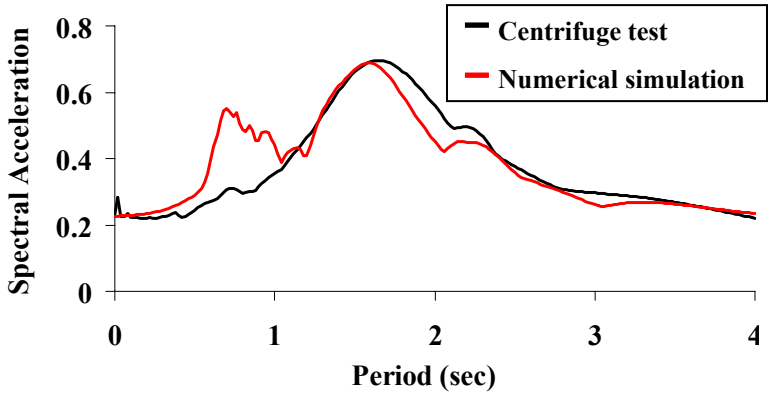

(b) Computed and measured response spectra at Top of the Raft (A4)

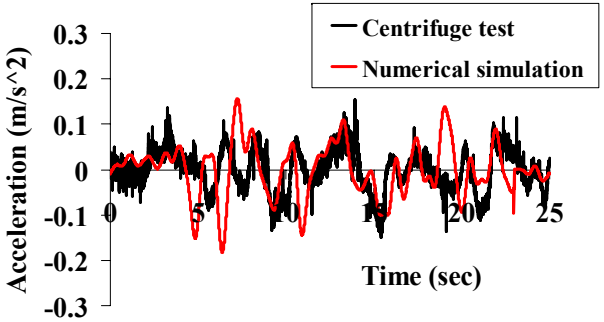

(c) Computed and measured accelerations at Clay Surface (A3)

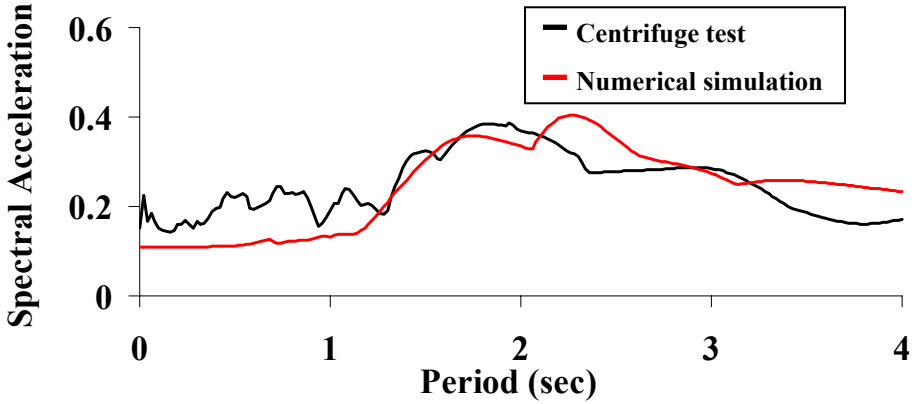

(d) Computed and measured response spectra at Clay Surface (A3)

Figure 5.30 Comparison of typical acceleration response recorded in centrifuge tests with numerical simulations (small earthquake)

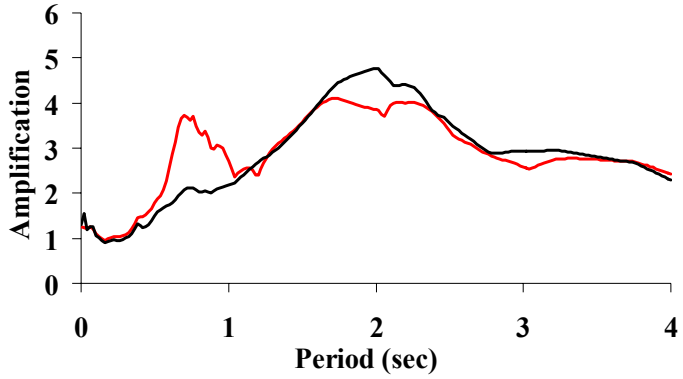

(a) Computed and measured amplification at top of the raft (A4)

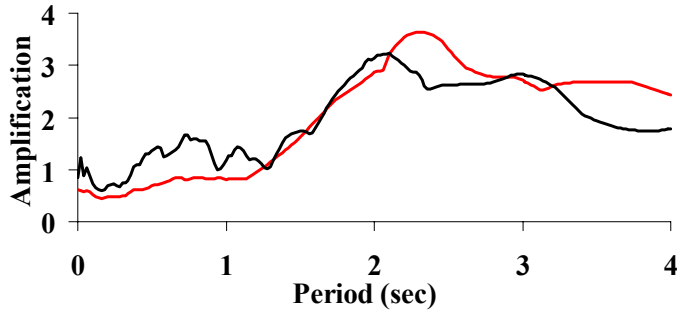

(b) Computed and measured amplification at clay surface (A3)

Figure 5.31 Comparison of measured and computed amplification (small earthquake)

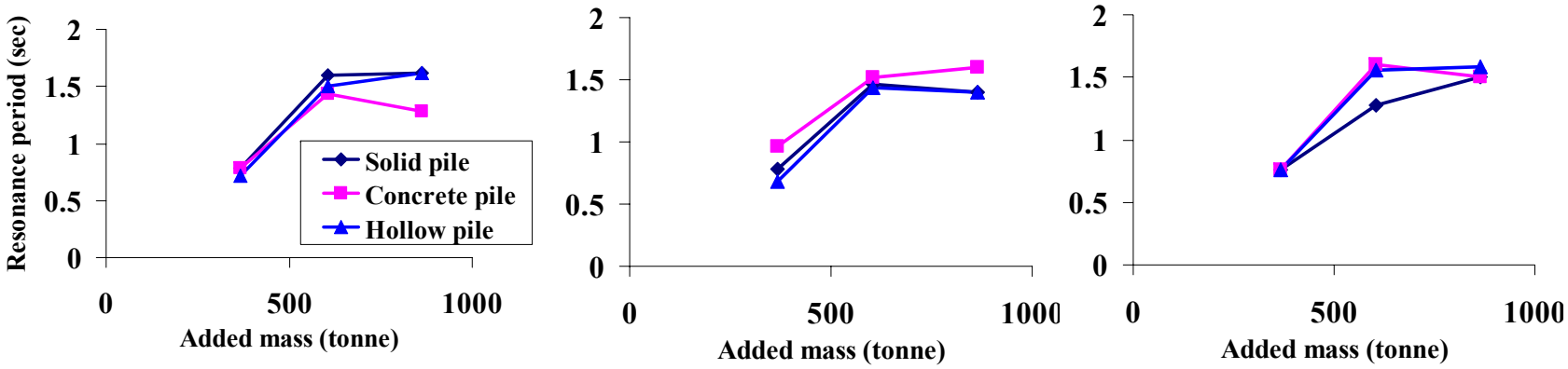

(a) Small earthquake (PGA=0.022g)

(b) Medium earthquake (PGA=0.07g)

(c) Large earthquake (PGA=0.1g)

Figure 5.32 Computed resonance period of the pile raft (A4) associated with a) Small, b) Medium and c) Large Earthquake

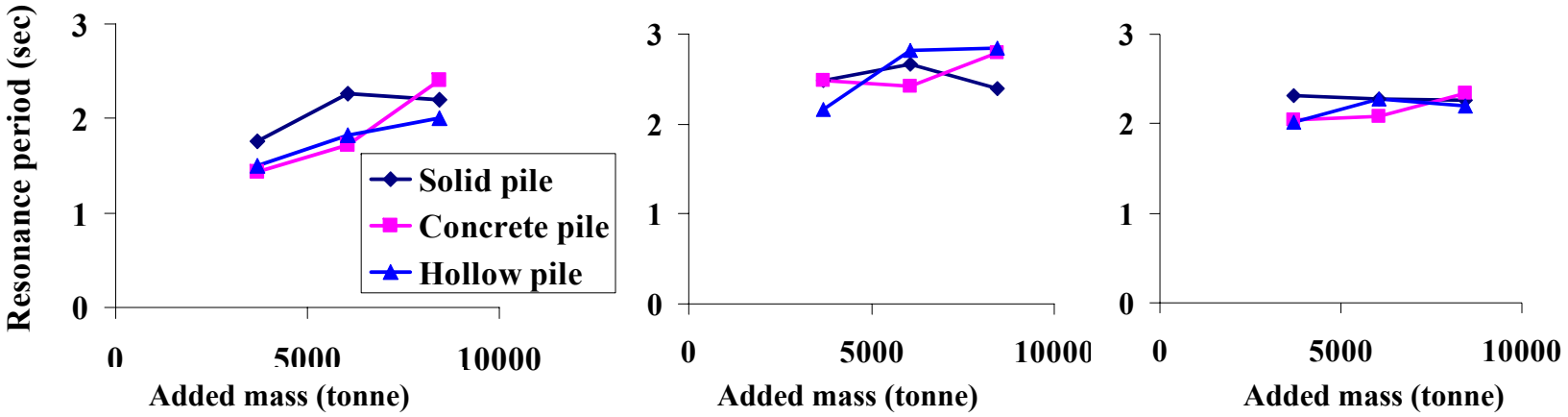

(a) Small earthquake (PGA=0.022g)

(b) Medium earthquake (PGA=0.07g)

(c) Large earthquake (PGA=0.1g)

Figure 5.33 Computed resonance period at the clay surface (A3) associated with a) Small, b) Medium and c) Large earthquake

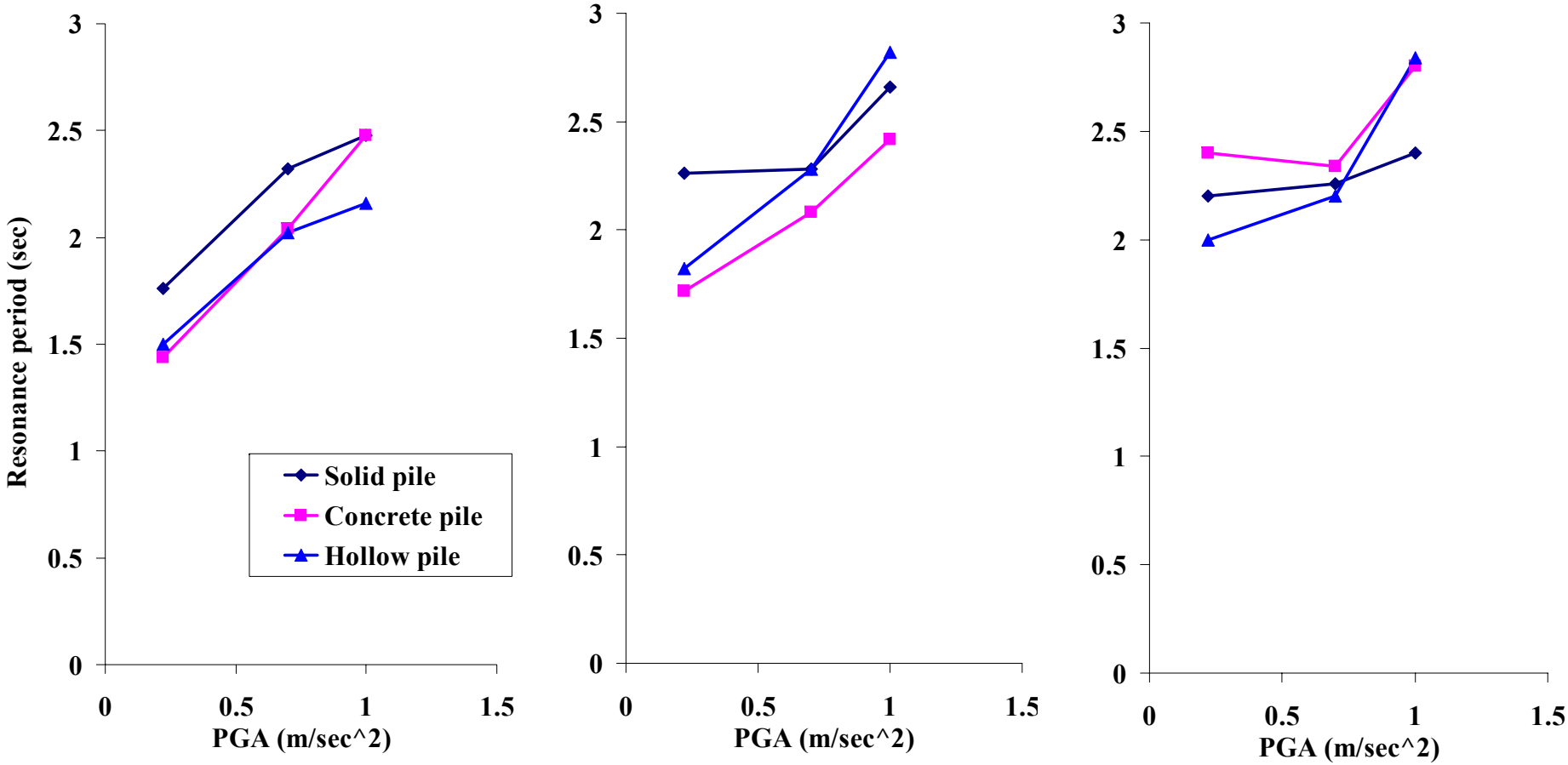

(a) Added mass = 368 tonne (b) Added mass = 605 tonne (c) Added mass = 863 tonne

Figure 5.34 Computed resonance period vs peak ground acceleration at clay surface under different added masses

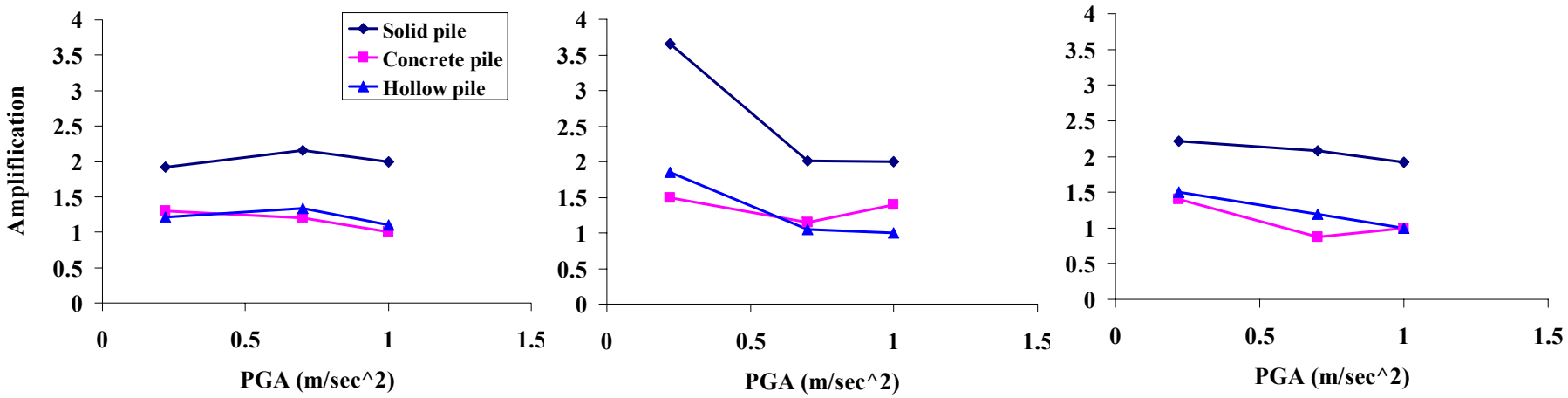

(a) Added mass = 368 tonne (b) Added mass = 605 tonne (c) Added mass = 863 tonne

Figure 5.35 Computed Amplification vs peak ground acceleration at clay surface for different piles under different added masses

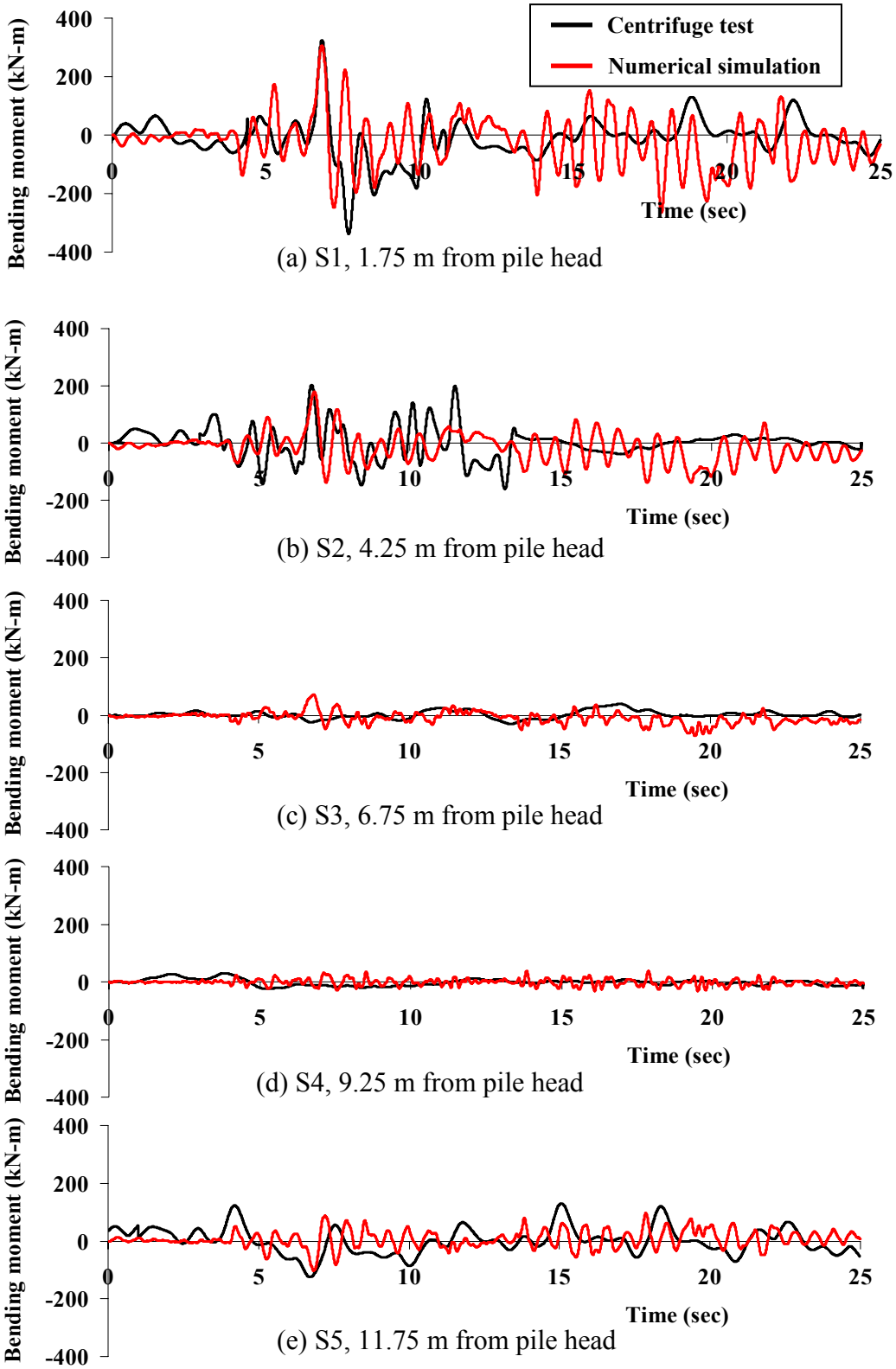

Figure 5.36 Comparison of bending moment time histories measured in centrifuge test with numerical simulation (small earthquake)

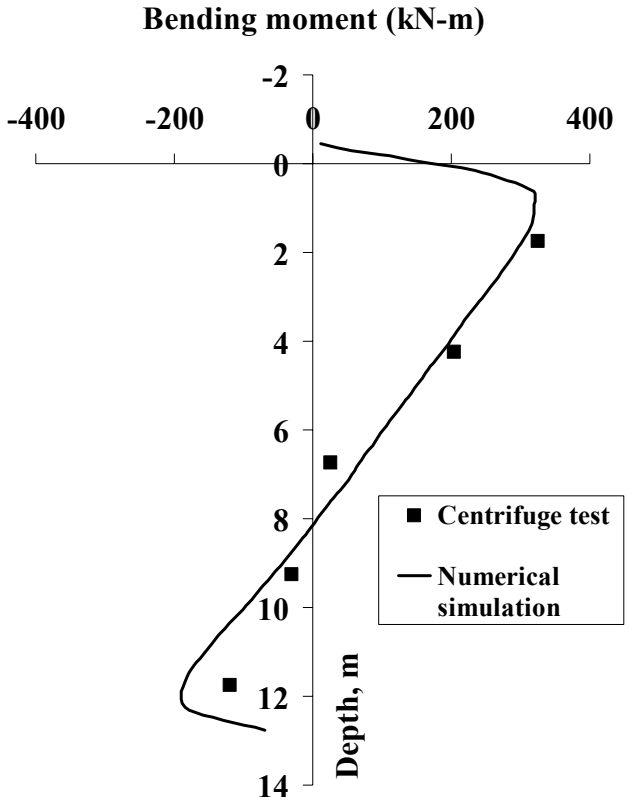

Figure 5.37 Comparison of Maximum bending moment envelope measured in centrifuge test with numerical simulation (small earthquake)

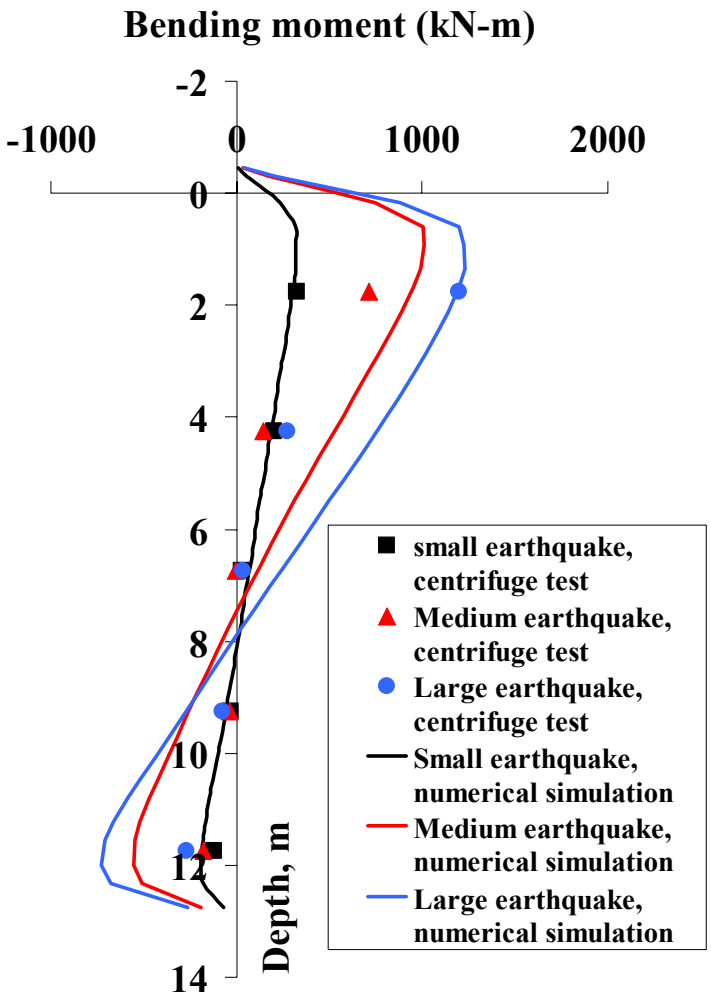

Figure 5.38 Computed and measured maximum bending moment envelope for three scaled earthquakes for concrete infill piles and added mass of 368 tonne

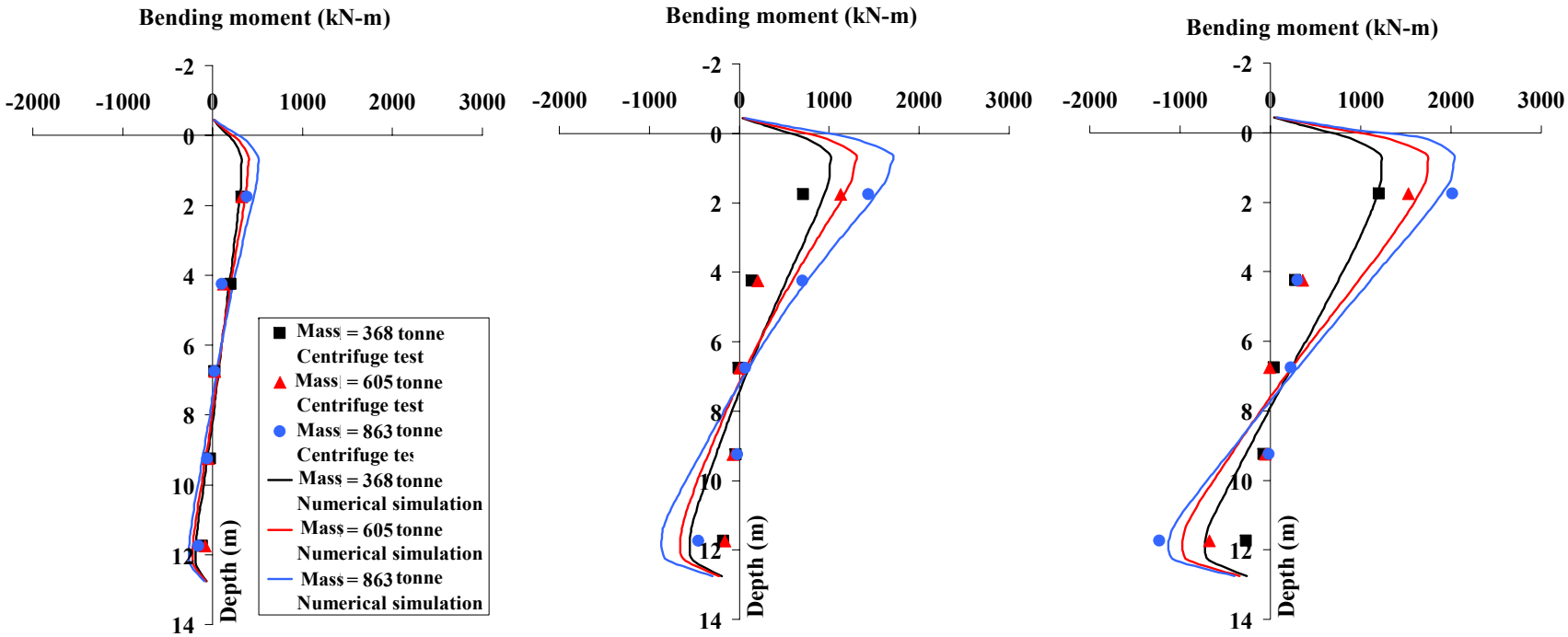

(a) Small earthquake (PGA=0.022g)

(b) Medium earthquake (PGA=0.07g)

(c) Large earthquake (PGA=0.1g)

Figure 5.39 Computed and measured maximum bending moment envelope for three different scaled earthquakes and different added mass (concrete in-fill pile)

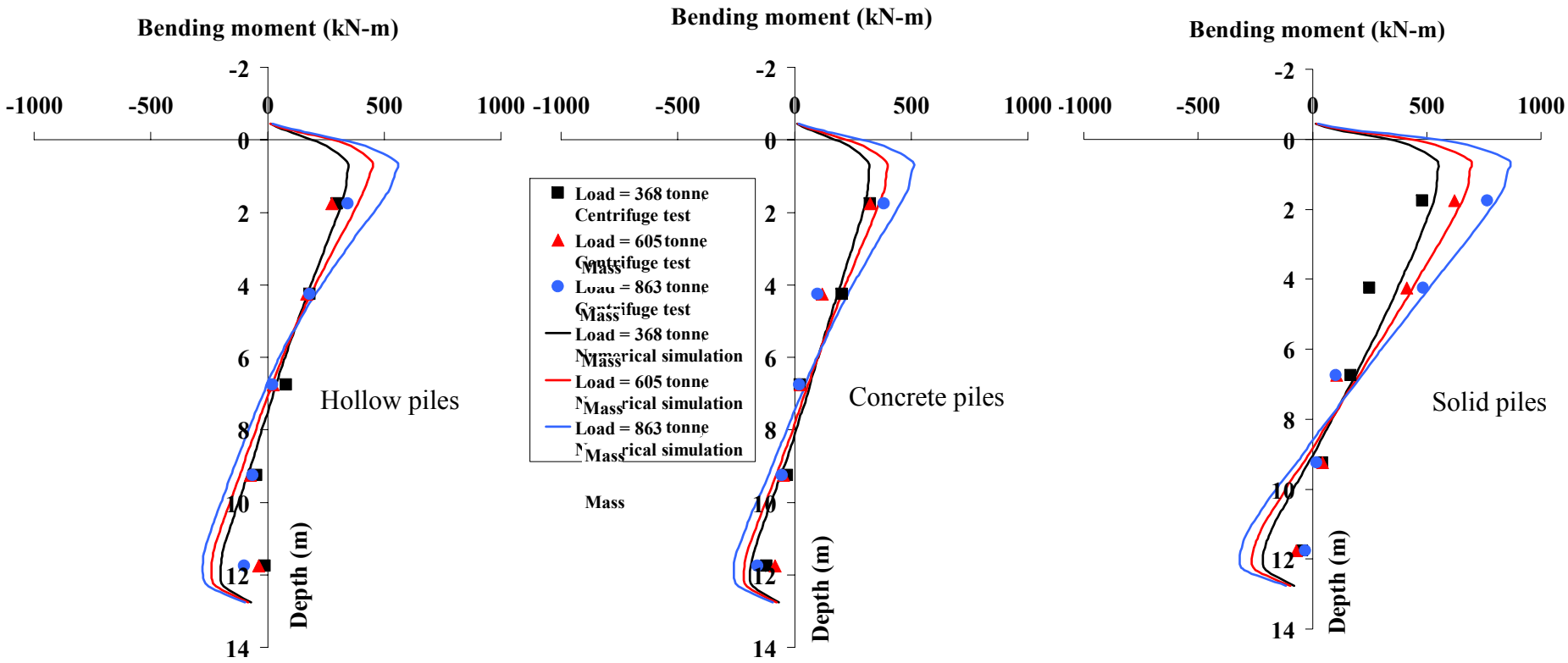

(a) Small earthquake (PGA=0.022g)

Figure 5.40 Computed and measured maximum bending moment envelopes for three scaled earthquakes and different added masses for three pile types

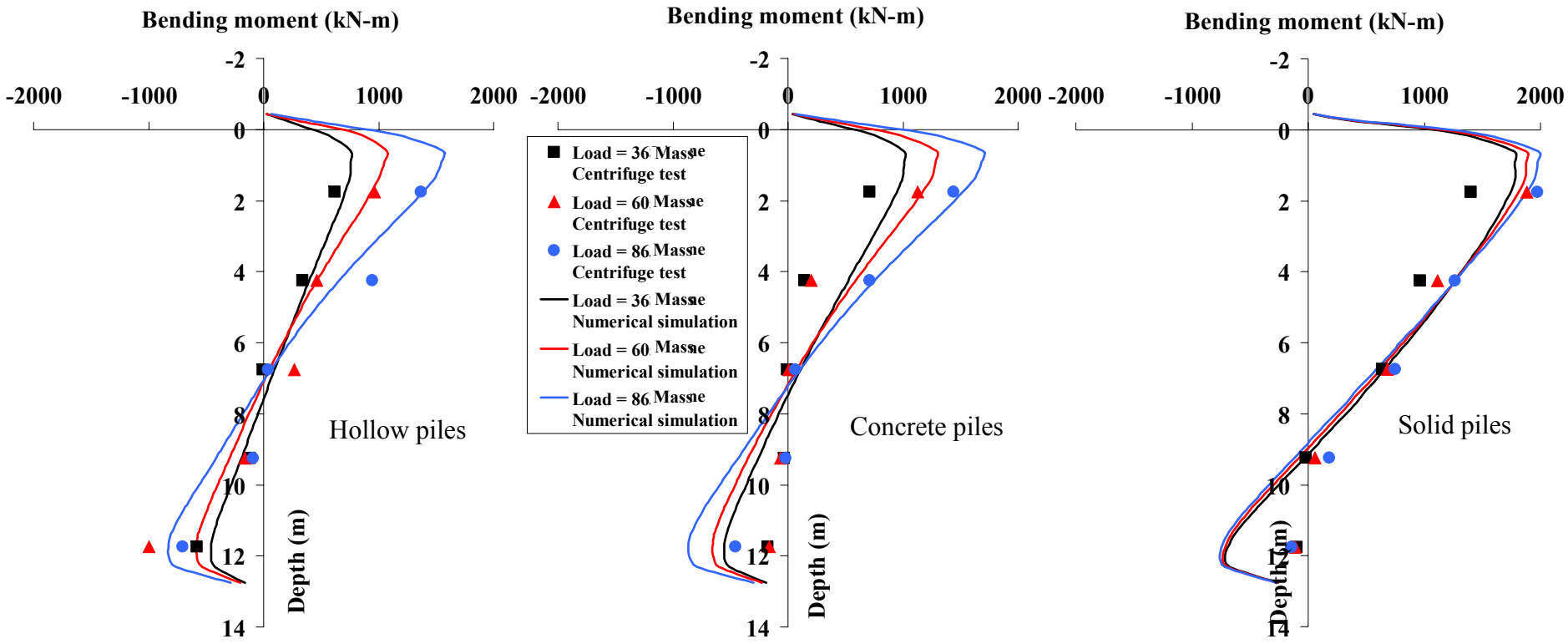

(b) Medium earthquake (PGA=0.07g)

Figure 5.40 Computed and measured maximum bending moment envelopes for three scaled earthquakes and different added masses for three pile types *(continued)*

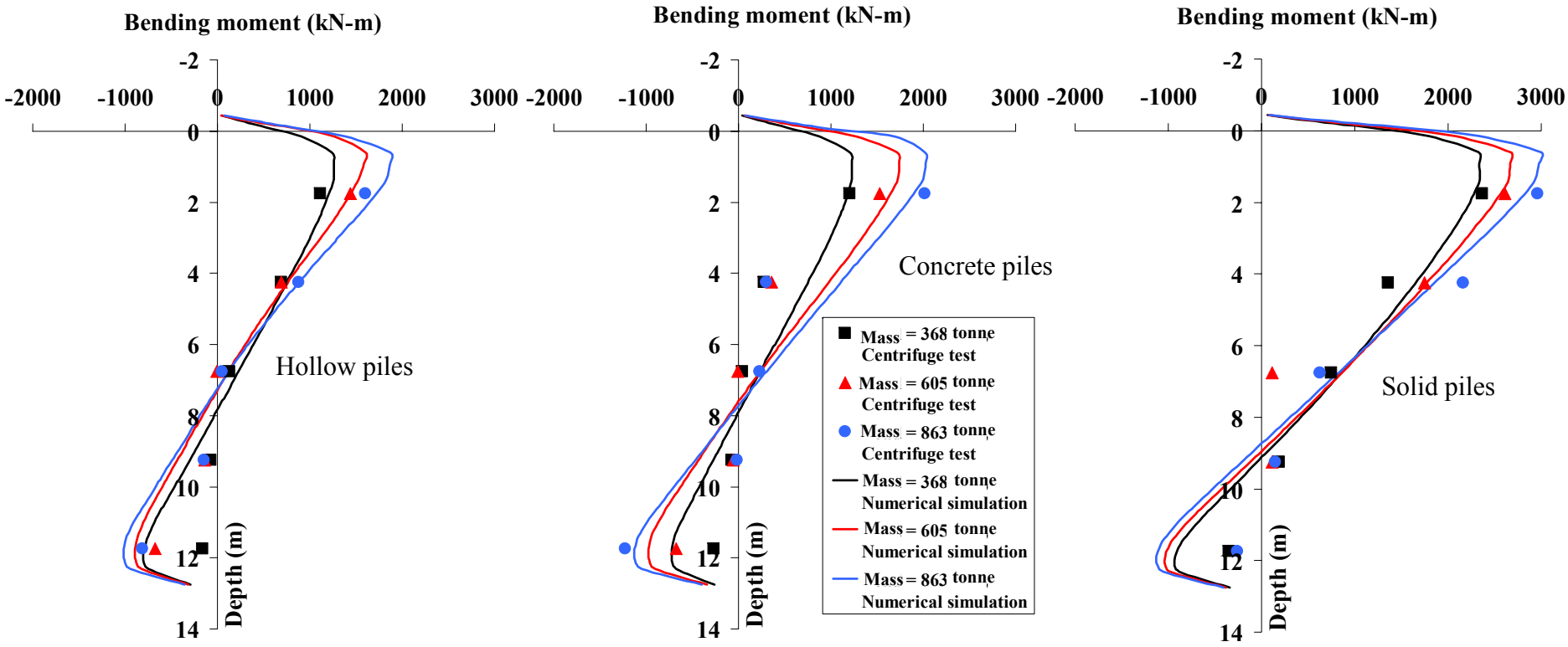

(c) Large earthquake (PGA=0.1g)

Figure 5.40 Computed and measured maximum bending moment envelopes for three scaled earthquakes and different added masses for three pile types *(continued)*

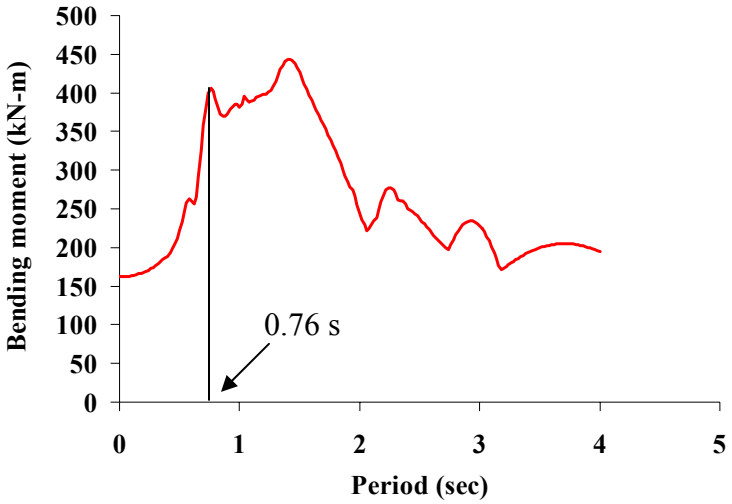

Figure 5.41 Response spectra of the computed bending moment history

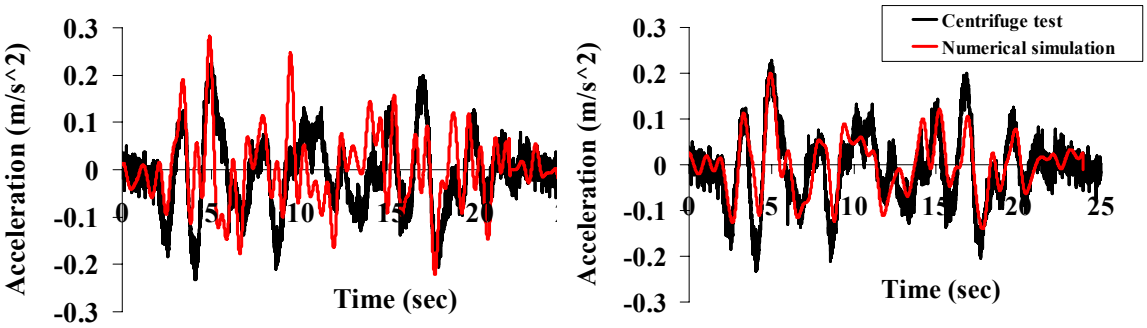

(a) Pile supported on elastic sand layer in ABAQUS analysis

(b) Pile supported on Mohr-Coulomb sand layer in ABAQUS analysis

Figure 5.42 Computed and measured acceleration time histories of the raft for different assumed pile tip condition in the ABAQUS analysis

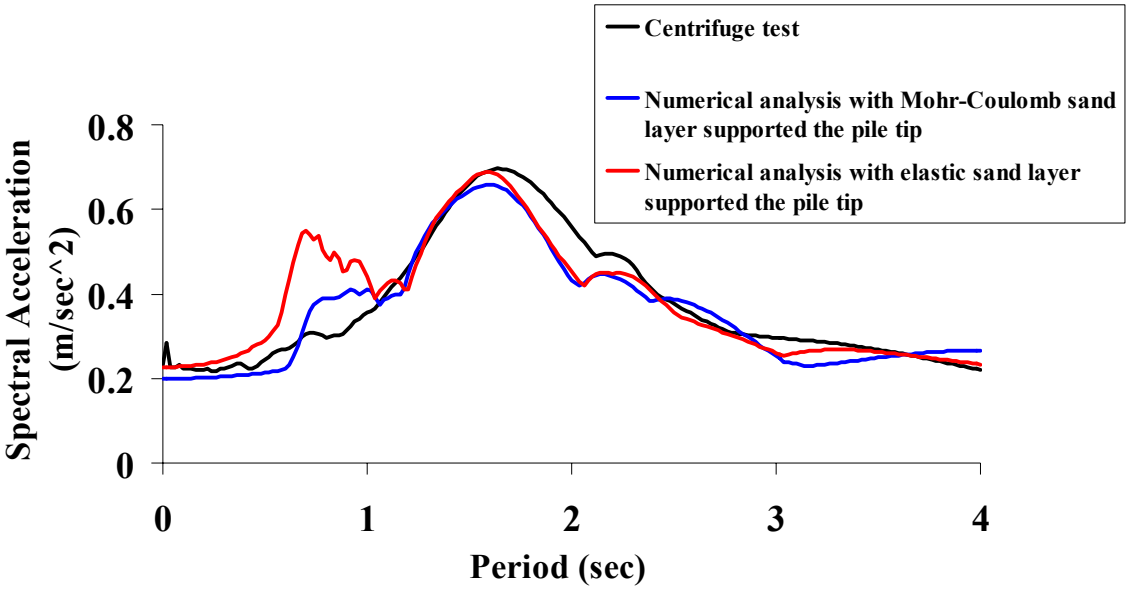

Figure 5.43 Computed and measured response spectra of the raft for different assumed material types supporting the pile types

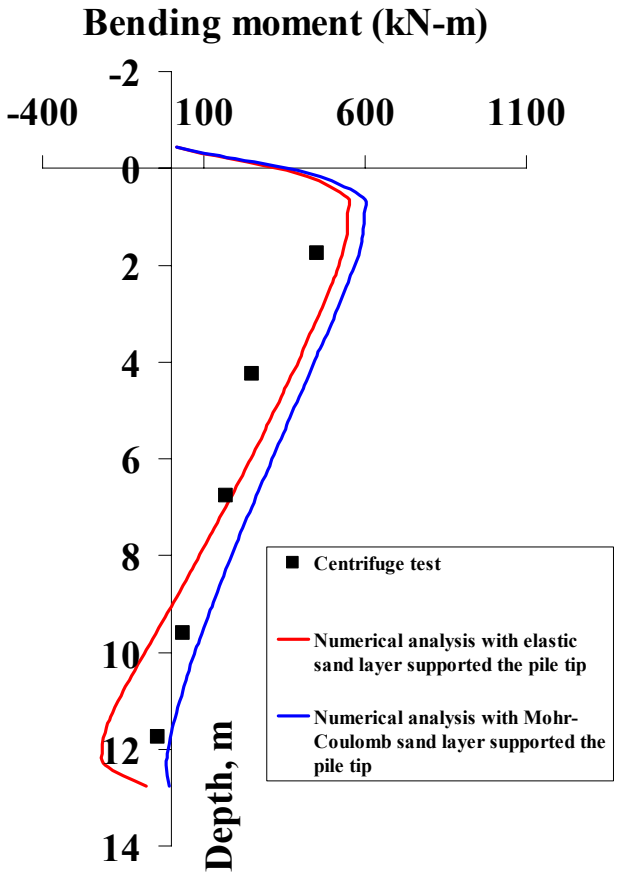

Figure 5.44 Effect of different material types supported the pile on the solid piles subjected to small earthquake

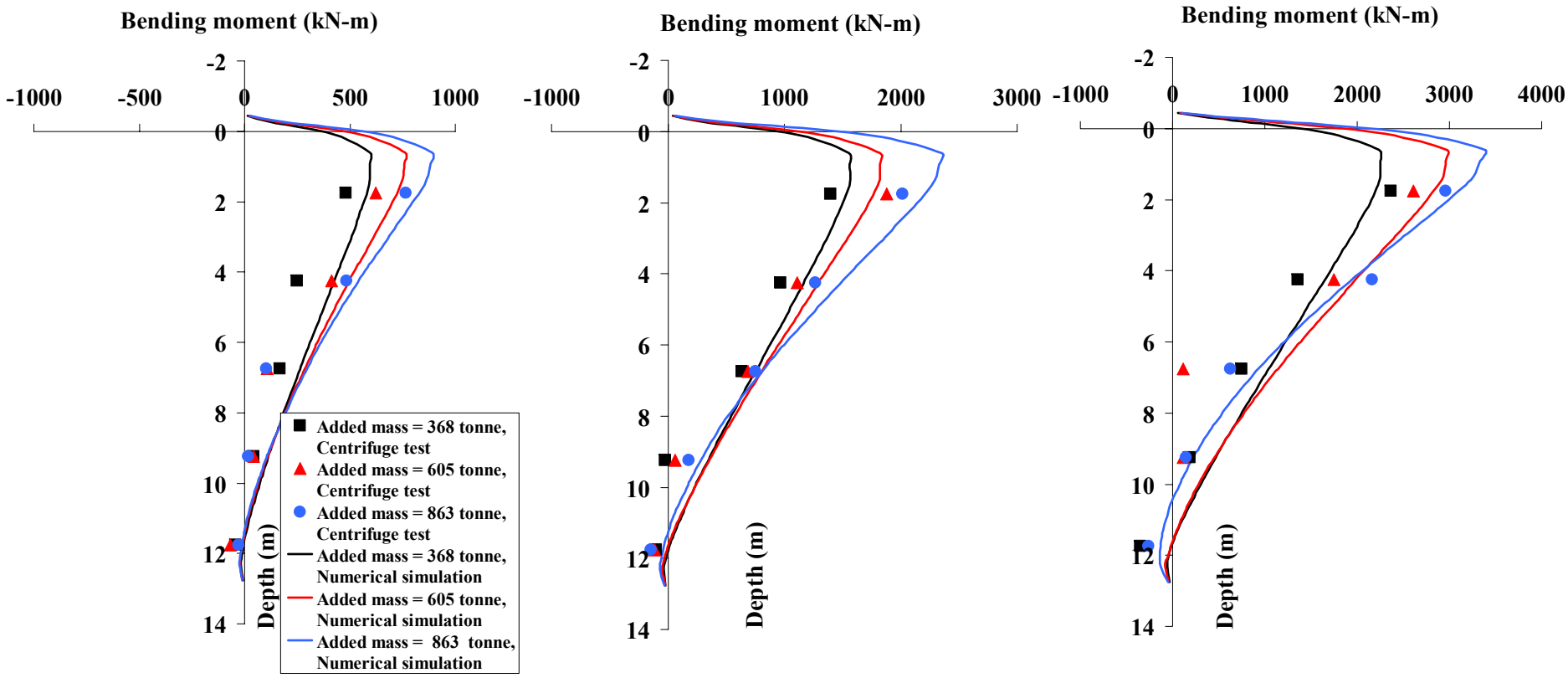

(a) Small earthquake (PGA=0.022g)

(b) Medium earthquake (PGA=0.07g)

(c) Large earthquake (PGA=0.1g)

Figure 5.45 Computed and measured maximum bending moment envelopes in the solid piles for different added masses and different scaled earthquakes with base sand layer modeled as a Mohr-Coulomb material

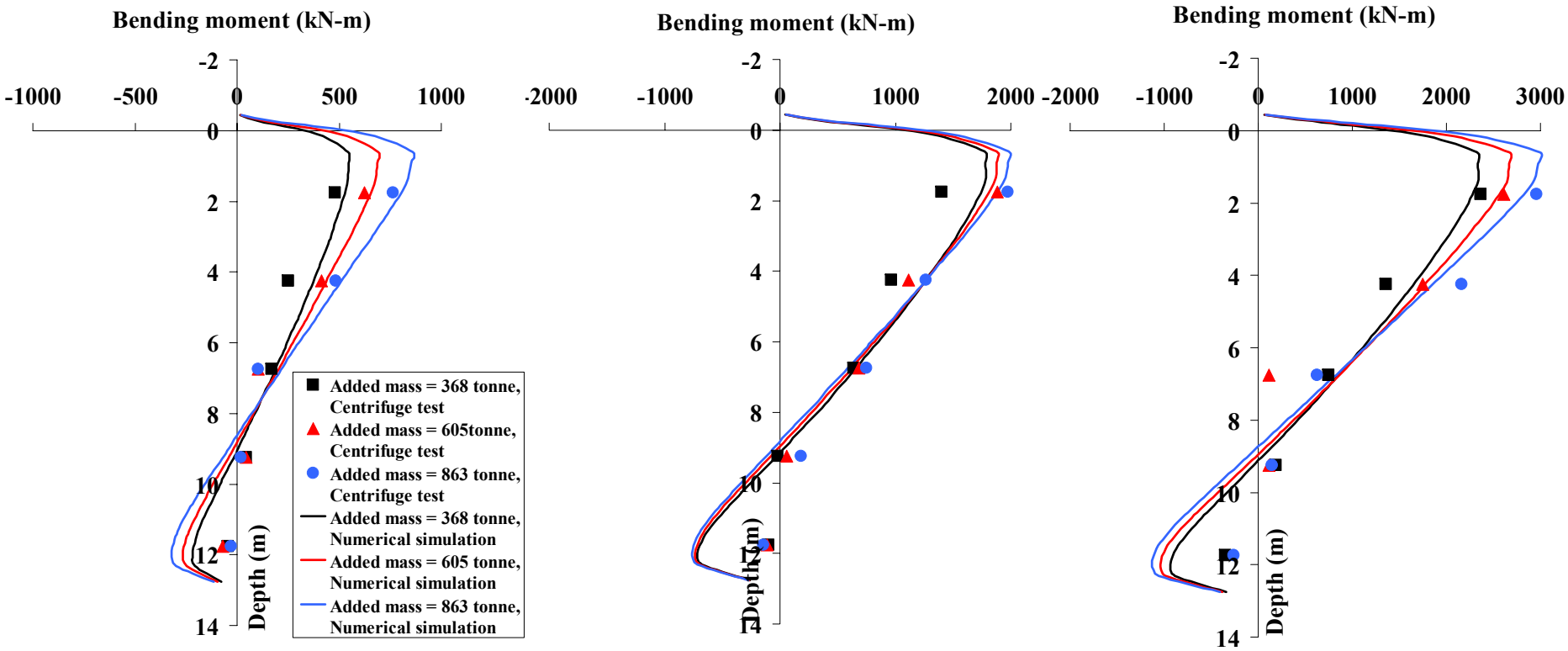

(a) Small earthquake (PGA=0.022g)

(b) Medium earthquake (PGA=0.07g)

(c) Large earthquake (PGA=0.1g)

Figure 5.46 Computed and measured maximum bending moment envelopes in the solid piles for different added masses and different scaled earthquakes with base sand layer modeled as an elastic material

CHAPTER 6 PARAMETRIC STUDIES ON EARTHQUAKE-INDUCED BENDING MOMENT ON A SINGLE PILE

6.1 Introduction

The centrifuge test results presented in Chapter 5 (see Section 5.2.4) indicate that the maximum bending moment which develops along a pile embedded in soft kaolin clay during earthquakes depends on various factors such as

(a) the magnitude of ground motion or peak ground acceleration of the earthquake,

(b) the mass introduced from the super-structure and

(c) the flexural rigidity EI of the pile material

The finite element numerical simulations using ABAQUS also show similar trends (Figure 5.40). The ability of the numerical model to reasonably replicate the centrifuge tests suggests that the former may be used to analyze conditions not considered in the centrifuge experiments, as well as to carry out sensitivity studies. In this Chapter, parameters studies on a single pile are presented to clarify how geometrical, loading and soil parameters affect the maximum bending moment in the pile.

To facilitate the parametric studies, dimensionless analysis is first used to clarify how various parameters interact with one another and what dimensionless groups can be identified. Dimensional analysis offers a tool for

reducing all the factors affecting the maximum bending moment to the simplest dimensionless form prior to obtaining a quantitative answer. Bridgman (1969) explained it thus: *"The principal use of dimensional analysis is to deduce from a study of the dimensions of the variables in any physical system certain limitations on the form of any possible relationship between those variables. The method is of great generality and mathematical simplicity"*.

6.2 Previous Works

Many studies have been carried out to examine single pile response under earthquake shaking in soft soils. However, most of these studies concentrated on the dynamic response at the pile heads ignoring moment and curvature that developed along the pile length (e.g. Margason, 1975; Blaney et al., 1976; Kagawa and Kraft, 1980; Flores-Berrones and Whitman, 1982; Kaynia and Kausel, 1982; Dobry and O'Rourke, 1983; Mamoon and Banerjee, 1990; Kaynia and Mahzooni, 1996; Guin and Banerjee, 1998; Luo and Murono, 2001). Hence piles are traditionally designed to withstand only the flexural stresses generated from the oscillations of the superstructure. However, in recent years, the importance of considering effect of soil movement along the pile length has started to be recognised (e.g. Nikolaou et al., 2001).

Kavvadas and Gazetas (1993) carried out parametric studies using the following dimensionless moment and shear terms:

$$M' = \frac{M}{\rho_p d^4 \ddot{u}_g}$$
$$Q' = \frac{Q}{\rho_p d^3 \ddot{u}_g} \qquad (6.1)$$

where M and Q are the bending moments and shears; d is the diameter of the pile and $\ddot{u}_g$ is the maximum input acceleration. The soil-pile system was modeled as a beam on Winkler foundation, subjected to vertically propagating harmonic S-waves. The results from the parametric studies were used to produce charts showing how the dimensionless moments and shears vary with depth in different types of layered grounds. These charts, however, were obtained using a free-head pile and did not include the effect of super-structural mass on the bending moment profiles.

Nikolaou et al. (1995) derived a closed-form solution of the maximum bending moment along a pile embedded in a two-layered soil where the lower layer is stiffer than upper layer (Figure 6.1). Their derivation was based on the relationship between the maximum strain, ε_m, and the corresponding bending moment, M, acting on a pile cross section of diameter, d, and Young's' modulus, E_p,

$$\varepsilon_m = \frac{M}{E_p I_p}\frac{d}{2} = \frac{M}{E_p(\pi\frac{d^4}{64})}\frac{d}{2} \approx \frac{10M}{E_p d^3} \qquad (6.2)$$

The corresponding closed-form solution is,

$$\max M = 2.7x10^{-7} E_p d^3 (\frac{a_{rock}}{g})(\frac{l}{d})^{1.3}(\frac{E_p}{E_1})^{0.7}(\frac{V_1}{V_2})^{-0.3}(\frac{h_1}{l})^{1.25} \qquad (6.3)$$

where, a_{rock} = peak ground motion

l = length of the pile

E_1= Young's' modulus of top layer

V_1 and V_2 = shear wave velocity of layer 1 and 2, respectively (Figure 6.1)

h_1= depth of the top layer

Although the expression provides a useful estimate of the maximum bending moment for a pile in layered soil, the effects of the superstructure and soil masses were not considered.

Nikolaou et al. (2001) subsequently proposed a modified dimensionless moment term as

$$M' = \frac{M}{\rho_1 h_1 d^3 a_{rock}} \tag{6.4}$$

where ρ_1 is the density of the top soil layer (Figure 6.1), which was incorporated to account for the inertial effect of the soil. The resulting expression for the maximum moment was thus obtained as,

$$\max M = 0.042 a_{rock} \rho_1 h_1 d^3 \left(\frac{l}{d}\right)^{0.30} \left(\frac{E_p}{E_1}\right)^{0.65} \left(\frac{V_1}{V_2}\right)^{-0.5} \tag{6.5}$$

The expression, however, still does not reflect the effect of the super-structural masses.

6.3 Dimensionless Groups for the Maximum Pile Bending Moment

In this section, Buckingham's π theorem will be used to obtain the dimensionless groups associated with the maximum bending moment in the pile during seismic excitation. This theorem states that when a complete relationship between n dimensional physical quantities is expressed in dimensionless form, the number of independent quantities that appear in it is reduced from the original n to n-k, where k is the maximum number of the fundamental dimensions.

Consider the single pile-raft system embedded in a uniform layer of clay underlain by bedrock, as shown on Figure 6.2. The clay thickness is equal to the pile length, and the pile tip is resting on the bedrock. The clay is detached from the raft and acts on the superstructure only through the pile. The system is subjected to rigid bedrock earthquake excitation.

This is a complex soil-pile-raft interaction problem in which there are many factors at work. To account for all these factors would make the problem unnecessarily complicated and almost intractable. Hence, for obtaining a semi-analytical expression that is useful for practical application, only the key factors affecting the maximum bending moment in the pile, M_{max}, of an equivalent circular pile are considered. These are:

1. pile length l_p
2. equivalent pile diameter d

   where $d = \sqrt{4A/\pi}$ for a non-circular pile of cross-section area A
3. flexural rigidity of pile E_pI_p

4. density of soil ρ
5. mass of raft m
6. shear modulus of soil G
7. bedrock acceleration a_b

Certain parameters have been omitted from this list. For instance, strength parameters of the soil have not been considered. The hyperbolic model discussed in Chapter 3 is actually a pseudo-effective stress model in that the ultimate deviator stress q_u is computed as a product of the friction coefficient M and the mean effective stress p' under geostatic conditions, see Equation 3.53. The friction coefficient M is related to the friction angle via the relation mentioned in Equation 3.29b. The friction angle is not included as a parameter at the outset because the soil is not really loaded to a state of failure, even for the large earthquakes. However, the sensitivity of the results to variation in friction angle will be studied in a separate section.

Another parameter which has been omitted is the frequency of the excitation. This parameter was omitted because natural earthquake ground motion is really a broad spectrum perturbation and cannot readily be characterized by a single frequency. Instead of considering the effect of frequency explicitly, the approach chosen herein is to study sensitivity of the results to two types of earthquakes. The first of these is the earthquake waveform used in the centrifuge model tests, which is representative of a far-field earthquake with a main energy spectrum lying between a period of 0.8s and 1.5s. The second type is a near-field earthquake with a main energy spectrum lying between a period of 0.2s and 1s, that is with higher frequency

content. Representative near-field earthquakes used in the sensitivity study are the El Centro and Loma Prieta earthquake ground motions.

Another parameter which has been discounted is the pile diameter. The pile diameter has two effects. Firstly, it is related to the 2nd moment of area, which in turn affects the flexural rigidity of the pile. Secondly, it is possible that changes in the projected area of the pile in the soft clay in the direction of earthquake shaking may have some effect on the pile bending moment, since it may affect the amount of soil stresses which are transferred between the soil and pile. The significance of the second effect is examined by carrying out an additional ABAQUS finite element analysis for a larger concrete infill pile diameter of 1.5m, but with a significantly reduced pile modulus (E_p) which yields a flexural rigidity (EI) identical to that of a 0.5m diameter concrete infill pile. Figure 6.3 compares the bending moment profiles for the 0.5m and 1.5m diameter piles with identical flexural rigidities. Near the pile head, the computed bending moment profiles are quite close. At greater depths, the larger diameter pile produced slightly larger (negative) moments. Overall, it appears that the computed bending moment profiles are not significantly different for the two pile diameters with identical flexural rigidity and maximum moment along the pile length remains largely unchanged. Hence, the flexural rigidity (EI) of the pile plays major role near the pile head. Hence, it can be concluded that for a single pile with relatively fixed head condition, soil-pile stress transfer may not depend significantly upon the pile diameter, within the range investigated. This would suggest that the main effect of the diameter (d) is to change the 2nd moment of area of the pile. Hence d can be replaced by an equivalent diameter, d_e, defined as,

$$d_e = \sqrt[4]{I_p} \tag{6.6}$$

Hence, there are altogether 8 quantities (including the maximum bending moment M_{max}) and 3 dimensions, and 8 – 3 = 5 dimensionless groups. The 5 dimensionless groups may be obtained as:

1. Dimensionless bending moment, $M^* = \frac{M_{\max} d_e}{E_p I_p}$

2. Slenderness ratio l* = $\frac{l_p}{d_e}$

3. Frequency ratio $a_0 = \frac{E_p I_p \rho}{G\, m l_p}$. This term expresses the ratio of the fundamental mode natural frequency of the pile-raft system to that of the clay layer. The derivation for this is shown in Appendix A.

4. Mass ratio $\beta = \frac{\rho d_e^{\,3}}{m}$. This group expresses the ratio of an equivalent mass of the soil around the pile to the mass of raft.

5. Dimensionless acceleration $\alpha = \frac{a_b}{g}$, where g is the gravitational free-fall acceleration.

6.4 Parametric Studies

This section examines the effects of the slenderness ratio, frequency ratio, mass ratio and dimensionless acceleration on the dimensionless moment. To facilitate a proper study, a sufficiently large number of cases have to be analysed. Apart from the finite element analyses presented and discussed in Chapter 5, where simulations were done with varying pile types and added masses, some additional simulations were carried out in this section by varying the pile lengths. Besides the 13 m pile length that was analyzed in Chapter 5 based on the experimental dimensions, all the analyses of Chapter 4 were repeated for four other pile lengths: 10, 7.6, 4.6 and 3 m.

Figure 6.4a shows the variation of dimensionless moment with slenderness ratio for various cases. In this figure, each line represents the cases corresponding to a certain combination of the dimensionless frequency, mass ratio and dimensionless acceleration. Figures 6.4b – d show the corresponding correlation of dimensionless moment to dimensionless frequency, mass ratio and dimensionless acceleration. As Figure 6.4d shows, the relationship between the dimensionless moment and base acceleration is almost linear for nearly all cases. This linear relationship may be due to two possible reasons. Firstly, the strain level is sufficiently low so that the soil remains in the small strain linear range and there is negligible softening and increase in damping ratio. However, this seems unlikely since the largest base acceleration is about 0.22g. The second possibility is that the behavior of the soil-pile-raft system may be dominated by the stiffness of the pile and the mass of the raft and soil, with the stiffness of the soil playing a relatively minor role. This is not

implausible since the natural frequency of the pile-raft system (without the soil) is much higher than the frequency bandwidth of the base acceleration.

Figures 6.4a and c show that both the slenderness ratio and mass ratio also have significant influence on the dimensionless moment. The variation of moment with mass ratio is nearly linear and indicates that both the mass of the soil and pile plays a significant role. The variation of moment with slenderness ratio appears to be linear in some cases and sub-linear in other cases. On the other hand, as Figure 6.4b shows, for the stiffer piles, the effect of the frequency ratio on the moment appears to be less than that of the other dimensionless groups. This would be consistent with the hypothesis above that the stiffness of the soil has a smaller effect than the rest of the other parameters.

6.5 Formulation of the Dimensionless Bending Moment Relationship

As discussed above, all four dimensionless groups have an effect on the dimensionless moment, with the frequency ratio having a relatively minor effect. In this section, the dimensionless moment will be correlated to the other four dimensionless groups. Following the usual convention in dimensional analysis, the effects of the various dimensionless groups are assumed to be multiplicative (e.g. Langhaar 1951; Nikolaou et al. 2001), that is, the dimensionless moment M^*) is assumed to be related to the other four dimensionless group via a relationship of the form,

$$M^* = \frac{M_{\max} d_e}{E_p I_p} = f\left(\frac{l_p}{d_e}, \frac{a_b}{g}, \frac{E_p I_p \rho}{G m l_p}, \frac{\rho d_e^3}{m}\right) = A\left(\frac{l_p}{d_e}\right)^{b_1}\left(\frac{a_b}{g}\right)^{b_2}\left(\frac{E_p I_p \rho}{G m l_p}\right)^{b_3}\left(\frac{\rho d_e^3}{m}\right)^{b_4} \quad \text{.....(6.7)}$$

The coefficients A, b_1 , b_2 , b_3 and b_4 may be determined through a trial and error process which involves the dimensionless maximum moment term (on the left hand side) calculated using the results from finite element analyses, and the various dimensionless groups (on the right hand side) based on the geometry and material parameters.

The trial and error process to obtain the mathematical form of Eq. 6.7 involves the systematic determination of the coefficients A, b_1 , b_2 , b_3 and b_4 that will minimize the scatter shown on Figure 6.4a. As a first step in this process, the dimensionless group $\frac{a_b}{g}$ is first introduced. As shown on Figure 6.5, the ordinates are condensed to some extent by plotting $(M^*)^{0.1}$ $(\frac{a_b}{g})^{-0.1}$ against $(\frac{l_p}{d_e})$. The exponents 0.1 and -0.1 are obtained through a trial and error procedure to yield the optimal minimization of the scatter.

In a similar manner, the other two dimensionless groups, $\frac{E_p I_p \rho_s}{G m l_p}$ and $\frac{\rho d_e^3}{m}$, may be introduced into the ordinate. As shown on Figures 6.6 and 6.7, the subsequent incorporation of these two groups with the appropriate exponents significantly improves the banding of the scattered plots.

Accordingly, the final ordinate can be expressed as

$$Y^* = (M^*)^{0.1}(\frac{a_b}{g})^{-0.1}(\frac{E_p I_p \rho}{G m l_p})^{-0.01}(\frac{\rho d_e^3}{m})^{0.09} \qquad (6.8)$$

The comparison of Figures 6.7 and 6.4a suggest, while a perfect condensation of the data scatter may not be possible, the data can be condensed within a narrow band by judicious choice of the various indices.

Furthermore, the condensed plot of Figure 6.7 is linearized in Figure 6.8 by taking an exponent on the slenderness ratio ($\frac{l_p}{d_e}$), such that the abscissa becomes

$$l^* = (\frac{l_p}{d_e})^{0.06} \tag{6.9}$$

Figure 6.8 suggests that the average slope of the condensed linear trend is 0.26. Hence the linear relation can be expressed as,

$$Y^* = 0.26(l^*)^{0.06} \tag{6.10}$$

Hence, from equation 6.8, 6.9 and 6.10,

$$(M^*)^{0.1}(\frac{a_b}{g})^{-0.1}(\frac{E_p I_p \rho}{Gml_p})^{-0.01}(\frac{\rho d_e^3}{m})^{0.09} = 0.26(l^*)^{0.06} \tag{6.11a}$$

$$\Rightarrow \frac{M_{\max} d}{E_p I_p} = 1.4x10^{-6}(\frac{a_b}{g})(\frac{E_p I_p \rho}{Gml_p})^{0.1} \frac{(l^*)^{0.6}}{(\frac{\rho d_e^3}{m})^{0.9}} \tag{6.11b}$$

$$\Rightarrow M_{\max} = 1.4x10^{-6} \frac{E_p I_p}{d}(\frac{a_b}{g})(\frac{E_p I_p \rho}{Gml_p})^{0.1} \frac{(\frac{l_p}{d})^{0.6}}{(\frac{\rho d_e^3}{m})^{0.9}} \tag{6.11c}$$

Equation 6.11 represents a correlated summary of the effects of various parameters on the maximum bending moment induced in a single piles under earthquake loading. The solution, however, is only valid for fixed pile-head condition with pile tip resting on a stiff soil layer.

6.6 Influence of Friction Angle

As mentioned earlier, Eq. 6.11 does not consider the effect of the friction angle of soil. In this subsection, the sensitivity of the bending moment results to the friction angle is examined. Besides the reference friction angle of 23°, three other friction angles are considered: 20°, 30° and 38°. Figure 6.9 shows the bending moment profiles associated with the different soil friction angles. As can be seen, in all cases, the bending moment distributions are almost identical. These results suggest that the friction angle does not significantly affect the bending moment developed along the pile. Hence, for all practical purposes, it appears that the effect of friction angle need not be considered in formulation of the dimensionless bending moment relationship. It is noted that the friction angle was also omitted from previously proposed solutions such as Eq. 6.3 and 6.5, (Nikolaou et al., 1995; 2001).

Figures 6.10 and 6.11 plot the modulus reduction and damping ratios with strain levels for different values of M corresponding to the friction angles considered in this section. The results shown on Figure 6.10 indicate that M=0.77 (φ=20°) and M=1.55 (φ=38°) provide approximate lower and upper bounds respectively to the modulus reduction curves compiled from the available published literature. On the other hand, Figure 6.11 shows that the same parameters, M=0.77 (φ=20°) and M=1.55 (φ=38°), result in approximate upper and lower bounds respectively to the published damping ratio curves. Hence, the friction angle ϕ affects both the strain-dependent modulus reduction and damping ratio responses of the soil. However, the 3-D FEM results presented earlier in this section suggest that the bending moments in

the pile are not significantly affected by the friction angle, from which it follows that the variations in the modulus reduction and damping ratio curves do not significantly affect the bending response of the pile

6.7 Comparison of Fitted Equation with Computed results

In this section, the predictions of Eq. 6.11 will be checked against the results from ABAQUS analyses performed using the 3-D soil-pile-raft model shown on Figure 5.24. The reference baseline of the parametric studies will adopt the identical geometries and material properties of the numerical verification study of Section 5.3, as tabulated in Table 6.1 for a concrete infill pile.

6.7.1 Effect of Pile Length

Figure 6.12 plots the maximum pile bending moments obtained from the ABAQUS analyses, for five different pile lengths of 13, 10, 7.6, 4.6 and 3 m. The analyses were carried out for the three pile types considered in Chapter 5, subjected to the small earthquake shown on Figure 4.11.

For all three pile types, Figure 6.12 shows that the maximum bending moment from the numerical analyses increases with pile length up to about 10 m, beyond which there is little or no change in the maximum value. Such a response is consistent with the idea of a critical pile length under dynamic loadings. Several formulas have been proposed for estimating the critical length under dynamic conditions (Gazetas, 1984), as shown on Table 6.2. Using the soil and pile parameters of the current analyses, the estimated

critical lengths are shown on Table 6.3. For all three pile types, the estimated critical lengths using Gazetas' (1984) relationships fall between 9 and 10m, which agrees well with the trend shown on Figure 6.12.

For the concrete infill pile, Figure 6.13 shows the maximum moment response predicted using Eq. 6.11 for different pile lengths, together with the corresponding ABAQUS results of Figure 6.12. It appears that that Eq. 6.11 is able to capture the increasing maximum bending moments quite reasonably up to the critical pile length of about 10 m, after which it continues to predict an increasing trend whereas the FEM results indicate that the maximum moments remain relatively constant. To account for the critical pile length effect, Eq. 6.11 may be modified as

$$M_{\max} = 9.7656x10^{-4}\frac{E_p I_p}{d}\left(\frac{a}{g}\right)\left(\frac{E_p I_p \rho}{GMl_p}\right)^{0.1}\left(\frac{l_p}{d}\right)^{0.6}\left(\frac{\rho r_0^3}{M}\right)^{-0.8} \quad \text{for } l_p \le l_c \qquad \ldots (6.12a)$$

$$M_{\max} = 9.7656x10^{-4}\frac{E_p I_p}{d}\left(\frac{a}{g}\right)\left(\frac{E_p I_p \rho}{GMl_c}\right)^{0.1}\left(\frac{l_c}{d}\right)^{0.6}\left(\frac{\rho r_0^3}{M}\right)^{-0.8} \quad \text{for } l_p > l_c \qquad \ldots (6.12b)$$

where l_p is the length of the pile and

l_c is the critical length of the pile and can be estimated using the relationships proposed in Table 6.2a.

6.7.2 Effect of Flexural Rigidity

As mentioned earlier that an increase in pile diameter increases the moment of inertia I_p and thereby the flexural rigidity E_pI_p, which contributes to an increase in the maximum bending moment M_{max}. Figure 6.14 shows the variation in maximum moment with flexural rigidity when the latter is varied from 700 MN-m^2 to 16500 MN-m^2 with the other parameters as shown in Table 6.1. As can be seen, the results show an almost linear increase in the maximum bending moments with E_pI_p.

Figure 6.14 also compares the prediction from Eq. 6.11 with the results from ABAQUS finite element analyses for E_pI_p = 14374, 10308.30, 7187, 4285.78 and 3545 MN-m^2. As can be seen, Eq. 6.11 appears to slightly under-predict the bending moments for lower pile modulus.

6.7.3 Effect of Soil Modulus

The soil shear modulus (G) in Eq. 6.11 is taken as the small strain shear modulus (G_{max}). G_{max} is chosen as a characteristic shear modulus in Eq. 6.11 largely because this quantity may be estimated with reasonable accuracy via a simple correlation with the shear wave velocity (V_s) of the soil layer

$$G_{max} = \rho V_s^2 \tag{6.13}$$

where ρ is the density of the soil layer.

The parametric study was carried out by varying G (= G_{max}) in Eq. 6.11 from a very small value to about 150 MPa. The predicted maximum bending moments decrease with increasing G, as shown by the solid line on Figure

6.15. A similar trend was reported by Nikolaou et al. (1995, 2001); see Eqs. 6.3 and 6.5.

Figure 6.15 also shows the results from ABAQUS finite element analyses, plotted as solid symbols. These were obtained using ten different G_{max} values ranging from 30 MPa to 150 MPa and the baseline parameters of Table 6.1. The maximum bending moments predicted using Eq. 6.11 appear to match the ABAQUS results quite well for all G_{max} values. Overall, the variation over the range of G_{max} investigated is relatively small. This is consistent with the earlier observation that the stiffness of the soil layer appears to play a relatively minor role in the bending moment of the pile.

6.7.4 Effect of Raft

As previously discussed in Section 5.2.4.2, increasing the added masses on the raft results in higher pile bending moments. Besides the three added mass levels considered in that section, additional analyses were carried out in ABAQUS for two higher masses of 1078 and 1406 tonnes, using the baseline parameters (Table 6.1). The ABAQUS results are plotted on Figure 6.16, together with the maximum bending moments obtained by varying the raft mass in the semi-analytical relationship of Eq. 6.11. Overall, the comparison is quite favorable.

6.7.5 Effect of Peak Ground Acceleration (PGA)

As mention earlier, Eq. 6.11 was established using the centrifuge earthquake, which comprises basically of long-period motion. In this section, finite element analyses were carried out to examine the effect of different bedrock motion. A total of 7 bedrock motions were used. Five of these motions were obtained by scaling the time histories of the input motion used in the centrifuge tests (Figure 4.11) to obtain different peak ground acceleration. As such, these five earthquakes possess the same frequency content, but different scaled accelerations of 0.02g, 0.07g, 0.1g, 0.125g and 0.2g. In addition, to vary the frequency content, the other two ground motions for the ABAQUS analyses were obtained by scaling the earthquake time histories associated with the El Centro and Loma Prieta earthquakes to obtain peak ground accelerations of 0.25g and 0.26g respectively, as shown on Figure 6.17a. Figure 6.17b shows the frequency spectra associated with the centrifuge, El Centro and Loma Prieta earthquakes.

The results from the seven ABAQUS analyses are plotted as solid symbols on Figure 6.18. It appears that the finite element results exhibit a relatively linear trend, which matches quite favorably with the predictions using Eq. 6.11. Thus, Eq. 6.11 seems to work reasonably well for both an idealized far-field earthquake as well as two near-field earthquakes.

6.8 Comparison with Centrifuge Results

In this section, the prediction of Eq. 6.11 will be compared against the centrifuge test results. Table 6.4 summarizes the maximum bending moments measured from the centrifuge tests along with the predicted results.

As can be seen**,** for majority of the cases (~75%), centrifuge test results fall within 10% of the predictions using Eq. 6.11. For about 15% cases, Eq. 6.11 tends to over predict the centrifuge results by more than 30%. This is probably because, for those particular cases, the ABAQUS analyses also considerably over-estimate the maximum bending moments compare to the centrifuge test results(see Section 5.3.3, Figure 5.39a). It can therefore be said that, in spite of a few discrepancies, the centrifuge test results match the predictions quite reasonably.

6.9 Comparison with Design Charts Provided by Tabesh And Poulos (2007)

Tabesh and Poulos (2007) published design charts of maximum bending moment in single piles embedded in a linearly elastic homogeneous clay layer and subjected to seismic excitation, based on dynamic analysis of a Winkler soil-beam system. The actual analysis is preceded by a seismic site response analysis, which gives the soil movement at the location of the pile element at each time step. By assuming that the site consists of horizontally infinite layers, the soil is modeled as a mass–spring–dashpot system and the pile is modelled as a beam that bends in the direction of loading. In the

analysis, the effects of super-structural loads were considered by applying an axial load on pile head (Figure 6.19).

The charts were plotted for different pile lengths and diameters, as well as different elastic soil modulus. The analyses considered a single fixed-head pile embedded in a homogeneous soil layer with a constant Young's modulus of 25, 50 or 100 MPa. The pile diameters ranged from 0.2 m to 1.5 m, in 0.1 m increment. The pile modulus values used for the study were 10,000 and 30,000 MPa. No account was taken of possible pile cracking during strong motion, and it was assumed that the pile preserved its integrity during the excitation.

In this analysis, the axial loads acting on the pile were evaluated as the ultimate load capacities of the pile, with factors of safety of 2, 2.5 and 3. All the earthquakes used in the analyses have a peak bedrock acceleration of 0.1g.

Figure 6.20 compares the present ABAQUS results with the design charts published by Tabesh and Poulos (2007) for different soil damping ratio. The results indicates that, for damping ratios of 10% and 5%, the maximum moments computed in ABAQUS are significantly lower than those shown on the design charts. For 0% damping (Figure 6.20c), there is favourable agreement up to a diameter of 1.1~1.2 m. This is probably because Tabesh and Poulos (2007) did not include damping in their analyses. Beyond 1.2 m, the design charts tend to over-estimate the maximum moments.

6.10 Concluding Remarks

In the current chapter, parametric study on maximum bending moment of pile was carried out using ABAQUS. The bending moment is found to be a function of length and diameter of the pile, pile and soil moduli, mass of the raft as well as magnitude of bed rock motion (PGA). The results of the parametric study can be summarized using a fit relationship of dimensionless groups. Comparison of the fitted relationship with centrifuge data show reasonably good agreement. Comparison of the fitted relationship with ABAQUS prediction using the El Centro and Loma Prieta earthquake ground motion as input also show reasonable agreement. Finally, comparison with Tabesh and Poulos' (2007) results shows good agreement if the damping is turned off. This is attributable to the fact that Tabesh and Poulos did not incorporate damping into their analyses.

Table 6.1 The reference baseline parameters for the parametric study

Pile modulus	E_p, kPa	59633427
Soil modulus	G, kPa	66590
Density of soil	ρ, kg/m^3	1600
Length of pile	l_p, m	13
Added mass on raft	m, kg	367968.7
Peak ground acceleration	PGA, m/s^2	0.22

Table 6.2 Calculation of critical length as recommended by Gazetas (1984)

Soil model	Active length l_a	
	Expression	Typical range
A $(E = E_s z/d)$	$3.2d\left(\frac{E_p}{E_s}\right)^{1/5}$	$6d - 15d$
B $(E = E_s\sqrt{z/d})$	$3.2d\left(\frac{E_p}{E_s}\right)^{2/11}$	$6d - 17d$
C $(E = E_s)$	$3.3d\left(\frac{E_p}{E_s}\right)^{1/5}$	$8d - 20d$

(a) Critical length as calculated by Gazetas (1984)

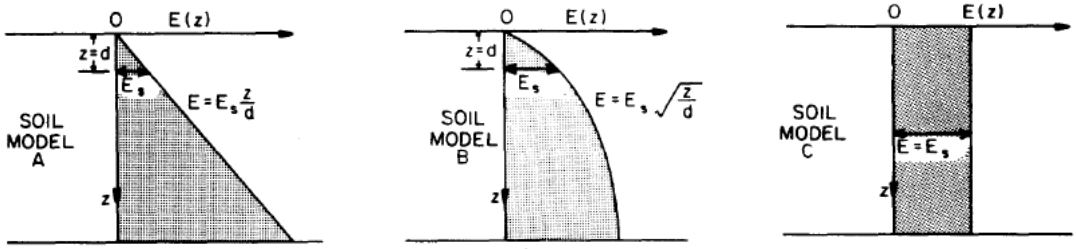

(b) Soil models used by Gazetas (1984)

Table 6.3 Critical length of the pile used in the current study calculated as per Gazetas (1984)

E_p, kPa	G_s, kPa	E_s, kPa	d, m	Soil model A	Soil model B	Soil model C
49326000	66590	199770	1.1	8.82	8.82	8.82
59633427	66590	199770	1.1	9.1	9.92	11
143432000	66590	199770	1.1	10.53	10.53	10.53

Table 6.4 Comparison of centrifuge tests results with the predictions using the fitted relationship (Eq. 6.11)

Pile type	E_p (kPa)	Added mass (tonnes)	PGA (m/sec^2)	Maximum moment (kN-m)		%error
				Eq. 6.11	Centrifuge tests	
Solid	143432000	368	0.22	577.62	481	20.09
		605	0.22	661.80	622	6.40
		863	0.22	862.38	765	12.73
		368	0.7	1382.34	1400	-1.26
		605	0.7	1930.24	1880	2.67
		863	0.7	2012.22	1974	1.94
		368	1	2406.75	2366	1.72
		605	1	2748.29	2610	5.30
		863	1	3020.73	2959	2.09
Concrete in-fill	59633427	368	0.22	396.91	324.49	22.93
		605	0.22	475.32	323.43	46.96
		863	0.22	567.77	383	48.24
		368	0.7	775.65	711	9.09
		605	0.7	1155.30	1130	2.24
		863	0.7	1505.46	1440	4.55
		368	1	1296.45	1200	8.04
		605	1	1644.92	1530	7.51
		863	1	2050.29	2020	1.50
Hollow	49326000	368	0.22	323.76	300	7.92
		605	0.22	385.77	275	40.28
		863	0.22	460.81	343	34.35
		368	0.7	671.49	618	8.66
		605	0.7	968.90	963	0.61
		863	0.7	1262.57	1370	-7.84
		368	1	1169.12	1110	5.33
		605	1	1451.12	1440	0.77
		863	1	1664.03	1600	4.00

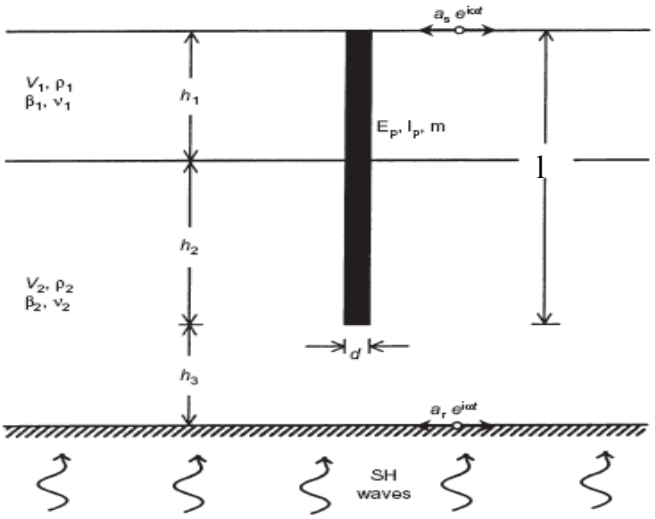

Figure 6.1 Numerical model used by Nikolau et al. (2001)

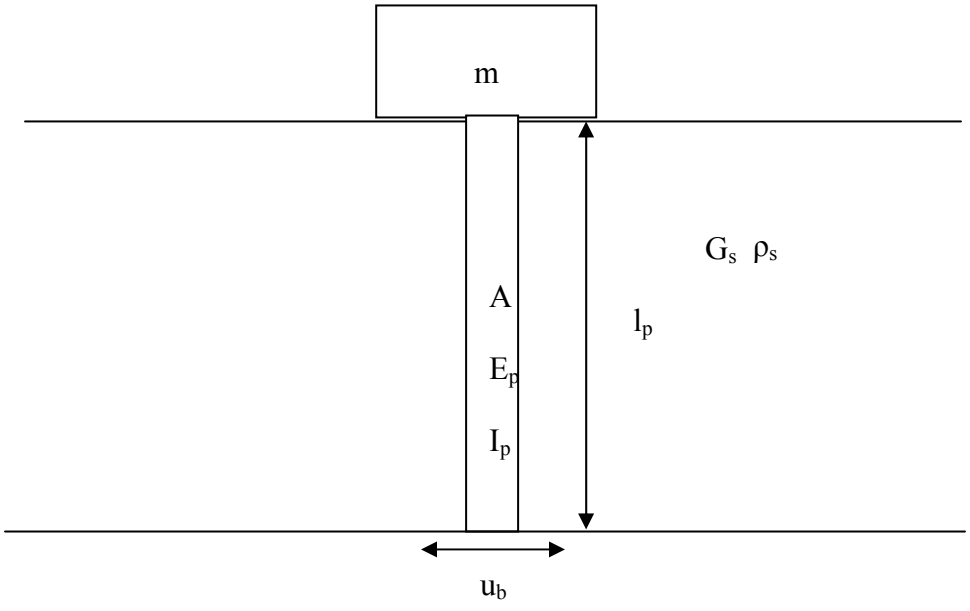

Figure 6.2 Idealized single pile-raft model used for dimensional analysis

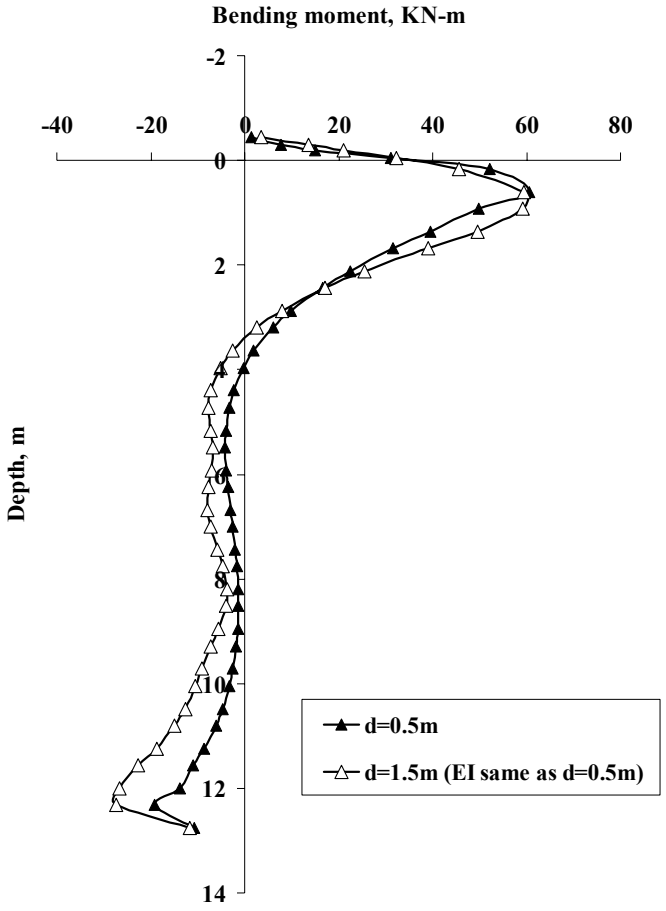

Figure 6.3 Comparison of maximum bending moment envelopes of different diameter (0.5 m and 1.5 m), but with the same flexural rigidity

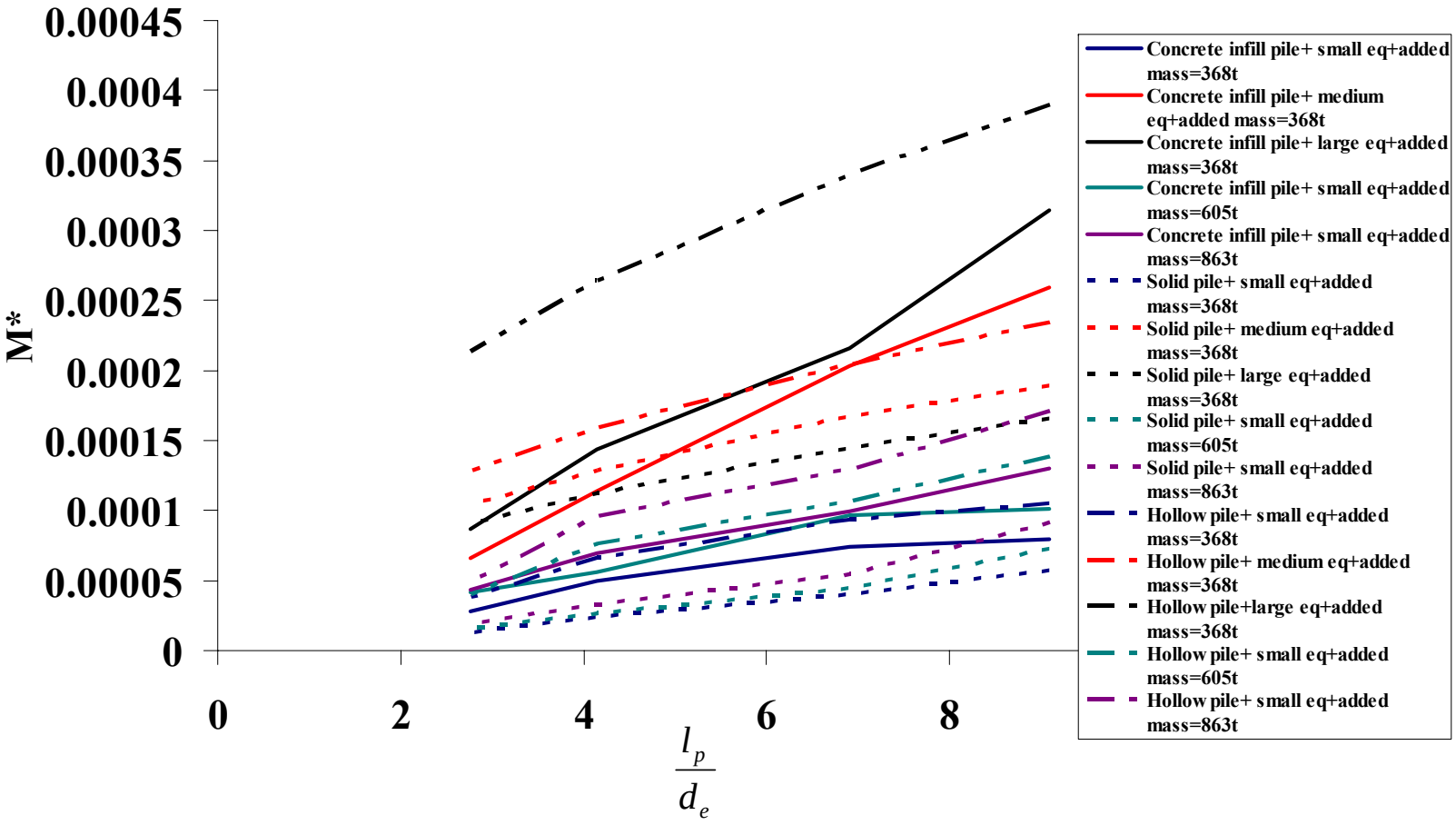

Figure 6.4a Dimensionless moment M^* vs Slenderness Ratio ($\frac{l_p}{d_e}$) for different combinations of pile types, added masses and scaled earthquakes

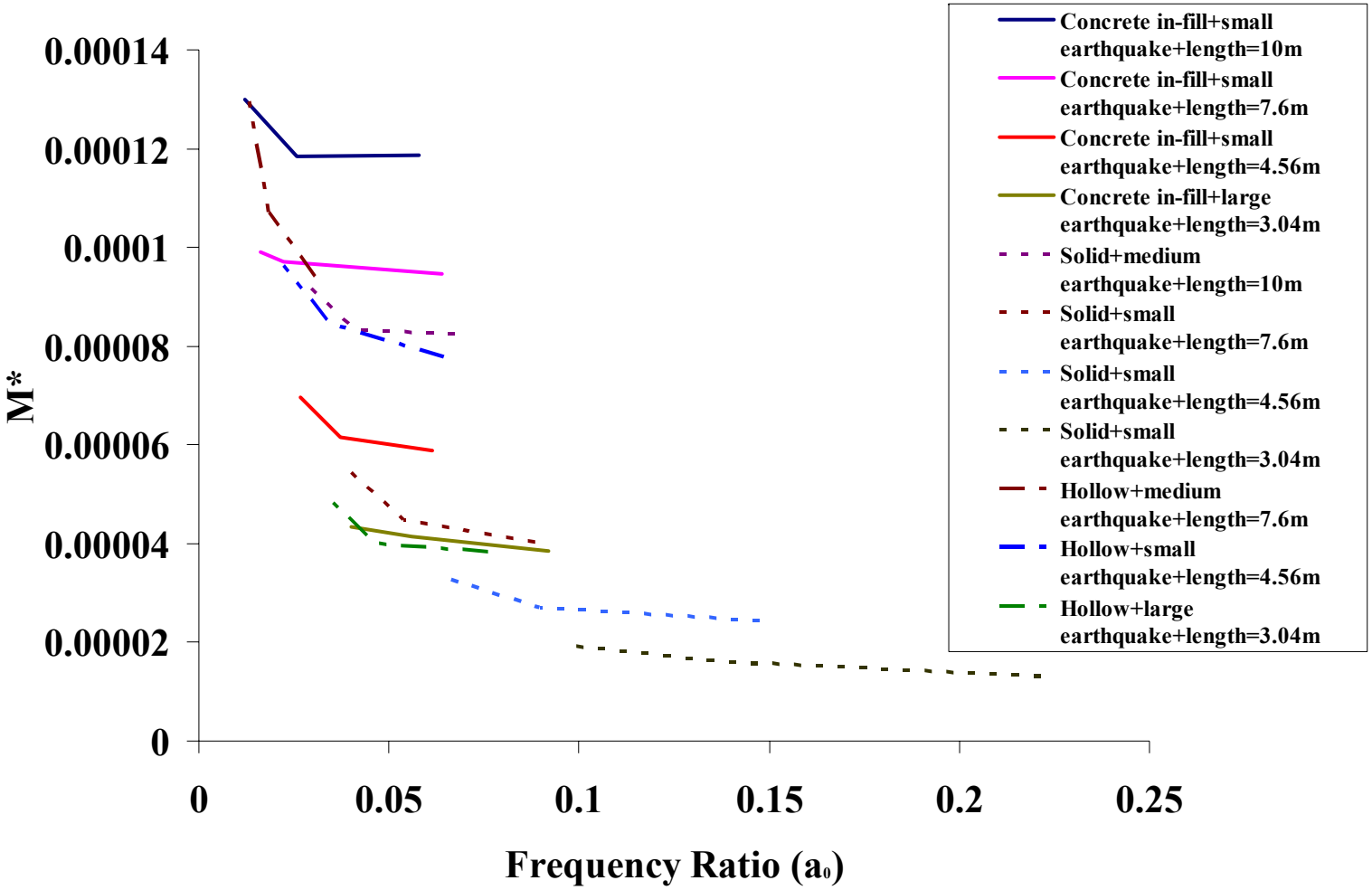

Figure 6.4b Dimensionless moment M^* vs Frequency Ratio (a_0) for different combinations of pile types, pile lengths and scaled earthquakes

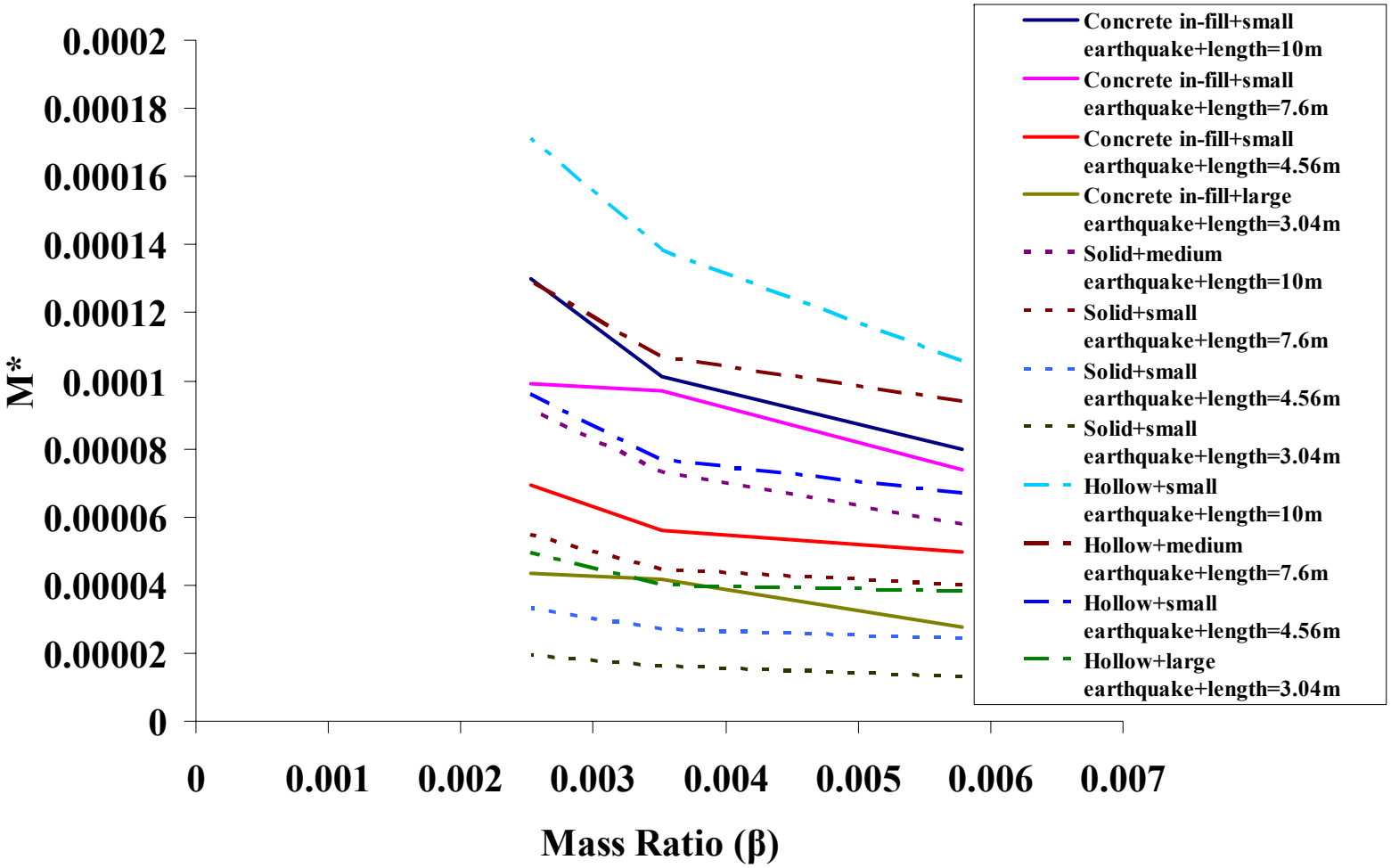

Figure 6.4c Dimensionless moment M^* vs Mass Ratio (β) for different combination of pile types, pile lengths and scaled earthquakes

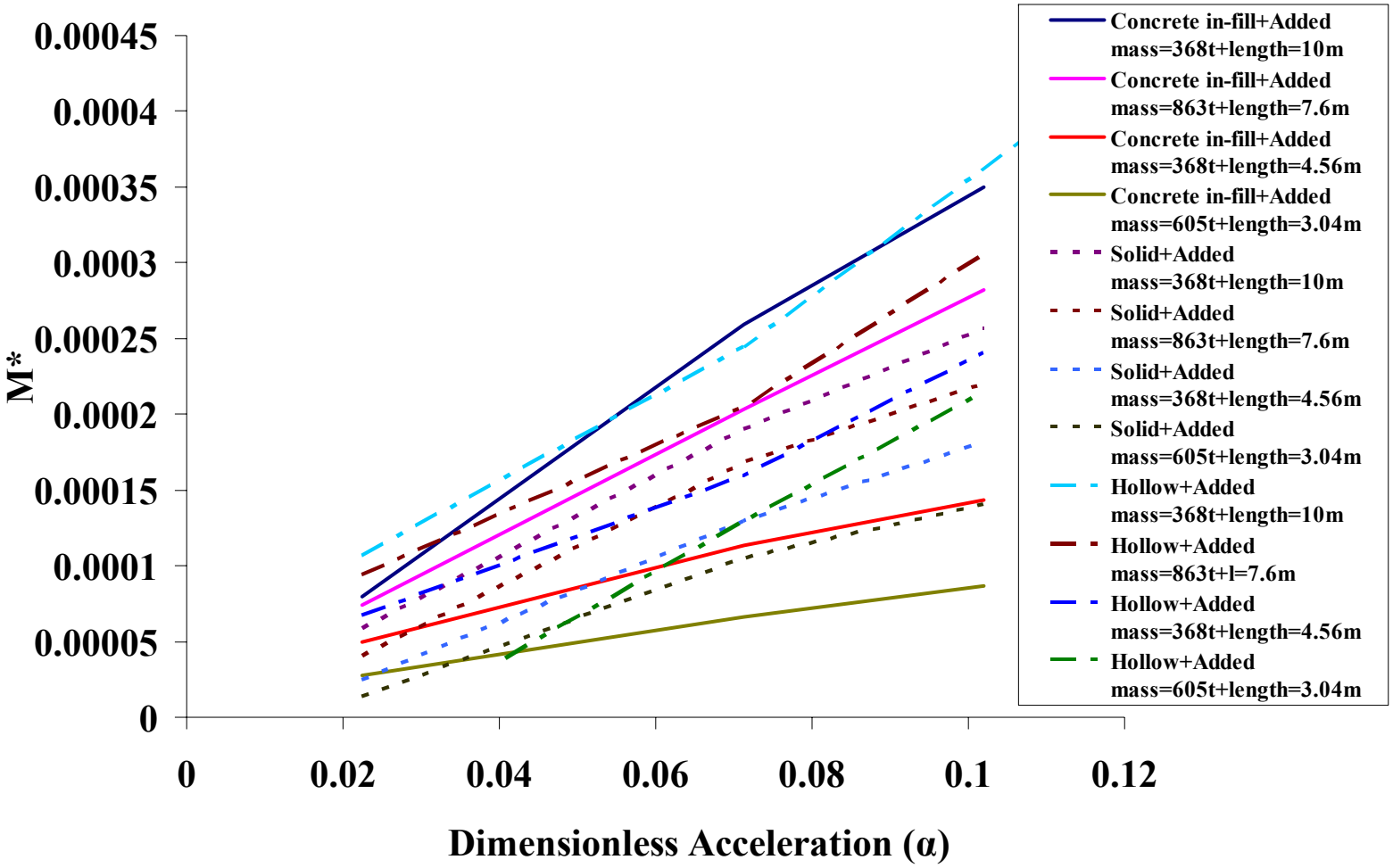

Figure 6.4d Dimensionless moment M^* vs Dimensionless Acceleration (α) for different combinations of pile types, pile lengths and added masses

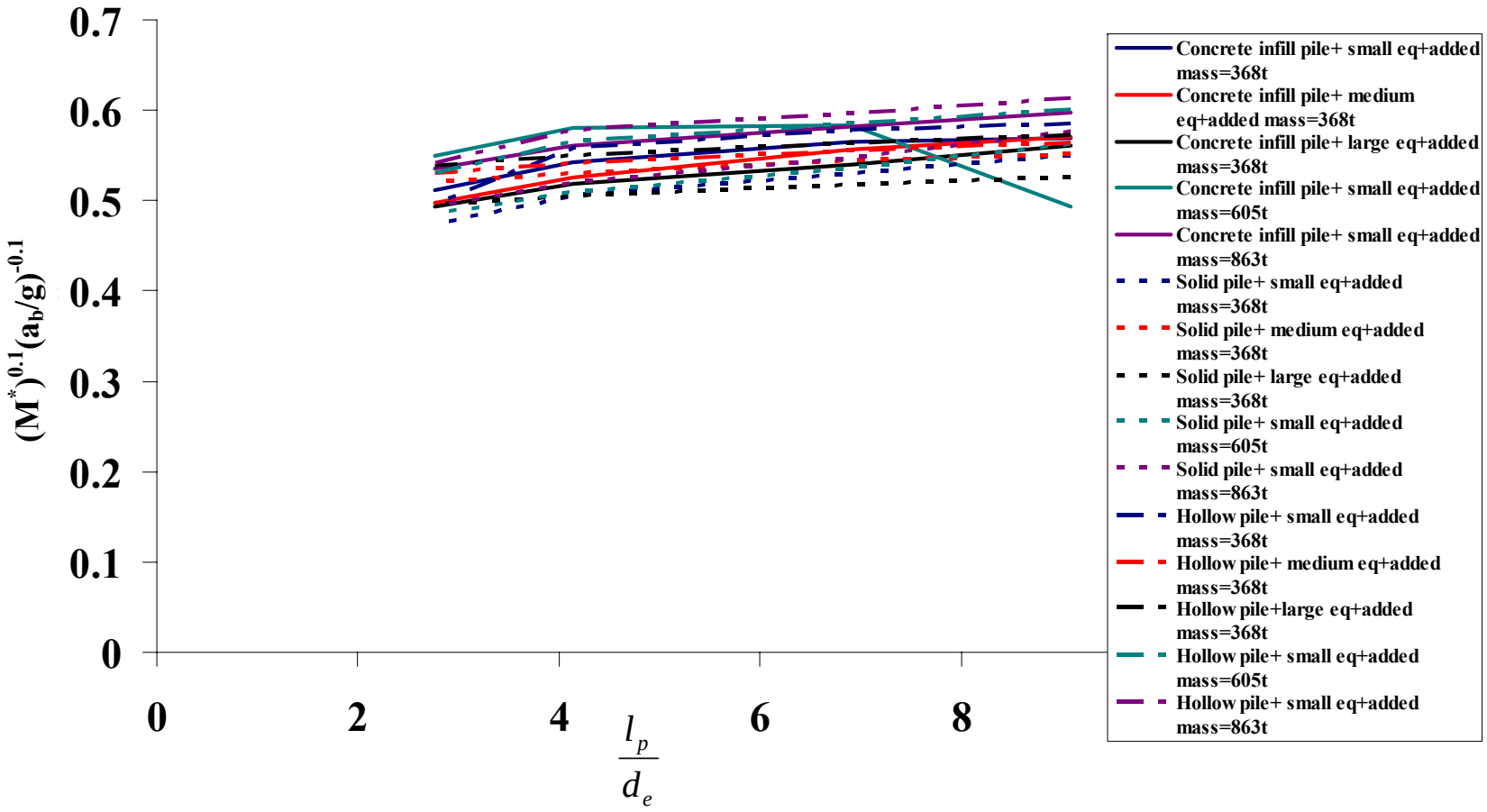

Figure 6.5 Condensation of dimensionless moment and dimensionless acceleration

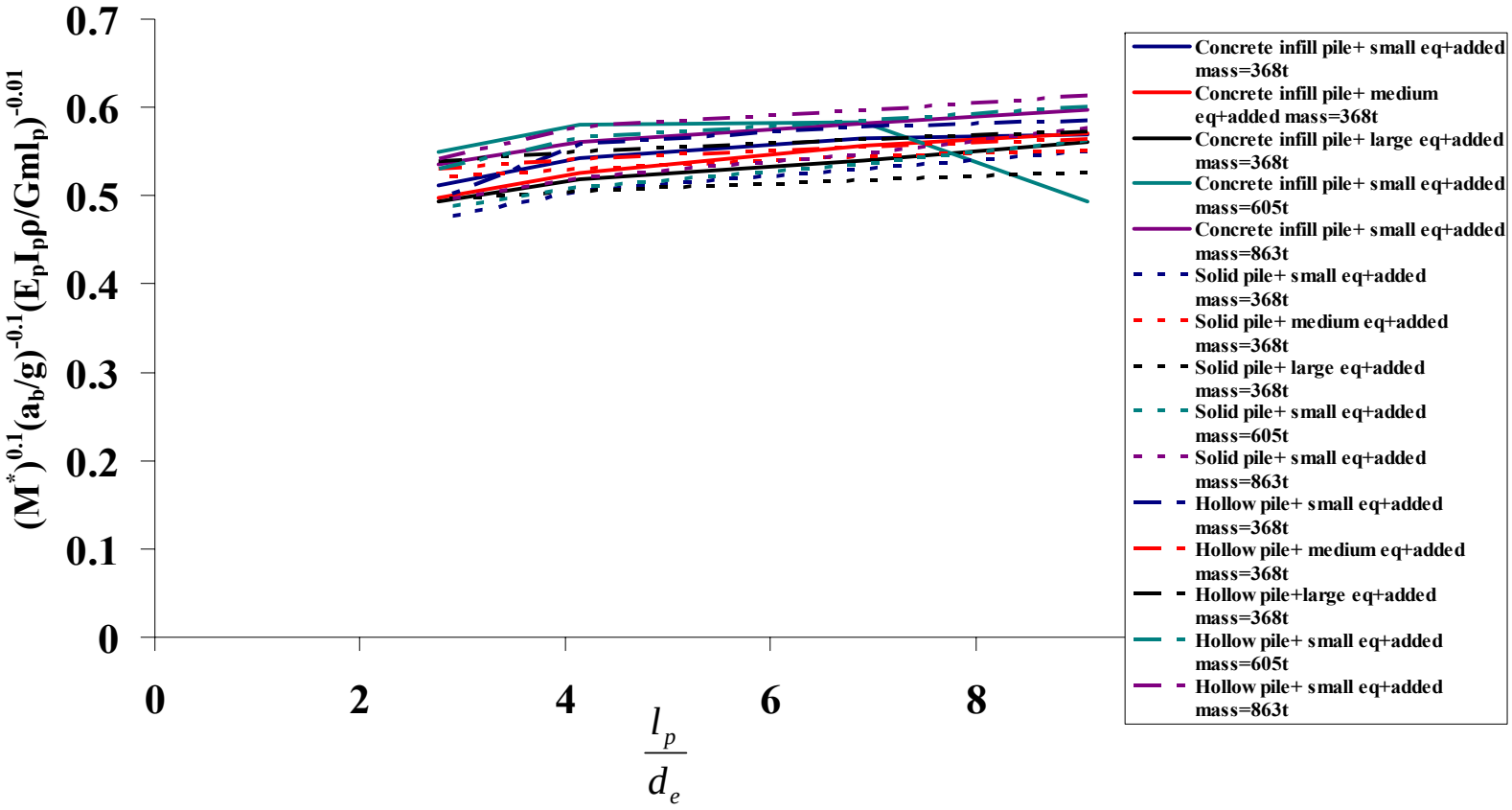

Figure 6.6 Further condensation of the dimensionless moment, incorporating the frequency ratio

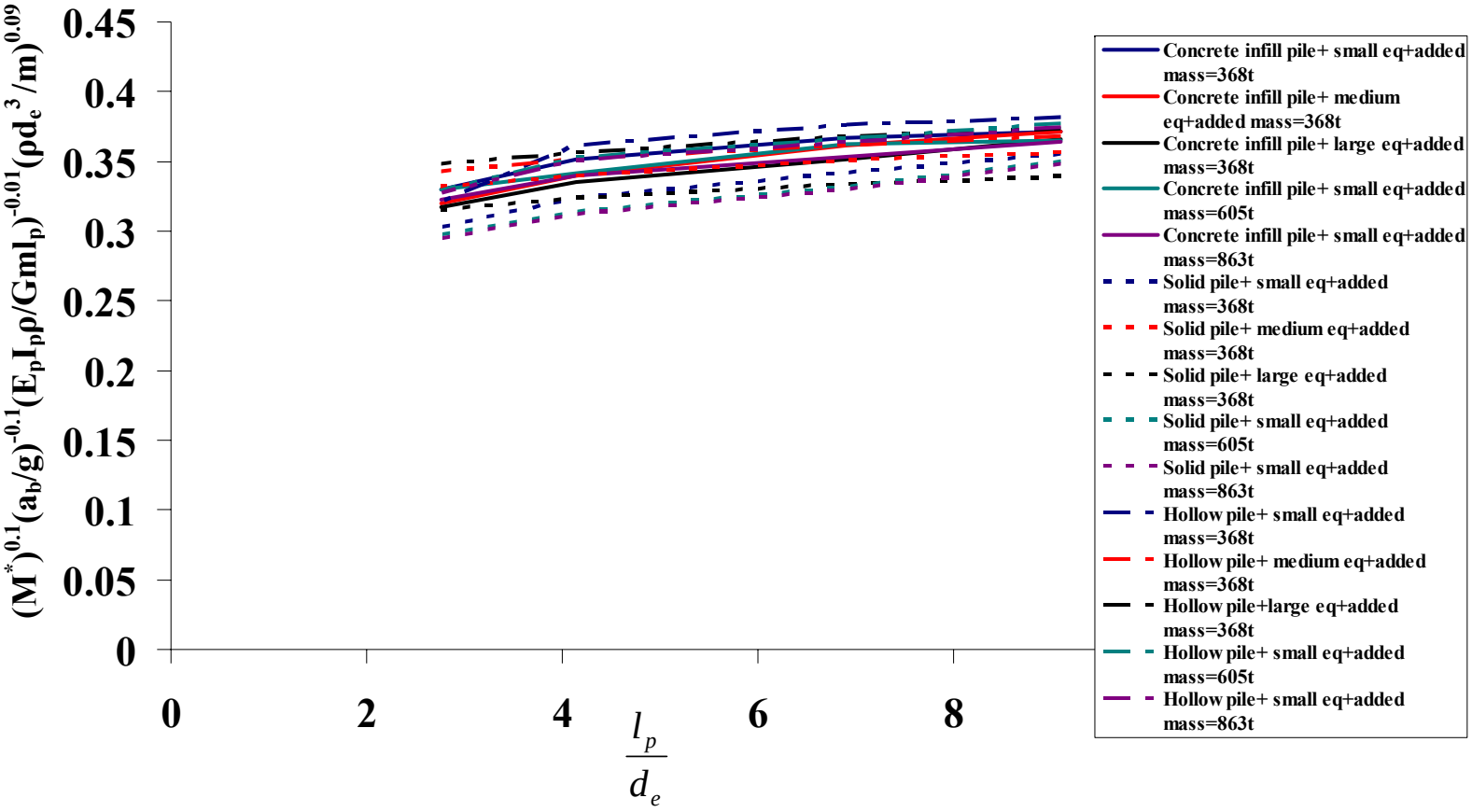

Figure 6.7 Final condensed plot of the dimensionless moment, incorporating the frequency ratio, mass ratio and dimensionless acceleration

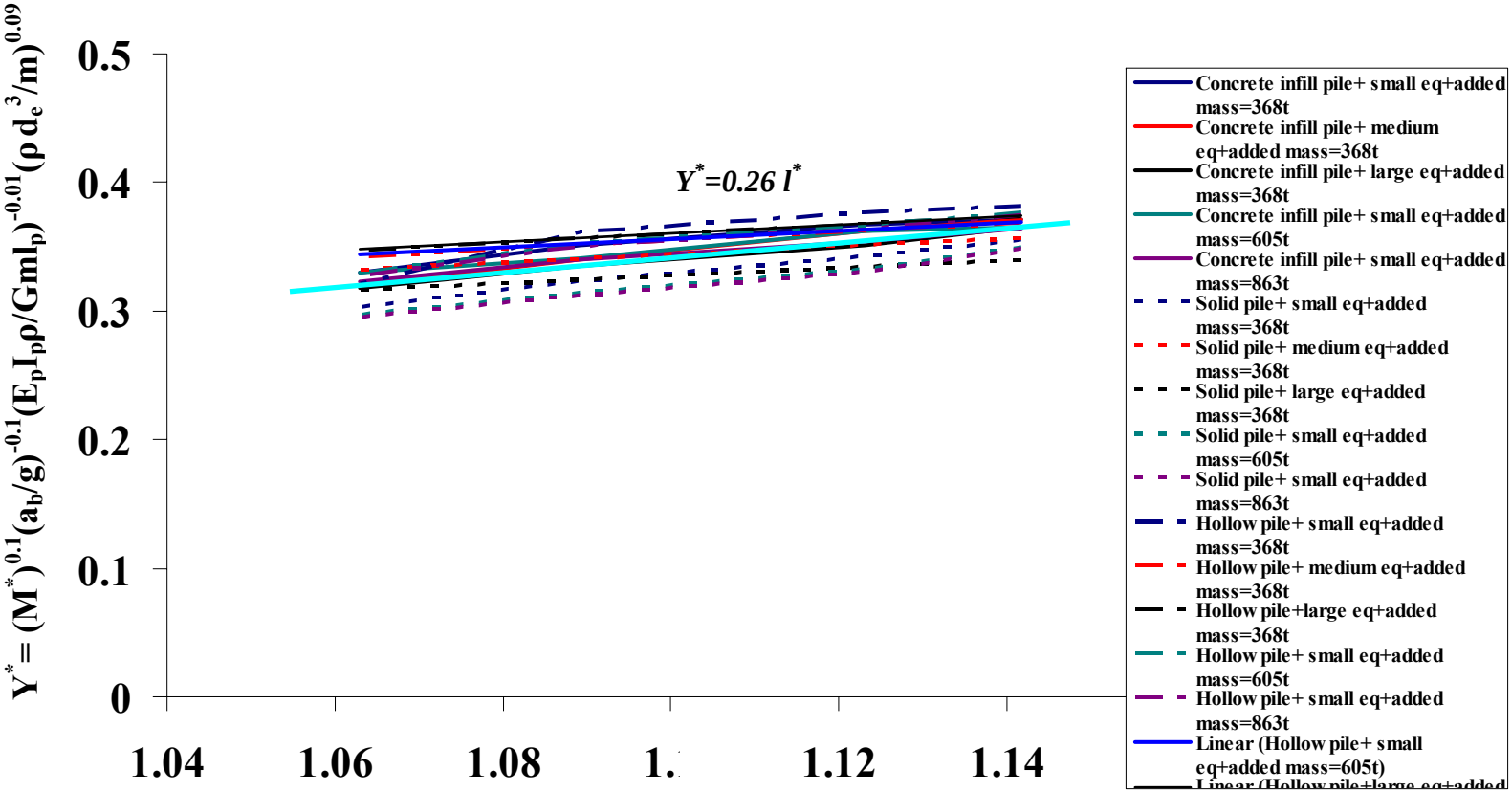

$$l^* = \left(\frac{l_p}{d_e}\right)^{0.06}$$

Figure 6.8 Final condensed plot after linearization

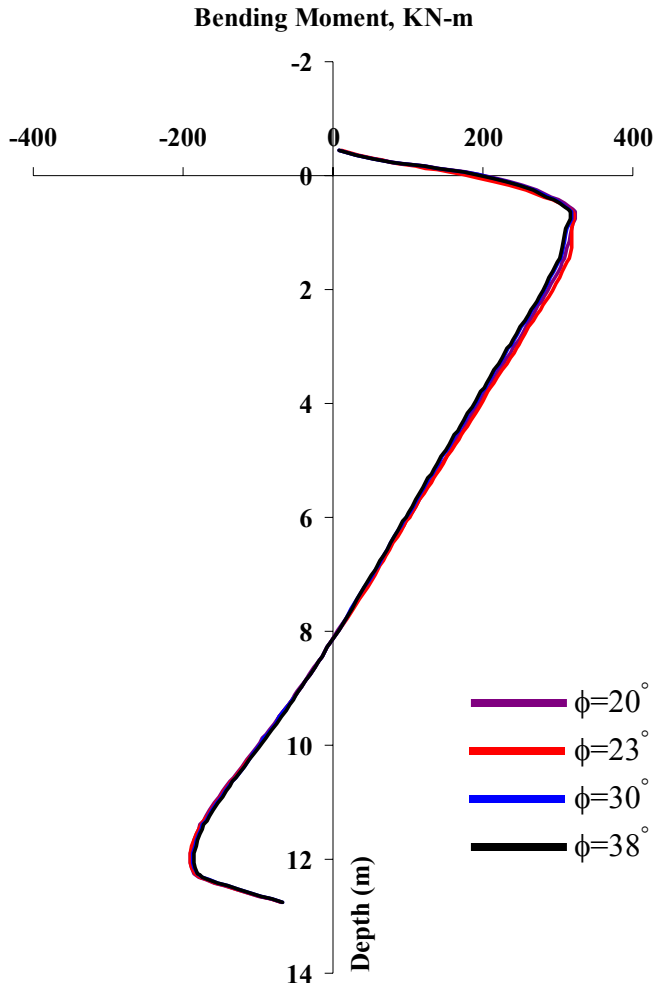

Figure 6.9 Bending moment profiles for different values of friction angle

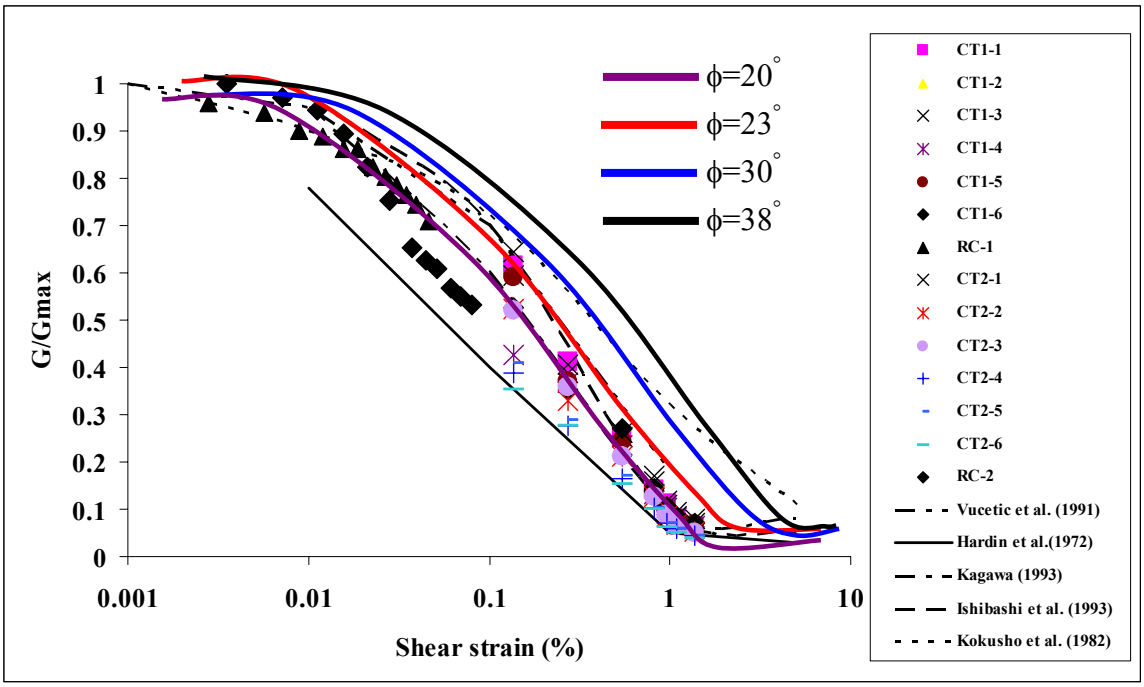

Figure 6.10 $\frac{G}{G_{max}}$ vs shear strain for different values of friction angle

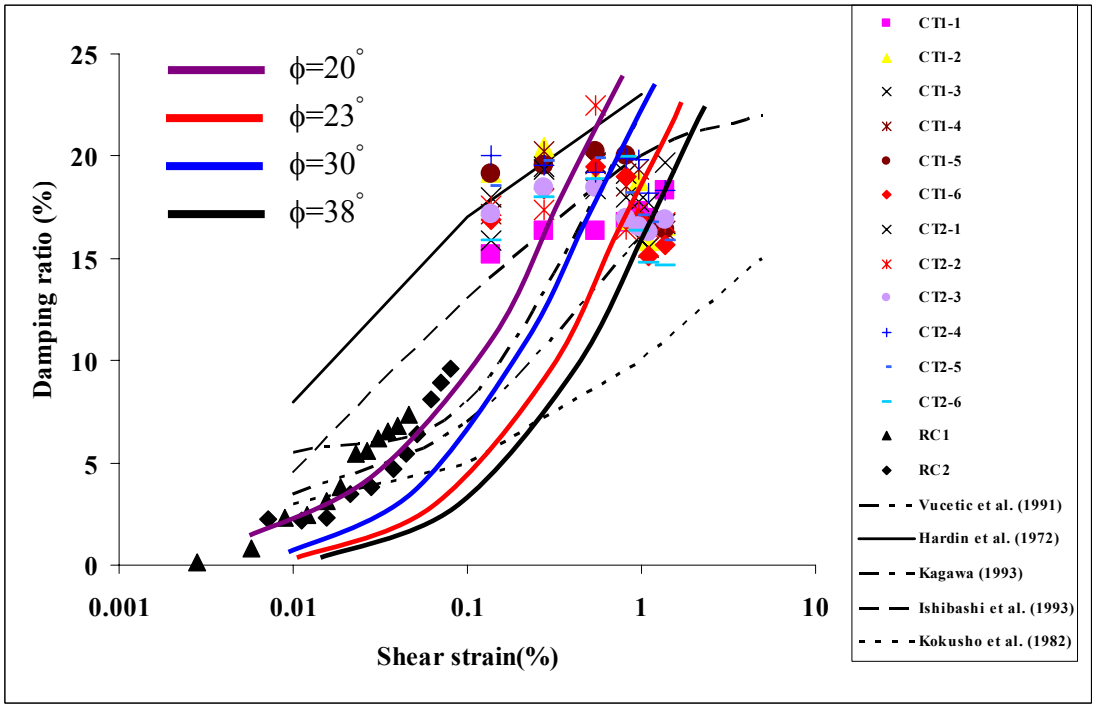

Figure 6.11 Damping ratio vs shear strain for different values of friction angle

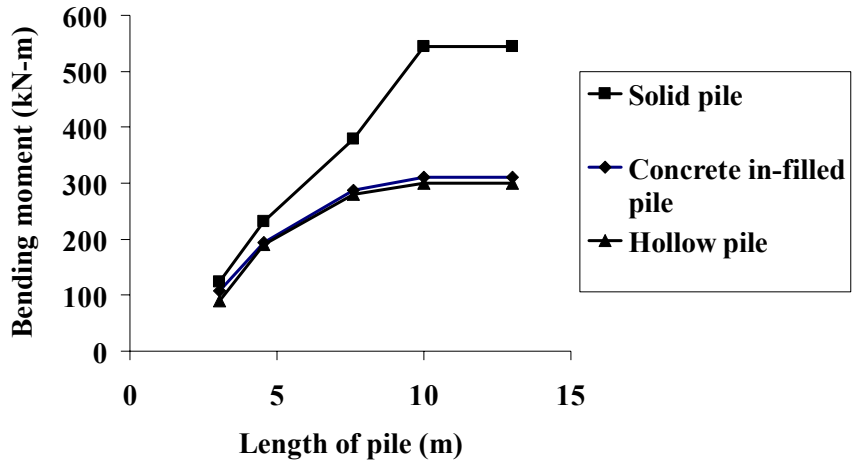

Figure 6.12 Variation of maximum bending moment with length for different pile types

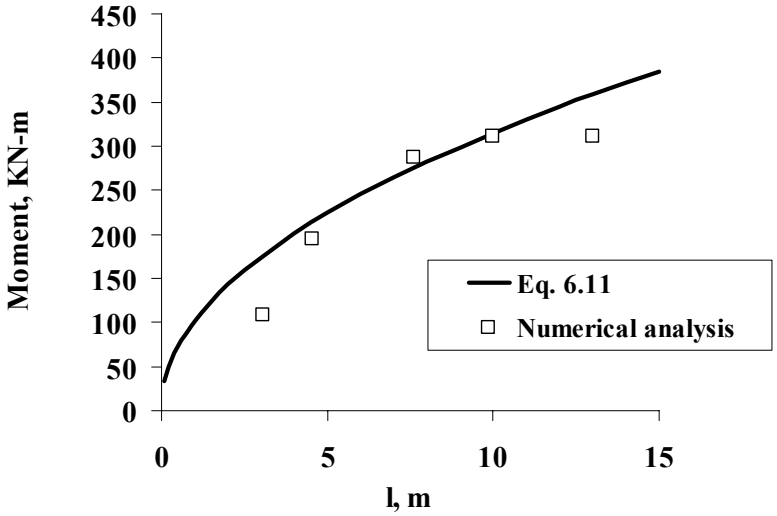

Figure 6.13 Comparison of ABAQUS results with fitted relationship: effect of pile length

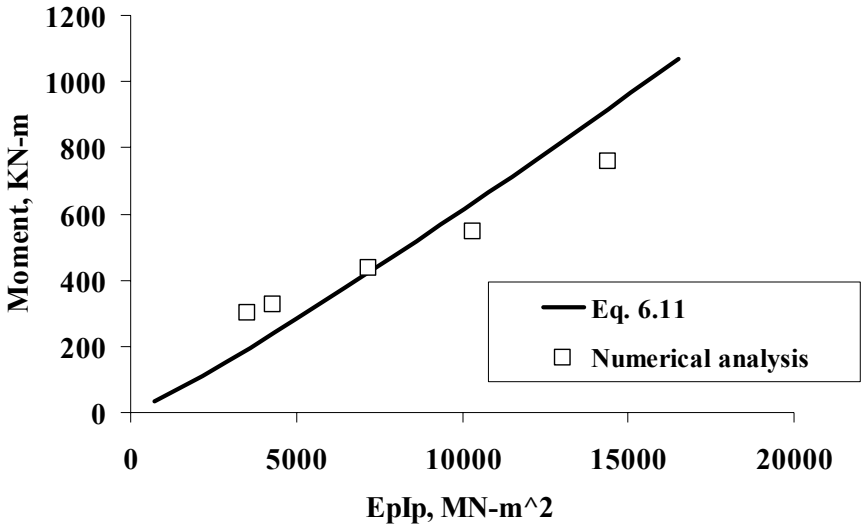

Figure 6.14 Comparison of ABAQUS results with fitted relationship: effect of flexural rigidity

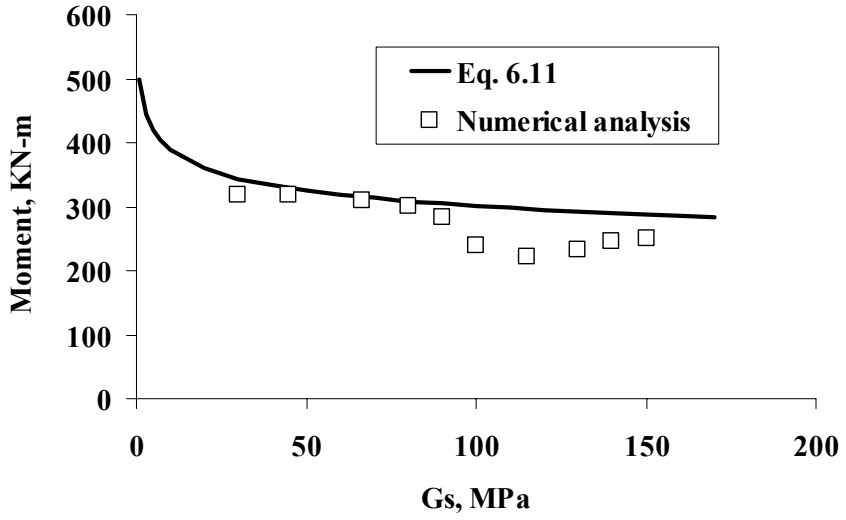

Figure 6.15 Comparison of ABAQUS results with fitted relationship: effect of soil modulus

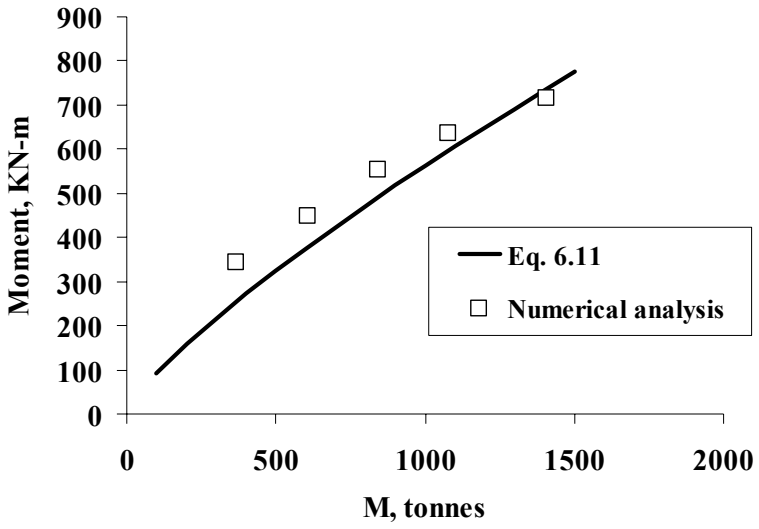

Figure 6.16 Comparison of ABAQUS results with fitted relationship: effect of added mass

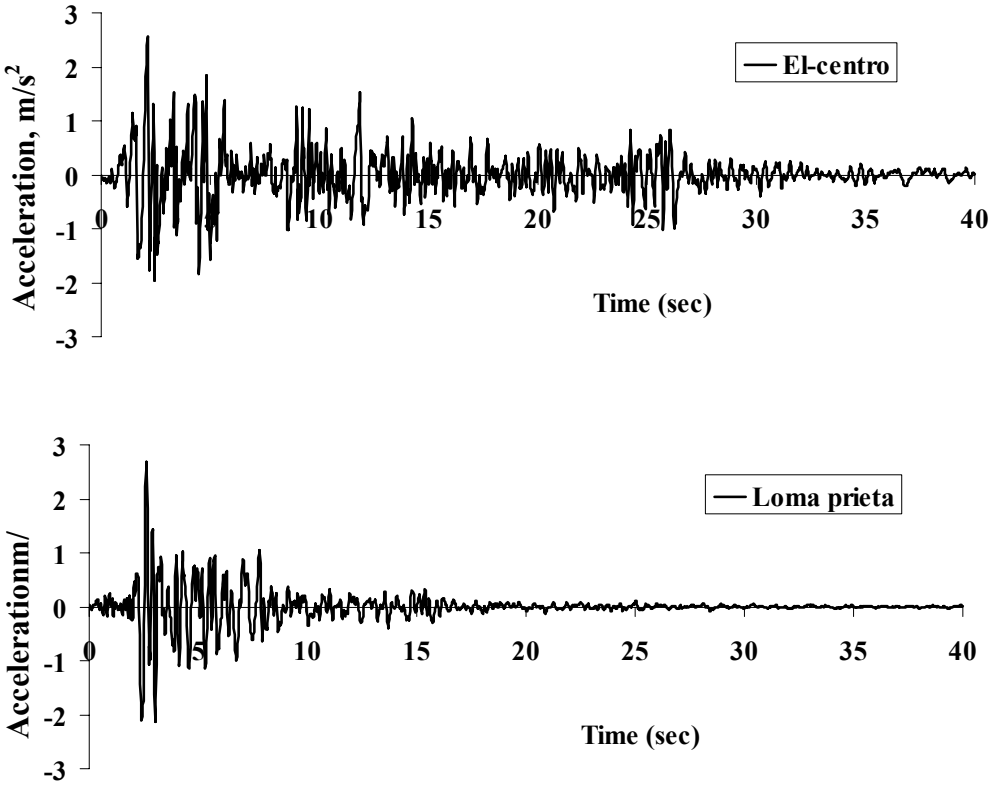

(a)

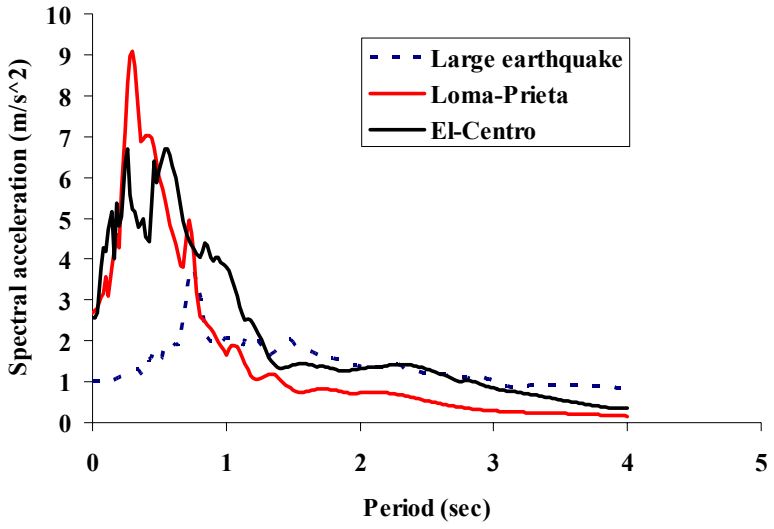

(b)

Figure 6.17 (a) Time histories and (b) Response spectra for the El-Centro and Loma-Prieta earthquake

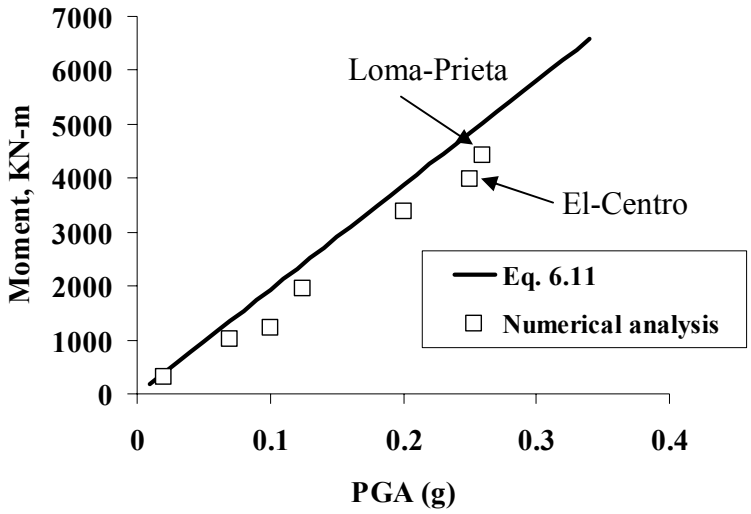

Figure 6.18 Comparison of ABAQUS results with fitted relationship: effect of peak ground acceleration

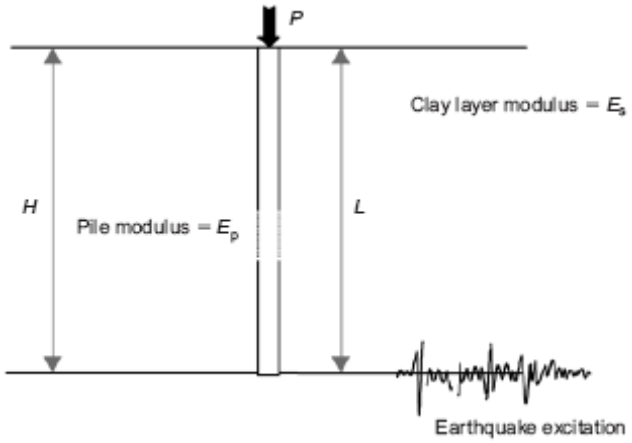

Figure 6.19 Variables used by Tabesh and Poulos (2007) in the development of design charts

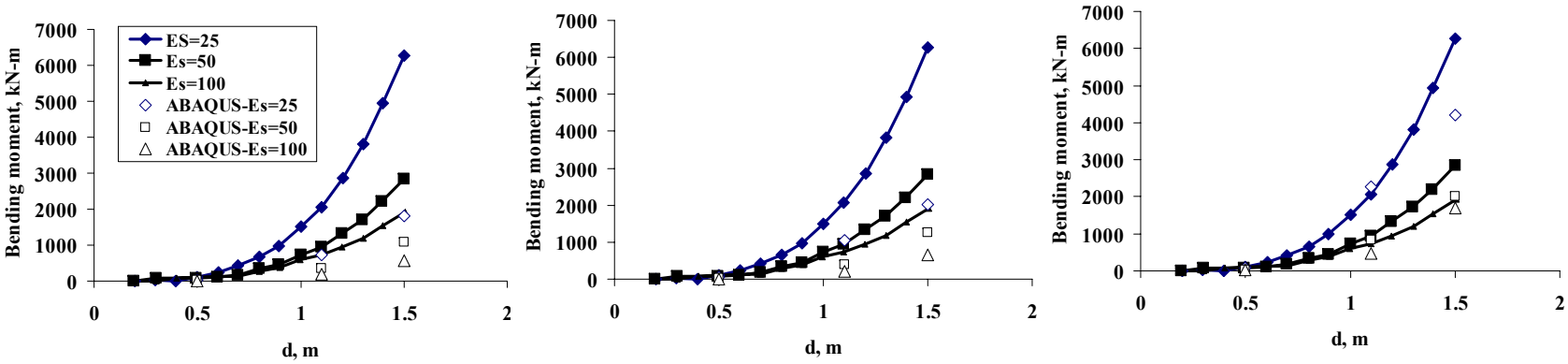

(a) Damping ratio = 10%

(b) Damping ratio = 5%

(c) Damping ratio = 0%

Figure 6.20 Comparison of bending moments from ABAQUS analysis with the Design charts from Tabesh and Poulos (2007)

CHAPTER 7 CONCLUSIONS

7.1 Introduction

Dynamic soil-pile-raft interaction is a complex problem involving nonlinear kinematic response of the soil and pile foundation, as well as inertial effects arising from the foundation-superstructure unit. As reviewed in Chapter 2, most of the reported experimental and numerical studies in this area were focused on foundation performance due to liquefaction in loose, sandy soils. There is limited information available on the performance of pile foundations in soft clays during earthquake loading.

The current thesis presents the details and results of a study on the seismic response of pile-raft systems in normally consolidated kaolin clay due to far-field earthquake motions. The research comprises four major components: (1) element testing using the cyclic triaxial and resonant column apparatus to characterize the dynamic properties of kaolin clay, the results of which were subsequently incorporated into a hyperbolic-hysteretic constitutive relationship; (2) dynamic centrifuge tests on pure kaolin clay beds (without structure) followed by 3-D finite element back-analyses using ABAQUS; (3) dynamic centrifuge tests on clay-pile-raft systems and the corresponding 3-D finite element back-analyses using ABAQUS; and (4) parametric studies leading to the derivation of a semi-analytical closed-form solution for the maximum bending moment in a pile under seismic excitation.

7.2 Summary of Research Findings

7.2.1 Dynamic Properties of Kaolin Clay

The suite of laboratory triaxial tests and resonant column tests performed in this study encompass very small to moderately large strains (0.002% to 1.37%), with cyclic frequencies varying from 0.05 to 50 Hz.

One significant finding from the results of the present laboratory element tests on kaolin clay is that the damping ratio is not significantly affected by the cyclic frequency. In other words, the influence of strain-rate on the damping ratio appears to be quite negligible. This result suggests that, for soils subjected to dynamic loadings, viscous (or rate-dependent) damping does not play a significant role compared to rate-independent hysteretic damping. Hence, in comparing the results between the numerical and centrifuge models, the errors associated with centrifuge viscosity mis-scaling (Brennan et al., 2005) are not expected to significantly affect the measured dynamic response, as damping in the soil arises primarily from hysteretic damping associated with the nonlinear stress-strain behavior of the clay.

Shear modulus degradation of the kaolin clay under dynamic loading is another important aspect of the current study. The present study shows that, at small shear strains of up to about 0.01%, the kaolin clay response is approximately linear, with a constant modulus usually denoted as G_{max}. Between 0.01% and 1% shear strain, there is significant modulus reduction to about 10% of G_{max}. Moreover, there exists a threshold strain of about 0.137% below which cyclic stiffness degradation does not take place.

The results of the laboratory element tests were used to calibrate the proposed hyperbolic-hysteretic constitutive model. Despite the relatively

simple total stress framework, numerical analyses performed using this model was able to reasonably replicate the modulus reduction and cyclic stiffness degradation of the measured kaolin clay response.

7.2.2 Centrifuge Model Tests

Centrifuge tests results show that modulus reduction and cyclic stiffness degradation affect soft clay and pile-raft foundations in several ways. In a uniform soft clay layer, the main effect is a lengthening of the resonance period of the clay bed with stronger ground motion and with successive shocks. Where pile-raft foundations are present, there are significant soil-structure effects which cause the resonance periods of the ground motion and pile-raft structure to differ from their respective uncoupled resonance periods.

For the relatively short piles tested in this study, the results of the study show that the effect of the surrounding soil is primarily one of imposing inertial loading onto the pile and raft. This leads to a lengthening of the resonance period of the pile-raft structure. The resonance period of the surrounding ground is also higher than that of a corresponding clay bed with equal thickness but without pile-raft, because of the larger shear strains arising from the relative motion between pile, raft and soil.

The engineering implication arising from this study is that, for the case of relatively short piles in soft clays, ground surface motions may not be representative of pile-raft motion. Furthermore, a short pile in soft clay under earthquake excitation is likely to behave differently from the same pile loaded dynamically from the pile top. In the latter case, the soil around the pile has a restraining effect on it. In the former, the foregoing centrifuge model results

show that the soil actually applies an inertial loading onto the pile. In view of this, it seems highly questionable as to whether dynamic or cyclic pile load tests will shed any light on the response of such piles to earthquake loading. This conclusion is only applicable to relatively short piles. More studies are needed on longer and more flexible piles.

In terms of bending moment response, the maximum bending moment is recorded near the fixed head connection between the pile and the raft. The bending moment is found to increase almost linearly with the scaled earthquake ground motion. It is also observed that the bending moment increases with the flexural rigidity of the pile material and with increasing added masses on the pile raft. The 3-D ABAQUS numerical simulations presented in Chapters 4 and 5 were able to replicate the centrifuge tests results reasonably well.

7.2.3 Parametric Studies

The method of non-dimensional analysis, using Buckingham-π's theorem, was carried out to derive the dimensionless terms associated with the maximum bending moment in a seismically loaded pile. The resulting semi-analytical solution for the maximum bending moment was calibrated through parametric studies involving the pile length, moment inertia, pile and soil modulus, mass of the raft and peak ground motion (PGA). It was found that:

1. The maximum bending moment increases almost hyperbolically with the pile length until it reaches a critical value, termed the critical length. The critical length obtained from this study is consistent with the values derived using Gazetas' approach (1984, 1991), as shown on

Table 6.2. Gazetas expressed the critical length as a function of the ratio of the soil and pile moduli, and the moment inertia of the pile.

2. The flexural rigidity (EI) of the pile has a major influence on the maximum bending moment. It is observed that the maximum bending moment increases with the EI of the pile.
3. It is also shown that for a single pile with relatively fixed head condition, soil-pile stress transfer may not depend significantly upon the pile diameter, within the range investigated. This would suggest that the main effect of the diameter (d) is to change the 2^{nd} moment of area of the pile.
4. The maximum bending moment in a seismically loaded pile reduces with increasing soil modulus. The observation is consistent with the results reported by Nikolaou et al. (1995, 2001).
5. The maximum bending moment in the pile increases with increasing added masses placed on the raft.
6. It is also observed that maximum bending increases linearly with the amount of peak ground acceleration (PGA). This is not implausible because the behavior of the soil-pile-raft system may be dominated by the stiffness of the pile and the mass of the raft and soil, with the stiffness of the soil playing a relatively minor role.

7.3 Recommendations for the Further Research

Some recommendations for further research are suggested below:

1. In the current study, pile group effects are not considered as the piles are spaced relatively far apart. Given that pile groups are commonly used in practice, further study is needed to study the seismic response of such foundations which incorporate group effects. Besides varying the pile spacing to diameter ratio, different pile group configurations (e.g. 3x3, 4x4 etc.) should also be considered.
2. The study described in this thesis is confined to relatively short and rigid piles. To examine the seismic response associated with longer and more flexible piles, the centrifuge and numerical studies should be extended to piles with larger length-to-diameter ratios. Hence, further study is needed to examine the seismic response effects associated with a thicker clay layer with longer piles.
3. The soil model considered in this study is total-stress based. To properly account for pore-pressure generation and dissipation during seismic loading, a more advanced effective stress model is required.
4. For bigger 3-D models with more than 50,000 elements, the computational memory requirements may exceed those available on a single computer, and/or the computational time required is excessive. For such cases, parallel computational methods may be a more feasible option.
5. Further study is also necessary to explore the cyclic triaxial tests on anisotropically consolidated samples. The performance of the soil

model (HyperMas) described in Chapter 3 has not been evaluated for such cases.

6. In this study, normally consolidated kaolin clay was used. Future study should examine the influence of overconsolidation effects on the resulting soil-pile-raft interaction response.
7. The different earthquakes considered in this study are scaled from the same reference motion to obtain the desired peak ground accelerations, thus resulting in identical frequency spectra. It would be useful to study the soil-pile-raft interaction effects for earthquakes with different frequency contents but comparable magnitudes.

The preceding suggestions for future research would contribute significantly to the understanding of seismic soil-pile-raft interaction, which will potentially lead to improvements in the state-of-the-practice for pile foundation analysis and design under earthquake conditions.

REFERENCES

Abdoun, T., Dobry, R., O'Rourke, T., and Chadhuri, D. (1996). Centrifuge modeling of seismically-induced lateral deformation during liquefaction and its effect on a pile foundation. Proceedings of 6th U.S.-Japan Workshop on Earthquake Resistant Design of Lifeline Facilities and Countermeasures Against Soil Liquefaction, Rpt. No. NCEER-96-0000, NCEER, 525-539.

Abghari, A. and Chai, J. (1995). Modeling of soil-pile-superstructure interaction for bridge foundations, in performance of deep foundations under seismic loading. Geotechnical Special Publication, ASCE, Vol. 51, 45-59.

Agarwal, S. (1973). Characterisation of clay as applicable to pile foundations under dynamic lateral loads. Proceedings of Symposium on Earth and Earth Structures Under Earthquakes and Dynamic Loads, Roorkee, India, 64-71.

Aggour, M.S, Tawfiq, K.S, and Amini, F. (1987). Effects of Frequency content on dynamic properties for cohesive soils. Proceedings, Third International Conference on Earthquake Engineering and Soil Dynamics, Princeton, June, 31-39.

Agrawal, S.L. (1973). Soil structure interaction of dynamically laterally loaded piles, based on discrete element method. Proc. of 5th WCEE, Rome, 157-179.

Alpan, I. (1973). The dynamic response of pile foundations to lateral forces. Proc. 5th World Conf. Earthquake Eng., Rome, Vol. 2, 256-271.

Andersen, K.H., Pool, J.H., Brown, S.F., Rosenbrand, W.F. (1980). Cyclic and static laboratory tests on Drammen clay. Journal of the Geotechnical Engineering Division, ASCE 106, 499–529.

Andrianopoulos, K. I. (2006). Numerical modeling of static & dynamic behavior of elastoplastic soils. Ph.D. Thesis, Geotechnical Division, National Technical University of Athens, Greece.

Angelides, Demosthenes C and Rosset, J.M. (1981). Nonlinear lateral dynamic stiffness of piles. Journal of the Geotechnical Engineering Division, ASCE, Vol-107, No.2, 1443-1459.

Atkinson, J.H. (2000). Non-linear soil stiffness in routine design. Rankine Lecture, Géotechnique, Vol. 50, No. 5, 487-508.

Badoni, D. and Makris, N. (1996). Nonlinear response of single piles under lateral inertial & seismic loads. Soil Dynamics and Earthquake Engineering, Vol-15, 29-43.

Banerjee, S., Goh, S.H. and Lee, F.H. (2007). Response of Soft Clay Strata and Clay-Pile-Raft Systems to Seismic Shaking. Journal of Earthquake and Tsunami, Vol. 1, No. 3, pp. 233 - 255.

Barkan, D.D. (1962). Dynamics of bases and Foundations. McGraw-Hill Book Co., NY.

Bhattacharya, S. and Bolton, M. (2004). Errors in design leading to pile failures during seismic liquefaction. Proc. Fifth International Conference on Case Histories in Geotechnical Engineering, NY, USA , 1-8.

Bhomik, S. and Long, J. (1991). An analytical investigation of the behavior of laterally loaded piles. Proceedings of Geotechnical Engineering Congress, ASCE Special Publication 27, Vol. 2, 1307-1318.

Bjerrum, L. (1967) , Engineering geology of Norwegian normally consolidated marine clays as related to settlements of buildings. Geotechnique, Vol.17, No. 2, 81–118.

Blaney, G. and O'Neill, M. (1989). Dynamic lateral response of a pile group in clay. Geotechnical Testing Journal, ASTM, Vol.12,No.1, 22-29.

Blaney, G. W., Kausel, E. and Roesset, J. M. (1976). Dynamic stiffness of piles. Proceedings of 2nd International Conference Numerical Methods in Geomechanics., Blacksburg VA, Vol. 2, 1010-1012.

Blaney, G., Muster, G., and O'Neill, M. (1987). Vertical vibration test of a full-scale group in dynamic response of pile foundations - experiment, analysis, and observation. Geotechnical Special Publication, No.11, ASCE, 149-165.

Bonilla, L. F. (2000). Computation of linear and nonlinear site response for near field ground motion. Ph.D. Thesis, University of California, Santa Barbara, USA

Bonilla, L. F., D. Lavallee, and R. J. Archuleta (1998). Nonlinear site response: Laboratory modeling as a constraint for modeling accelerograms. Proceedings of Second International Symposium on the Effects of Surface Geology on Seismic Motion, Vol. 2, 793–800.

Bowles, J. E. (1974). Analytical and computer methods in foundation engineering. McGraw-Hill Book Co., NY.

Brennan, A. J., Thusyanthan, N. I. and Madabhushi, S. P. G. (2005). Evaluation of shear modulus and damping in dynamic centrifuge tests. Journal of Geotechnical and Geoenvironmental Engineering, ASCE, Vol.131, No.12, 1488-1497.

Bridgman. P. W. (1969). Dimensional Analysis. Encyclopaedia Britannica (Wm. Haley, Editor-in-Chief). Vol. 7, 439-449: Encyclopaedia Britannica, Chicago.

Broms, B. (1964). The lateral resistance in piles in cohesive soils. Journal of Soil Mechancis and Foundation Division, ASCE, Vol. 90, SM2, 27-63.

Budhu, M. and Davies, T. (1987). Nonlinear analysis of laterally loaded piles in cohesionless soils. Canadian Geotechnical Journal, Vol. 24, No. 2, 289-296.

Budhu, M. and Davies, T. (1988). Analysis of laterally loaded piles in soft clays. Journal of Geotechnical Engineering. ASCE, Vol. 114, No. 1, 21-39.

Burland, J. B. (1990). On the compressibility and shear strength of natural clays. Geotechnique, Vol.40, No. 3, 329–378.

Burland, J.B. (1989). „Small is beautiful - the stiffness of soils at small strains. Ninth Laurits Bjerrum Memorial Lecture. Canadian Geotechnical Journal. Vol. 26, 499-516.

Burr, J., Pender, M., and Larkin, T. (1997). Dynamic response of laterally excited pile groups, Journal of Geotechnical and Geoenvironmental Engineering, ASCE, Vol. 123, No. 1, 1-8.

Cafe, P. (1991). Dynamic response of a pile-supported bridge on soft soil, M.S. Thesis, University of California, Davis, USA.

Casagrande, A. (1976). Liquefaction and cyclic deformation of sands: a critical review Harvard Soil Mechanics Series No. 88, 909-927.

Cavallaro, A. and Maugeri M. (2004). Modeling of cyclic behavior of a cohesive soil by shear torsional and triaxial tests, Cyclic Behavior of Soils and Liquefaction, Triantafyllidis (ed). 109-114.

Celebi, M. and Safak, E. (1992). Seismic Response of Pacific Park Plaza, I: Data and preliminary analysis. J. Struct. Eng., ASCE, 118(6), 1547-1565.

Chandrasekaran, V. and Prakash, S. (1980). Pile under lateral dynamic loading. Proc. of 8th Int. Conf. on S.M.F.E., Moscow, Vol.-2, 199-207.

Chandrasekaran, V., Cook, D.J. & Cao, H.T. (1987). Static & dynamic behavior of pile foundations. Proc. of 9th S.E.A.G.C., Bangkok, Vol.-2, 265-279.

Chang, D.W. and Lin, B.S. (2006). EQWEAP ~ A simplified procedure to analyze dynamic pile-soil interaction with soil liquefaction concerns. Second Taiwan-Japan Joint Workshop on Geotechnical Hazards from Large Earthquake and Heavy Rainfall: 155-162. Japan.

Chang, D.W., Lin, B.S., Yeh, C.H. and Cheng, S.H (2008). FD solutions for static and dynamic winkler models with lateral spread induced earth pressures on piles. Pro. Geotechnical Earthquake Engineering and Soil Dynamics IV. Sacramento, CA (USA).

Christina, J. Curras, Boulanger, Ross W., Kutter Bruce L., Wilson, D. (1999). Seismic soil-pile-structure interaction experiments and analyses. Journal of Geotechnical Engineering, ASCE, Vol-125, No.9, 345-369.

Dasari, G. R. (1996). Modeling of the variation of soil stiffness during sequential construction. PhD Thesis, Cambridge University, United Kingdom.

Dobry, R. (1982). Horizontal stiffness and damping of single piles. Journal of Geotechnical Engineering, ASCE, Vol-108, GT3, 439-456.

Dobry, R. and O'Rourke, M. J. (1983). Discussion on Seismic response of end-bearing piles by Flores-Berrones, R. and Whitman, R. V., Journal of Geotechnical Engineering, ASCE, 109.

Drnevich, V.P., Hardin B.O. and Shippy D.J. (1978). Modulus and damping of soils by resonant column method. Dynamic Geotechnical Testing, ASTM STP 654, American Society for Testing and Materials, 91-125.

Duncan, J.M. and Chang, C-Y. (1970) Nonlinear analysis of stress and strain in soils Journal of Soil Mechanics and Foundation Division, ASCE, Vol. 96, No. SM5, Proc. Paper 7513.

Dupas, J. M., Pecker, A., Bozetto, P. and Fry J. J. (1988). A 300mm-diameter triaxial cell with a double measuring device. Advanced Triaxial Testing of Soil and Rock (ASTM Special Technical Publication). 132-142.

El Naggar, M.H. and Novak, M. (1995). Nonlinear lateral interaction in pile dynamics. Soil Dynamics and Earthquake Engineering, Vol-14, 141-154.

Esashi, Y. and Yoshida, Y. (1980). Convenient aseismic design of pile foundation. Proc. 7th World Conf. Earthquake Eng., Istanbul, Vol. 3, 419-426.

Fenves, G., and Serino, G. (1992). Evaluation of soil-structure interaction in buildings during earthquakes. Data Utilization Rpt. CSMIP/92-01, Rpt. to Offc. of Strong Motion Studies, Div. of Mines and Geology, California Dept. of Conservation, June.

Finn, W. and Gohl, B. (1987). Centrifuge model studies of piles under simulated earthquake lateral loading in dynamic response of pile foundations - experiment, analysis, and observation. Geotechnical Special Publication, ASCE, Vol. 11, 21-38.

Finn, W. and Gohl, W. (1999). Centrifuge model studies of piles under simulated earthquake lateral loading. Canadian Geotechnical Journal, Vol-32, 44-56.

Finn, W. D. L. (2005). A study of piles during earthquakes: issues of design and analysis. Bulletin of Earthquake Engineering, Vol. 3, 141–234.

Flores-Berrones, R. and Whitman, R. V. (1982). Seismic response of end-bearing piles. Journal of the Geotechnical Engineering Division, ASCE, Vol. 108, No. 4, 554-569.

Fowler, M., Johnston, R., and Nagle, G. (1994). Seismic Retrofit of Foundations for a Double-Deck Viaduct. Proceedings of International Conference on Design and Construction of Deep Foundations, FHWA, Vol. 2, 439-453.

Frederick, D. and Chang, T. S. (1965). Continuum mechanics. Cambridge, MA: Scientific Publishers.

Fukoka, M. (1966). Damage to civil engineering structures. Soils and Foundations, Vol. 6, No. 2, 45-52.

Fukuoka, A., Adachi, N., Miyamoto, Y., Sako, Y. (1996). Centrifuge model tests of pile foundation in liquefiable sand deposit. 11th WCEE, Paper no.368.

Fuse, Y., Ashihara, E., Kikuchi, T., and Goto, Y.(1992). Vibration test of bridge pier with large-scale group-pile foundation. Proc. 10th WCEE, Madrid, Vol. 3, 1961-1966.

Gazetas, G. (1984). Seismic response of end-bearing single piles. Soil Dynamics and Earthquake Engineering, Vol. 3, No. 2, 82-93.

Gazetas, G., Velveg, A. and Krishnan, R. (1983). Static & dynamic lateral deflection of piles in non-homogeneous soil system. Geotechnique, Vol-33, No.3, 307-329.

Gazetas, G., Fan, K., Tazoh, T., and Shimizu, K. (1993). "Seismic response of the pile foundation of Ohba-Ohashi bridge," Proc. 3rd Intl. Conf. on Case Histories in Geotech. Eng., St. Louis, Vol. 3, 1803-1809.

Girault, P. (1986). Analysis of foundation failures in the Mexico earthquake, 1985 - factors involved and lessons learned, ASCE, 178-192.

Goh, T. L. (2003). Stabilization of an excavation by an embedded improved soil layer. Ph.D. thesis, National University of Singapore.

Guin, J. and Banerjee, P. K. (1998). Coupled soil-pile-structure interaction analysis under seismic excitation. Journal Structural Engineering, ASCE, Vol. 124, No. 4, 434-444.

Gyoten, Y., Mizuhata, K., Fukusumi, T., Fukui, M., and Ono, T. (1980). Study on the earthquake response of the structure-pile-soil system considering liquefaction and nonlinear restoring force characteristics of soil layers. Proc. 7th World Conf.Earthquake Eng., Istanbul, Vol. 6, 113-120.

Hadjian, A., Fallgren, R., and Lau, L. (1990). Imperial County Services Building revisited: A reevaluation with pile-soil-structure interaction. Proc. 4th U.S. Natl. Conf. Earthquake Eng., Palm Springs, Vol. 3, 835-844.

Hadjian, A., Fallgren, R., and Tufenkjian, S. (1992). Dynamic soil-pile-structure interaction - the state-of-the-practice in piles under dynamic loads. Geotechnical Special Publication, ASCE, Vol. 34, 1-26.

Hamada, M. and Ishida, O. (1980). Earthquake observation and numerical analysis of dynamic strain of foundation pile. Proc. 7th World Conf. Earthquake Eng., Istanbul, Vol. 3, 435-442.

Hamilton, J., Dunnavant, T., Murff, J., and Phillips, R. (1991). Centrifuge study of laterally loaded behavior in clay. Proc. Intl. Conf. Centrifuge ’91, Boulder, 285-292.

Han, Y. and Vaziri, H. (1992). Dynamic response of pile groups under lateral loading. Soil Dyn. and Earthquake Eng., Vol. 11, No. 2, 87-99.

Hardin, B.O. and Drnevich, V.P. (1972a). Shear modulus and damping in soils: design equations and curves. Journal of the Geotechnical Engineering Division, ASCE, Vol. 98, No. 7, 667–692.

Hardin, B.O. and Drnevich, V.P. (1972b). Shear modulus and damping in soils: Measurement and parameter effects (Terzaghi Lecture).. Journal of the Geotechnical Engineering Division, ASCE, Vol. 98, No. 6, 603–624

Hartzell, S., Bonilla, L. F. and Williams, R. A. (2004). Prediction of nonlinear soil effects. Bulletin of the Seismological Society of America, Vol. 94, No. 5, 1609–1629.

Hayashi, S., Miyajima, N., and Yamashita, I. (1965). Horizontal resistance of steel piles under static and dynamic loads. Proc. 3rd World Conf. Earthquake Eng., Auckland, Vol. 2, 146-167.

Hazen I. and Penumadu D. (1999). Resonant column testing of clay specimens with controlled microfabric. Report No. 99-02, , Department of Civil and Environmental Engineering, Clarkson University, Potsdam, NY, USA.

Hoek, E. (1965). The design of a centrifuge for the simulation of gravitational fields in mine models. Journal of South African Institute of Mining and Metallurgy, Vol. 65, 455-487.

Housner, G. (1957). Interaction of Building and Ground During an Earthquake. Bulletin of Seismological Society of America, Vol. 47, No. 3, 179-186.

Howe, R. J. (1955). A numerical method for predicting the behaviour of laterally loaded piling. Exploration Research Division Pub. No. 412, Shell Oil Co., Houston, TX.

Huang, Y., Zhang, F., Yashima, A., Sawada, K., Ye, G.-L. and Kubota, N. (2004). Three-dimensional numerical simulation of pile-soil seismic interaction in saturated deposits with liquefiable sand and soft clay. COMPUTATIONAL MECHANICS WCCM VI in conjunction with APCOM'04, Sept. 5-10, 2004, Beijing, China

Hyodo, M., Tanimizu, H., Yasufuku, N. and Murata, H. (1994). Undrained cyclic and monotonic triaxial behaviour of saturated loose sand. Soils and Foundations, Vol. 34, No. 1, 19-32,

Idriss, I. (1990). Response of Soft Soil Sites During Earthquakes. in H.B. Seed Memorial Symposium, Vol. 2, BiTech, 273-289.

Idriss, I. M., Lysmer, J., Hwang, R. N. and Seed, H. B. (1973). QUAD-4: a computer program for evaluating the seismic response of soil structures by variable damping finite element procedures. UCB/EERC-73/16, Earthquake Engineering Research Center, University of California, Berkeley, 1973-07, 79 pages (480.2/I34/1973).

Idriss, I.M., Dobry, R., Doyle, E.H. and Singh, R.D. (1978). Nonlinear behaviour of soft clays during cyclic loading conditions. Journal of the Geotechnical Engineering Division, ASCE, Vol. 104, 1427–1447.

Idriss, I.M., Moriwaki, Y., Wright, S. G., Doyle, E.H. and Ladd, R. S. (1980). Behaviour of normally consolidated clay under simulated earthquake and ocean wave loading conditions. proceeding of International Symposium on Soils under Cyclic and Transient loading, 1, Swansea, United Kingdom, 437-445.

Ishibashi, I., and Zhang, X. (1993). Unified dynamic shear moduli and damping ratios of sand and clay. Soils and Foundations, Vol. 33, No. 1, 182-191.

Ishihara, K. (1996). Soil behavior in earthquake geotechnics, Clarendon Press, Oxford

Ishii, Y. and Fujita, K. (1965). Field test on the lateral resistance of large diameter steel pipe piles and its application to the aseismic design of pile bent-type pier . Proc. 3rd World Conf. Earthquake Eng., Auckland, Vol. 4, 256-271.

Iwan, W.D. (1967). On a class of models for the yielding behaviour of continuous and composite systems. Journal of Applied Mechanics, Vol. 67, 612–617.

Jang, J.J. and Chein, C.W. (2006). The performance-based seismic design method for pile-supported wharf structures. Proceedings of the SixteenthInternational Offshore and Polar Engineering Conference San Francisco, California, USA, May 28-June 2, 2006

Jardine R. J., Potts, D. M., Fourie, A. B. and Burland, J. B. (1986). Studies of the influence of non-linear stree-strain characteristics in soil-structure interaction. Geotechnique, Vol. 36, No. 3, 377-396.

Jardine R. J., Potts, D. M., St. John, H. D. and High, D. W. (1991). Some practical application of a non-linear ground model. Proceedings of 10th European Conference on Soil Mechanics and Foundation Engineering, Florence, Vol. 1, 223-228.

Joyner, W. B., and A. T. F. Chen (1975). Calculation of nonlinear ground response in earthquakes. Bulletin of the Seismological Society of America, Vol. 65, 1315–1336.

Kagawa T., Sato M., Minowa C., Abe A., Tazoh T. (2004). Centrifuge simulations of large-scale shaking table tests: case studies. Journal of Geotechnical Engineering. ASCE, Vol. 130, No.7, 663-672.

Kagawa, T. (1980). Soil-pile-structure interaction of offshore structures during an earthquake. 12th Annual Offshore Technology Conference, Houston, Texas, OTC 3820.

Kagawa, T. (1991). Dynamic Soil Reaction to Axially Loaded Piles. Journal of Geotechnical Engineering, ASCE, Vol. 117, No. 7, 1001-1020.

Kagawa, T. (1992). Moduli and damping factors of soft marine clays. Journal of Geotechnical Engineering, ASCE, Vol. 118, No. 9, 1360–1375.

Kagawa, T. and Kraft, L. (1981). Lateral Pile Response During Earthquakes. Journal of Geotechnical Engineering. ASCE, Vol. 107, No. 12, 1713-1731.

Kagawa, T. and Kraft, L. M. (1980). Lateral load-deflection relationships of piles subjected to dynamic loads. Soils and Foundations, Vol. 20, No. 4, 19-36.

Kagawa, T. and Kraft, L.M. (1981a). Seismic p-y Responses of Flexible Piles. Journal of the Geotechnical Engineering Division , ASCE, Vol-106, No.8, 899-910.

Kagawa, T. and Kraft, L.M. (1981b). Lateral Pile response during earthquake. Journal of the Geotechnical Engineering Division, ASCE, Vol-107, GT12, 1713-1739.

Kana, D., Boyce, L., and Blaney, G. (1986). Development of a scale model for the dynamic interaction of a pile in clay. Journal of Energy Resources Technology, ASME, Vol. 108, No. 3, 254-261.

Kavvadas, M. and Gazetas, G. (1993). Kinematic seismic response and bending of free-head piles in layered soil. Geotechnique, Vol. 43, No. 2, 207-222.

Kaynia, A. M. and Kausel, E. (1982). Dynamic stiffness and seismic response of pile groups. Research Report R82-03, Massachusetts Institute of Technology, USA.

Kaynia, A. M. and Mahzooni, S. (1996). Forces in pile foundations under seismic loading. Journal of Engineering Mechanics, ASCE, Vol. 122, No. 1, 46-53.

Khodair, Y.A. and S. Hassiotis (2003). Analysis of Pile Soil Interaction. Available online at: www.ce.washington.edu/em2003/proceedings/papers/686.pdf.

Klusmeyer, L. and Harn, R. E. (2006). Displacement-based seismic design of a large naval pier. An in-house report to US Dept. Navy by BERGER/ABAM Engineers Inc.

Kim D.-S. Stokoe K.H. and Roesset J.M (1991). Characterization of material damping of soils using resonant column and torsional shear tests. Proceedings, Fifth International Conference on Soil Dynamics and Earthquake Engineering, September 23-26, 189-200

Kokushko, S., Wada, A., Kobayashi, K., Hayashi, S., Horii, M., Kihara, H., and Saito, S. (1984). Experimental study on plastic deformability of high strength prestressed concrete piles under axial and lateral forces, Proc. 8th World Conference on Earthquake Engineering, San Francisco, USA, Vol. 3, 609-616.

Kokusho, T. (1980). Cyclic triaxial test of dynamic soil properties for wide strain range. Soils and Foundations, Vol. 20, No. 2, 45–60.

Kokusho, T., Yoshida, Y., and Esashi, Y. (1982). Dynamic properties of soft clay for wide strain range. Soils and Foundations, Vol. 22, No. 4, 1-18.

Kramer, S. (1993). Seismic Response - Foundations in Soft Soils. WSDOT Rrport, WA-RD264.1, Washington State University.

Kreyszig, E. (2006). Advanced Engineering Mathematics. 9th Edition, John Wiley Inc.

Kubo, K. (1969). Vibration test of a structure supported by pile foundation. Proceedings of 4th World Conference on Earthquake Engineering, Santiago, Chile, A6:1-12.

Kuhlemeyer, R.L. (1979). Static & Dynamic Laterally Loaded Floating Piles. Journal of the Geotechnical Engineering Division , ASCE, Vol-105, No.2, 289-304.

Lacasse, S. and Berre, T. (1988). State-of-the-art paper triaxial testing methods for soils. Advanced Triaxial Testing of Soil and Rock (ASTM Special Technical Publication). 264-289.

Lam, I. and Cheang, L. (1995). Dynamic soil-pile interaction behavior in submerged sands in earthquake-induced movements and seismic remediation of existing foundations and abutments. Geotechnical Special Publication, ASCE, Vol. 55, 110-135.

Lam, I.P., Kapuskar, M. and Chaudhuri, D. (1998). Modeling of pile footings and drilled shafts for seismic design. MCEER-98-0018.

Langhaar, H.L. (1951). Dimensional Analysis and theory of Models. John Wiley, New York.

Lee, C. H. (2006). Centrifuge modeling of wet deep mixing process in soft clays. PhD Dissertation, National University of Singapore.

Lee, F. H. and Schofield, A. N. (1988). Centrifuge modeling of sand embankments and islands in earthquake. Geotechnique, Vol. 80, No. 1, 45-58.

Lee, F.H., Leung, C.F., Tan, T.S., Yong K.Y., Karunaratne, G.P. and Lee, S. L. (1991). Development of geotechnical centrifuge facility at the National University of Singapore. Proceedings of Centrifuge 91, Singapore, 11-20.

Leroueil, S. & Vaughan, P. R. (1990) , The general and congruent effects of structure in natural soils and weak rocks. Geotechnique, Vol.40, No. 3, 467–488.

Leroueil, S., Kabbaj, M., Tavenas, F. & Bouchard, R. (1985) , Stress–strain-strain rate relation for the compressibility of sensitive natural clays. Geotechnique, Vol.35, No.2, 159–180.

Leung, C.F., Lee, F.H. and Tan, T.S. (1991). Principles and application of geotechnical centrifuge model testing. Journal of Institution of Engineers Singapore, Vol.-31, 39-49.

Liu, H. and Chen, K. (1991). Test on Behavior of Pile Foundation in Liquefiable Soils, Proceedings of 2nd International Conference on Recent Advances in Geotechnical Engineering and Soil Dynamics, St. Louis, USA, Vol. 1, 233-235.

Liu, H.and Ling, H. I. (2006). Modeling cyclic behavior of geosynthetics using mathematical functions combined with Masing rule and bounding surface plasticity. Geosynthetics International, Vol. 13, No. 6, 234-245.

Liu, L. and Dobry, R. (1995). Effect of liquefaction on lateral response of piles by centrifuge model tests. NCEER Bulletin, SUNY-Buffalo, 7-11, January.

Liu, W. and Novak, M. (1994) , Dynamic response of single piles embedded in transversely isotropic layered media. Earthquake Engineering and Structure Dynamics, Vol-23, 1239-1251.

Lo-Presti, D. C. F. (1989). Proprieta dinamiche dei terreni. Atti Deile Conference di Geotechnica di Torino, Vol. 2, 1-62.

Luo, X. and Murono, Y. (2001). Seismic analysis of pile foundations damaged in the January 17, 1995 South Hyogo earthquake by using the seismic deformation method. Proceedings of 4th International Conference Recent Advances in Geotechnical Earthquake Engineering and Soil Dynamics, San Diego, USA.

Madabhushi, S. P. G., Schofield, A. N., and Lesley, S. (1998). A new stored angular momentum (SAM) based actuator. Proc. Centrifuge 98, Balkema, Rotterdam, The Netherlands, 111–116.

Makris, N., Gazetas, G., and Delis, E. (1996). "Dynamic soil-pile foundation-structure interaction: Records and Predictions," Geotechnique, 46(1), 33-50.

Mair, R.J. (1993). Developments in geotechnical engineering research: applications to tunnels and deep excavations. Unwin Memorial Lecture 1992, Proceedings of the Institution of Civil Engineers. ICE, London, Vol. 97, No. 1, 27-41.

Mamoon, S. M. and Banerjee, P. K. (1990). Response of piles and pile groups to traveling SH-waves. Earthquake Engineering and Structural Dynamics, Vol. 19, No. 4, 597-610.

Maragakis, E.A., Douglas, B.M. ans Abdel-Ghaffar, S.M. (1994) , An Equivalent Linear Finite Element Approach for the Estimation of Pile Foundation Stiffness. Earthquake Engineering. And Structure Dynamics, Vol-23, 1115-1129

Margason, E. (1975). Pile bending during earthquakes. Lecture, 6 March 1975, ASCE-UC/Berkeley Seminar on Design Construction and Performance of Deep Foundations (unpublished).

Margasson, E. (1977). Pile Bending During Earthquakes. Design, Construction, and Performance of Deep Foundations Seminar, ASCE, Berkeley, California.

Masing, G. (1926). 'Eigenspannungen und Verfestigung beim Messing. Proceedings of 2nd International Congress of Applied Mechanics, Zurich, Switzerland, 332–335.

Matasovic, N. and Vucetic, M. (1995). Generalized cyclic degradation pore pressure generation model for clays. Journal of Geotechnical Engineering, Vol. 121, No. 1, 33-42

Matlock, H. (1962). Correlations for design of laterally loaded piles in soft clay. Rpt.To Shell Oil Co., Engineering Science Consultants, September.

Matlock, H. and Reese, L.C. (1960). Generalized solutions for laterally loaded piles, Transaction of the American Society of Civil Engineers, Vol.127, part 1, pp.1220-1247.

Matlock, H., Foo, S.H., and Bryant, L.L. (1978). Simulation of lateral pile behavior. Proceedings, Earthquake Engineering and Soil Dynamics, ASCE, 600-619.

Meli, R., Faccioli, E., Muria-Vila, D., Quass, R. and Paolucci, R. (1998). A study of site effects and seismic response of an instrumented building in Mexico City. Journal of Earthquake Engineering, Vol. 2, No. 1, 89-111.

Mendoza, M. and Romo, M. (1989). Behavior of Building Foundations in Mexico City During the 1985 Earthquake: Second Stage. Lessons Learned from the 1985 Mexico Earthquake, *Pub. 89-02*, Earthquake Eng. Research Inst., 66-70.

Messerklinger, S. (2006). Non-linearity and small strain behaviour in lacustrine clay**.** PhD thesis, ETH-Zurich, Switzerland.

Meymand, P. J. (1998). Shaking table scale model tests of nonlinear soil-pile-superstructure interaction in soft clay. PhD thesis, Univ. of California, Berkeley, USA.

Mizuno, H. and Iiba, M. (1992). Dynamic Effects of Backfill and Piles on Foundation Impedance. *Proc.* 10th WCEE, Madrid, Vol. 3, 1823-1828.

Nasim, A. S. M. (1999). Numerical modeling of soil profile and behaviour in deep excavation analyses. M. Eng. Thesis. National University of Singapore.

Ng, T .G. and Lee, F. H. (2002). Cyclic settlement behaviour of spudcan foundations. Geotechnique, Vol. 52, No. 7, 469-480.

Nikolaou, A. S., Mylonakis, G. and Gazetas, G. (1995). Kinematic bending moments in seismically stressed piles. Report NCEER-95-0022, National Center for Earthquake Engineering Research. Buffalo: State University of New York, USA.

Nikolaou, S., Mylonakis, G., Gazetas, G. and Tazoh, T. (2001). Kinematic pile bending during earthquakes: analysis and field measurements. Geotechnique, Vol. 51, No. 5, 425-440.

Nishimura, I. and Jardine, R. J. (2005). Laboratory study of anisotropy of natural London clay. Report to LMA. Funding: EPSRC, London, United Kingdom.

Novak, M. (1974). Dynamic Stiffness and Damping of Piles. Canadian Geotech. Journal, Vol-11, 574- 598.

Novak, M. (1974). Dynamic stiffness and damping of piles. Canadian Geotechnical Journal, Vol. 11, No. 4, 574-598.

Novak, M. and El-Sharnouby, B. (1983). Stiffness and damping constants of single piles. Journal of the Geotechnical Engineering Division, ASCE , Vol. 109, No.7, 961-974.

Novak, M. and Grigg, R. (1976). Dynamic experiments with small pile foundations. Canadian Geotechnical Journal, Vol. 13, No. 4, 372-385.

Ohira, A., Tazoh, T, Dewa, K., Shimizu, K., and Shimada, M. (1984). Observations of earthquake response behaviors of foundation piles for road bridge. Proc. 8th World Conf. Earthquake Eng., San Francisco, Vol. 3, 577-584.

Okahara, M., Nakatani, S., & Matsui, K. 1991a. A study on vertical and horizontal bearing characteristics of piles, JSCE J. of Struct. Engrg. 37, 1453-1466. In Japanese.

Okahara, M., Takagi, S., Nakatani, S., & Kimura, Y. 1991b. A study on the bearing capacity of single piles and design method of column shaped foundations. Technical Memorandum of PWRI (2919), Public Works Research Institute. In Japanese.

Pan, T. C., Megawati, K. and Lim, C. L. (2007). Seismic shaking in Singapore due to past Sumatran earthquakes. Journal of Earthquake and Tsunami, Vol. 1, 49–70.

Papa, V. Silvestri, F. and Vinale, F. (1988). Analisti delle proprieta di un tipico terrano piroclastico mediante prove di taglio semplice. In Atti del I Convegno del Gruppo Nazionale di Coordinamento per gli Studi di Ingengneria Geotechnica, Moselice, 265-286

Penzien, J., Scheffy, C., and Parmelee, R. (1964). Seismic analysis of bridges on long piles. Journal of Engineering Mechanics Division, Vol. 90, No. 3, 223-254.

Perzyna, J.K. (1966). Fundamental problems in viscoplasticity. Adv. Appl. Math., Vol.9, 243–377.

Perzyna, P. (1963). The constitutive equations for rate sensitivem plastic materials. Q. Appl. Math., Vol.20, 321–332.

Pitts, J. (1984). A review of geology and engineering geology in Singapore. Q. Journal of Engineering Geology, Vol. 17, 93-101.

Prakash, S. (1962). Behavior of pile groups subjected to lateral loads. Ph.D. Thesis, Univ. of Illinois, USA.

Prakash, S. and Chandrasekaran, V. (1977). Free vibration characteristics of piles. Proceedings of Ninth International Conference of Soil Mechanics and Foundation Engineering, Tokyo, Vol. 2, 333-336.

Puri, V. and Prakash, S. (1992). Observed and predicted response of piles under dynamic loads, Geotech. Spec. Pub. 34, ASCE, 153-169.

Puri, V. K. and Prakash S. (2008). Pile design in liquefying soil. Proceedings of 14th World Conference on Earthquake Engineering, Beijing, China, 1-8.

Puzrin, A. M. and Burland, J. B. (1998). Non-linear model of small-strain behaviour of soils. Geotechnique, Vol. 48, No. 2, 217-233.

Puzrin, A., Frydman, S. and Talesnick, M., (1995). Normalising degrading behaviour of soft clay under cyclic simple shear loading, Journal of the Geotechnical Engineering Division, ASCE , Vol. 121, No.12, 836–843.

Pyke, R. (1979). Nonlinear soil models for irregular cyclic loadings. Journal of the Geotechnical Engineering Division, ASCE, Vol.105, 715–726.

Rao, S. N. and Panda, A.P. (1999). Non-linear analysis of undrained cyclic strength of soft marine clay. Ocean Engineering, Vol. 26, 241–253.

Reese, L. and Wang, S. (1990). Documentation of Computer Program APILE2 Version 1.0: Axial Load-Settlement Analysis of Piles. Ensoft, Inc.

Richardson, D. (1988). Investigations of threshold effects in soil deformations, PhD thesis, City University, London, United Kingdom.

Richart, F. E. (1962). Foundation vibrations. Transactions , ASCE, Vol. 127, Part 1, 863-898.

Roscoe, K. (1968). Soils and model tests. Journal of Strain Analysis, Vol. 3, No.1, 57-64.

Saha, S. and Ghosh, D.P. (1986). Dynamic lateral response of piles in coupled mode of vibration. Soils and Foundations, Vol. 26, No.1, 1-10.

Sangrey, D. A. (1968). The behaviour of soils subjected to repeated loading. PhD Thesis, Cornell University, USA.

Santagata, M.C. (1999). Factors affecting the initial stiffness and stiffness degradation of cohesive soils. PhD Thesis, Massachusetts Institute of Technology, Boston, USA.

Schnabel, P. B., Lysmer, J. and Seed, H. B. (1972). SHAKE: a computer program for earthquake response analysis of horizontally layered sites. UCB/EERC-72/12, Earthquake Engineering Research Center, University of California, Berkeley, 1972-12, 92 pages (480/S36/1972)

Schofield, A. and Roth, P. (1968). Critical State Soil Mechanics. McGraw-Hill Book Company.

Scott, R., Liu, H., and Ting, J. (1977). Dynamic pile tests by centrifuge modeling. Proceedings of 6th World Conference on Earthquake Engineering, New Delhi, Vol. 2, 1670-1674.

Seed, H. B. (1979). Soil liquefaction and cycic mobility evaluation for level ground during earthquakes. Geotech. Spec. Pub. 103(GT4). ASCE, 201-255.

Seed, H. B., Wong, R. T., Idriss, I. M., and Tokimatsu, K. (1986). Moduli and damping factors for dynamic analyses of cohesionless soils. Journal of Geotechnical Engineering, ASCE, Vol.112, No.11, 1016–1032.

Seed, R., Dickenson, S., Riemer, M., Bray, J., Sitar, N., Mitchell, J., Idriss, I., Kayen, R., Kropp, A., Harder, L. Jr., and Power, M. (1990). Preliminary Report on the Principal Geotechnical Aspects of the October 17, 1989 Loma Prieta Earthquake. Rpt. No. UCB/EERC-90/05, Earthquake Eng. Research Ctr., Univ. of California.

Shen, W.Y. & Teh, C.I. (2004). Analysis of Laterally Loaded Piles in Soil with Stiffness Increasing with Depth. Journal of Geotechnical and Geoenvironmental Engineering, ASCE, Vol-130, No.8, 179-215.

Sheta, N. and Novak, M. (1982). Vertical vibrations of pile groups. Journal of the Geotechnical Engineering, ASCE , Vol. 108, No. GT4, 570-590.

Shibuya, S., Mitachi, T., Fukuda, F. and Degoshi, T. (1995). Strain rate effects on shear modulus and damping of normally consolidated clay. Geotechnical Testing Journal, Vol. 18, No. 3, 365–375.

Shirato, M., Nakatani, S., Matsui, K. and Nakaura, T. (2005).Geotechnical criterion for serviceability limit state of horizontally-loaded deep foundations. In-house report to Public Works Research Institute, Tokyo, Japan.

Silvestri, F. (1991). Stress-strain behaviour of natural soils by means of cyclic dynamic torsional shear tests. International Conference on Experimental Characterization and Modeling of Soils and Soft rocks. University pf Napoli, Federico II, 7-73.

Simpson, B. (1992). Retaining structures: displacement and design. Rankine Lecture, Géotechnique, Vol. 42, No. 2, 541-576.

Singh, J.P. (1977). Design of Machine Foundation on Piles. Journal of Geotechnical Engineering, ASCE, Vol-103, GT8, 863-870.

Singh, J.P. (1977). Design of machine foundation on piles. Journal of Geotechnical Engineering. ASCE, Vol. 103, GT8, 863.

Snyder, J. L. (2004). Full scale test lateral load tests of a 3x5 pile group in soft clays and silts. MSc thesis, Brigham Young University, USA.

Sreerama, K. (1993). Dynamic pile-soil-pile interaction using model tests under simulated earthquakes. Ph.D. Thesis, University of Missouri-Rolla, USA.

Stallebrass, S.E. (1990). Modelling the effect of recent stress history on the deformation of overconsolidated soils. Ph.D. Thesis, The City University, London, UK.

Stewart, J., and Stewart, A. (1997). Analysis of soil-structure interaction effects on building response from earthquake strong motion recordings at 58 sites. Rpt. No.UCB/EERC-97/01, Earthquake Eng. Research Ctr., Univ. of California.

Stokoe, K. H., Hwang, S. H., Lee, J. N.-K., and Andrus, R. D. (1995). Effects of various parameters on the stiffness and damping of soils at small to medium strains. Proceedings of 1st International Conference on Pre-Failure Deformation Characteristics of Geomaterials: Pre-failure Deformation of Geomaterials, Balkema, Rotterdam, The Netherlands, 785–816.

Streeter, V.L., Wylie, E.B. and Richart, F.E. (1975). Soil motion computations by characteristics method. Journal of the Geotechnical Engineering Division, ASCE, Vol.100, 247–263.

Sy, A. and Siu, D. (1992) Forced vibration testing of an expanded base concrete pile. Geotech. Spec. Pub. 34, ASCE, 170-186.

Tabesh, A. (1997). Lateral seismic analysis of piles. PhD Thesis, University of Sydney, Australia.

Tabesh, A. and Poulos, H. G. (2007). Design charts for seismic analysis of single piles in clay. Proceedings of the Institution of Civil Engineers Geotechnical Engineering 160, Issue GE2, 85–96.

Tamura, K., Fujiwara, T., and Morishige, R. (1973). Damage of Rigid Frame Bridges in the Off Tokachi Earthquake 1968. Proceedings of Japan Earthquake Eng. Symposium, Tokyo, 47-154.

Tao, X., Kagawa, T., Minowa, C., and Abe, A. (1998). Verification of Dynamic Soil-Pile Interaction. Proceedings of 3rd International Conference on Geotechnical Earthquake Engineering and Soil Dynamics, ASCE, Seattle, USA, 1199-1210.

Taylor, P.W. and Bacchus, D.R. (1969). Dynamic cyclic strain tests on clay, Proceedings of 7th International Conference on Soil Mechanics, Mexico, Vol.1, 401-409.

Tazoh, T., Shimizu, K., and Wakahara, T. (1987). Seismic observations and analysis of grouped piles. in Dynamic Response of Pile Foundations - Experiment, Analysis, and Observation, Geotech. Spec. Pub. 11, ASCE, 1-20.

Teachavorasinskun, S., Thongchim, P., and Lukkunaprasit, P. (2001). Shear modulus and damping ratio of a clay during undrained cyclic loading. Geotechnique, Vol. 51, No.5, 467–470.

Teachavorasinskun, S., Thongchim, P., and Lukkunaprasit, P. (2002). Stress rate effect on the stiffness of a soft clay from cyclic, compression and extension triaxial tests. Geotechnique, Vol. 52, No.1, 51-54.

Thammathiwat, A and Weeraya, C.(2004). Behavior of strength and pore pressure of soft Bangkok Clay under cyclic loading. Thammasat International Journal of Science and Technology, Vol. 9, No. 4, 21-28.

Thiers, G.R. and Seed, H.B. (1968). Cyclic stress–strain characteristics of clay. Journal of the Soil Mechanics and Foundations Division, ASCE 94, 555–569.

Ting, C. P. (2002). Characterisation of Singapore lower marine clay. Ph.D. thesis, National University of Singapore.

Ting, J. and Scott, R. (1984). Static and Dynamic Lateral Group Action, Proceedings of 8th World Conference on Earthquake Engineering, San Francisco, Vol. 3, 641-648.

Trochanis, A.M., Bielak, J., and Christiano, P. (1991). Simplified model for analysis of one or two piles. Journal of Geotechnical Engineering, ASCE, Vol. 117, No. 3, 448-466.

Tsujino, K., Asai, K., Yanabu, K, and Goto, Y. (1987). "Earthquake response of on-ground LNG storage tank founding on pile group. Proc. Pacific Conf. Earthquake Eng., New Zealand, Vol. 3, 163-171.

Unjoh, S. and Terayama, T. (1998). Design Specifications of Highway Bridges, Part V., Seismic Design. Earthquake Engineering Division, Earthquake Disaster Prevention Research Center, Public Works Research Institute.

Viggiani, G. and Atkinson, J. H. (1995). Stiffness of fine-grained soils at very small strains. Geotechnique, Vol. 45, No. 2, 249-265.

Vucetic, M and Dobry, R. (1991). Effect of soil plasticity on cyclic response. Journal of Geotechnical Engineering, ASCE, Vol. 117, No. 1, 89-107.

Vucetic, M. (1988). Normalised behaviour of offshore clay under uniform cyclic loading. Canadian Geotechnical Journal, Vol. 25, 33–41.

Vucetic, M. and Dobry, R. (1988). Degradation of marine clays under cyclic loading. Journal of the Geotechnical Engineering Division, ASCE, Vol. 114, No.2, 133–149.

Wang, S., Kutter, B.L., Chacko, M.J., Wilson, D.W., Boulanger, R.W., and Abghari, A. (1998). Nonlinear seismic soil-pile structure interaction. Earthquake Spectra, EERI, Vol. 14, No. 2, 377-396.

Wen, R. (1955). Model studies of laterally loaded pile foundations. Proc. 34th Annual Meeting, Highway Research Board, 140-152.

Wen, Y.-K. (1976). Method for random vibration of hysteretic systems, Journal of the Engineering Mechanics Division, ASCE, Vol. 102, No. EM2, 249-263.

Whittle, A.J. (1993). Evaluation of a constitutive model for overconsolidated clays. Géotechnique, Vol. 43, No. 2, 289-313.

Wilson, D. (1998). Dynamic centrifuge tests of pile supported structures in liquefiable sand. PhD thesis, Univ. of California, Davis, USA.

Wood, H. (1908). Distribution of Apparent Intensity in San Francisco in The California Earthquake of April 18, 1906. Report of the State Earthquake Investigation Comm. (Source: UC Berkley Archives).

Carnegie Inst. of Washington, Washington, D.C., 220-245.

Wood, D. M. (1974). Some aspects of mechanical behaviour of kaolin clay under truly triaxial conditions of stress and strain. PhD Thesis, Cambridge University, United Kingdom.

Wood, D. M. (1982). Laboratory investigations of the behavior of soils under cyclic loading: A review. Soil mechanics—Transient and cyclic loads. Wiley, New York, 513–582.

Yasuhara K., Yamanouchi T. and Hirao K. (1982). Cyclic stress – strain and strength performance of soft clay. Symposium on Recent Development in Laboratory and Field Tests and Analysis of Geotechnical Problems. 206-229.

Yu, Y. and Lee, F. H. (2002). Seismic response of soft ground. Proceedings of Physical Modeling in Geotechnics-ICPMG'02, St. Jhon's, Canada, 519-524.

Zanvoral, D. Z. and Campanella, R.G., (1994). Frequency effects on damping/modulus of cohesive soil. Dynamic Geotechnical Testing II, ASTM STP 1213, 191-201.

Zhang, X .Y. (2006). Behaviour of caisson breakwater subject to breaking waves. PhD Thesis, National University of Singapore.

Zhang, F., Kimura, M., Nakai, T. and Hoshikawa, T. (2000). Mechanical behavior of pile foundations subjected to cyclic lateral loading up to the ultimate state. Soils and Foundations, Vol. 40, No. 5, 1-17.

Zhu, H. and Chang, M. F. (2002). Load transfer curves along bored piles considering modulus degradation. Journal of Geotechnical and Geoenvironmental Engineering, ASCE, Vol. 128, No. 9, 764-774.

APPENDIX A RATIO OF FUNDAMENTAL FREQUENCY OF PILE-RAFT SYSTEM TO THAT OF CLAY

The pile-raft structure can be considered as a single degree of freedom system where, m is the mass of the raft, mass of pile is negligible compared to raft and E_pI_p is flexural rigidity of the pile.

Now, stiffness of the system can be worked out from simple structural analysis as,

$$K = \frac{a * E_p I_p}{l_p^3}, \tag{A.1}$$

where, a is a constant whose value depends on the end condition. Hence natural frequency of the pile-raft system without soil,

$$w_m = \sqrt{\frac{a * E_p I_p}{m l_p^3}} \tag{A.2}$$

Now, for a soil layer of thickness equal to length of pile (l_p), fundament period can be expressed as,

$$T_s = \frac{4 l_p}{V_s}, \tag{A.3}$$

where V_s is the shear wave velocity in soil, $V_s = \sqrt{\frac{G_s}{\rho_s}}$

Hence natural frequency of the soil,

$$w_s = \frac{2\pi}{T_s} = \frac{2\pi V_s}{4l_p} = \frac{\pi}{2l_p}\sqrt{\frac{G_s}{\rho_s}} \tag{A.4}$$

Therefore, from equation A.2 and A.4, the ratio of the fundamental frequency of the pile-raft system to that of the clay,

$$\frac{w_m}{w_s} = \frac{\sqrt{\frac{a * E_p I_p}{m l_p^3}}}{\frac{\pi}{2l_p}\sqrt{\frac{G_s}{\rho_s}}} = Cx\sqrt{\frac{E_p I_p \rho_s}{G_s m l_p}} \tag{A.5}$$

Hence the dimensionless group can be chosen as frequency ratio,

$$a_0 \approx \frac{E_p I_p \rho_s}{G_s m l_p} \tag{A.6}$$